DESIGN AND ANALYSIS OF A TEST RIG FOR MODELING THE

BIT/FORMATION INTERFACE IN PETROLEUM DRILLING APPLICATIONS

A Thesis

by

JOSHUA KYLE WILSON

Submitted to the Office of Graduate Studies of
Texas A&M University
in partial fulfillment of the requirements for the degree of

MASTER OF SCIENCE

Approved by:

Chair of Committee,   Alan Palazzolo
Co-Chair of Committee,   Mansour Karkoub
Committee Member,   Edward White
Head of Department,   Andreas Polycarpou

May 2013

Major Subject: Mechanical Engineering

ABSTRACT

Equipment failure and well deviations are prevailing contributors to production delays within the petroleum industry. Particular monetary focus is given to the drilling operations of wells to overcome these deficits, in order to extract natural resources as efficiently, and as safely, as possible. The research presented here focuses on minimizing vibrations of the drill string near the bottom-hole assembly (BHA) by identifying the cause of external forcing on the drillstring in vertical and horizontal wells and measuring the effects of various factors on the stability of perturbations on the system. A test rig concept has been developed to accurately measure the interaction forces and torques between the bit, formation and fluids during drilling in order to clearly define a bit/formation interface law (BFIL) for the purpose vibrational analysis. As a secondary function, the rig will be able to measure the potential inputs to a drilling simulation code that can be used to model drillstring vibrations. All notable quantities will be measured including torque on bit (TOB), weight on bit (WOB), lateral impact loads (LIL), formation stiffness, bit specific properties, fluid damping coefficients and rate of penetration (ROP). The conceptual design has been analyzed and refined, in detail, to verify its operational integrity and range of measurement error. The operational envelope of the rig is such that a drill bit of up to 8 ½ inches in diameter can be effectively tested at desired operational parameters (WOB: 0-55,000 lb_f, RPM: 60-200) with various rock formations and multiple fluid types. Future use and design possibilities are also discussed to enhance the functionality of the rig and the potential for further research in the area of oil and gas drilling and vibrational modeling.

DEDICATION

To my loving fiancé, without whom this thesis would not have been written.

ACKNOWLEDGEMENTS

NOMENCLATURE

A	cross sectional area of lateral force measurement rod
A_c	cutting area
A_f	frictional area
$A_{Nozzles}$	nozzle area
BFIL	Bit Formation Interface Law
BHA	Bottom Hole Assembly
C_d	nozzle coefficient
C_S	cutter size
CAD	Computer Aided Design
CSS	Confined Compressive Strength
δ	small displacement
d	depth of cut per bit revolution
D_B	bit diameter
D_{EFF}	effective diameter
D_H	hydraulic diameter
D_{IP}	inner pipe diameter
D_{OP}	outer pipe diameter
D_i	inner diameter
D_o	outer diameter
ΔP	change in pressure
ΔP_P	pressure loss through pipe
ΔP_B	pressure loss through bit
ΔP_A	pressure loss in annulus
ε	mechanical specific energy
ϵ	material roughness
ϵ_a	axial strain from axial loading
ϵ_t	axial strain from transverse loading

f	fluid friction factor
F_s	side load on formation
F_t	transverse force
FEA	Finite Element Analysis
FOS	Factor of Safety
γ	general bit property
$\dot{\gamma}$	fluid shear rate
GF	gauge Factor
H_e	Hedstrom Number
η	mechanical bit efficiency
I	area moment of inertia
K	power law fluid coefficient
k	coefficient
l	wear-flat length
L	length between gauge and cantilevered load
LIL	Lateral Impact Loads
μ	friction coefficient
μ_p	plastic liquid viscosity
MWD	Measure While Drilling
n	number of blades per bit
Ω	bit rotational speed
P	pressure
ppg	pound per gallon
Q	fluid flow rate
QNRF	Qatar National Research Fund
R_e	Reynolds Number
R_{ecrit}	critical Reynolds number
ρ_m	density of drilling fluid
R_o	outer radius

R_i	inner radius
ROP	Rate of Penetration
RPM	Rotations per Minute
S	compressive strength of formation
σ_*	uncertainty of specified variable (*)
σ_y	yield stress
T	temperature
T_c	cutting component of torque on bit
T_d	drilling component of torque on bit
T_f	frictional component of torque on bit
T_o	torque applied at bit
TOB	Torque on Bit
τ	shear stress
τ_y	fluid yield stress
θ	back rake angle
UCS	Un-confined Compressive Strength
VCEL	Vibration Control and Electro-Mechanics Laboratory
v_{ann}	fluid velocity in annulus
v_{pipe}	fluid velocity in pipe
V_{EX}	excitation voltage
V_o	voltage output
mV_o	millivolt output
W_c	cutting component of weight on bit
W_d	drilling component of weight on bit
W_f	frictional component of weight on bit
W_o	weight applied at bit
$\dot{W}_p$	pump power
WOB	Weight on Bit
x	characteristic cutter dimension

TABLE OF CONTENTS

LIST OF FIGURES

LIST OF TABLES

1. INTRODUCTION

1.1. Background

Rotary drilling has become the global standard in the exploration and production of hydrocarbon resources. A typical operation consists of a derrick, rotary drive system, mud circulation equipment, a drill string and bit (Figure 1.1). The drill string is comprised of several lengths of pipe that serve as a means to transmit torque, apply adequate weight to the bit (WOB), transport fluids down hole and more recently has been used as a telemetry tool for relaying logging information to the surface [1, 2]. Drillstrings are typically subdivided into two main tubing sections: the drill pipe and the drill collars. The collars are usually much thicker than the drill pipe and have a primary function of applying the WOB. Together, the collars and the bit are typically referred to as the Bottom Hole Assembly (BHA). In practice, many BHAs include measurement components, operational tools or mud motors, which are frequently seen in directional drilling applications.
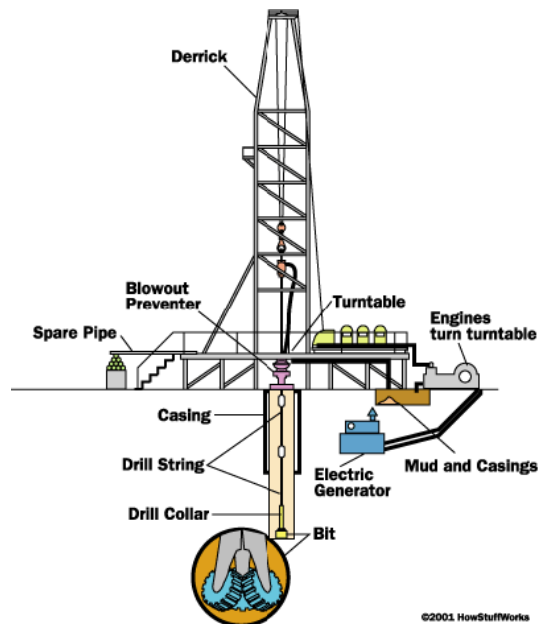
Figure 1.1:   Typical Drilling Rig Setup (From [3])

While early 20th century technology has limited wells to primarily vertical configurations, the world starting seeing its first dose of directional drilling as early as 1930 [4]. It wasn't until 1980 however, that the appeal of horizontal wells really took hold [5] as an economical means of reservoir exploitation. Over the past 30 years, modern advancements in technology have led to directional well configurations being a customary occurrence in large scale operations, particularly in low permeability formations such as the large shale plays in the US [6]. With modern BHA configurations and derrick structures, drillers have been able to reach reservoirs that were previously thought to be unobtainable; with measured depths in excess of 30,000 feet, as can be seen with ExxonMobil's z-12 well in the Chayvo Field of Russia with a measured depth of 38,320 feet or Maersk Oil Qatar's BD-04A well with a measured depth of 40,320 feet [7]. The drilling of such wells requires accurate guidance of the bit while rotating, which naturally presents challenging structural and control problems. In addition to the extensive engineering that accompanies this type of dynamic execution, the process of steering a bit becomes even more complicated by the presence of vibrations that are inherent in all drilling systems.

Uncontrolled vibrations can lead to a multitude of unfavorable conditions such as bit deviation (bit walking), damage of equipment or even catastrophic failure of the BHA. Losses contributed to vibrations during drilling are estimated to be on the order of $300 Million per year on a global scale [8] and these financial penalties tend to grow exponentially as a well gets deeper [9]. Reports of such deficits, along with the standardized use of directional drilling on deeper and further reaching wells, allude to a needed improvement in monitoring, evaluating and controlling vibrations of the BHA. A full understanding of the vibrational tendencies of a system will inevitably lead to a better means of controlling such oscillations and reduced costs associated with well development.

1.2. Literature Review

Numerous efforts have gone in to the characterization of drillstring dynamics for both vertical and horizontal wells, all of which perpetuate the understanding of what exactly goes on down-hole. A couple of authors have been able to identify key frequencies in drilling systems and the type of vibration they are typically associated with, as can be seen by Figure 1.2 and Figure 1.3. Others have expressed observations of dynamic stability zones shown in Figure 1.4 and Figure 1.5.
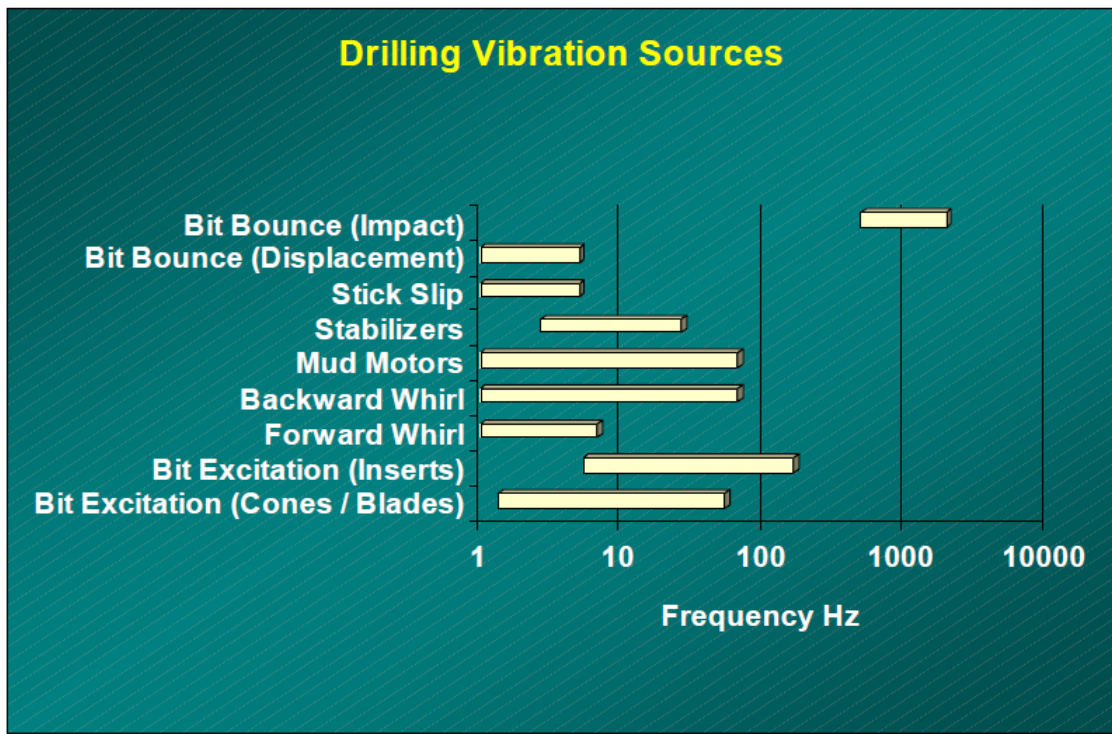
Figure 1.2:   Sources of Vibration in Drilling (From [10])
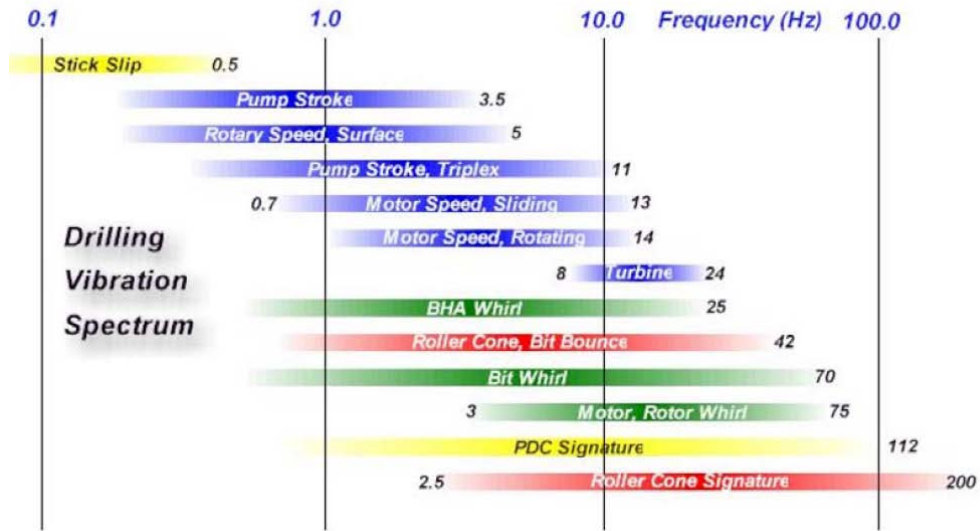
Figure 1.3: **Frequency Domain of Drilling Systems (From [11])**
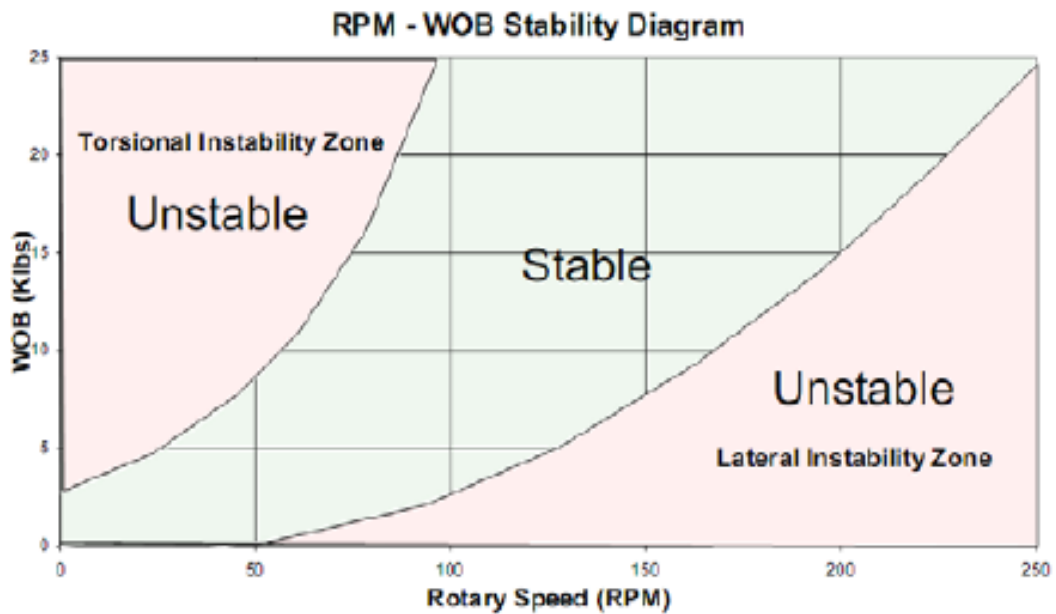
Figure 1.4: **Operational Stability Zone of PDC Bits (From [12])**
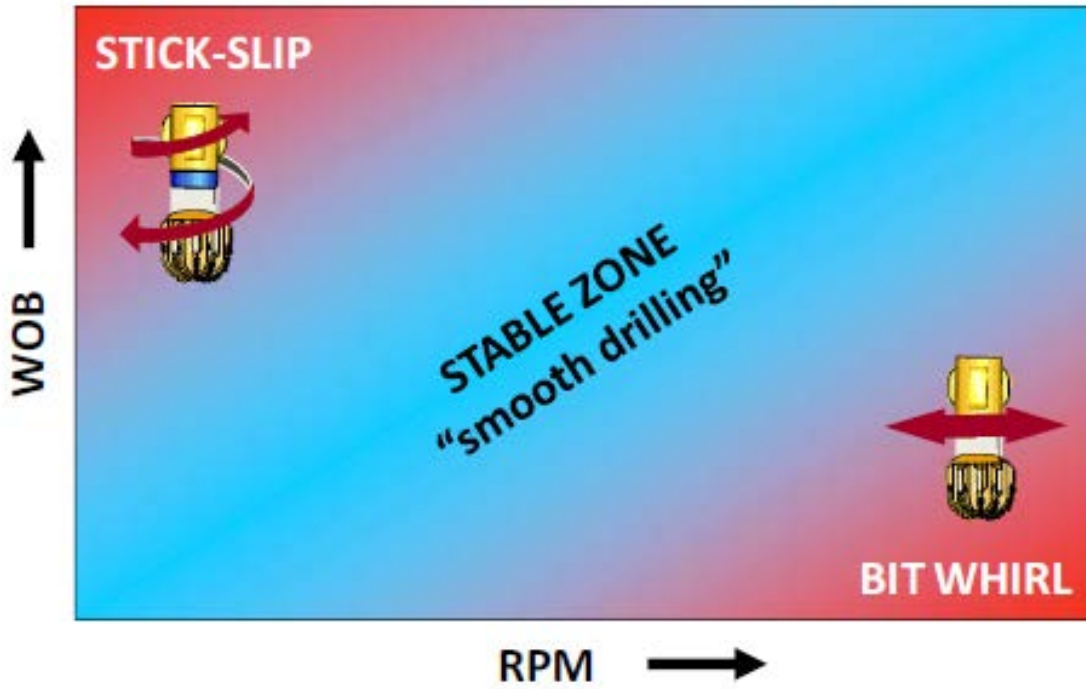
Figure 1.5:   Operational Stability Zone of PDC Bits (From [13])

It is apparent from these figures that vibrations have a significant presence in drilling and are virtually intrinsic to all drilling systems. Because of this fact, vibrations have been a large area of study over the years. A sizeable undertaking in characterizing the oscillations in drill stings is prevalent in the literature; however due to the complexities involved in modeling such systems, the majority of authors narrow their focus to one or two types of vibrations in attempts to isolate variables of the dynamic study. The focus of many PDC bit investigations, for example, are related to torsional phenomena [14-24] or various oscillations coupled with stick-slip [25-30]. Other authors shed light on lateral motions and the contact forces induced by these vibrations [31-34]. A recent course of study has involved the exploration of the coupling between different modes of oscillation in an attempt to better understand the complete dynamics of the system [35, 36]. While there have been a few efforts to model drill string fluctuations in a comprehensive manner [37-39], these approaches lack a thorough understanding of the mechanics behind the drilling and attenuate their focus strictly on the motion of the drillstring rather than the root cause and continued external forcing of such phenomena.

Thus, a question presents itself: What is the root cause of vibration in drilling, and how does the drillstring's interaction with the wellbore affect these induced oscillations? Many authors have explored this problem [16, 22, 25, 40] and most investigations can trace back their understanding of drillstring stimulation to the same principal, which has come to be referred to as the Bit/Formation Interface Law (BFIL). This ill-defined law ultimately dictates the means of external forcing of the drillstring and how the bit reacts to environmental and operational parameters [19, 40-42]. The potential of such a governing relation, gives rise to an important area of study: Defining the principles behind the correct formulation of the BFIL. Much work on the subject has been focused on understanding the behavior of PDC bits and their inherent torsional vibrations, since these are the bits most prevalent in the industry today. An early course of thought on the subject was describing a velocity weakening friction coefficient [14, 17] as being responsible for stick-slip oscillations. This idea, however, has been contradicted by

several authors [22, 25, 43] on the basis that single cutter experiments do not support velocity-dependent friction models [44-46] and there have been numerous investigations into the instability of frictional contact [47-51] that would suggest the apparent "velocity weakening effect" is a function of the dynamics invoked by the precariousness of the interface contact between the bit and the formation not the friction coefficients (i.e. bit lift-off would give the appearance of less TOB).

More promisingly, a method presented by Detournay et al. [43, 52] that has also been explored by others [25] suggests that a time-delay in the surface cutting of PDC bits is to blame for their notorious stick-slip mode of vibration. Detournay's efforts not only lack contradiction, but mark the first notable application of a BFIL into vibrational analysis. The relation derived in this previous work was one that was first suggested by Fairhurst and Lacabanne [53], in which the WOB and TOB are divided into two separate processes: one related to drilling, or cutting, and the other representing friction.
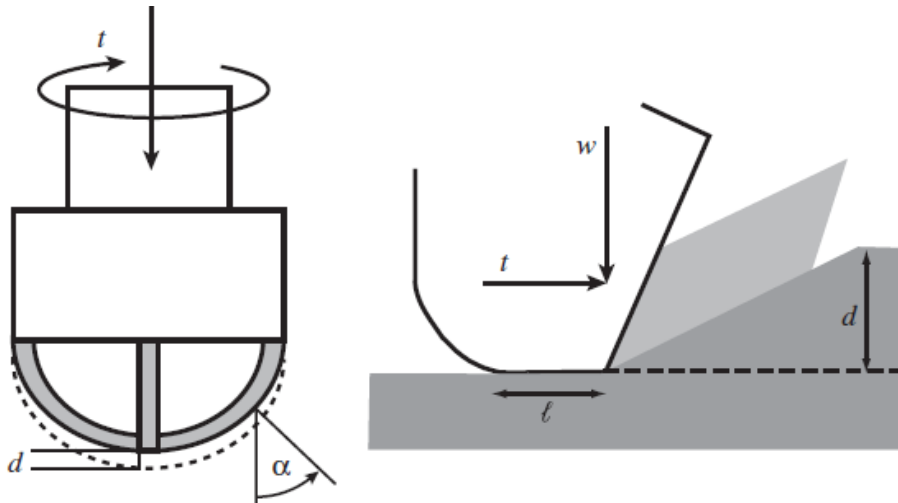
Figure 1.6:   Generalized PDC Bit Model (From [52])

The aforementioned method can be seen in the generalized bit model depicted in Figure 1.6. Models of this type are based on general bit configurations that rely on an idealized

PDC bit geometry. Franca and Mahjoob [54] conducted experiments under a similar assumption to develop a relationship for tri-cone bits in rotary operations and later developed a correlation for tri-cone bits being used in a rotary-percussive manner [55]. While these relationships have led to valuable insights about drilling, the approaches are too broad for proper vibrational analysis. Fixed cutter bits and roller cone bits cannot be generalized by one "common" interface relation. To illustrate this point, Figure 1.7 depicts a variation of bit types that are seen in the field and displays bits that are yet to be developed for large scale operations. A small amount of time looking at the diversity of these rotary bits quickly reveals the necessity of understanding the behavior of each, on an individual basis.

Literature suggests [56],as well as common sense, that the mechanisms of rock destruction are dissimilar for various bits, which inevitably leads to significantly different dynamic behavior for varying bit configurations. For example, roller cone bits have been known to experience a 3-cycle per revolution axial vibration [19, 29, 40] that is not seen in PDC bits, while drag bits are notorious for their ability to excite torsional oscillations [18, 22, 23] that are not as prevalent in roller cone bits. Focusing on each bit's specific drilling mechanism, it is more clearly understood why bits can have such a wide range of dynamic response. Roller cone bits, for instance, rely on a crushing effect to pulverize the rock [57, 58] underneath each tooth and then sweep it out of the way with the bit rotation. This is why tri-cone bits typically require less torque than drag bits, which simply shear the formation [59, 60] as would be seen in a typical machining process. The observable distinction between bit types dictates the need for bit specific interaction laws based on the mechanism enveloped and the operational parameters of the bit.

(a) PDC Bit Profiles

(b) 2-Cone Roller Bit with

Large Milled Teeth

(c) 3-Cone Roller Bit with Small

Insert Teeth

(d) Hybrid Bits

Figure 1.7:   Bit Layout Variations (a –[61], b –[62], c –[54], d –[63])

Several works have presented BFILs of this nature. As mentioned previously, Detournay and Defourny [43] discuss the "divided process" premise in the application of PDC bits while Franca and Mahjoob [54, 55, 64] explore the method as applied to tri-cone bits in rotary and rotary-percussive applications. Dareing et al., Elsayed et al. and Spanos at al. [19, 41, 42] explain how the bit face generates uneven surfaces in the formation as it cuts, leading to a regenerative effect that excites axial motions of fixed cutter bits. Elsayed et al. actually goes on to point out, along with other authors [13, 30, 65], that changes in bit layout can either stabilize or destabilize vibrations, which clearly suggests that a proper definition of the BFIL can lead to better bit designs that minimize oscillations during use. Most authors however have presented general models of this interface that were not intended for vibrational analysis. These models were typically developed for averaged Rates of Penetration (ROP) predictions in attempts to optimize bit selection or predict formation compressive strength. Many works have defined a relation for tri-cone bits in hard and abrasive formations [66-72] and industry standards for this practice are presented in textbooks [9]. A more recent trend of study is the development of relations for PDC bits [56, 73, 74] as these are very common in drilling the large shale plays in the US natural gas surge [6] of today. However, methods applied for PDC bits have been used to also encompass all bit types [56, 75-81] thanks to the concept of Mechanical Specific Energy first presented by Teale [82]. A summary of notable interface relationships can be seen in Appendix A.

An important consideration that has been left out of previously defined BFILs in vibrational studies is the inclusion of walking tendencies of the bit. This is due in part to the fact that authors tend to limit the scope of their investigations, with most being focused on axial and torsional vibrations of PDC bits. However, as directional drilling has become the "norm" of reservoir exploitation, controlling and steering the direction of the bit is more important than ever. Lubinski and Woods [83] first presented the idea of indexing bits based on their operational side force characteristics, or their walking tendency, which has proven to be useful in BHA planning. Mathematically predicting

the direction and magnitude of apparent force based on environment and operating conditions will be imperative to properly evaluating the BFIL.

In addition to the drilling interface, it is also appropriate to investigate other interactions in the drilling process that are not as prevalent in the literature. An appealing subject that is present in most rotor bearing seal systems is the investigation of the fluid film characteristics (typically separating the rotor and the stator in sealing applications) and its effect on system damping. Several authors have explored the rotor and bearing assemblies [84-88] and it is easy to see how these investigations are paralleled to interactions that take place in drill string dynamics. These parallels suggest a course of study beyond what has been investigated solely for drill string oscillations.

1.3. Scope of Research

The study of vibrations in drilling consists of three main areas: The source (initial excitation), the external forcing (BFIL and continued excitation) and the dynamic response (drill string motions). The source of vibrations in these systems has been studied tremendously and is still a topic of discussion, but it is well understood [40-42, 47-51, 89]. The dynamic response of the drilling system has also been studied in detail, as previously outlined, and the motion of the drill string is well characterized by previous endeavors. The focus of the present study is developing the middle ground, the external forcing at the bit/formation interface.

Texas A&M's Vibration Control and Electro-Mechanics Laboratory (VCEL), in collaboration with Dr. Mansour Karkoub (Texas A&M University at Qatar), has received sponsorship from the Qatar National Research Fund (QNRF) as part of a three tier research venture to develop a thorough understanding of the down hole vibrations encountered while drilling. The current stage of the project is the design of a drilling test rig whose main purpose is to validate, disprove or generate bit/formation interface laws that fully define the interaction of the bit with the formation during the drilling process

and its contribution to drillstring vibrations. This relationship will be used as the starting point for modeling oscillations of various BHA assemblies. The rig will also have a secondary function as it will be used to measure and quantify all potential variables affecting the motion of the drill string, such as formation stiffness, fluid damping coefficients, etc. The testing of the rig will result in the identification of these key variables and the development of a drill string simulation code that will be compared to, and validated by, drilling data that is to be obtained from a test well at Texas A&M University's Riverside Campus. Advancements made in the project will lead to a more comprehensive understanding of drillstring dynamics, ultimately supporting the planning and design of future drilling operations and equipment.

1.4. Design Objectives

Recent works on BHA and bit optimization [11, 13, 61, 90-96] have greatly advanced the efforts of vibration mitigation in drilling operations. The QNRF drilling rig project hopes to expand on these previous efforts by identifying and quantifying a clear and definite Bit/Formation Interface Law for various bit types. The data obtained can then be indexed for quick reference in a potential drillstring vibration simulation code.

There are several bit classification systems today; most of which focus on performance characteristics. The aforementioned indexing approach presented by Lubinski and Woods [83] as applied to walking tendencies, or side load characteristics has led to numerous applications of deviation control in today's complex directional drilling operations [97-101]. The database created by the test rig could function in a similar fashion as a "quick bit reference" which could then be implemented into a field tool such as the one presented by Bailey et al [90]. The program presented in this paper provides an efficient field evaluation tool for optimizing BHAs for desired operating conditions. The development of a computational tool and its database counterpart could lead to tremendous economic gains in the drilling industry.

The drilling test rig design presented here is the first step in reaching these goals and its objectives are as follows

a) Design a system that simulates the drilling process and accurately measures all necessary data for complete dynamic modeling of the bit/formation interface.
b) Complete analysis of design to confirm the system's integrity and sustainability.
c) Construction and initial testing of the force/torque measurement system to validate feasibility.
d) Propose necessary tests for pertinent rig data and modeling considerations for vibrational analysis.

The objectives are outlined in detail in the following sections. The rig's development and general layout are discussed in Section 2, followed by a detailed analysis of the design in Section 3. Section 4 and 5 are dedicated to friction testing and measurement calibration, respectively while Section 6 outlines the necessary tests of the rig for adequate BFIL development. Section 7 closes the study with conclusions about the project and an outline of future work.

2. CONCEPT DEVELOPMENT

Complexities in modern engineering have led to the need for an organized method of concept development and technical design. This section is a detailed road map to the rig's design process and an outline of the methodical steps taken to reach a finalized layout of the test rig. A systematic approach was used for the design of the rig; starting with identifying the bare essentials, then transforming the 'basics' into a list of functional requirements, and refining the details as the project progresses to ultimately generate a final design that fulfills the initial requirements. These successive steps, depicted in Figure 2.1, lead to the final design of the rig.

Project development begins with a statement of need that clarifies the overall goal of the rig and is the foundation for which all other ideas are supported. The needs statement reveals the most basic project requirements that would deem the design a success. Once a clear needs statement is presented, then it is broken down into sub-categories using a Function Structure analysis. The Function Structure is a crucial step in identifying the critical needs of the rig and how to meet those needs through engineering considerations; it is a means to identify and examine the details of a design without having prior intuition in regards to the nature of the design. After the function structure is established, performance requirements can be almost directly extracted from it through analytical reasoning or observations of previous operations. Once presented with a list of performance requirements, the iterative design process can be undertaken. Idea generation is comingled with design analysis and eventually the result is a working representation of an adequate test rig.
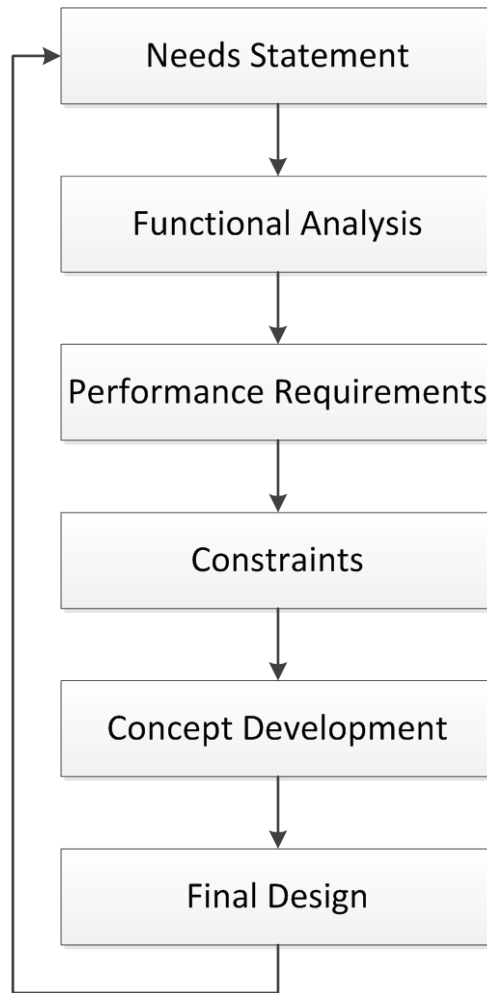
Figure 2.1:   Systems Flow Chart of the Design Process

2.1. Needs Statement

The primary need for the test rig is to be able to effectively, and accurately, measure interaction phenomena occurring at the bit/formation interface. Through the measurement process, it is the hope of the project that a clear Interface Law will be defined. This relationship between the bit and the rock can then be indexed into a database for various bit types. The development of the aforementioned database can lead to vibrational analysis tool that can be used to quickly estimate the response of a system

for various BHA configurations much like the approach shown by Bailey et al [92]. The VybsSM$^{©}$ program presented in this paper gives a good estimate of the general behavior of a specified BHA configuration; the current effort would be able to expand on that idea and employ a database of governing equations for each bit type that would dictate the excitation present at various operating conditions. This tool could be useful in BHA optimization for more adequate well planning.

A secondary, yet still important, utilization of the rig is to be able to identify and measure potential inputs to an adequate drilling simulation code. Items to be quantified include: fluid damping coefficients, bit specific properties, formation stiffness and their relationship to WOB, TOB and lateral impact loads (See section 6).

As a tertiary need, thought is being given to extended use of the rig, beyond the conclusion of the current investigation. For example, the rig's appeal could be marketed to industry bit designers in need of testing. Full scale testing on drilling rigs can be expensive in terms of time and lost profit, so the test rig could serve as an economic alternative.

2.2. Functional Analysis

A functional analysis begins with identifying the overall goal of the project and successively breaking the idea down into smaller components. Starting with the need to define a Bit/Formation Interface Law the most fundamental requirements are extracted through expanding each branch until the structure can no longer be expanded. The results of such an analysis can be seen in Figure 2.2 by following the chart to the bottom of the structure.
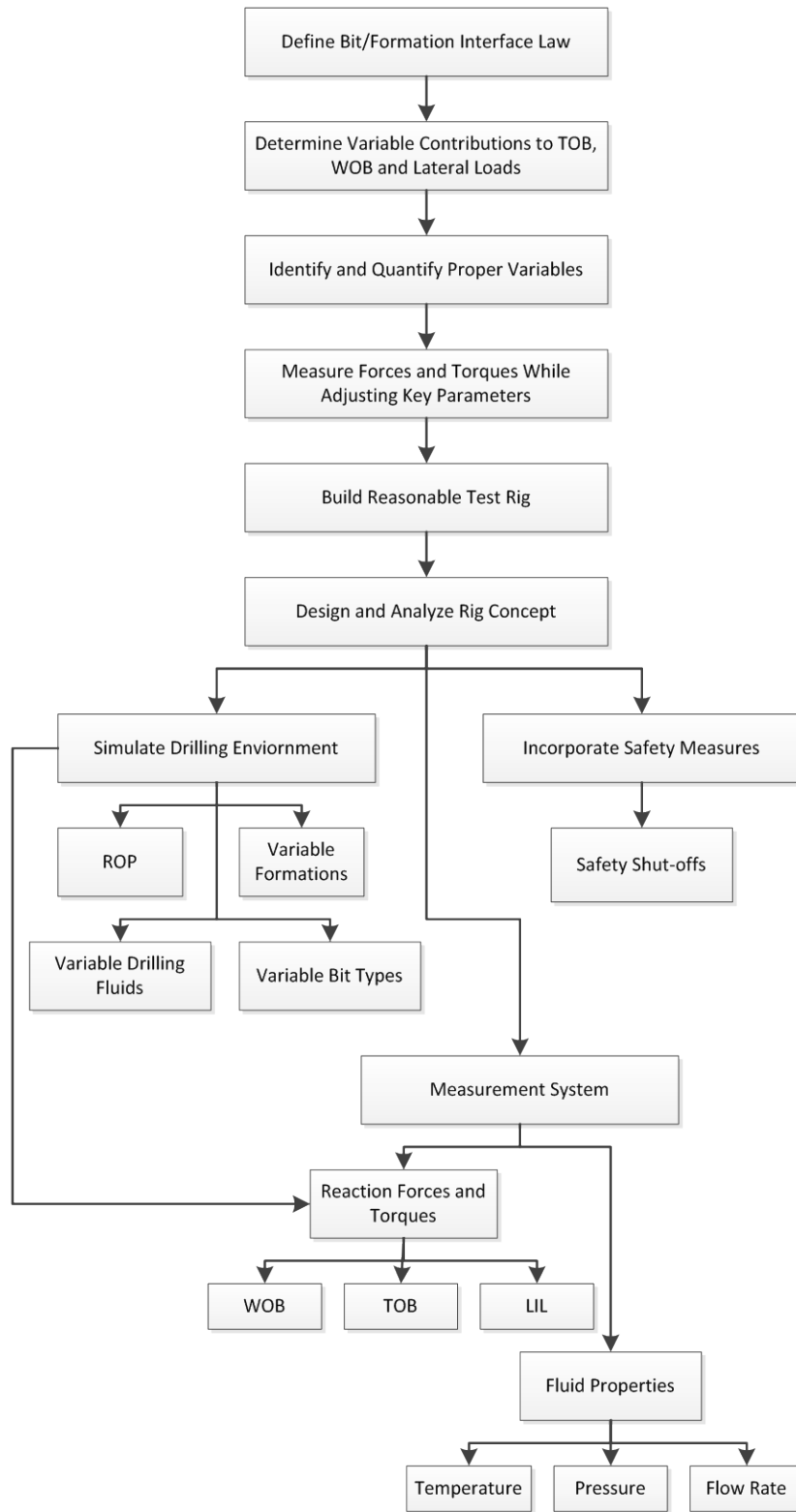
Figure 2.2:   Function Structure

2.3. Performance Requirements and Design Considerations

From the function structure, performance and design requirements can be extracted to identify the rig requirements and give quantifiable understanding of performance needs. Table 2.1 shows the performance requirements that have been determined through computational methods (analytical or numerical) or observation and exploration of field practices.

Table 2.1: Performance Requirements

Functional Requirement	Performance Requirement	Source
Linear Actuation Force	WOB: 55,000 lb_f	Field/ Budget
Linear Actuation Speed	ROP: 0-120 ft/hr	Field
Bit Torque	14,000 ft-lb_f	Calculated
Bit Rotation	60-200 rpm	Field
Max Input System Power	200 HP	Calculated/ Field
Lateral Force	0-4,000 lb_f	Simulation
Transverse Bit Actuation	0-4,000 lb_f	Simulation
Formation Displacement Measurement	0-.01 in.	Calculated/ Simulation
Fluid Pressure Potential	up to 200 psi	Calculated
Fluid Temperature Capability	up to 150 °F	Field
Fluid Flow Rate	up to 300 gpm	Calculated/Field

2.3.1. Design Constraints

The design constraints for the project are based on 3 primary considerations: location, re-location and necessary testing. The location of the rig will dictate the need and layout of any securing connections such as foundation bolts and other "rigid" links. The need to re-locate the rig inspires efficiency of the design in terms of assembly and ease of transportation. The testing procedures required from the rig serve as a template for detailed design. As long as all pieces of the template (testing capabilities) are present, the remainder of the design work is dedicated to creating a more efficient and user friendly machine. Design Constraints include the following:

1. Testing multiple formations
2. Interchangeable bits
3. Multiple fluid types
4. Complete data acquisition of all forces and torques
   a. normal drilling
   b. side loading on bit
   c. lateral impact loads
   d. fluid damping
   e. friction
5. A force/torque measurement system that is external to the bit (i.e. a system that measures the forces on the well bore, not just the bit)

2.3.2. Budget Requirements

As with all projects, there were budget limitations for the test rig. The proposed finances allowed for $50,000 in parts and services each year for two years. It was also projected that there would be additional, external funding to support the Year 2 budget which means that the "over Budget" amount in this table would be covered by this external source. The project was designed around this monetary constraint (Table 2.2 and Table 2.3).

Table 2.2: Year 1 Budget (Measurement System)

	Year 1 Part List	Cost	Source	Part #
	Rock Sample Measurement System			
1	Ball Transfers (x8 @ 147.99 each)	$1,183.92	Balltransfer.com	45 MPS
2	Screw Jack (Inverted - 12" travel)	$574.20	McMaster.com	62255K26
3	Screw Jack Motor	$776.58	McMaster.com	6470K55
4	Screw Jack Mounting Plate Attachment	$53.37	McMaster.com	62255K92
5	Linear Bearings (x4 @ $150.56each)	$602.24	McMaster.com	6489K68
	Drilling Mechanism			
6	Side Inlet Swivel	$5,738.00	AWDS	Swivel 4.5 PE
7	Rail Carriages (x16 @ $543.53 each)	$8,696.48	Purvis (Thomson)	512P55C2
8	Roller Carriage Guide Rails (x4 @ $593.2 each)	$2,372.80	Purvis (Thomson)	
9	Shaft Bearing (Sph Roll Thrust x2 @$764.95)	$1,529.90	http://www.ebay.com/	Nachi Spheri
	Metal Pricing			
10	Inner Sample Container	$700.00	Specialty Pipe of Texas	HFS A106B/C
11	Inner Sample Container Base Weldment	$241.72	McMaster.com	1388K561
12	Outer Sample Container	$2,725.00	Specialty Pipe of Texas	HFS A106B/C
13	Rectangular Steel Tubing	$1,388.66	Discountsteel.com	
14	Steel Plating 24x24x2	$580.85	McMaster.com	1388K881
15	Steel Plating 24x24x1 (x2 @ $416.40 each)	$832.80	McMaster.com	1388K881
16	Steel Plating 36x5x1 (x2 @ $158.65 each)	$317.30	McMaster.com	8910K461
17	Inner Can Support Rods (x8 @ $143.05 each)	$1,144.40	McMaster.com	89495K441
18	Outer Can Support Rods (x2 @ $345.10 each)	$690.20	McMaster.com	88985K811
19	Safety Catch Rods (x8 @ $41.07 each)	$328.56	McMaster.com	9210K191
20	Linear Bearing Supports (x2 @ 306.55 each)	$666.40	McMaster.com	8910K931
21	Hydraulic Pin Support	$416.62	McMaster.com	8846K38
22	Hydraulic Connecting Pin	$104.18	McMaster.com	87205K521
23	Hydraulic Base Plate Stiffening Beams (x4 @$26.83ea.)	$107.32	McMaster.com	8910K845
24	Hoist Ring Plates (x4 6x6x1 @ $129.91/2ft)	$129.91	McMaster.com	8910K63
25	Year 1 Frame Brace Plates (x10 @ $83.32 ea.)	$833.20	McMaster.com	6544K37
26	Screw Jack Motor Mount	$200.00	McMaster.com	8910K925
	Miscellaneous			
27	Screw Jack Torque Coupling	$24.76	Lovejoy	
28	Metric High-Speed Steel Spiral Point Tap (M-14x2)	$47.10	McMaster.com	2605A28
29	Hex Key (12mm)	$4.94	McMaster.com	71285A196
30	Linear Bearing Retaining Rings (x8 @$12.91 each)	$103.28	McMaster.com	9968K31
31	Retaining Ring Pliers	$26.81	McMaster.com	5449A83
32	Lubricating Hand Pump	$30.12	McMaster.com	136K27
33	Rail Carriage Grease (10@ $11.40)	$114.00	McMaster.com	3246K32
34	Washers for M12 Screws (x16 @ $7.17/25)	$7.17	McMaster.com	90965A210
35	Hoist Rings Year 1 Structure (4,000 lbf) - (x4 @ $64.90ea.)	$259.60	McMaster.com	2994T94
36	Wheels Rigid(x4 @ $112each)	$448.00	McMaster.com	2435T43
37	Wheels Swivel (x2 @ $141.73)	$283.46	McMaster.com	2435T33
38	Wheel Screws (x16 @ $13.45/10)	$26.90	McMaster.com	91783A710
	Fasteners			
39	Bolt - Screw Jack Mounting Bolts 3/8"-16 (x4 @ $9.97/5)	$9.97	McMaster.com	91772A687
40	Bolt - Transducer to Inner Can M20x2.5mm(x8 @ $4.02 ea)	$32.16	McMaster.com	91290A070
41	Bolt - Transducer to Base Plate M20x2.5mm(x8 @ 5.17 ea)	$41.36	McMaster.com	91290A074
42	Bolt - Guide Rail to Guide Rail Beam Long M14x2mm(x22 @$2.92 ea.)	$64.24	McMaster.com	91290A778
43	Bolt - Screw jack Support Beam (x3 @ $7.28 ea)	$21.84	McMaster.com	91257A965
44	Bolt- Guide Rail to Guide Rail Beam short M14x2mm(x8 @$14.44/5)	$28.88	McMaster.com	91290A770
45	Bolt - Year 1 Hoist Ring Plates (x16 @ $8.61/5)	$34.44	McMaster.com	91251A120
46	Nut - Screw Jack Bolt Nuts 3/8"-16 (x4 @ $12.49/100)	$12.49	McMaster.com	93827A225
47	Nut - Transducer M20x2.5mm(x16 @ $5.72 ea)	$91.52	McMaster.com	91005A041
48	Nut - Guide Rail to Guide Rail Beam M14x2mm(x3 @ $10.12/10)	$30.36	McMaster.com	90725A730
49	Nut - Screw jack Support Beam (x3 @ $10.01/5)	$10.01	McMaster.com	90949A133
50	Nut - Year 1 Hoist Ring Plate (x16 @ $10.72/25)	$10.72	McMaster.com	90949A033
51	Screw - Roller Carriage Guide Rail Screws M-14 (x30 @ $7.84 per 5)	$54.88	McMaster.com	91290A735
52	Screw - (Roller Carriage to Base Plate)M12x1.75mm(x16 @ $9.59/10)	$19.18	McMaster.com	91290A634
	Machining Costs (Estimated)	$15,092.60		
	TOTAL	**$49,865.40**		
	Under Budget	**$134.60**		

Table 2.3: Year 2 Budget (Rig Frame)

	Year 2 Part List	Cost	Source	Part #
	Hydraulic WOB			
1	Hydraulic Cylinder	$549.97	International Hydraulics	IMW-5040
2	Double Acting Power Unit	$423.74	International Hydraulics	IH-MTE-DA-101-B
	Drilling Mechanism			
3	Trash Pump	$1,695.00	American Machine and Tool	393A-95
4	Three-Phase Enclosed Magnetic Starter	$535.00	American Machine and Tool	A378-90
5	Suction Hose (x2 @ $110 each)	$110.00	American Machine and Tool	C221-90
6	Suction Strainer	$19.00	American Machine and Tool	C230-90
7	Mounting Base	$415.00	American Machine and Tool	A200-90
8	Rubber Expansion Joint	$861.00	Flexicraft Industries	USL11000
9	Roller Carriage Guide Rails (x2 @ 2409.17)	$4,818.34		
10	Roller Carriages for Swivel (x4 @$56.25 ea.)	$225.00	McMaster.com	3249K2
11	Rails for Swivel Carriages (x2 36in @ $0.07/mm)	$140.00	McMaster.com	
12	Roller Carriage Guide Rails for Motor (x2 @ $593.2 each)	$1,186.40	Purvis (Thomson)	See Roller Carriage Data
13	Axial/Rotaional Shaft Seal (x2 @ $290 each)	$580.00	AHP Seal	VS-RS19B Profile Rod Seal - Perm
14	Mud Tank	$300.00		
15	Belleville Washers (x8 @ $317.65 each)	$2,541.20	Belleville Springs Ltd.	DIN 2029: 2006
16	Proximity Probe	$246.00	Bently Nevada	3300 8MM Bently Probe - 3/8-24 U
17	Proximity Probe Extension Cable	$211.00	Bently Nevada	3300 5MM&8MM Extension cable
18	Proximeter	$329.00	Bently Nevada	3300 XL Proximeter
	Metal Pricing			
19	Large Hoisting Hooks (x4 @ $146.76 ea.)	$587.04	McMaster.com	2994T72
20	Small Hoisting Hooks (x8@ $53.58ea.)	$519.20	McMaster.com	2994T41
21	Drill Shaft (OD: 8in, t:2.25in)	$1,245.00	Specialty Pipe & Tube	HF Seamless Round Tube
22	Shaft Support Tube (OD:12in, ID:6in, L:18in)	$1,325.00	Specialty Pipe & Tube	HRS 4140 & 4142
23	Shaft Support Structure ([x3] 24"x24"x1" @ $416.39 ea.)	$1,249.17	McMaster.com	1388K581
24	Steel Members	$6,483.08	Discountsteel.com	See Year 2 Beam List
25	Torque Coupling (OD:6in, L:14in)	$217.82	Discountsteel.com	ASTM A576 12L14 Cold Rolled Ste
26	Plating (Large and Small Shaft Support)-t:1"-(x2 @ $355.80ea.)	$711.60	Discountsteel.com	ASTM A36 Hot Rolled Steel Plate
27	Plating (Webbing) - t:1/2"	$291.79	McMaster.com	1388K381
28	Plating Frame Connections - t: 1/2" (36"x36")	$205.11	Discountsteel.com	ASTM A5145 AR200 Abrasion Res
	Metal for Sample Container Cap			
29	Seal End (OD: 10" - L:6")	$682.18	McMaster.com	9086K48
30	Container End (16"x16"x1")	$242.99	McMaster.com	1388K561
	Metal for Swivel Support			
31	Steel Plate (24"x32"x1.25")	$720.76	Discountsteel.com	ASTM A514 T1
32	Rectangular Tube (4"x4"x.25"@ $64.63 ea.)	$193.89	Discountsteel.com	
33	Hydrailc Cylinder Support	$682.18	McMaster.com	9086K48
34	Hydrailc Cylinder Support Pin	$416.62	McMaster.com	8846K38
35	Hydraulic Cylinder Buckle Support	$168.12	McMaster.com	1388K821
36	Torque Catches (x4 @ $38.81 ea.)	$153.24	McMaster.com	9017K694
	Fasteners			
37	Bolt[1"-8] - Rig Frame Connections (x32 @ $5.37ea.)	$171.84	McMaster.com	92620A957
38	Bolt[1"-8] - Year 1 structure to Sliding Structure (x4 @ $11.52 ea.)	$46.08	McMaster.com	91251A928
39	Bolt[M14x2mm] - Guide Rails to Rig Frame P2 (x26 @ $12.85/5)	$77.10	McMaster.com	91290A769
40	Bolt[1"-8] - Shaft Support (x8 @ $5.24 ea.)	$41.92	McMaster.com	91251A916
41	Bolt[1"-8] - Sample Containment (x12 @ $6.17 ea.)	$74.04	McMaster.com	91251A912
42	Nut[1"-8] - Rig Frame Connections (x32 @ $10.01/5)	$70.07	McMaster.com	90949A133
43	Nut[1"-8] - Year 1 Structure to Sliding Structure (x4 @ $10.01/5)	$10.01	McMaster.com	90949A133
44	Nut[1"-8] -Shaft Support (x8 @ $10.01/5)	$20.02	McMaster.com	90949A133
45	Nut[M14x2mm] - Guide Rails to Rig Frame P2 (x26 @ $11.08/10)	$33.24	McMaster.com	94645A240
46	Screw - Swivel and Shaft Latches (.5"-13 @ $11.24/10)	$11.24	McMaster.com	91274A460
47	Screw - Hoisting Beams (x16 @ $14.32/5)	$57.28	McMaster.com	92620A724
48	Screw - Roller Carriage to Sliding (x16 @ $11.99/10)	$23.98	McMaster.com	91290A636
49	Screw - Hydraulic Buckling (x4 @ $2.48 ea.)	$9.92	McMaster.com	91251A015
50	Screw - motor to rail guide (x14 @ $10.14/10)	$20.28	McMaster.com	91303A336
51	Screw - Wheels (x24 @ $13.45 / 10)	$40.35	McMaster.com	91783A710
52	Screw - Roller Carriage Guide Rail Screws M-14 (x30 @ $7.84 per 5)	$54.88	McMaster.com	91290A735
	Drive Motor			
53	Motor	$4,875.00	http://www.ebay.com/itm/2	PE447T-200-4 (from PTJ Industrial
54	Variable Speed Drive	$7,247.00	Driveswarehouse.com	L700-1600HFF
55	Speed Reducing Gear Box	$6,184.00	North American Electric	NBS-407-8-15
56	Mountings and Couplings	$2,500.00		
	Machining Costs (Estimated)	$15,000.00		
	TOTAL	**$67,848.69**		
	Over Budget	**-$17,848.69**		

2.4. Project Scheduling

Proper scheduling is "key" to any project's success. Every effort was made to keep the rig's progress moving towards the encompassing goal. The complete design of the test rig was a monumental task that was not taken lightly. Every inch of the machine had to be specified and proven to work under all possible loading conditions. Figure 2.3 displays the scheduling of the design of project.

2.5. Concept Generation

A pertinent question that arose during the "brain-storming" phase of the project was whether or not the rig should be a scaled down machine for testing miniaturized drilling components (such as that shown previously in the literature [102]) or a full sized drilling apparatus capable of handling equipment used in the field. From a budget stand point, a scaled down rig is the ideal choice, but it introduces the risk of error that comes with scaling effects [103]. It is also important to think about potential comparative studies with the data obtained from the test rig. With a larger rig, any results obtained could be directly compared to field data, which can then validate experimental results. A full scale rig also allows for a multitude of future research opportunities as well as commercial bit testing, bit indexing or for testing new bit designs or emerging technologies that would otherwise be too costly to try on an actual drilling platform. Taking these thoughts into consideration, it was decided to design a full-sized test rig within the allowable budget.

Observing previous efforts of test rig development [1, 38, 54, 81, 104] and implementing the design process outlined by Figure 2.4, concepts were developed and refined to arrive at a final rig design that meets all of the necessary requirements and in some instances, exceeds prior expectations. From the data provided in Table 2.1, a rough sketch of a potential configuration was drawn (Figure 2.5). Then following the iterative process, the idea was slowly refined (Figure 2.6 through Figure 2.9) into the final design configuration (Figure 2.11).

ID	Task Name	Start	Finish	Duration
1	Initial Planning	1/2/2012	4/23/2012	16.2w
2	Background Investigation	2/20/2012	5/4/2012	11w
3	Concept Development	4/2/2012	8/10/2012	19w
4	Analysis	5/3/2012	10/31/2012	26w
5	Finalize Calculations	10/1/2012	1/21/2013	16.2w
6	Finalize FEA Models	10/30/2012	1/31/2013	13.6w
7	Specify all components	12/3/2012	1/31/2013	8.8w
8	Procurement	7/30/2012	10/26/2012	13w
9	Machining	10/24/2012	2/15/2013	16.6w
10	Friction testing	12/3/2012	12/28/2012	4w
11	Measurement Rod Calibration	1/31/2013	2/25/2013	3.6w
12	Assembly	2/14/2013	5/7/2013	11.8w
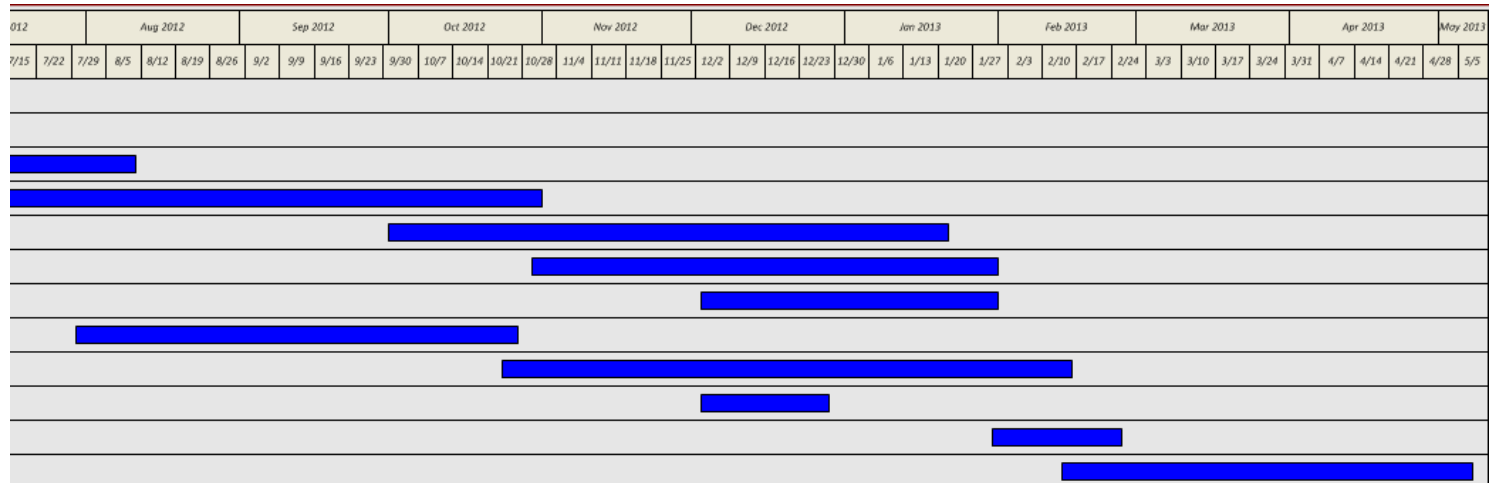
Figure 2.3:   Gantt Chart of Project Tasks

23
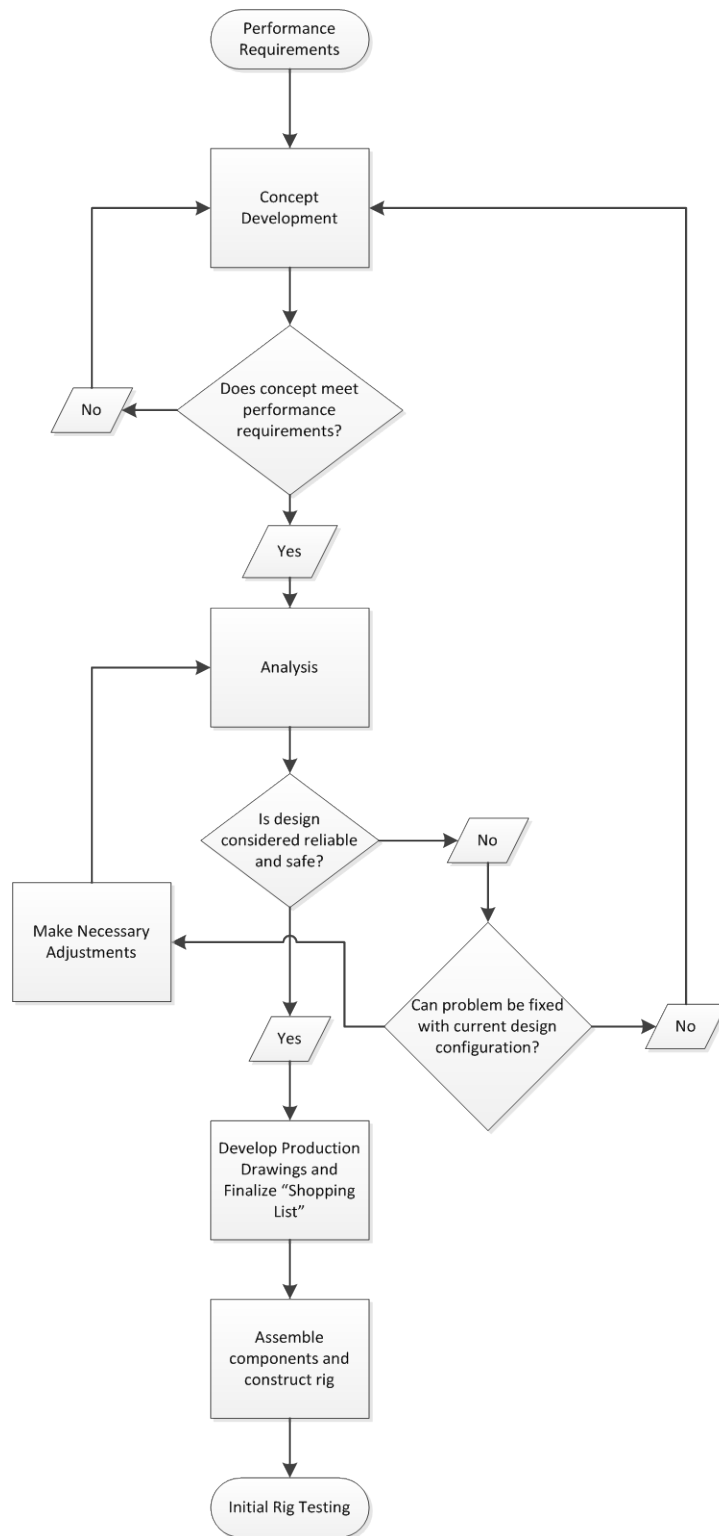
Figure 2.4: **Concept Design Development Process**
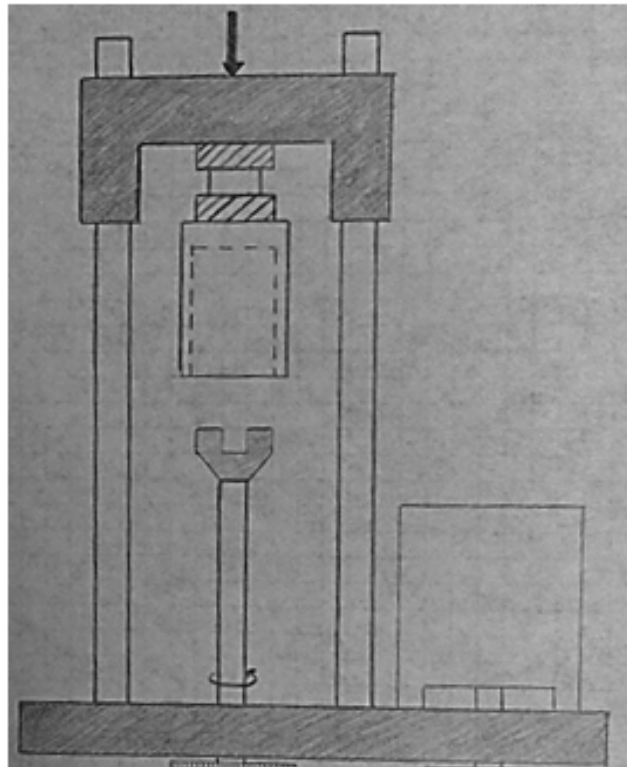
Figure 2.5:   Initial Concept Sketch
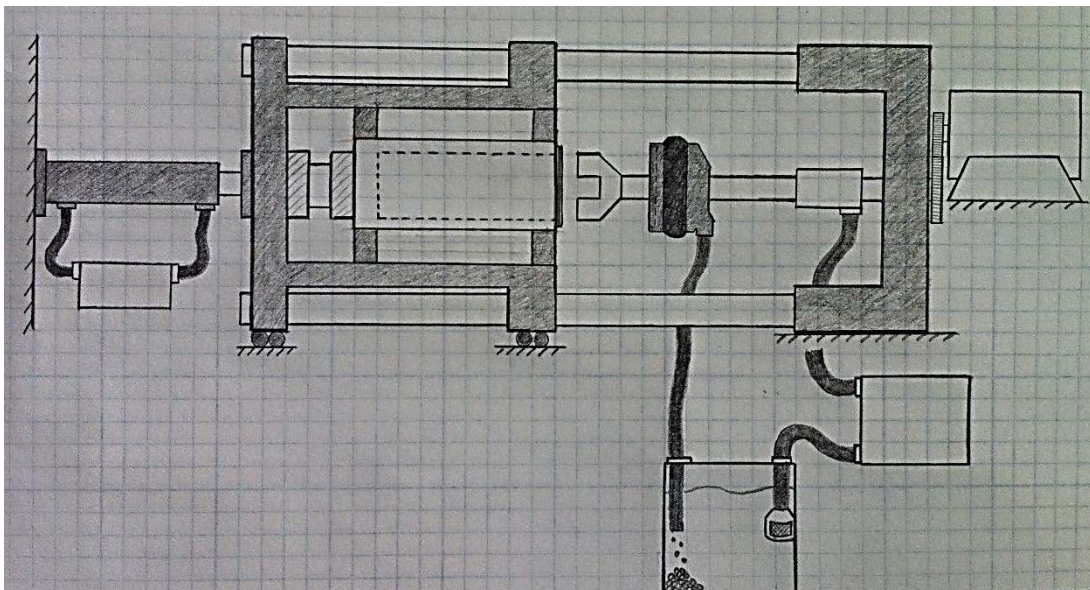
Figure 2.6:   Mark 2 Sketch
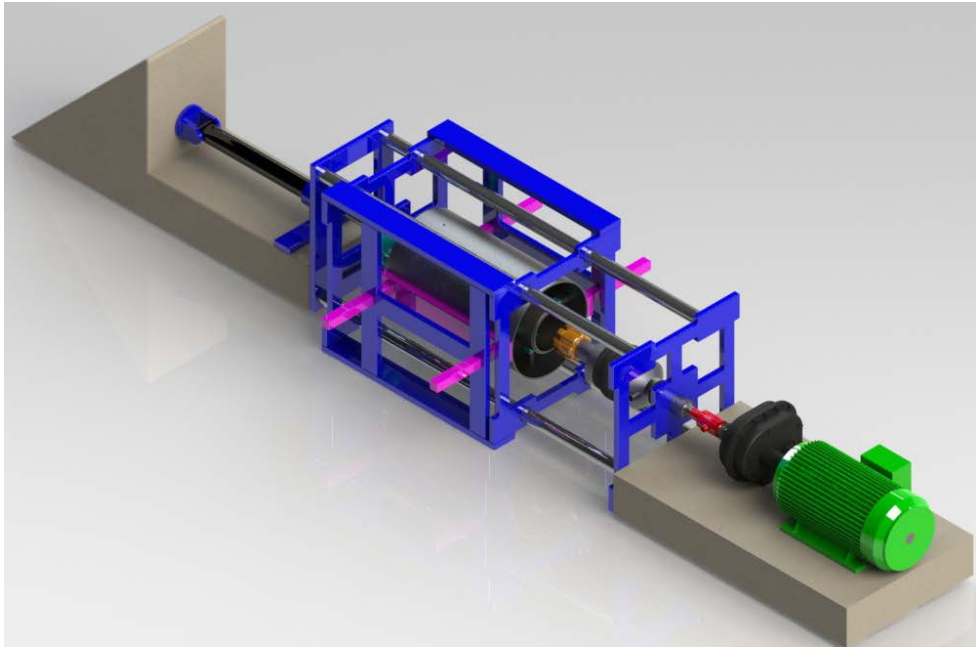
Figure 2.7: **Mark 3 Solidworks® Rendering**
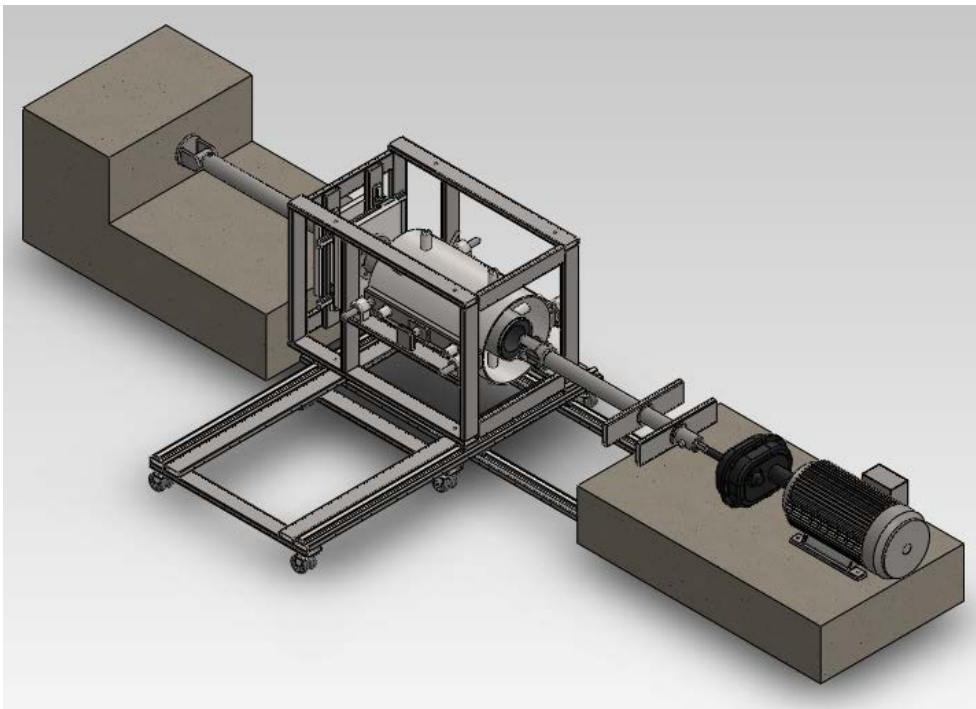
Figure 2.8: **Mark 4 Solidworks® Rendering**
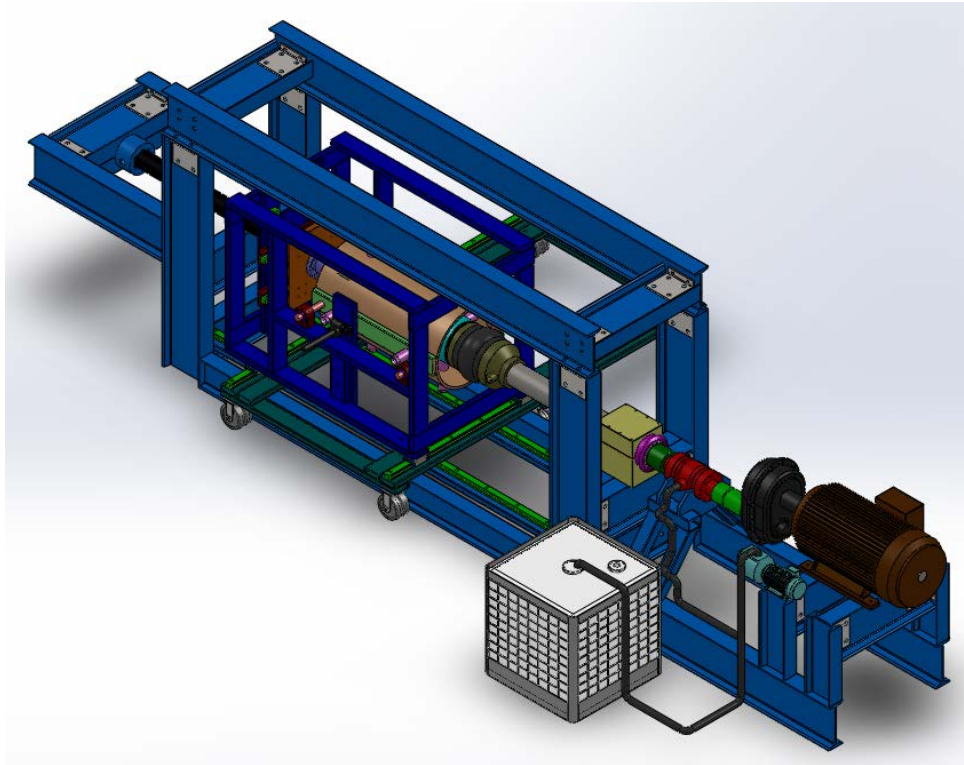
Figure 2.9:   Mark 5 Solidworks® Rendering
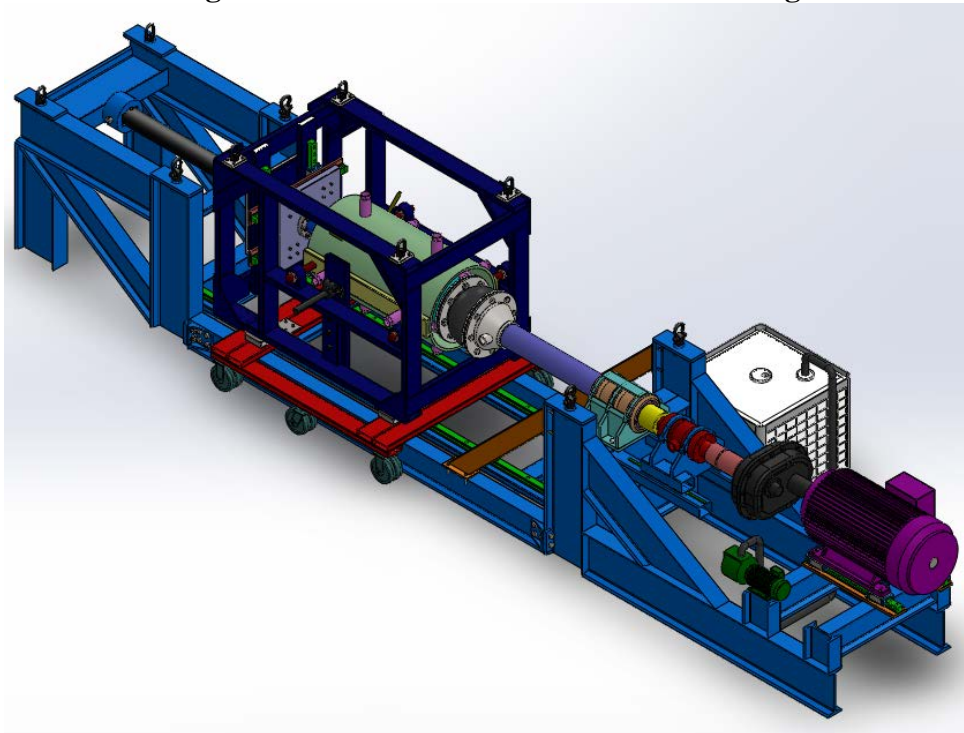
Figure 2.10:   Mark 6 Solidworks® Rendering

2.6. Final Design
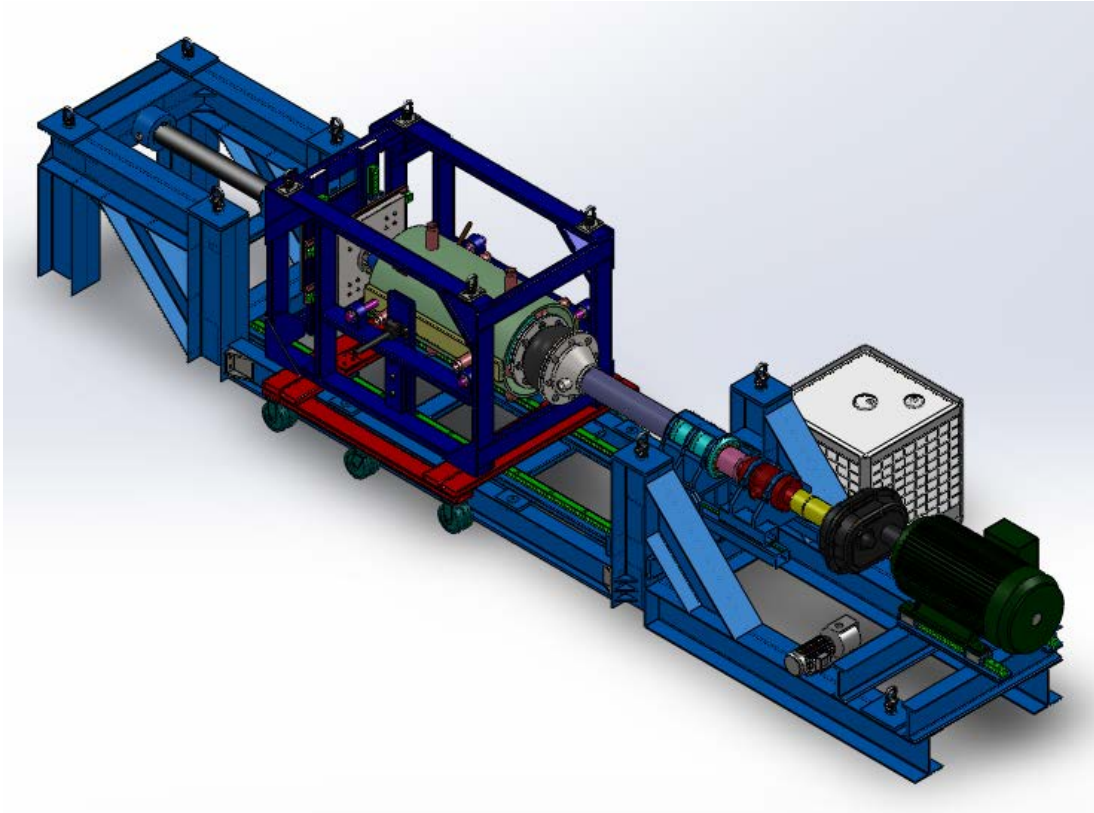
Figure 2.11:   Final Design Configuration

Figure 2.11 is a 3D CAD model of the drilling test rig created in Solidworks®. The design shown is the original, full-scale 200 hp test rig. It is capable of delivering 14,000 ft-lb$_f$ of torque at 60 rpm to 5,252 ft-lb$_f$ at 200 rpm for a variety drill bits. WOB ranges from 0-55,000 lb$_f$. Basic dimensions of the rig are 27ft x 6ft x 6ft with a gross weight of nearly 17,500 lb$_f$.

Key Design Features
- Horizontal configuration for ease of access of entire rig and safety of operation
- External mud tank for alternating drilling fluids

- Removable/refillable sample containment cylinder for testing multiple formation types
- Threaded bit connection for testing multiple bit types
- Sectional assembly with hoisting points for ease of rig transport and relocation

2.6.1. General Layout and Assembly

27 ft
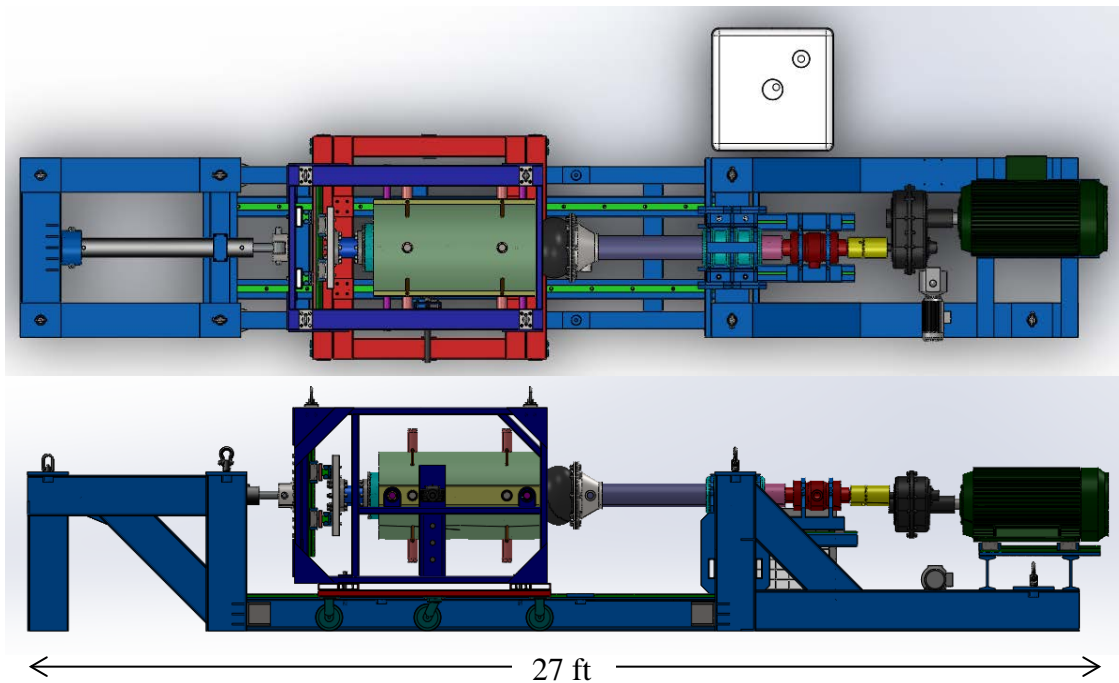
Figure 2.12: Top and Side Views of Final Design Configuration

Figure 2.12 depicts a top and side perspective of the rig. A front view at the drive motor end of the rig can be seen in Figure 2.13. The external mud tank is roughly 3ft by 3ft by 3 ft and can be located anywhere around the rig. Figure 2.14 displays how the rig is separated into 5 main components for ease of transport. It is noted that certain items have been left out of the CAD model because their location with respect to the rig is subject to the preference of the operator and available space in the rig's vicinity. These

29

items include: the variable frequency drive (VFD), hydraulic cylinder pump, mud pump tubing and wiring. General rig assembly drawings can be found in Appendix B.
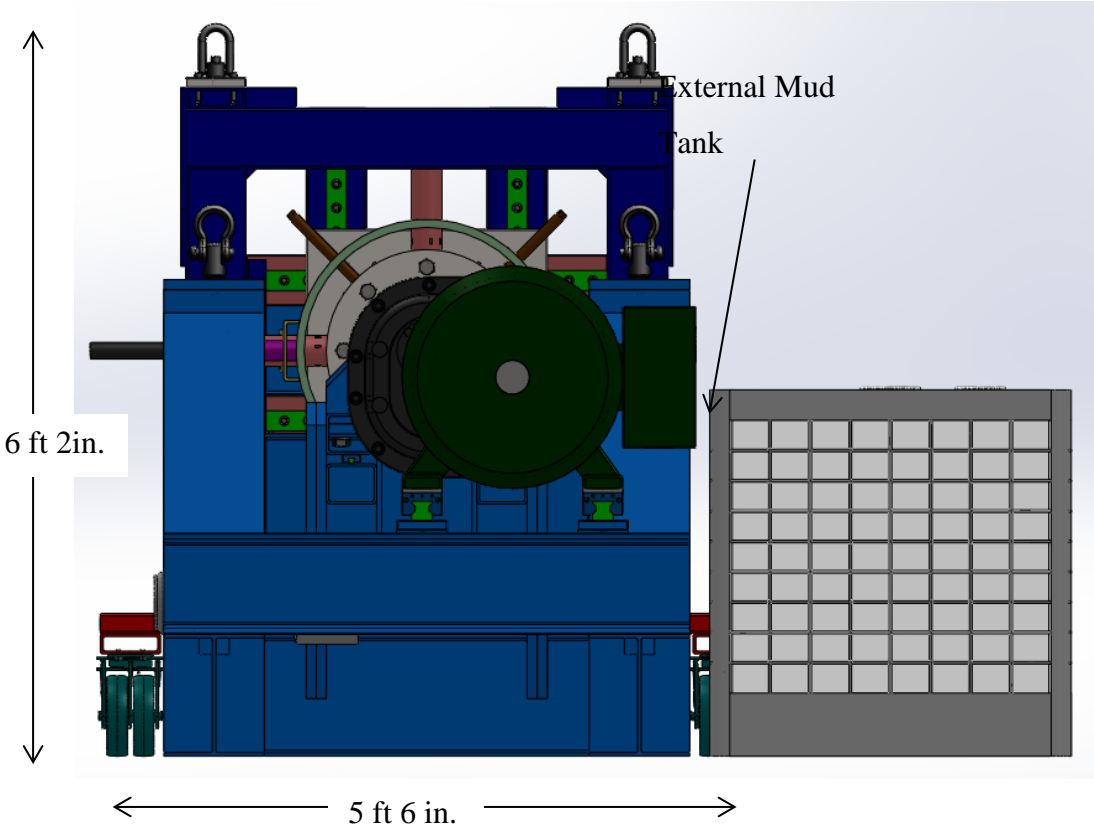
Figure 2.13:   Front View of Final Design Configuration
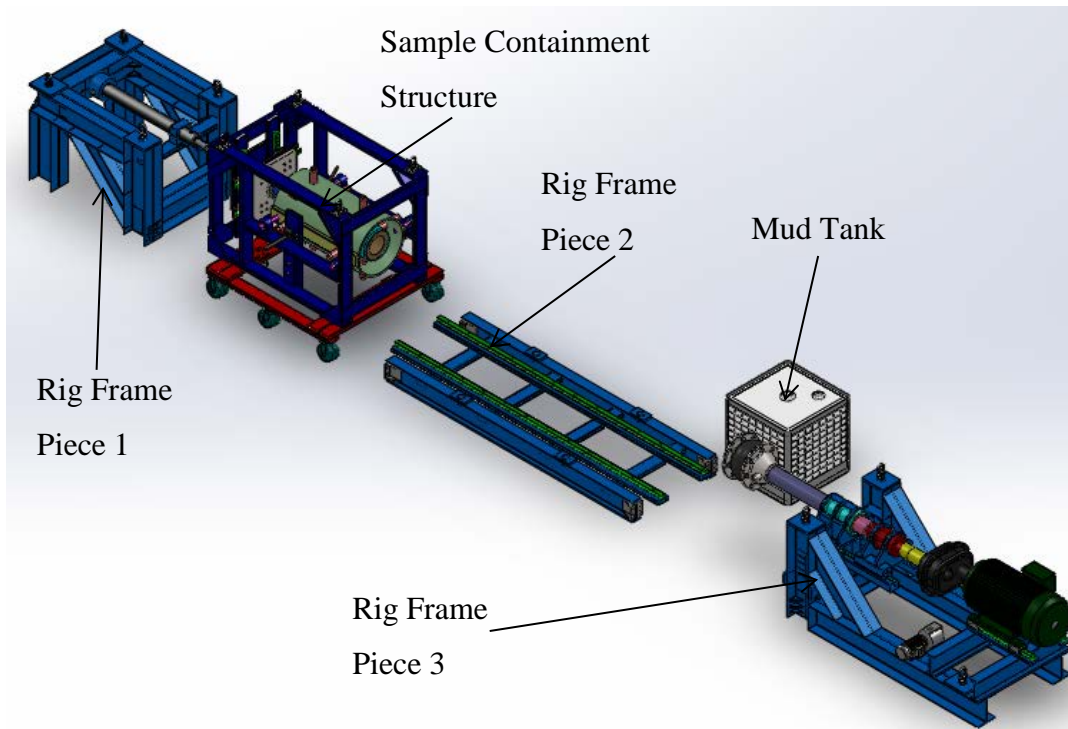
Figure 2.14:   Main Separable Rig Components

2.6.2. Force Measurement System

The force measurement system is the "heart" of the rig's design. This is the first attempt to measure the bit reactions from the perspective of the formation rather than the drill string. Not only does this approach remove the need to mount and remount gauges to various dill pipes, but it allows for the investigation of non-bit wellbore forces such as mud viscous effects or coefficients of friction between the bit and formation. Figure 2.15 depicts an isolated view of the force/torque measurements system. The system consists of the Inner Sample Container which houses the formation, the Axial/Torsional Transducer (axial load capacity: 150,000 lb_f, torsional load capacity: 200,000 in-lb_f) , 8 Lateral Force Measurement Rods each of which have the ability to measure transverse loading in two directions (axial and torsional loading on sample) and normal loading (lateral loading on sample), and the XY-Translator table which consists of two perpendicular rows of roller bearing carriages that are stacked one in front of the other so

31

as to allow for translational motion in two directions (lateral motions for the sample container) but restrict torsional and axial motions of the formation.

Figure 2.16 aides in the understanding of how the measurement system works. Again, the XY-Translator table prevents rotation and axial movement, thus allowing for the axial/torsional load cell to measure the majority of the TOB and WOB. However, due to friction at the support points of the Lateral Force Measurement Rods, a small portion of the axial and torsional loads will be carried by the rods. For this reason, each rod is mounted with strain gauges to measure its respective contribution to the loading of the formation. The measurement rods also provide the majority of the lateral support for the sample container since the only transverse support provided by the XY-Translator comes from the friction between the roller carriages and the guide rails. The functionality, details, calibration and possible measurement errors of the system are discussed in subsequent sections.
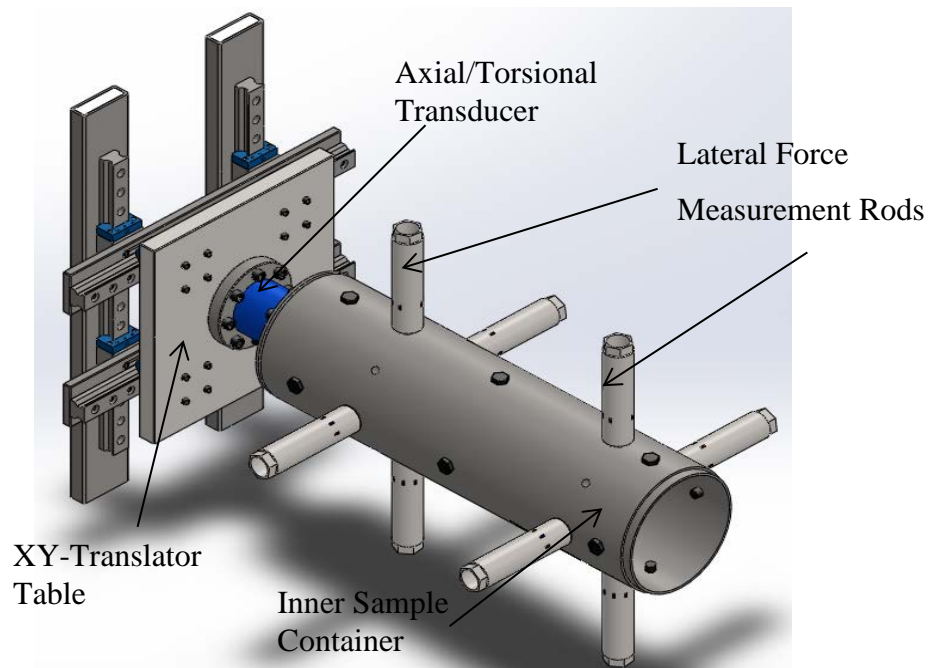
Figure 2.15: Force/Torque Measurement System
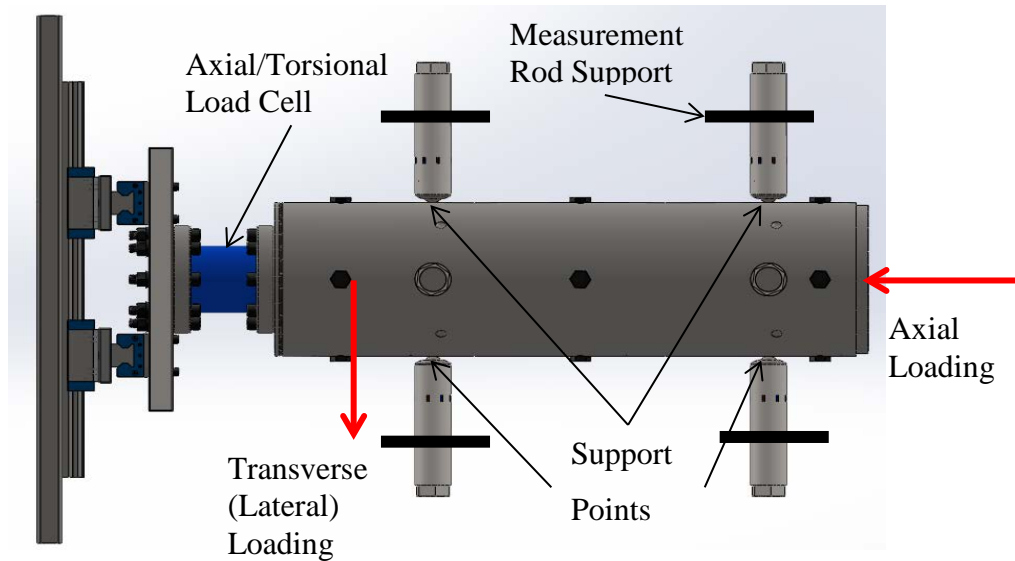
Figure 2.16:   Side View of Force/Torque Measurement System

2.6.1.   Alternative Reduced Power Rig Design

It was originally thought that there would be adequate power available at the rig's location to run the drive system and additional financial support would be available to cover the year 2 budget overdraw. Towards the close of the design process however, it was determined that the rig would not have the necessary power available at its destination location, nor would it have increased monetary support. Thus, an alternative design that fit the new constraints was necessary. A reduced power rig is introduced in this section. The corresponding analysis of the alternative rig is shown in Appendix C. The alternative Year 2 Budget is presented in Table 2.4. This secondary budget allows for the testing of 3 to 4 inch PDC bits, which will still lead to meaningful results for these bit sizes and will draw in future funding opportunities to expand the rig to its full capacity. The key changes between the original rig and the low power design are the reduction in the capacities of the drive motor, gearing system, variable frequency drive, structural frame members and the hydraulic actuator. The focus for this manuscript is the design and analysis of the original test rig since the concept is identical and only differs in the size and magnitude of components.

Table 2.4: Alternative Year 2 Budget (Reduced Rig for Testing 3 ½ inch Bits)

	Alt Year 2 Part List	Cost	Source	Part #
	Hydraulic WOB			
1	Hydraulic Cylinder (36" stroke)	$292.87	International Hydraulics	ICW-4036
2	Double Acting Power Unit	$423.74	International Hydraulics	IH-MTE-DA-101-B
	Drilling Mechanism			
3	Trash Pump	$1,695.00	American Machine and Tool	393A-95
4	Three-Phase Enclosed Magnetic Starter	$535.00	American Machine and Tool	A378-90
5	Suction Hose (x2 @ $110 each)	$110.00	American Machine and Tool	C221-90
6	Suction Strainer	$19.00	American Machine and Tool	C230-90
7	Mounting Base	$415.00	American Machine and Tool	A200-90
8	Rubber Expansion Joint	$861.00	Flexicraft Industries	USL11000
9	Roller Carriage Guide Rails (x2 @ 2409.17)	$4,818.34		See Roller Carriage Data
10	Roller Carriages for Swivel (x4 @$56.25 ea.)	$225.00	McMaster.com	3249K2
11	Rails for Swivel Carriages (x2 36in @ $0.07/mm)	$140.00	McMaster.com	
12	Shaft Bearings (Spherical Roller Thrust x2 @ 500.95 ea.)	$1,001.90	Ebay.com	Nachi 29412EX
13	Proximity Probe	$246.00	Bently Nevada	3300 8MM Bently Probe - 3/8-24 UNF
14	Proximity Probe Extension Cable	$211.00	Bently Nevada	3300 5MM&8MM Extension cable
15	Proximeter	$329.00	Bently Nevada	3300 XL Proximeter
	Metal Pricing			
16	Large Hoisting Hooks (x4 @ $146.76 ea.)	$587.04	McMaster.com	2994T72
17	Small Hoisting Hooks (x8@ $53.58ea.)	$519.20	McMaster.com	2994T41
18	Drill Shaft (OD: 4in, t:1.25in)	$550.00	Specialty Pipe & Tube	HF Seamless Round Tube
19	Shaft Support Tube (OD:8in, ID:3in, L:24in)	$735.00	Specialty Pipe & Tube	HRS 4140 & 4142
20	Shaft Support Structure ([x3] 24"x24"x1" @ $416.39 ea.)	$1,249.17	McMaster.com	1388K581
21	Steel Members	$4,677.72	Discountsteel.com	See Alt Year 2 Beam List
22	Torque Coupling (OD:6in, L:14in)	$217.82	Discountsteel.com	ASTM A576 12L14 Cold Rolled Steel Round Bar
	Metal for Sample Container Cap			
23	Seal End (OD: 10" - L:6")	$682.18	McMaster.com	9086K48
24	Container End (16"x16"x1")	$242.99	McMaster.com	1388K561
	Metal for Swivel Support			
25	Steel Plate (24"x32"x1.25")	$720.76	Discountsteel.com	ASTM A514 T1
26	Rectangular Tube (4"x4"x.25"@ $64.63 ea.)	$193.89	Discountsteel.com	
27	Plating (Large and Small Shaft Support)-t:1"-(x2 @ $355.80ea	$711.60	Discountsteel.com	ASTM A36 Hot Rolled Steel Plate
28	Plating (Webbing) - t:1/2"	$291.79	McMaster.com	1388K381
29	Plating Frame Connections - t: 1/2" (36"x36")	$205.11	Discountsteel.com	ASTM A5145 AR200 Abrasion Res Steel
30	Mud Tank	$300.00		
31	Axial/Rotaional Shaft Seal (x2 @ $290 each)	$580.00	AHP Seal	VS-RS19B Profile Rod Seal - Permachem 6233
32	Hydrailc Cylinder Support	$682.18	McMaster.com	9086K48
33	Hydrailc Cylinder Support Pin	$416.62	McMaster.com	8846K38
34	Hydraulic Cylinder Buckle Support	$168.12	McMaster.com	1388K821
35	Belleville Washers (x8 @ $69.44 each)	$555.52	Belleville Springs Ltd.	DIN 2029: 2006
36	Torque Catches (x4 @ $38.81 ea.)	$153.24	McMaster.com	9017K694
	Fasteners			
37	Bolt[1"-8] - Rig Frame Connections (x32 @ $5.37ea.)	$171.84	McMaster.com	92620A957
38	Bolt[1"-8] - Year 1 structure to Sliding Structure (x4 @ $11.52	$46.08	McMaster.com	91251A928
39	Bolt[M14x2mm] - Guide Rails to Rig Frame P2 (x26 @ $12.85/	$77.10	McMaster.com	91290A769
40	Bolt[1"-8] - Shaft Support (x8 @ $5.24 ea.)	$41.92	McMaster.com	91251A916
41	Bolt[1"-8] - Sample Containment (x12 @ $6.17 ea.)	$74.04	McMaster.com	91251A912
42	Nut[1"-8] - Rig Frame Connections (x32 @ $10.01/5)	$70.07	McMaster.com	90949A133
43	Nut[1"-8] - Year 1 Structure to Sliding Structure (x4 @ $10.01	$10.01	McMaster.com	90949A133
44	Nut[1"-8] -Shaft Support (x8 @ $10.01/5)	$20.02	McMaster.com	90949A133
45	Nut[M14x2mm] - Guide Rails to Rig Frame P2 (x26 @ $11.08/	$33.24	McMaster.com	94645A240
46	Screw - Swivel and Shaft Latches (.5"-13 @ $11.24/10)	$11.24	McMaster.com	91274A460
47	Screw - Hoisting Beams (x16 @ $14.32/5)	$57.28	McMaster.com	92620A724
48	Screw - Roller Carriage to Sliding (x16 @ $11.99/10)	$23.98	McMaster.com	91290A636
49	Screw - Hydraulic Buckling (x4 @ $2.48 ea.)	$9.92	McMaster.com	91251A015
50	Screw - motor to rail guide (x14 @ $10.14/10)	$20.28	McMaster.com	91303A336
51	Screw - Wheels (x24 @ $13.45 / 10)	$40.35	McMaster.com	91783A710
52	Screw - Roller Carriage Guide Rail Screws M-14 (x30 @ $7.84	$54.88	McMaster.com	91290A735
	Drive Motor			
53	Motor	$1,360.00	http://www.ebay.com/itm/:	PE286T-30-4 (from PTJ Industrial online store)
54	Variable Speed Drive	$1,369.00	Driveswarehouse.com	L700-220HFF
55	Speed Reducing Gear Box	$911.00	North American Electric	NBS-115-2-15
56	Mountings and Couplings	$2,500.00		
	Machining Costs (Estimated)	$15,000.00		
	TOTAL	**$47,665.05**		
	Under Budget	**$2,334.95**		

3. DESIGN ANALYSIS

3.1. Power Requirements

The first step in developing an appropriately sized test rig, is determining the magnitude of forces and torques that will be present during operation. An extensive literature review has presented various papers on average TOB for several bit types [70, 72, 74, 75, 77, 79, 105]. Most of the articles express the information as predictions of in-situ rock strength [64, 66, 67, 78] or as efficiency studies by comparing bit performance [68, 73, 77, 80, 97, 106], but the current work is more interested in the general reactions at the bit encountered while drilling. Utilizing the ideas found in the literature and imploring minor adjustments for the needs of the investigation, relationships have been developed that give reasonable insight into the magnitude of the bit reactions and thus give a better understanding of what to expect during rig operation.

3.1.1. Equations
3.1.1.1. PDC Bits

The majority of TOB relationships developed are functions of bit constants or specific geometries. The effort presented here did not have a sufficient amount of information related to these constants, so it was necessary to develop equations based on very general bit characteristics. Following an idea that was first presented by Fairhurst and Lacabanne [53], and later expanded by Detournay et al [43, 52], the drilling components of the bit have been divided into 2 separate processes in order to develop a relationship between TOB and general bit characteristics as a means for power estimates for the rig's operation.

Figure 3.1 and Figure 3.2 express the idea behind the TOB equations. The primary method of rock destruction in PDC bits is the shearing action generated by the scraping of PDC cutters along the surface of the rock. By analyzing the contribution of one PDC cutter, one can estimate the total moment on the drag bit.
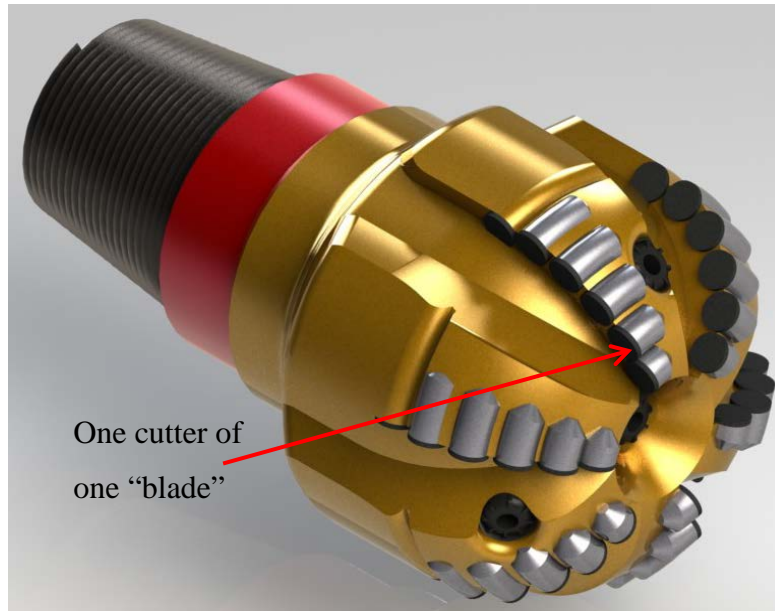
Figure 3.1:   Solidworks® Rendering of 3D PDC Bit CAD Model
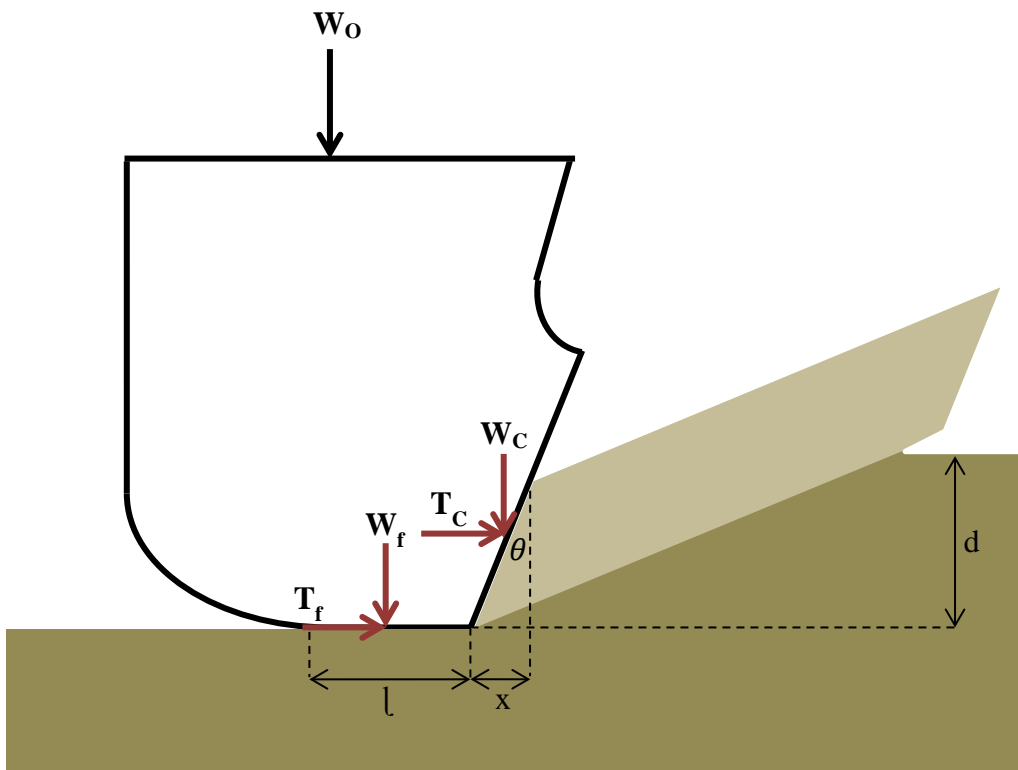
Figure 3.2:   PDC Torque Modeling, after Detournay et al [43, 52]

The total WOB (W_O) can be considered a summation of the weight contributing to frictional losses, W_f, and the weight contributing to the cutting of the formations, W_C as outlined in Figure 3.2. A bit can be simplified by assuming the rows of cutters, or blades, are evenly spaced around the face of the bit as shown in Figure 3.3. The number of blades will be denoted by **n**, and the bit diameter will be expressed as D_B.

"Blade" of
PDC cutters

D_B
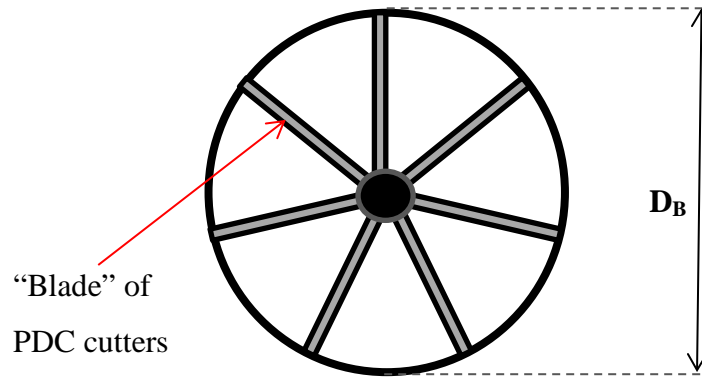
Figure 3.3:   "Blade" Layout

From the figures, frictional and contact areas can be evaluated (Equations 1 and 2).

$$A_f = \frac{n \lfloor D_B}{2} \ [in^2] \tag{Eq. 1}$$

$$A_C = \frac{nxD_B}{2} \ [in^2] \tag{Eq. 2}$$

The characteristic cutting dimension, **x**, is found by a simple trigonometric relation given as,

$$x = d \tan \theta \ [in] \tag{Eq. 3}$$

where **d** is the depth of cut and θ is the back rake angle of the cutter (typically between 10° and 20°[52]). It should be pointed out that a maximum $\mathbf{W_C}$ exists when $d = \frac{C_s}{25.4}\sin\theta$, where $\mathbf{C_S}$ is the diameter of the cutter surface in millimeters. To determine the frictional weight component, an area ratio can be utilized from the above equations to obtain

$$W_f = \frac{W_o l}{l+x} \; [lb_f] \qquad\qquad \textbf{Eq. 4}$$

in which l is the wear-flat length. Equation 4 leads to an expression for the frictional torque, which is found to be (see Appendix D for derivation).

$$T_f = \frac{W_f D_B \mu}{48} \; [ft \cdot lb_f] \qquad\qquad \textbf{Eq. 5}$$

A relation for the coefficient of friction, **μ**, is presented by Caicedo et al [75] and is given by the following equation,

$$\mu = \left(0.9402 e^{(-8x10^{-6})S}\right)(-0.8876\ln(\rho_m) + 2.998)(0.0177 C_s + 0.6637)$$

$$\textbf{Eq. 6}$$

where $\boldsymbol{\rho_m}$ is the density of the drilling fluid in pounds per gallon and **S** is the formation strength. It should be noted that the derivation of the friction coefficient shown above encompasses the entire process of drilling it is not meant to be strictly a contact friction coefficient. In the present calculations, it is understood that this will lead to more conservative results.

The torque required for cutting the formation is found by including the contribution of each blade to the "Cutting Torque on Bit" equation given by Detournay et al [43] as,

$$T_C = \frac{n}{192\pi} D_B^2 \varepsilon d \; [ft * lb_f] \qquad\qquad \textbf{Eq. 7}$$

The depth of cut per revolution, **d**, is a quantification of the amount of formation removed for every turn of the bit

$$d = \frac{ROP}{5\Omega} \ [in/rot] \qquad \text{Eq. 8}$$

where **ROP** is the rate of penetration in ft/hr, Ω is the rotational speed of the bit in RPM. Specific energy (ε - The energy required to remove a volume of rock) and the mechanical bit efficiency (η) are presented by Pessier and Fear [79] and Caicedo et al [75] as

$$\varepsilon = \frac{S}{\eta} \ [psi] \qquad \text{Eq. 9}$$

$$\eta = \frac{\eta_{min} + \eta_{max}}{2} \qquad \text{Eq. 10}$$

$$\eta_{min} = (0.0008S + 8.834)(-1.0144 ln[\rho_m] + 3.2836) \qquad \text{Eq. 11}$$

$$\eta_{max} = (0.0011S + 13.804)(-1.0144 ln[\rho_m] + 3.2836) \qquad \text{Eq. 12}$$

where ρ_m is the density of the drilling fluid in pounds per gallon (ppg) and **S** is the compressive strength of the rock in psi. It should again be noted that the efficiency, Equation 11 and 12, are only valid for PDC bits with 7 or more blades. For the design of the test rig, this will lead to more conservative results which, in turn, lead to a more conservative design (i.e. the rig will be able to handle greater stresses than it will be subjected to).

3.1.1.2. Tri-cone Bits

Figure 3.4:   Image of Tri-Cone Bit (From [107])

Tri-cone bits (Figure 3.4) differ in their methods of rock destruction; instead of shearing the formation like a PDC bit, the rock below is crushed under the pressure exerted by the teeth of the bit, while the rotation of the bit and the circulation of the drilling fluid remove the pulverized rock cuttings. Franca and Mahjoob [64] present an interface relation for tri-cone bits and explain how the drilling, or cutting, torque can sometimes be close to zero such as in the case of cone off-set roller bits and subsequently all of the torque would be due to drag or bearing friction. For the present case, it is assumed that the drilling torque is not zero and has the same form as it does for PDC bits.

$$T_d = \frac{1}{8} D_B^2 \varepsilon d \qquad\qquad\qquad \textbf{Eq. 13}$$

Of course, the main difference being the exclusion of the **n** factor (number of blades on bit), which would be meaningless for the tri-cone bit. Instead, the roller-cone geometry

can be thought of as a single "blade". A depiction from Franca and Mahjoob illustrates this reasoning (Figure 3.5).
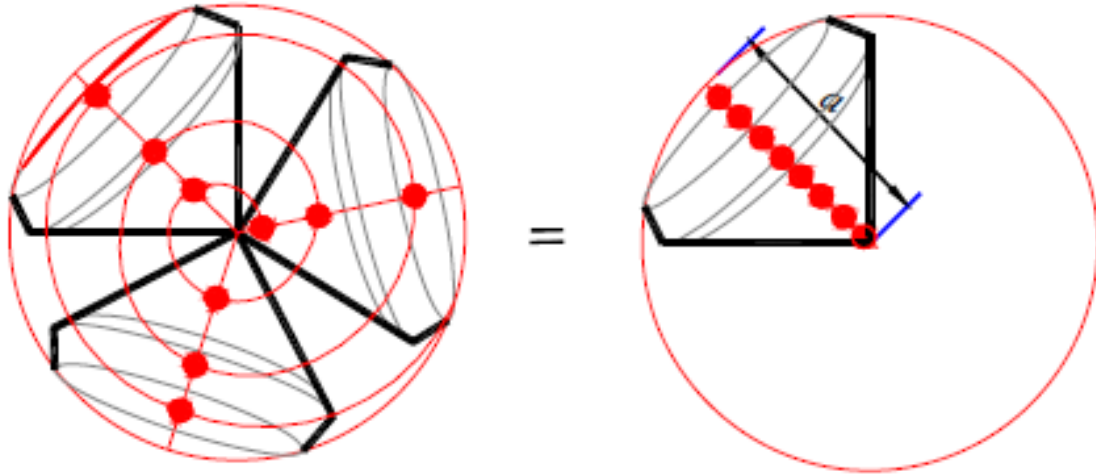
Figure 3.5:   Equivalent Bit Geometry of a Tri-Cone Bit (From [64])

The frictional component of the torque on roller-cone bits is not as easily derived as it is for PDC bits. For the sake of simplicity and for conservative design considerations, the drag torque of the roller cone bit is estimated using the method presented by Caicedo et al. [75] and presented as

$$T_f = \frac{D_B W_O \mu}{36}$$ **Eq. 14**

where the coefficient of friction, **µ**, is assumed to be **0.6**.

It should be noted that for the purposes of power estimates, the specific energy needed to destroy rock for both the PDC and Tri-cone bits (i.e. mechanical efficiency) is assumed to be the same. In reality, this assumption would be an unrealistic expectation as the different bit types utilize very distinct methods of rock destruction. To illustrate this

point one can examine the work of Alehossein et al. and Haung et al. [57, 58], who outline how rock failure is instigated with roller-cone bits by idealizing the teeth as blunt objects. A depiction of the mechanics invoked is shown in Figure 3.6 which conveys the distribution of the elastic, plastic and particle (core) zones under the blunt object indentation force.
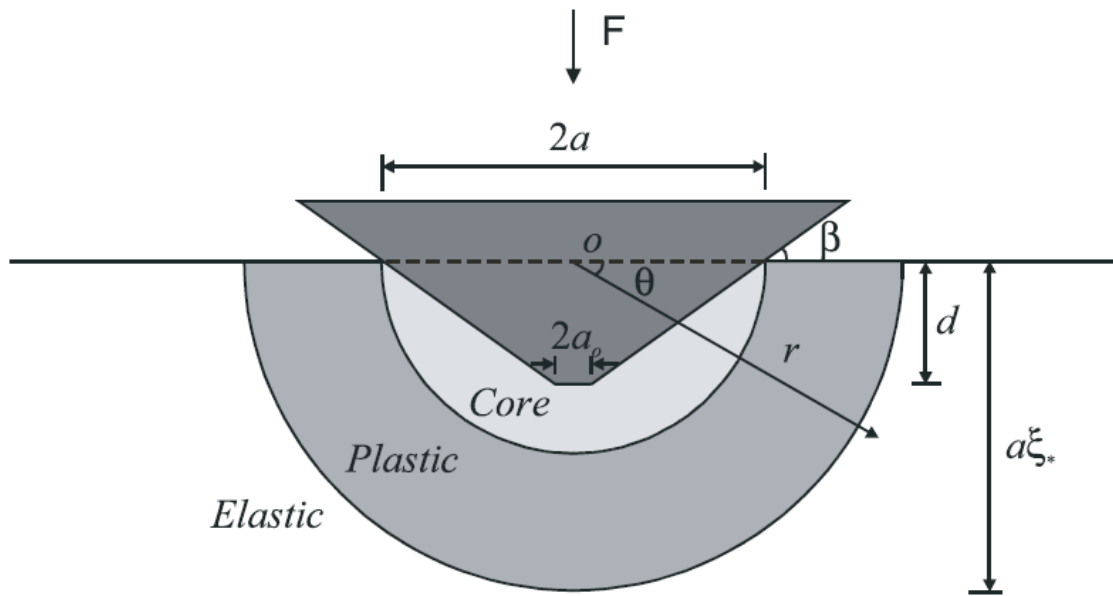
Figure 3.6:   Formation Indentation Model with a Blunt Tool (From [57])

When comparing Figure 3.2 and Figure 3.6, a clear distinction can be made with regards to the cutting efficiency of each bit type. The differences in efficiency can easily be understood to be greatly dependent on bit characteristics, operational parameters and formation properties. One can infer from these observations that different bits require separate interface models that govern this formation interaction. It is the hope of the project that the design and use of the test rig will directly lead to the identification and derivation of such an Interface Law for a multiplicity of bit types.

3.1.2. Input Variables

Table 3.1: Rock Properties (From [108])

Properties	Quartz	Granite	Dolerite	Sand Stone	Limestone (Grade 1)	Limestone (Grade 2)	Shale
Physical Properties							
Specific Gravity	2.658	2.764	2.84	2.06	2.65	2.04	2.01
Density (MN/m^3)	2.58	2.61	2.7	2.45	2.7	2.63	2.25
Porosity	0.2	0.77	3.44	16.87	11.23	15.52	18.5
Strength Properties							
Compressive (MPa)	188.89	169.81	89.45	44.96	59.92	47.2	48.53
Tensile (MPa)	8.69	9	6.93	4.99	6.35	5.2	4.64
Punch Shear (MPa)	25.4	20.63	13.29	8.44	12.79	11.55	7.69
Cohesion (MPa)	34.5	32	20	18	14	6	4
Angle of Internal Friction	63	56	48	42	46	40	42
Elastic Properties							
Static Young's Modulus (GPa)	102	92	58	41.6	47.5	35	12.5
Poisson's Ratio	0.26	0.33	0.3	0.28	0.24	0.3	0.22
Dynamic Properties							
Longitudinal Wave Velocity (m/sec)	5225	4350	3270	2000	3200	3016	990
Shear Wave Velocity (m/sec)	4058.7	2851	2430	850	1430	1280	690
Index Properties							
Shore hardness	82	76	46	41	35.27	26.3	35.86
Vickers Hardness	710	630	330	285	240	180	230
Hardness Based on Micro Bit Drilling Rate (mm)	0	0	0.383	0.852	0.76	1.4	1.54
Abrasivity based on Micro Bit Drilling tools loss in weight (x 10^-4)	115	100	65	85	37	22.5	11
Cerchar's index	6.8	6.1	5	5.6	4.8	3.4	2.6
Quartz Percent	100	35-40	0	40-45	15-20	10	22
Protodyakonov index	20	20	10.4	3.4	8.24	6.3	5.54

Table 3.1 lists the rock properties that were used for the power estimate calculations. The formation data was compared to a multitude of documented, experimentally determined rock properties [109-112] and it appears to be a valid summary of general formation characteristics seen on a global scale.

The operational parameters of the drill bits (WOB and RPM) are not part of a standardized practice and typically have recommended values given by the bit manufacturers. Attempts have been made to optimize a WOB and RPM combinations

based on bit parameters [113], but this approach is too equipment specific. Since the test rig needs to handle various bit types and multiple formations, a general "rule of thumb" approach is needed to estimate the proper operating conditions. Kennedy **[114]** recommends these types of guidelines in the following way:

"*In general, the recommended weight on bit for softer formations is less than that for harder formations. For example the recommended weight to be run on a typical milled-tooth bit fir very soft formation is 3,000-5,000 lbs./in. of diameter, while a typical bit for a very high strength, abrasive formation should be run with 6,000-8,000 lbs./in. of diameter*

.
The same trend is true for insert bits. Recommended bit weight for a typical soft-formation insert bit is 2,500-4,500 lbs./in. of diameter, while the recommended weight on bit for the insert bit used in hard formations is 4,500-6,000 lbs./in. bit diameter.

Rotary speeds recommended by manufacturers often decrease as the formations hardness increases, It is usually recommended that, within the recommended rotary speed, the lower speeds be used with higher weights on bit. For example, the manufacturer recommends the bit to be run at 120-90 rpm, the bit at 70-50 rpm. Recommended rotary speeds for the insert bit are 150-60 rpm, while the hard-formation bit should be run at 60-45 rpm."

Using these ground rules, a linear relationship was kept between the WOB and the rock strength as shown in Figure 3.7. For the rotational speed, Nguyen's [115] presents suggestion of keeping the product of WOB and Rotational speed constant for a particular bit type.

$$WOB \cdot ROP = Const_{Bit}$$ **Eq. 15**

Since the current project lacks particular bit constants, it was assumed that the hardest formation would be drilled with 76,000 lb$_f$ on the bit, at a rotational speed of 50 rpm. From this starting point, the RPM trend can be seen in Figure 3.8, against increasing compressive strength of the formation.
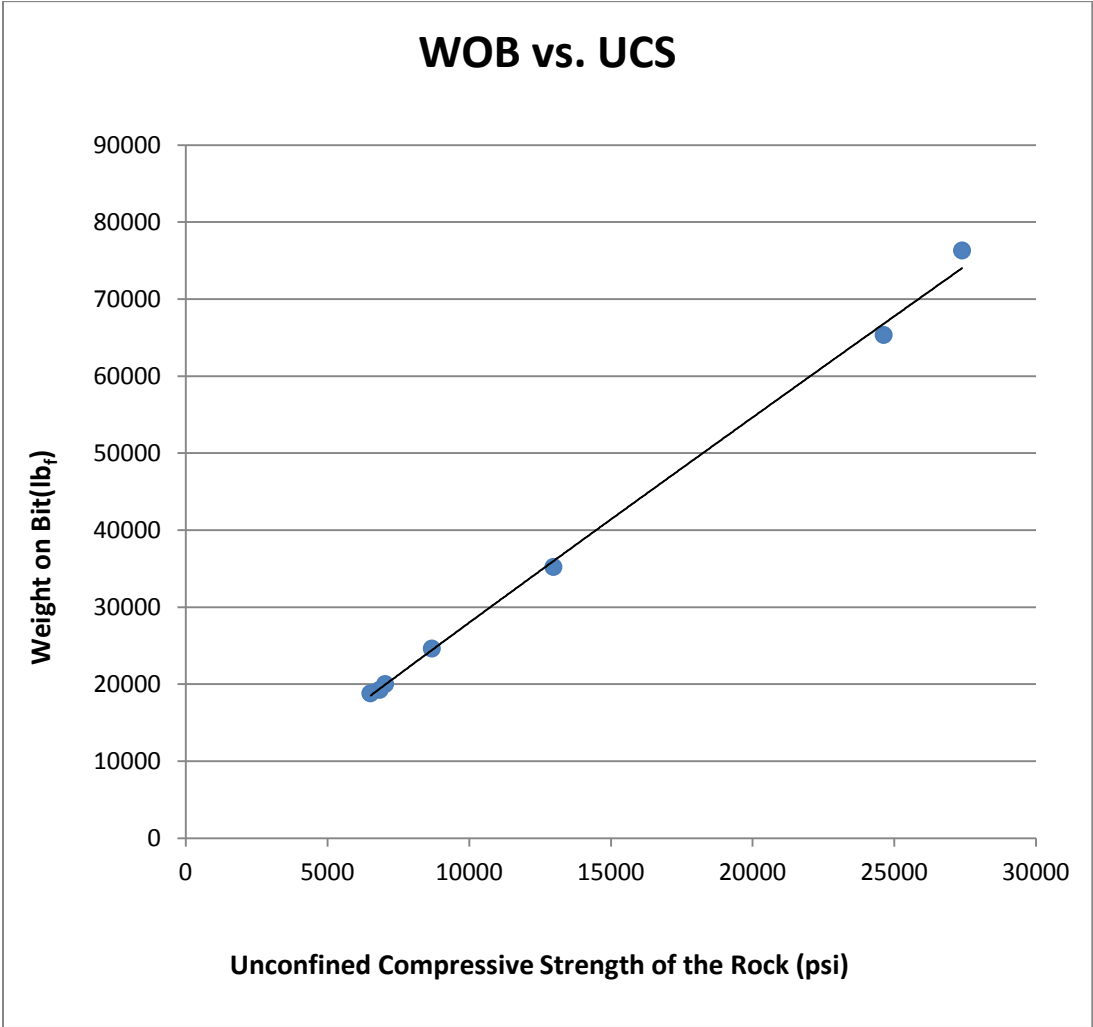
Figure 3.7:   WOB vs. Compressive Strength of the Rock
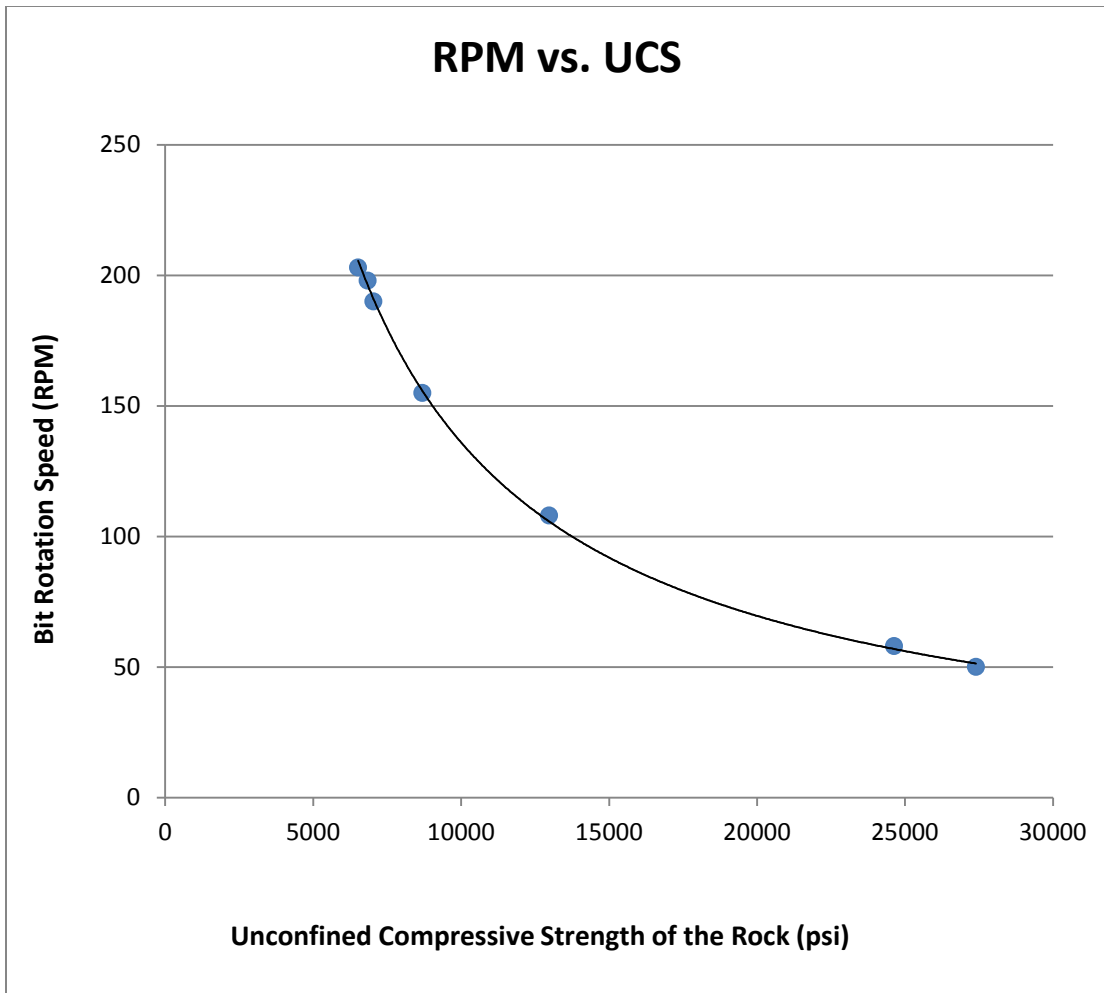
Figure 3.8:   RPM vs Compressive Strength of the Rock

3.1.3. Results

The results of the calculations are expressed in the figures on the following pages.

However, one cannot take the data at "face value" due to the assumptions involved in the

derivation of the equations. It is reasonable to assume that the PDC results (Figure 3.9

and Figure 3.10) are more reliable than that of the Tri-cone (Figure 3.11 and Figure

3.12) for power estimates, but the Tri-cone data does give some insight into the

magnitude of the torque encountered. As is expected, the drag on the tri-cone bit is much

smaller than the PDC bit. Intuitively, this result makes sense as the primary method of

rock destruction for tri-cone bits is from the crushing action that takes place underneath the teeth while for PDC bits it is the cutting and shearing of the formation by the cutters and the bit/formation interface.

From this information, it can be justified to discern the maximum horsepower needed solely from the PDC graph (Figure 3.9). However, the application of the bit types must also be taken into account. In practice, extremely hard formations would not be drilled with drag bits, simply because it would generate excessive amounts of torque on the bit and probably lead to premature failure of the cutting surfaces or the drill pipe. Instead, a Tri-cone bit would be used with more weight applied to the bit to induce rock failure by pulverization. With this thought in mind, and a comparison of Figure 3.9 and Figure 3.11, it was reasoned that a 200 hp supply to the bit would be sufficient to drill through any practical formation that would be loaded into the test rig. In order to validate the decision, a comparison of actual drilling data was needed. Pessier and Fear present Measurement While Drilling (MWD) data from a North Sea run with an 8 ½ inch PDC bit that can be seen in Table 3.2 (Maximum horsepower outlined in red). Comparing this data table to Cooper's take on possible formation layering in the North Sea [116], data presented by Pessier [80], and the calculation charts, 200 hp is considered to be a reasonable maximum for the power required during test rig operation. It should be noted that the impact force and erosion caused by the nozzle jet streams was not considered for the purposes of obtaining conservative results.
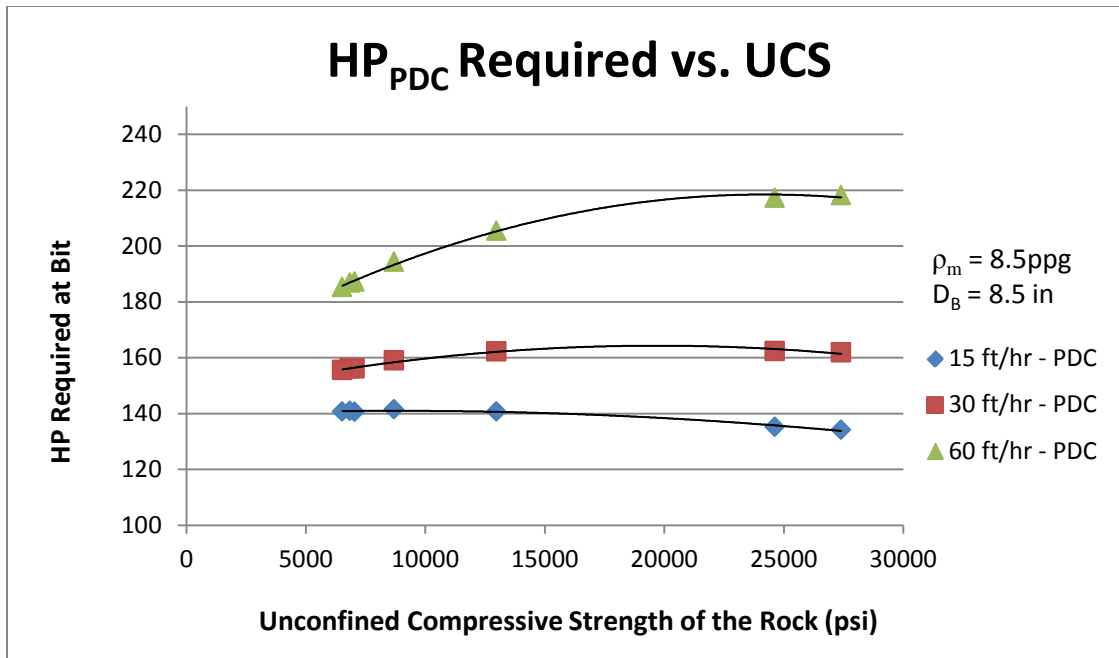
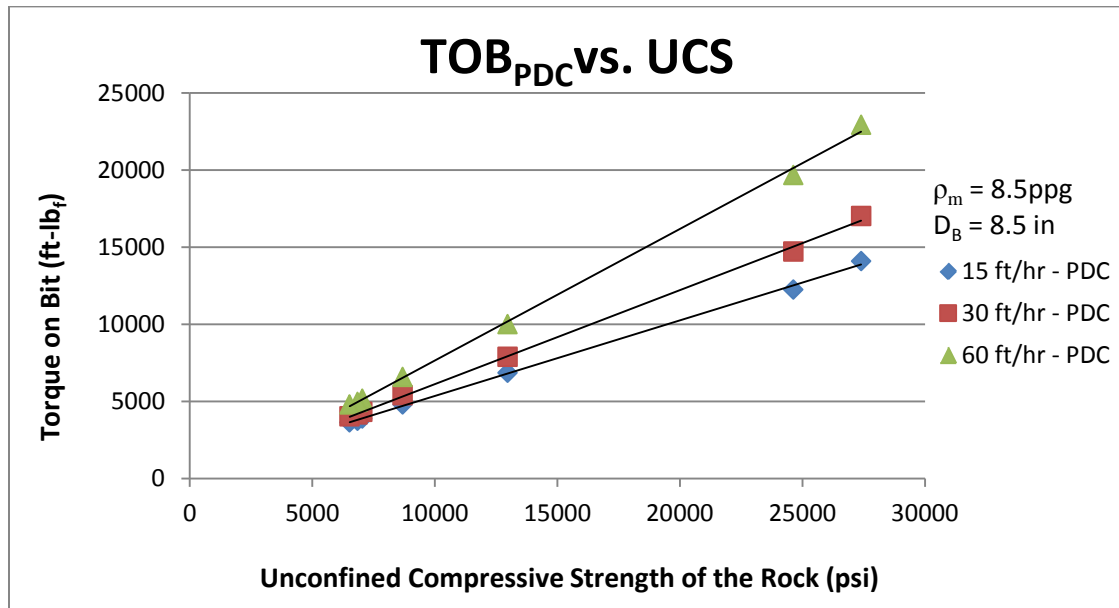**Figure 3.9:   HP Required vs. UCS for PDC Bit**

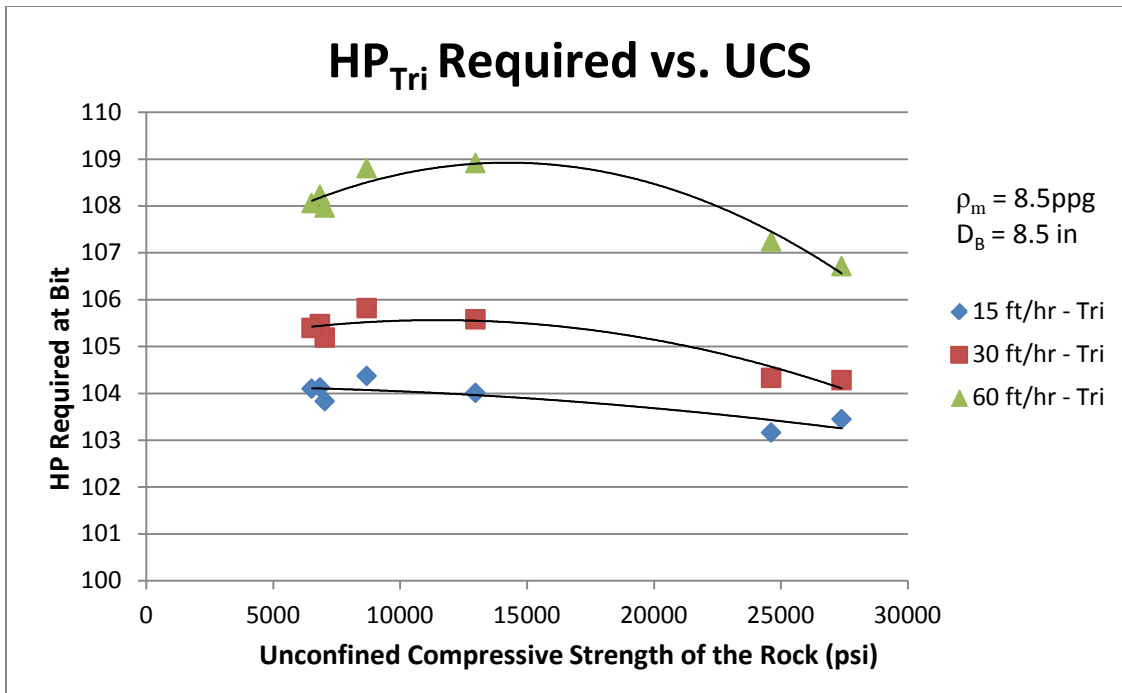**Figure 3.10:   TOB Required vs. UCS for PDC Bit**

48

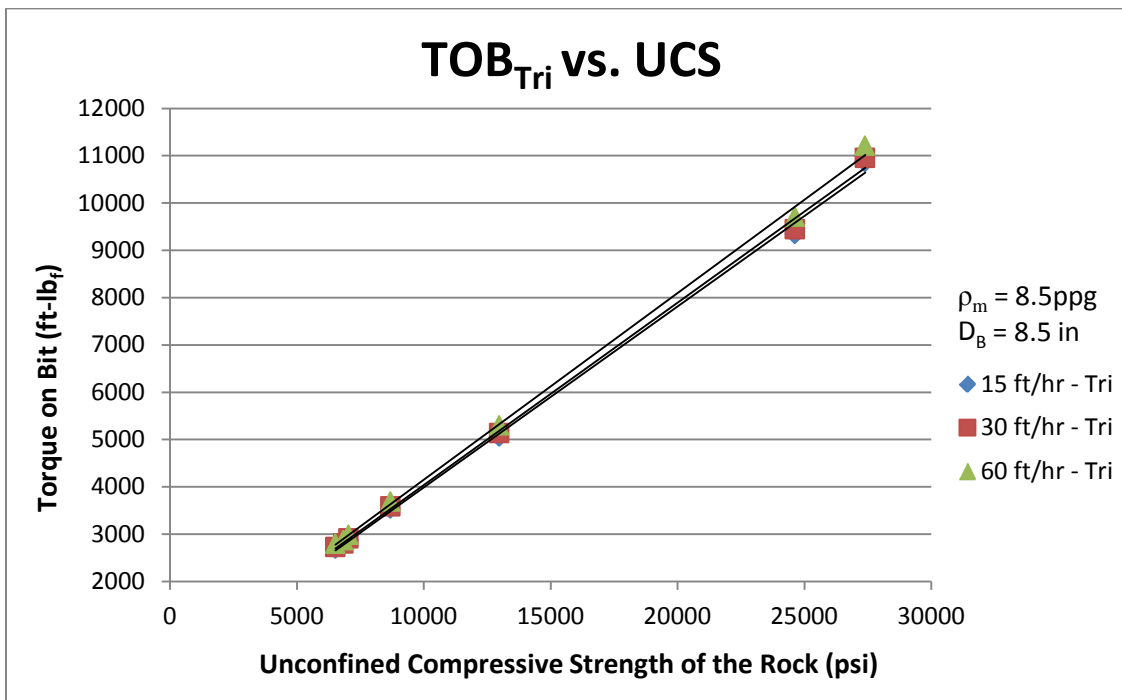**Figure 3.11:** HP Required vs. UCS for Tri-Cone Bit

Figure 3.12: TOB Required vs. UCS for Tri-Cone Bit

Table 3.2: MWD Data from an 8.5 inch Bit Run in the North Sea (From [79])

DEPTH (m)	ROP (ft/hr)	RPM	WOB (klb)	ROTARY TORQUE (ft lb) AVG	MAX	BIT TORQUE (ft lb)	MECHANICAL HORSEPOWER (hp)	DEPTH OF CUT (in./rev.)	E_s (psi)	μ
2470.00	49.9	133	9	4169	8945	2060	52.17	0.07499	18073	0.67
2471.02	34.8	117	15	4509	9404	2400	53.47	0.05945	26562	0.47
2472.02	35.1	125	17	4938	9863	2829	67.33	0.05617	33138	0.49
2473.02	52.8	110	20	7783	11087	5674	118.84	0.09604	38870	0.83
2474.06	35.1	116	21	7293	10475	5184	114.50	0.06053	56351	0.72
2475.00	30.2	123	20	6590	10322	4481	104.94	0.04908	60070	0.66
2476.00	31.2	124	21	6437	10016	4328	102.18	0.05027	56609	0.61
2477.01	15.7	120	24	5611	11699	3502	80.02	0.02625	87785	0.43
2478.02	24.9	108	24	7280	12311	5171	106.33	0.04617	73680	0.63
2479.02	23.3	112	20	5156	9557	3047	64.98	0.04160	48162	0.45
2480.00	28.7	105	20	5745	10016	3636	72.69	0.05437	44001	0.53
2481.00	22.5	106	20	5610	10016	3501	70.66	0.04271	53928	0.51
2482.06	21.2	105	22	5623	8945	3514	70.25	0.04062	56917	0.47
2483.00	23.8	115	25	6667	10934	4558	99.80	0.04165	71997	0.54
2484.00	42.0	115	28	8123	10475	6014	131.69	0.07303	54177	0.63
2485.02	46.7	117	28	9090	12158	6981	155.52	0.07964	57674	0.73
2486.00	55.9	121	29	8965	11852	6856	157.95	0.09219	48930	0.69
2487.09	53.2	113	29	9610	12311	7501	161.39	0.09407	52462	0.76
2488.09	31.3	118	27	8831	12005	6722	151.03	0.05283	83718	0.73
2489.00	52.1	137	29	10067	12617	7958	207.59	0.07615	68753	0.81
2490.00	54.3	136	28	9412	11393	7303	189.11	0.07961	60356	0.77
2491.00	67.3	137	29	9455	12617	7346	191.62	0.09819	49225	0.74
2492.04	49.3	138	30	8939	13382	6830	179.46	0.07132	63005	0.67
2493.05	56.7	129	28	9085	12923	6976	171.34	0.08800	52157	0.73
2494.00	42.5	133	26	8521	11240	6412	162.38	0.06364	66286	0.72
2495.00	37.9	123	19	7345	12005	5236	122.63	0.06135	56153	0.81
2496.00	57.9	126	23	8827	12464	6718	161.17	0.09166	48223	0.86
2497.00	56.5	123	22	8450	12464	6341	148.50	0.09176	45467	0.85
2498.04	61.5	129	22	7745	11852	5636	138.43	0.09512	38983	0.75
2499.00	57.6	125	23	8499	13076	6390	152.08	0.09239	45505	0.82
2500.02	53.1	126	22	8514	12158	6405	153.66	0.08436	49950	0.86
2705.05	6.8	129	28	5272	12770	2440	59.93	0.01068	150288	0.26
2731.00	12.6	118	7	9914	13076	7189	161.52	0.02113	233836	3.02
2827.00	5.6	126	39	6590	12770	4676	112.18	0.00885	347504	0.35

3.2. Mud Pump Requirements

One of the most important components on any type of drilling rig is the fluid circulation system, or more commonly referred to as the mud pump. The removal of rock cuttings, wellbore pressure control, bit lubrication and heat dissipation are some of the aspects of drilling that are greatly dependent on adequate fluid circulation. For the purpose of the test rig, the primary needs of the mud pump are to provide a means of bit lubrication and adequate removal of formation cuttings. In order to specify an appropriate mud pump for this application, it is necessary to predict the power required from the pump. Horsepower of a fluid flow can be expressed as the product of the pressure differential across the interval in question, and the flow rate.

$$\dot{W}_{pump} = \frac{Q(\Delta P)}{1714.2857}$$ **Eq. 16**

where $\dot{W}_{pump}$ is in horsepower, **Q** is the flow rate in gallons per minute and **ΔP** is the pressure differential across the pump in psi.

The proper flow rate for a drilling application, and its associated bit, is typically specified by bit manufacturers through extensive testing. For the purposes of analysis, a general flow speed needed to be determined that is independent of the bit being used. Following Nguyen's [115] recommendation of an annular fluid flow back speed, v_{ann}, of between 25 and 40 m/min (1.37 ft/s and 2.19 ft/s) for adequate removal of formation particles from the wellbore, a conservative flow speed can be estimated to be around 3 ft/s. From the flow speed in the annulus, a volumetric flow rate can be calculated based on the dimensions of the wellbore. If it is then assumed that the drilling fluid is relatively incompressible for the test rig's operation, the flow velocity in each section of the system is readily calculated as can be seen by Figure 3.13 along with Equations 17 and 18.
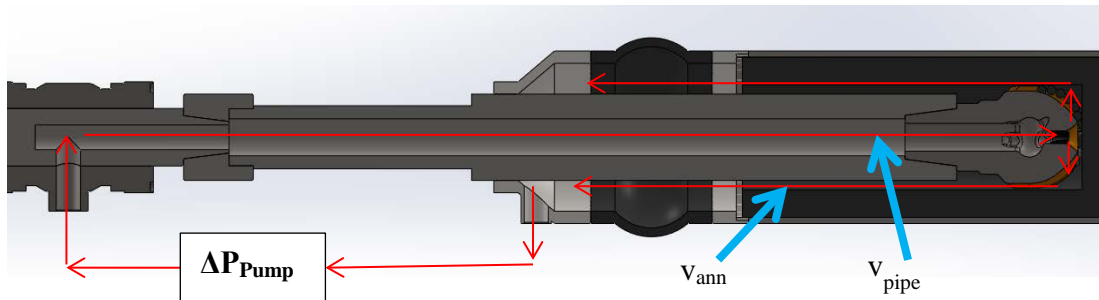

Figure 3.13: Trajectory of Fluid Flow in Test Rig

$$Q = \frac{\pi v_{ann}}{1.2833}\left(D_B^2 - D_{OP}^2\right)$$ **Eq. 17**

$$v_{pipe} = \frac{1.2833Q}{\pi D_{IP}^2}$$

Eq. 18

in which v_{pipe} is the fluid velocity in the drill shaft in ft/s, D_B is the bit diameter in inches, D_{OP} is the outer diameter of the drill shaft, and D_{IP} is the inner diameter of the drill shaft.

3.2.1. Fluid Properties

The analytical approach to the problem begins with defining the appropriate fluid model, which leads to the need of relevant rheological properties of the drilling mud.
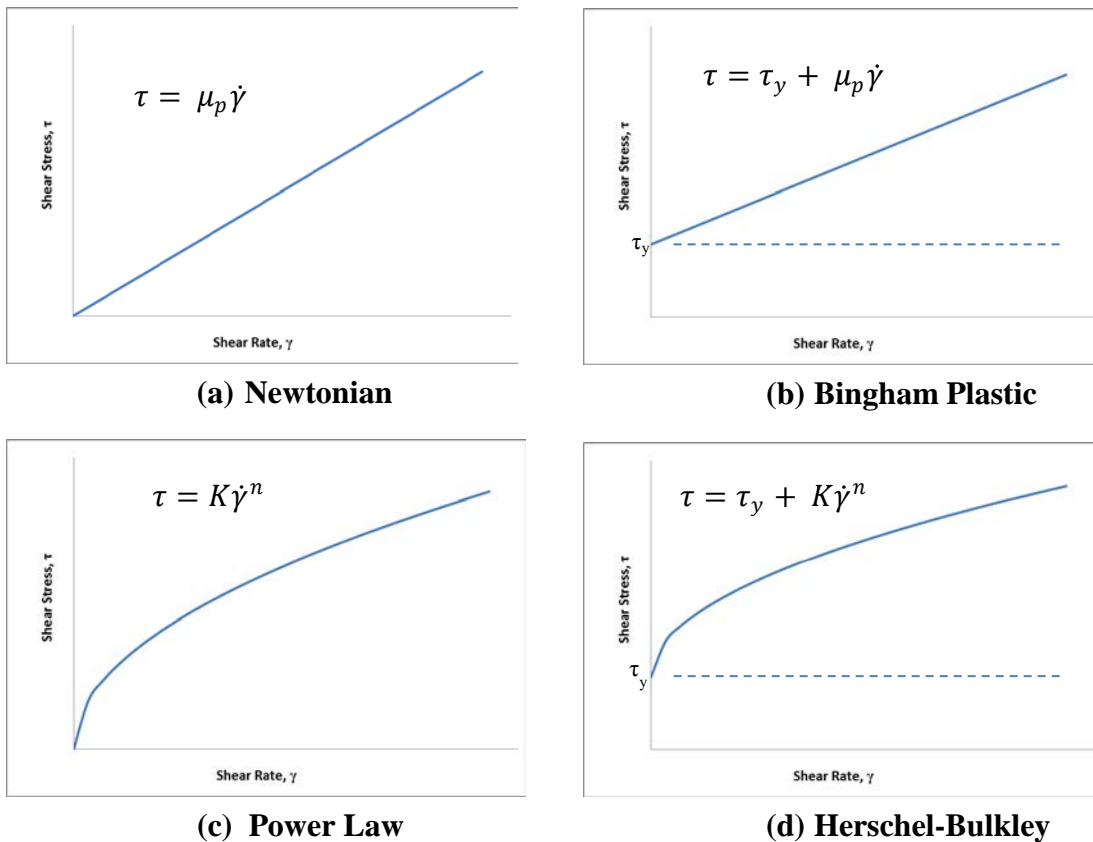

(a) Newtonian   **(b) Bingham Plastic**

(c) Power Law   **(d) Herschel-Bulkley**

Figure 3.14:   Rheological Fluid Models

Fluids are typically classified based on their observed relationship between shear rate, $\dot{\gamma}$, and shear stress, τ. Figure 3.14 illustrates the differences in popular fluid models used in the petroleum industry [9]. It has been shown [117-120] that drilling fluids can accurately be modeled by Bingham Plastic fluids, which allows for a seemingly accurate analytical representation of the flow through the system.

The coefficient, **n**, in this case represents the power law index and **K** is simply a fluid constant. Demirdal et al [118] presents an analytical tool (Equations 19-23) to determine rheological properties of Paraffin-based synthetic drilling fluid which, due its reflection of Bingham Plastic behavior and the fact that Paraffin-based drilling fluids are not uncommon to the industry, will be used to estimate the fluid properties for the mud pump.

$$\mu_P = \left(2750e^{1.9*10^{-4}*P}\right)T^{-\left(1.04e^{2.0*10^{-5}}\right)} \qquad \text{Eq. 19}$$

$$\tau_Y = \left[-1.494*10^{-13}P^5 + 2.3751*10^{-9}P^4 - 1.315*10^{-5}P^3 + 2.075*10^{-2}P^2 - 6.511P + 797.8\right]T^{-\left(-2.234*10^{-8}P^2+3.660*10^{-4}P+0.882\right)} \qquad \text{Eq. 20}$$

$$\rho_m = \rho_i e^{XP} \qquad \text{Eq. 21}$$

$$\rho_i = (-5.357*10^{-6})T^2 + (-1.267*10^{-3})T + 8.717 \qquad \text{Eq. 22}$$

$$X = (9.452*10^{-11})T^2 + (-1.530*10^{-8})T + 4.192*10^{-6} \qquad \text{Eq. 23}$$

where ρ is in ppg, μ_P is the plastic viscosity in centipoise, **P** is in psi, **T** is in °F and τ_y is the fluid yield stress expressed in lb$_f$/100ft^2.

3.2.2. Flow Calculations

When calculating the pressure drop in a turbulent flow of Bingham Plastics, it is sufficient to use conventional flow equations to solve the problem [120] by substituting a hydraulic diameter, D_H, for the characteristic diameter in the relations. However, as pointed out by Laird [120], for the laminar flow of Bingham Plastic fluids one cannot

assume a hydraulic diameter. In the analysis, turbulent flows of the drilling mud were
modeled by basic fluid mechanics equations [121] and laminar flows were modeled as
presented by Fredrickson, Bird and Laird [119, 120].

3.2.2.1. Turbulent Bingham Plastic Flow in Pipes and Annuli [121]

$$\Delta P = \frac{f L v^2 \rho_m}{102.88 D_H}$$

Eq. 24

where **L** is the length of the section of interest in feet, D_H is the hydraulic diameter
which is the pipe diameter for flow in circular tubes or $D_B - D_{OP}$ for the flow in the
annulus, and **f** is the dimensionless friction factor and is found by

$$\frac{1}{\sqrt{f}} = -2.0 \log\left(\frac{\left(\epsilon/D_{EFF}\right)}{3.7} + \frac{2.51}{R_e\sqrt{f}}\right)$$

Eq. 25

where ϵ is the material roughness, R_e is the Reynolds Number as outlined on the next
page. D_{EFF} is an effective diameter that, for pipe flow, is simply the pipe diameter. For
flow in an annulus it takes the following form

$$a = \frac{D_B}{2}$$

Eq. 26

$$b = \frac{D_{OP}}{2}$$

Eq. 27

$$Z = \frac{(a-b)^2(a^2-b^2)}{a^2-b^2-\frac{(a^2-b^2)^2}{\ln(a/b)}}$$

Eq. 28

$$D_t = 2(a-b)$$

Eq. 29

$$D_{EFF} = \frac{D_t}{Z}$$

Eq. 30

The friction factor equation was presented by Colebrook and White [122] and modified
later [121] to support flow in an annulus. It should be noted that the equation presented

for calculation of the friction factor, **f**, must be solved for numerically. Economides et al [123] presents an alternative analytical equation for the friction factor as well that gives very reasonable results expressed by Equation 26.

$$\frac{1}{\sqrt{f}} = -4log\left\{\frac{\epsilon}{3.7065} - \frac{5.0452}{R_e}log\left[\frac{\epsilon^{1.1098}}{2.8257} + \left(\frac{7.149}{R_e}\right)^{0.8981}\right]\right\}$$

Eq. 31

3.2.2.2.   Laminar Bingham Plastic Flow in Circular Tubes [119]

$$Q = \frac{\pi(R_{IP})^4\Delta P}{0.000032\mu_p}\left(1 - \frac{4}{3}\xi_o + \frac{1}{3}\xi_o^4\right)$$

Eq. 32

$$\xi_o = \frac{\tau_y}{525.195\Delta P(R_{IP})}$$

Eq. 33

3.2.2.1.   Laminar Bingham Plastic Flow in Annuli [120]

$$\Delta P = \frac{L\left\{\frac{Q8\mu_p}{\pi} + \frac{8}{3}\tau_y[(R_B^3 + R_{OP}^3) + 4r_o^3 - 3r_o^2(R_B + R_{OP})]\right\}}{(R_B^4 - R_{OP}^4) - \frac{\left(R_B^2 - R_{OP}^2\right)^2}{\ln\frac{R_B}{R_{OP}}}}$$

Eq. 34

$$r_o^2 = \frac{R_B^2 - R_{OP}^2}{2\ln\frac{R_B}{R_{OP}}}$$

Eq. 35

Where **R**$_*$ represents the radii of the bit, $_B$, the inner pipe, $_{IP}$, and the outer pipe, $_{OP}$.

The determination of the flow regime for Bingham Plastic is slightly different than that of Newtonian Fluids. As with Newtonian fluids, the Reynolds number must be calculated in order to determine the regime (laminar or turbulent) of the flow in question, but Bingham Plastics require the definition of another value known as the Hedstrom Number, **H$_e$** [124, 125].

$$R_e = 930.79 \frac{\rho v D_H}{\mu_p} \qquad\qquad \textbf{Eq. 36}$$

$$H_e = 37138.81 \frac{\rho \tau_y D_H}{\mu_p^2} \qquad\qquad \textbf{Eq. 37}$$

From the dimensionless Reynolds and Hedstrom numbers, it follows that there exists a critical Reynolds number which dictates whether the flow is laminar or turbulent and is governed by the following equations [118]

$$\frac{\left(\frac{\tau_y}{\tau_w}\right)}{\left(1-\frac{\tau_y}{\tau_w}\right)^3} = \frac{H_e}{16,800} \qquad\qquad \textbf{Eq. 38}$$

$$R_{e_{crit}} = \frac{1-\frac{4}{3}\left(\frac{\tau_y}{\tau_w}\right)+\frac{1}{3}\left(\frac{\tau_y}{\tau_w}\right)^4}{8\left(\frac{\tau_y}{\tau_w}\right)} \qquad\qquad \textbf{Eq. 39}$$

One would solve Equation 38 for the shear ratio, τ_y/τ_w, and use that in Equation 39. If the Reynolds number is larger than the critical value the flow is considered turbulent, likewise if the Reynolds number is less than the critical value then the flow is considered laminar.

The greatest contribution of pressure loss in the test rig circulation system will come from the flow through the drill bit. Robinson [126] presents the industry standard equation for this pressure drop but suggests an alternative value for the bit coefficient(C_d=1.03), however the commonly used bit coefficient (C_d=.95) gives a more conservative result and was therefore a more appropriate choice for the current study.

$$\Delta P_B = \frac{\rho Q^2}{12032 C_d^2 A_{Nozzles}^2} \qquad\qquad \textbf{Eq. 40}$$

The total pressure loss in the system is, of course, the summation of all of pipe, bit and annulus components.

$$\Delta P_{tot} = \Delta P_P + \Delta P_B + \Delta P_A \qquad\qquad\qquad \textbf{Eq. 41}$$

3.2.3. Analytical Results

To arrive at an appropriate pump requirement, it becomes necessary to determine the minimum requirements for operation. Using equations 19-23 and assuming standard conditions (**T =70°, P=14.7 psi**), leads to fluid properties that are close to that of water. In conventional drilling operations, water is the lightest fluid that would be drilled with, which in the case of the drilling rig will lead to a minimum requirement for the mud pump's operation. Wall roughness was estimated using data presented by White (Table 3.3) and by assuming that the walls adjacent to the fluid flow are characterized by an equivalent roughness that is comparable to rusted steel and course concrete.

Table 3.3: Surface Roughness for Various Materials [121]

Material	Condition	ε ft	mm	Uncertainty, %	ε, Worst Case ft	in	mm	Microinches
Steel	Sheet Metal, new	0.00016	0.048768	60	0.000256	0.003072	0.078029	3072
	Stainless, new	0.000007	0.002134	50	0.0000105	0.000126	0.0032	126
	Commercial, new	0.00015	0.04572	30	0.000195	0.00234	0.059436	2340
	Riveted	0.01	3.048	70	0.017	0.204	5.1816	204000
	Rusted	0.007	2.1336	50	0.0105	0.126	3.2004	126000
Iron	Cast, new	0.00085	0.25908	50	0.001275	0.0153	0.38862	15300
	Wrought, new	0.00015	0.04572	20	0.00018	0.00216	0.054864	2160
	Galvanized, new	0.0005	0.1524	40	0.0007	0.0084	0.21336	8400
	Asphalted, cast	0.0004	0.12192	50	0.0006	0.0072	0.18288	7200
Brass	Drawn, new	0.000007	0.002134	50	0.0000105	0.000126	0.0032	126
Plastic	Drawn tubing	0.000005	0.001524	60	0.000008	0.000096	0.002438	96
Glass		Smooth	Smooth					
Concrete	Smoothed	0.00013	0.039624	60	0.000208	0.002496	0.063398	2496
	Roughed	0.007	2.1336	50	0.0105	0.126	3.2004	126000
Rubber	Smoothed	0.000033	0.010058	60	0.0000528	0.000634	0.016093	633.6
Wood	Stave	0.0016	0.48768	40	0.00224	0.02688	0.682752	26880

Calculation was done using Maple[TM] and is shown in Appendix E. The results of the analytical equations can be seen in Figure 3.15. Total pressure loss is compared to pressure drop across the bit. A percentage of total pressure drop that occurs through the bit nozzles is also seen in the figure. The nozzle sizes in Figure 3.15 are presented in 32[nds] of an inch, as is the typical industry practice of nozzle sizing. It can be seen, as

previously mentioned, that the majority of the pressure loss for this system comes from the flow through the nozzles, ranging from nearly 100 percent for the smaller sizes to just below 60 percent for the larger diameter nozzles.
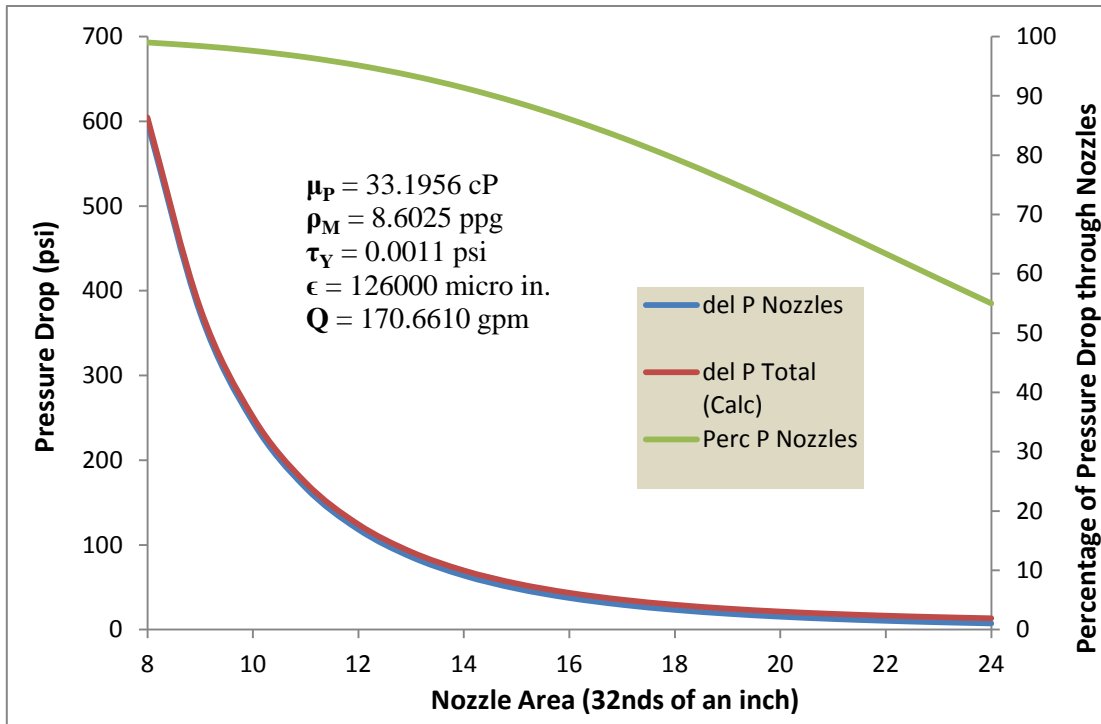

The figure contains the following annotations:

$\mu_P = 33.1956$ cP
$\rho_M = 8.6025$ ppg
$\tau_Y = 0.0011$ psi
$\epsilon = 126000$ micro in.
$Q = 170.6610$ gpm

Legend: del P Nozzles; del P Total (Calc); Perc P Nozzles

X-axis: Nozzle Area (32nds of an inch)
Left Y-axis: Pressure Drop (psi)
Right Y-axis: Percentage of Pressure Drop through Nozzles

Figure 3.15:   Variation of Pressure Drop Across the Bit due to Nozzle Size

3.2.4. CFD Comparison

As a means of comparison, a CFD model was constructed using Solidworks[©] Flow Simulation[©] 2012-2013. Incorporating the same fluid properties into the numerical modeling, a very similar pressure loss trend can be seen by adjusting the nozzle size. Figure 3.16 through Figure 3.18 depict the solid modeling and computational results for a nozzle size of 13 (32[nds]) with Figure 3.19 providing alternative views of the pressure distribution in the wellbore. As the analytical results suggest, again the figures clearly show that the primary pressure loss in the system is a result of the flow through the

nozzles of the bit. It can clearly be seen in Figure 3.18 that again, most of the pressure drop is through the nozzles on the bit as was implied by the analytical results.
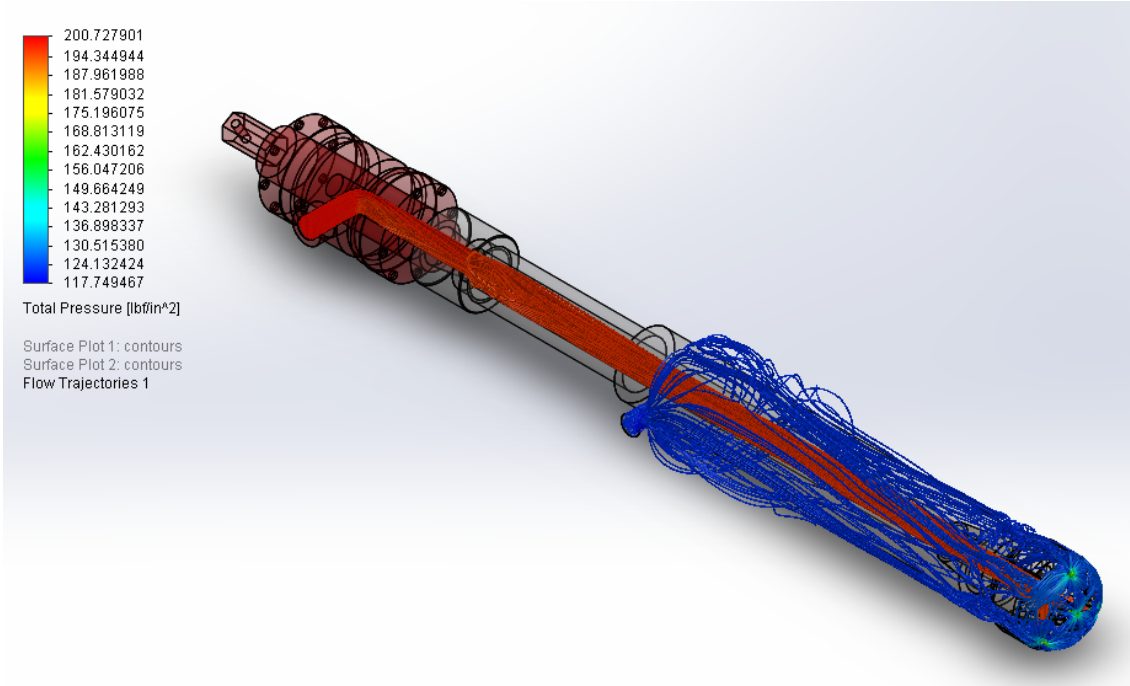

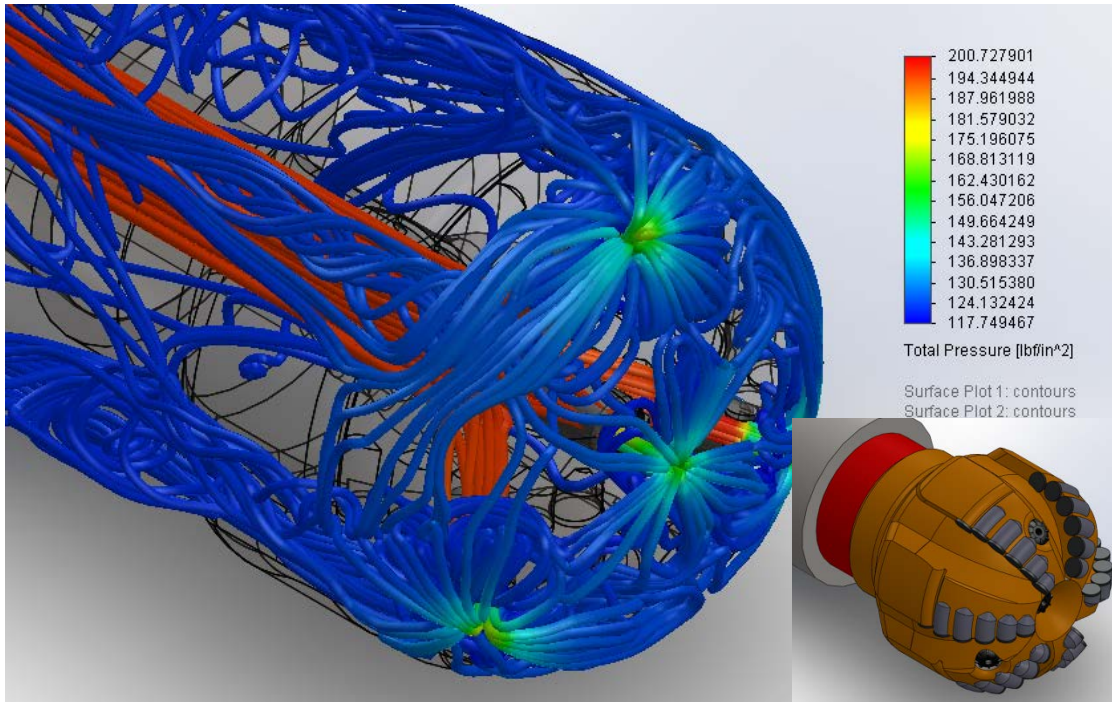**Figure 3.16:   CFD of Test Rig Fluid Flow (Nozzle Size: 13)**

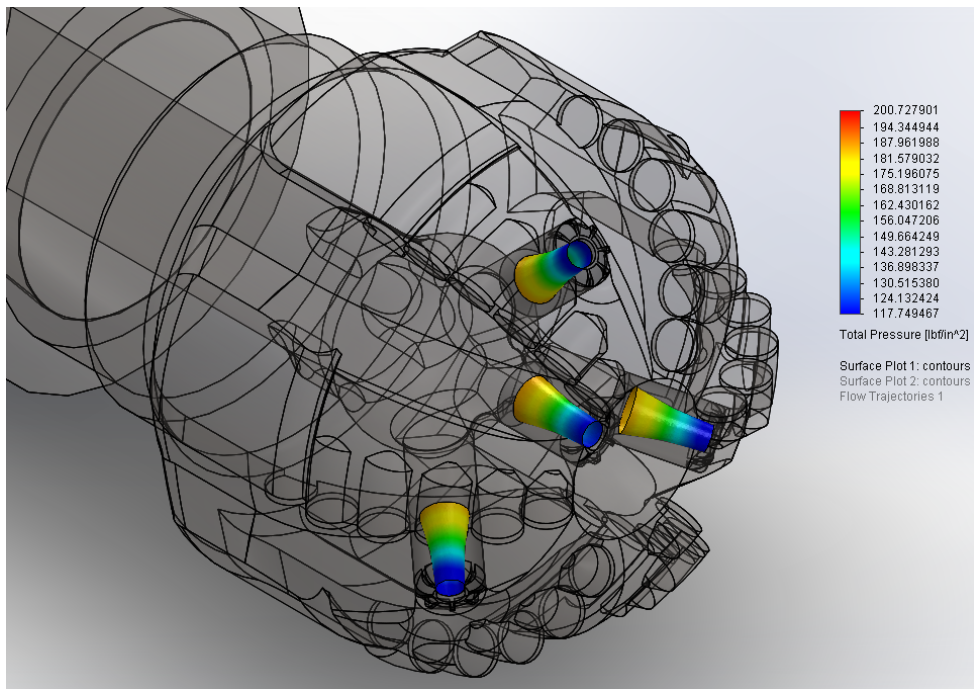**Figure 3.17:   CFD Bit Flow (Nozzle Size: 13)**

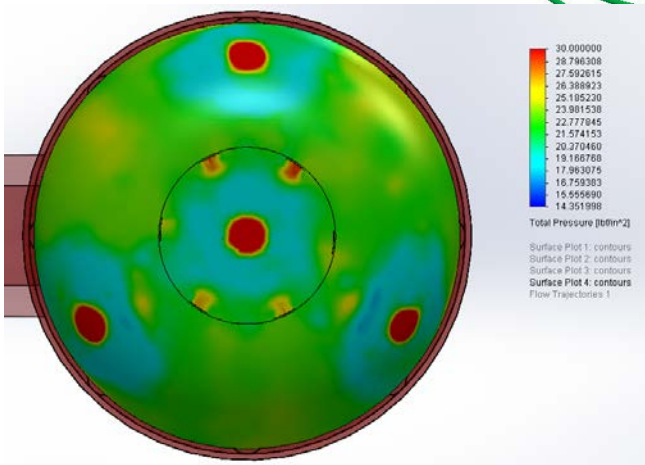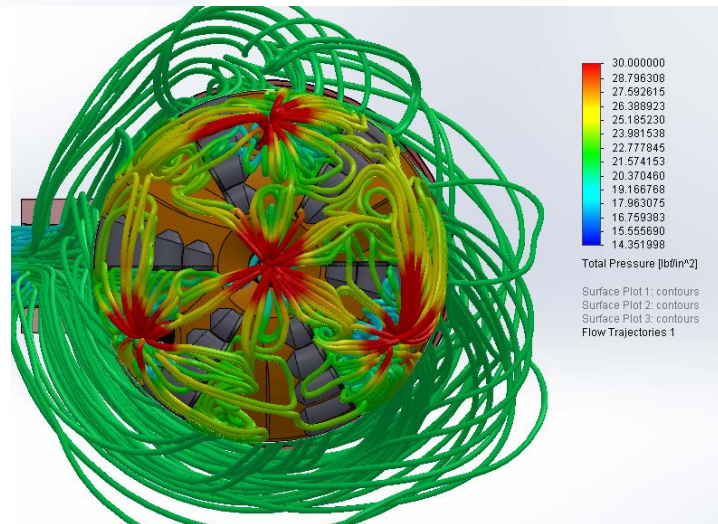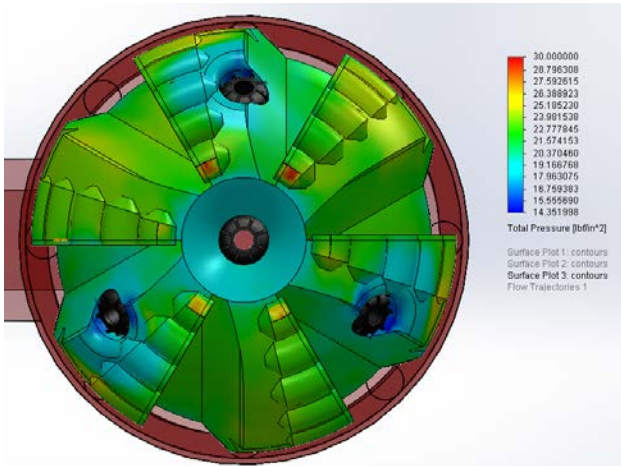**Figure 3.18:   CFD Surface Plot of Nozzle Pressure Loss (Nozzle Size: 13)**
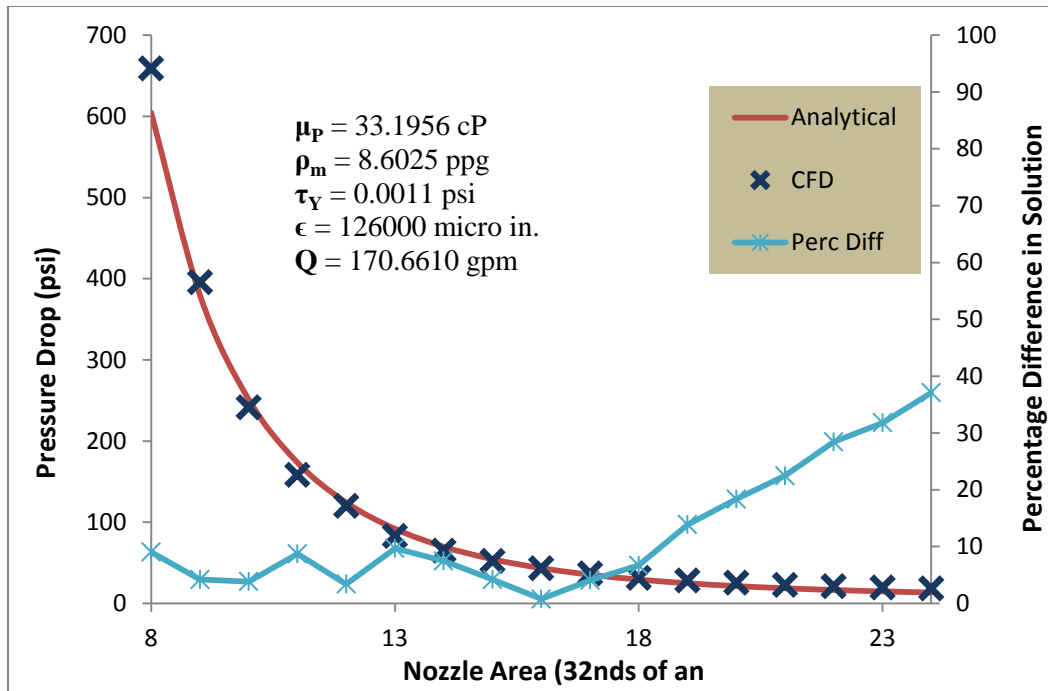
Figure 3.19:   Wellbore and External Bit Pressure Distribution
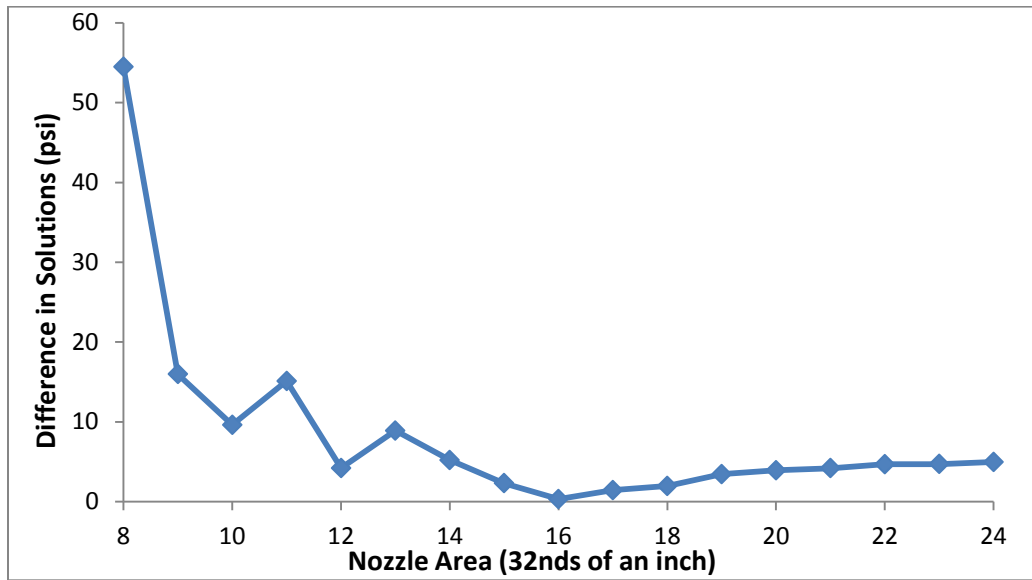
Figure 3.20: CFD Comparison of Pressure Loss

Figure 3.21: Difference in Analytical and Numerical Results

Figure 3.20 gives a graphical illustration of the similarities in the calculated and simulated pressure loss. The blue line in the figure suggests a sizeable percentage increase in the error of the system with an increase in nozzle size. Figure 3.21 is presented to express how this percentage is not necessarily an accurate representation in the error of solution. The reason for the larger percentage difference as the nozzle area increases is simply because the total pressure loss of the system is going down as the difference in solution is remaining relatively constant.

From the analysis the desired mud pump can be selected based on flow rate needs or pressure requirements. For the purposes of the rig's design a pump was specified based on performance as well as budget considerations. The pump meets the needs of an 8 ½ inch bit with four, size 13, nozzles flowing fluid at a rate of 170 gpm.

3.3. Structural Analysis

Extensive structural analysis was undertaken using analytical techniques coupled with commercially available software, namely Solidworks® Simulation® 2012-1013. The following section is devoted to the presentation of key finite element simulations and their analytical counterpart, referenced where appropriate.

3.3.1. Design Factors

In modern engineering "factors of safety" are a standard practice used to design for unanticipated loading scenarios. Two primary loading conditions exist during operation of the rig, axial (WOB) force actuation and torsional (TOB). The axial design factor is calculated by assuming that, while drilling, the formation will "bounce", or lift, off of the bit by 1 inch. This assumption is meant to anticipate a severe axial impact occurring at the bit/formation interface. The calculation of the impact loading is presented in Appendix F where a **FOS of 2** has been determined. For the torsional case, the allowable factor of safety is more of a function of the sensor capabilities. Since the rated torsional loading for the transducer is 200,000 in-lb$_f$ and the maximum anticipated torque required

is 168,000 in-lb$_f$, a torsional **FOS of 1.45** is assumed. An electronic shut-off switch will be activated in the event that 200,000 in-lb$_f$ is reached during operation so as to protect the rig and its measurement components.

3.3.2.   Finite Elements in Solidworks® Simulation®

While FEA can be considered a means to an end, it should never be considered an end in itself. In order to properly take advantage of a finite element utility such as Solidworks®, one must have a thorough understanding through extensive experience and/or accredited coursework. Analysis of the test rig was possible through an educated understanding of finite elements as applied to structural mechanics and the theory behind the governing equations of linear elasticity as well as a vast experience with numerical simulation in Solidworks® and its associated add-ins. Other sources of knowledge on the subject were also utilized [127, 128] to arrive at accurate solutions. Care was given to obtain proper meshing characteristics, boundary conditions and loading conditions. Materials and their respective properties can be found in Appendix G. Due to the size of the components being analyzed and the limitations in computing resources, the rig was divided and examined by sections. The associated reaction forces and boundary conditions where then transferred between models.

3.3.3.   Year 1 Component Simulations

The first piece of the rig to be analyzed was the sample containment structure (Figure 3.22). This formation housing is the component that all the power of the drive and drilling system will be transferred to. The structure is also the "heart" of the rig's design and where all of the force and torque measurement will take place.
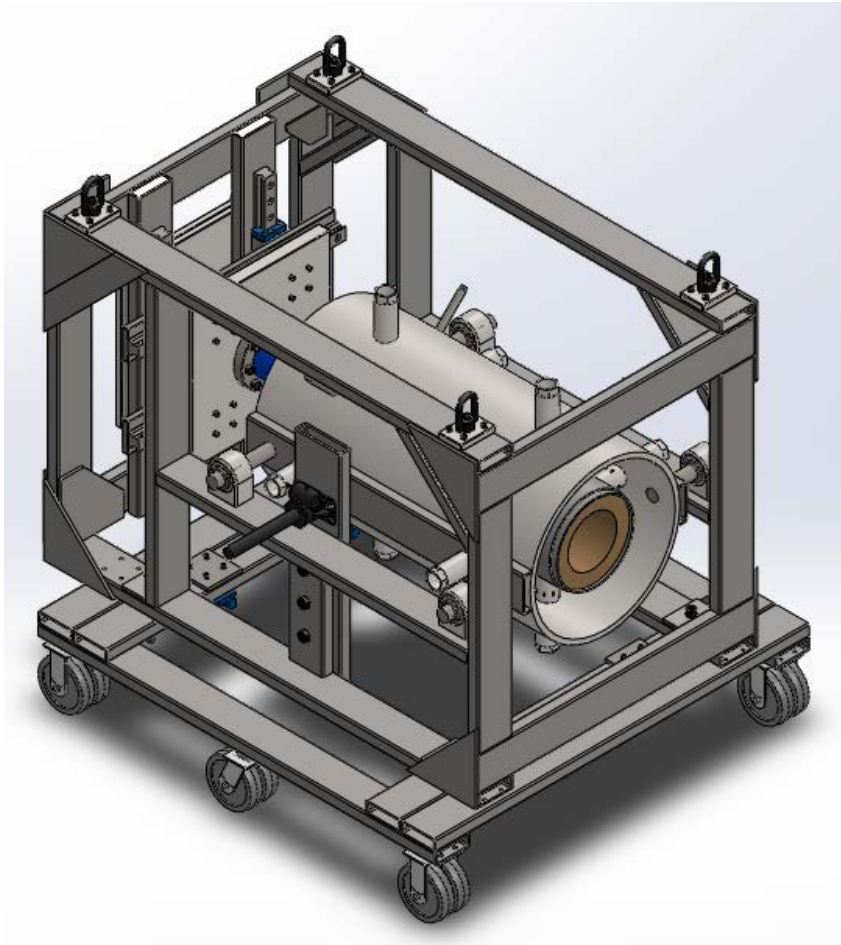
Figure 3.22:   Sample Containment Structure

3.3.3.1.   Sample Containers

The approach of analysis was to start with the point of loading (Formation Sample) and build outwards to the structure supports. Figure 3.23 depicts the sample containers of the containment structure with applied loading and boundary conditions.
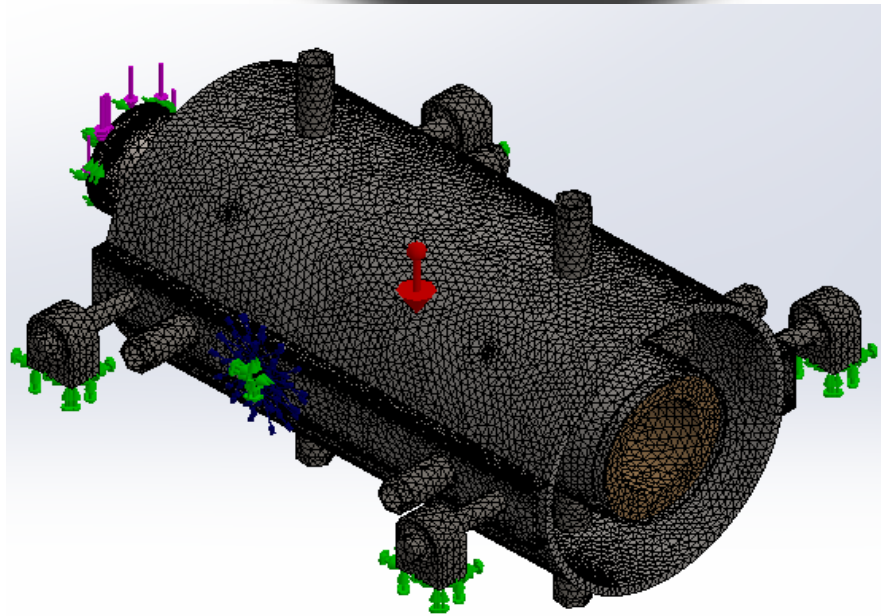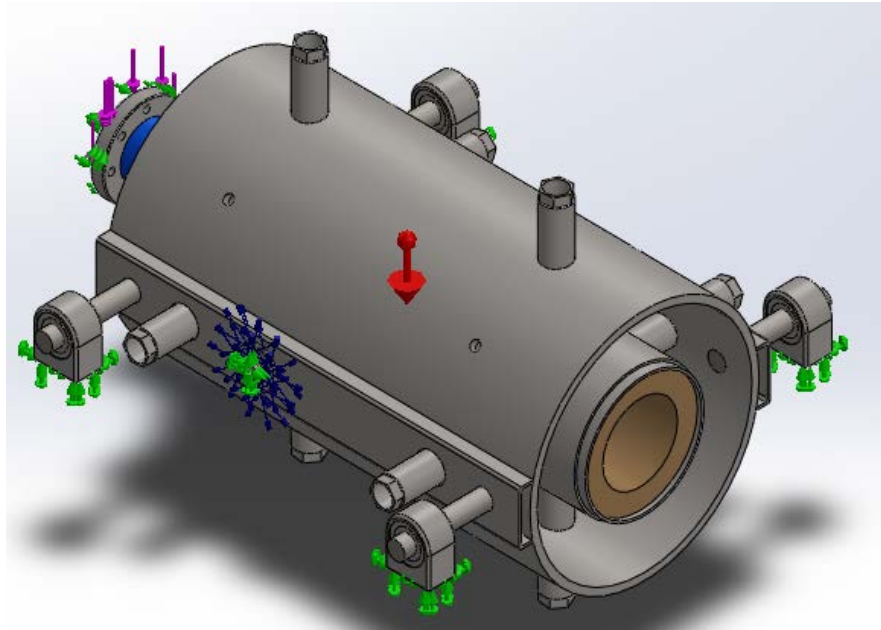
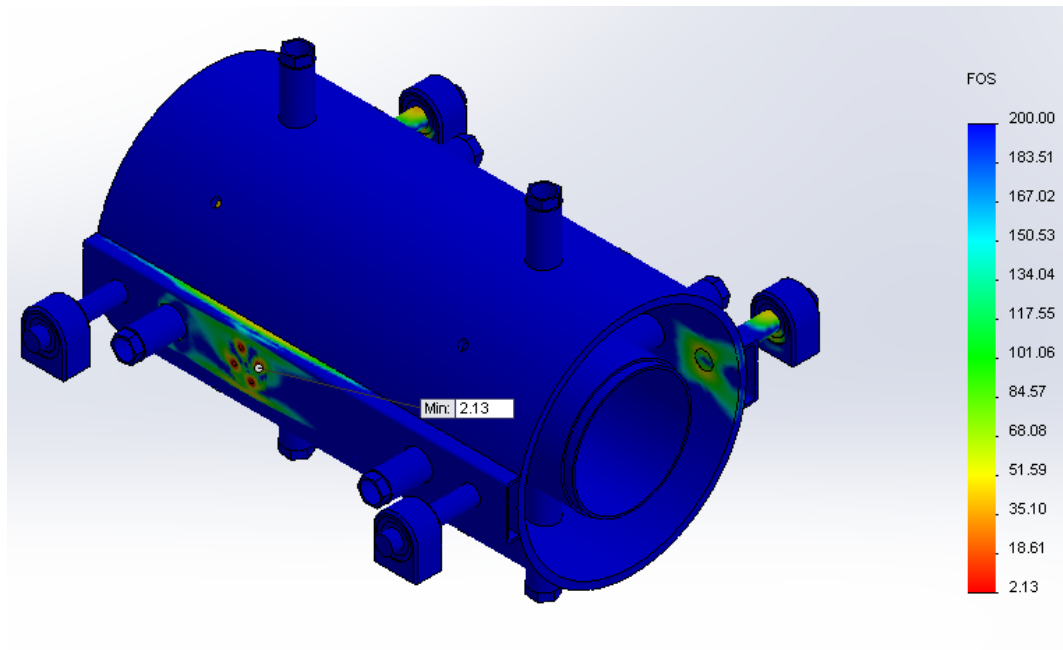**Figure 3.23:   Sample Containers and Associated Mesh Plot**

$W_o = 55,000 lb_f$
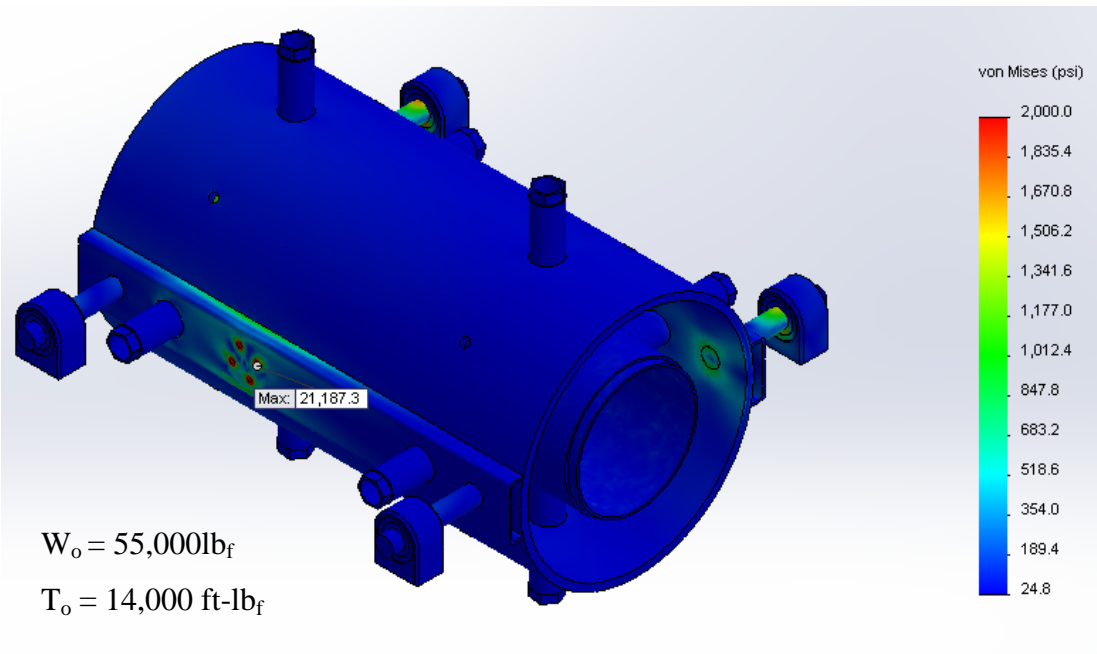
$T_o = 14,000$ ft-lb_f

Figure 3.24:   Stress and FOS Plots of Sample Containers

Figure 3.24 gives the stress and FOS distributions of the solution. It can be seen that the minimum design factor is greater than the aforementioned axial FOS therefore this component of the design is considered approved for operation. The remainder of the finite element analysis is presented in a similar fashion with explanations of results where appropriate.
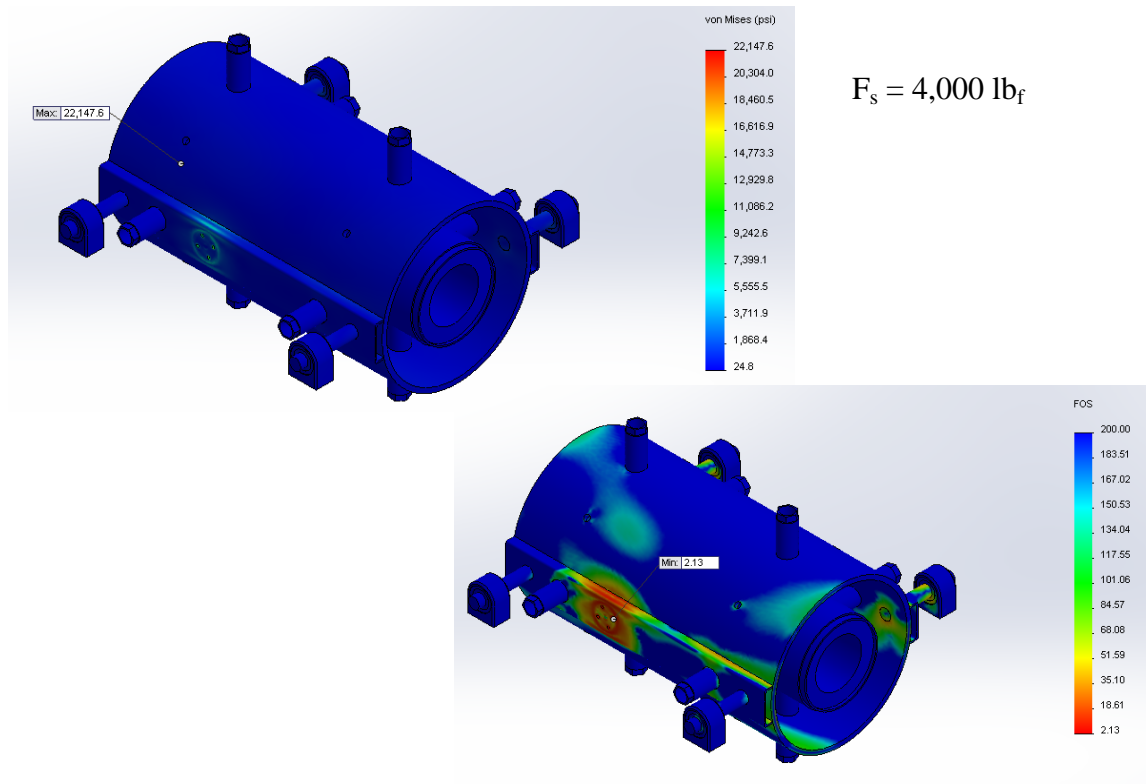

$$F_s = 4{,}000 \ \text{lb}_f$$

Figure 3.25:   Stress and FOS Plots of Inner Sample Containers with Side Load

Figure 3.25 displays the results of a side loading simulation of the inner sample containers. This simulation mimics what could be seen under the formation deflection testing (See Section 6).

3.3.3.2. Sample Securing Bolts

The formation sample will be cemented inside of the inner container. To assure adequate adhesion to the container, twelve securing bolts will be placed along the outside of the cylinder to maintain a firm connection between the rock and the metal housing. This will ensure an adequate transfer of torque and force to the measurement system. The results of a stress study in the securing bolts are shown in Figure 3.26. This analysis assumes that the formation is not adhering to the inner container and thus transfers all torque through the securing bolts, which is a worst-case-scenario that leads to more conservative solution.
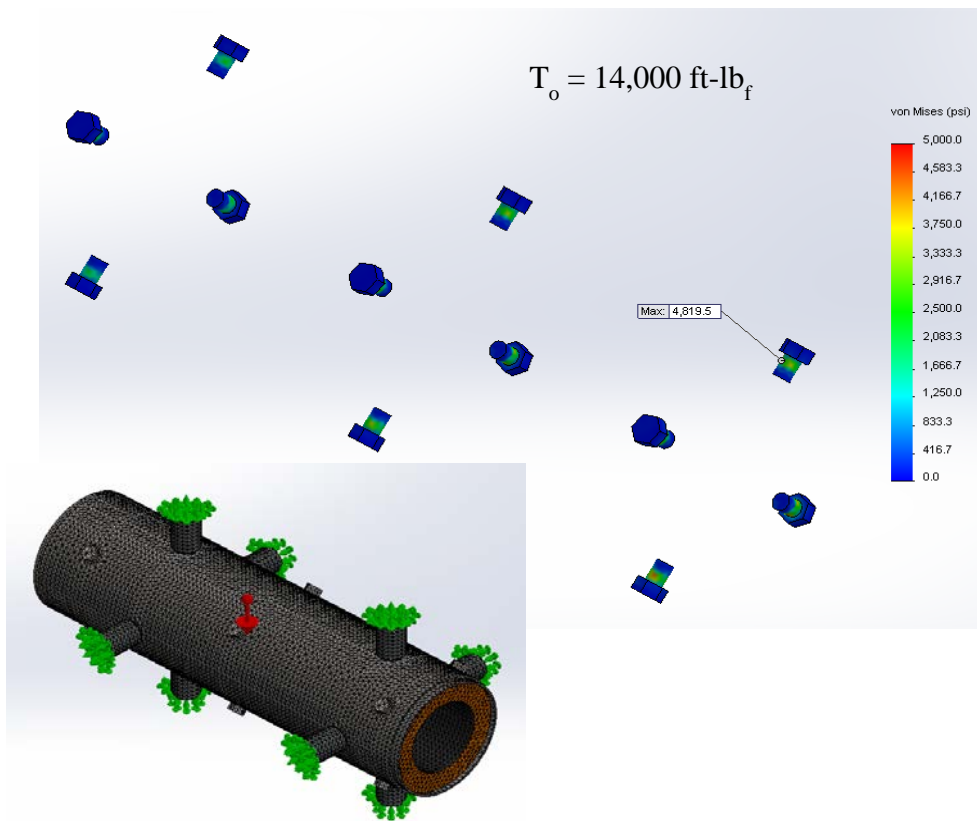

Figure 3.26:   Sample Securing Bolts FEA Results

3.3.3.3.   XY-Translator Table

The XY-translator table is an essential part of the force/torque measurement system. The table provides free translational movement of the axial/torsional transducer which removes any transverse loading on the transducer. Since the transducer (and Inner Sample Container) is laterally supported by the lateral force measurement rods, any and all lateral loading while drilling will be measured.
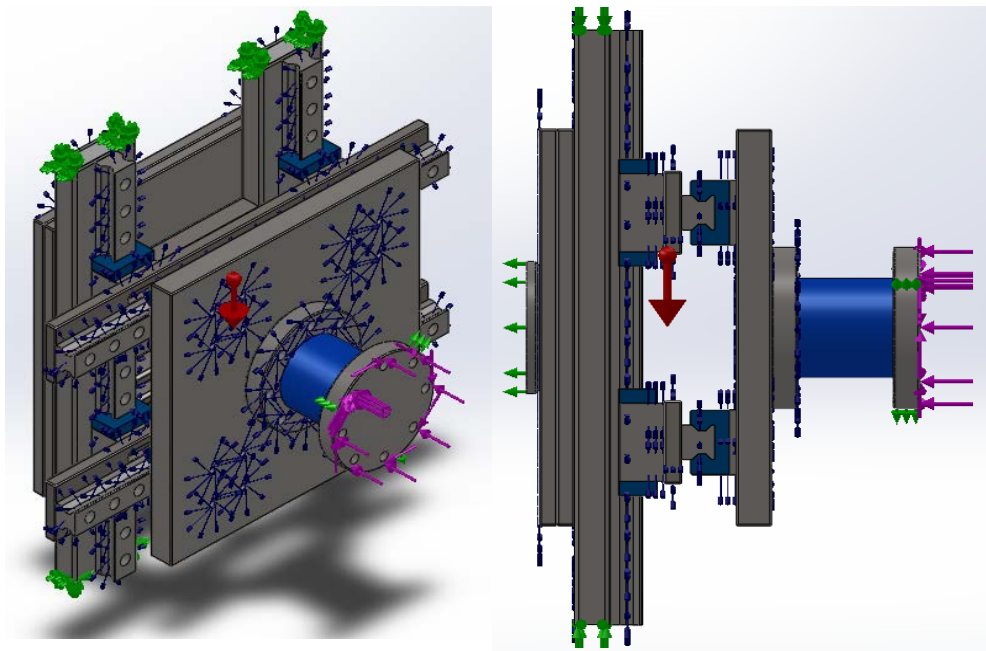

Figure 3.27:   XY-Translator Table with Loads and Boundary Conditions

Figure 3.27 and Figure 3.28 depict the FEA modeling of the XY-translator assembly. The stress plot shown in Figure 3.29 clearly shows significant stress levels that would exceed the yield strength of any readily available steel. Figure 3.30 further explores the location of the excessive stress. It can be seen that it occurs at the roller carriage and guide rail interface. However, the CAD models of the roller carriages are over simplified for purposes of analysis. In actuality, the interface that is generating the high stress does not exist. Therefore, it is important to look at the loading on each rail carriage.
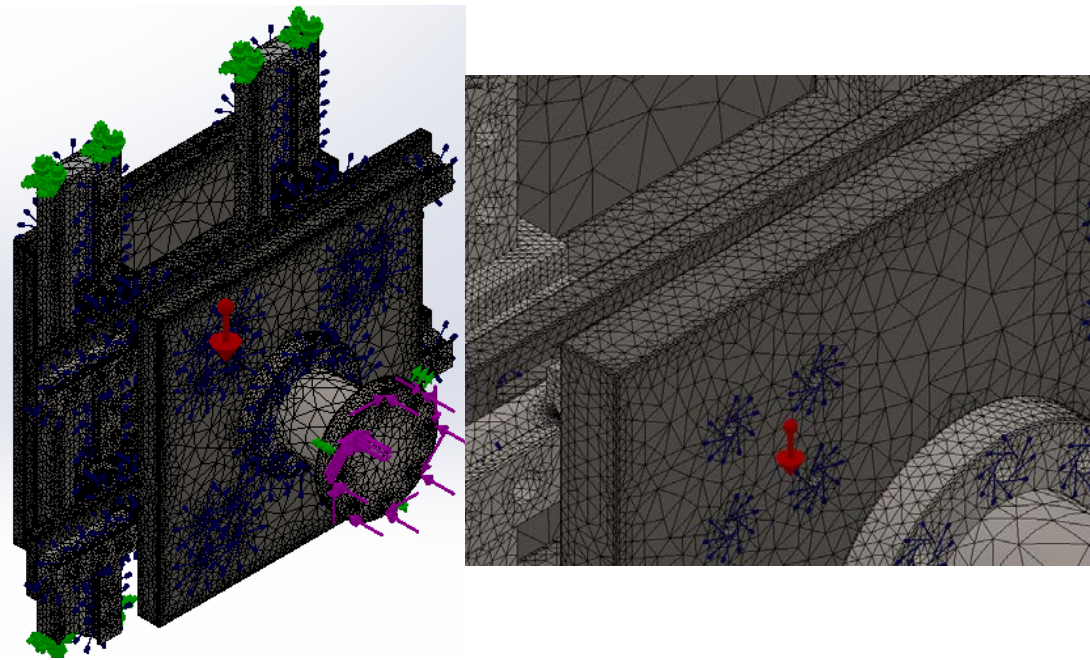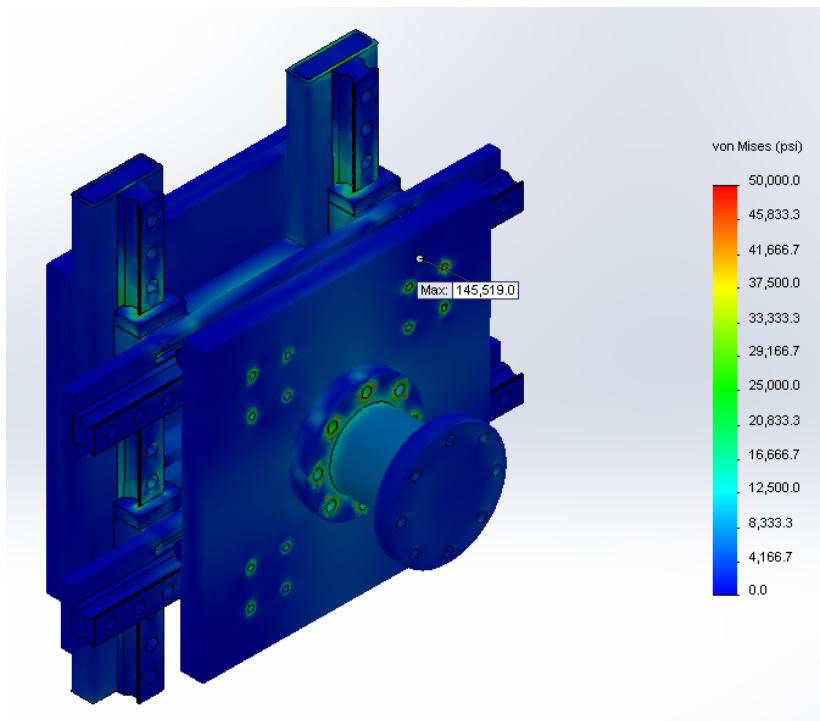
Figure 3.28:   Mesh Plot of XY-Translator Table
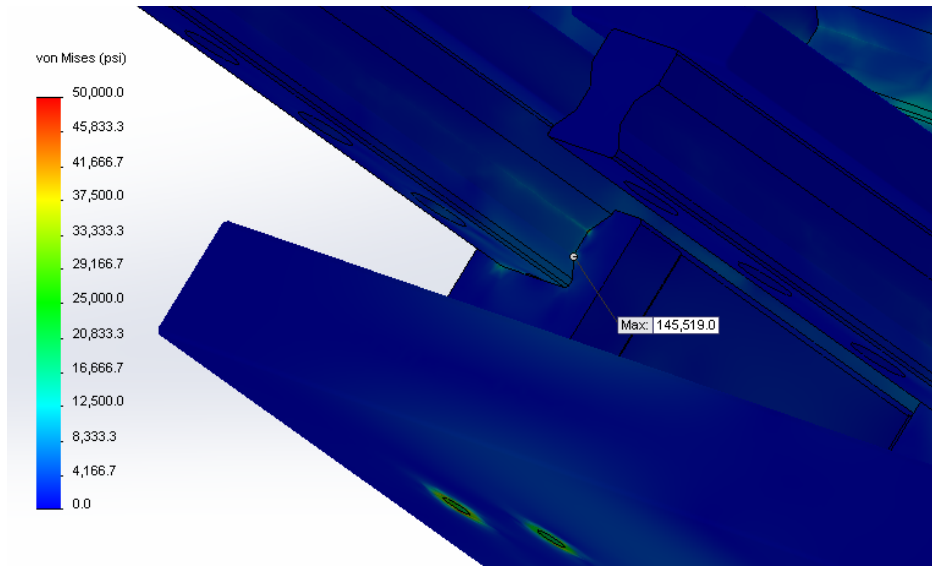

Figure 3.29:   Stress Plot of XY-Translator Assembly

71

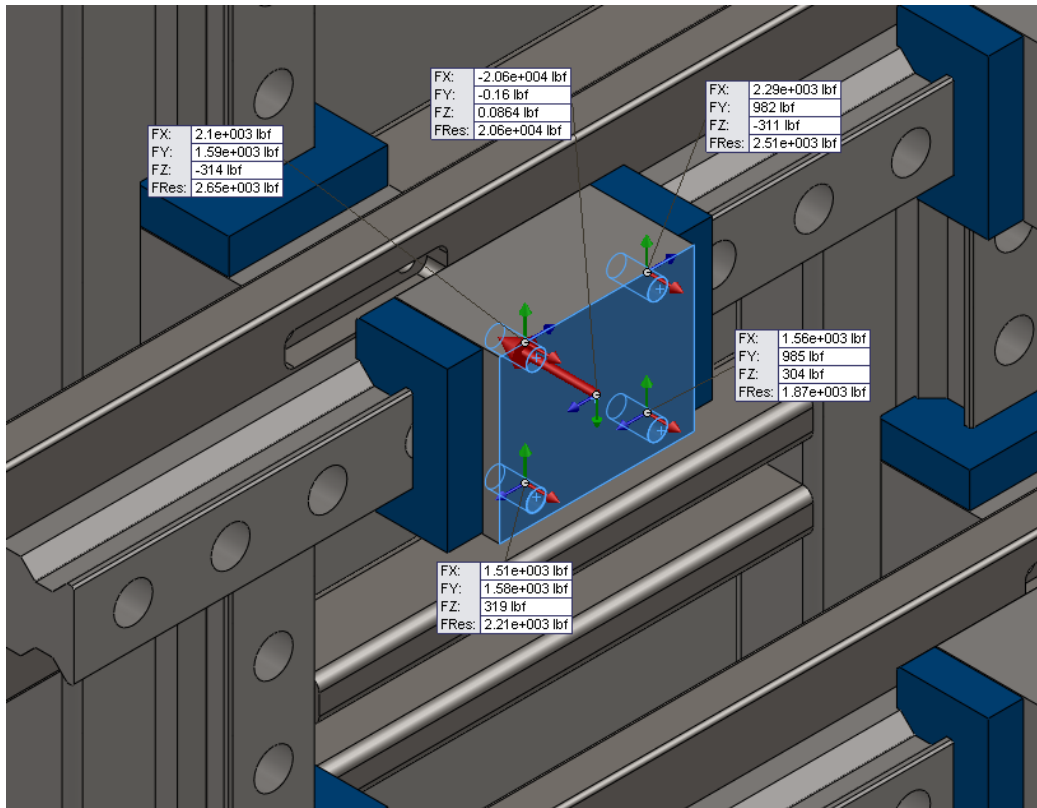**Figure 3.30:   Stress Concentration at Roller Carriage/Rail Interface**

Figure 3.31:   Roller Carriage Loading Validation

Figure 3.31depicts the free body forces acting on the roller carriage, as calculated from the FEA model. Since the loading (X_{tot} = -13,159 lb$_f$, Y_{tot} = 5,137.4 lb$_f$, Z_{tot} = -1.7642) is well within the rated operating range of the carriages (Thomson 512P55C3 Rail Carriages, Dynamic Load Rating: 29,652 lb$_f$) it is assumed that the stress induced are readily handled by the carriages. Knowing this, the remaining components of the assembly need to be looked at to make sure that the stress levels are acceptable.

Figure 3.32 displays the stress distribution in the components of the XY-translator assembly that are not pre-engineered. The term "pre-engineered" references anything that is boaught and use "as is" as part of the test rig. Pre-engineered components are assumed to be designed to handle the loads that are advertised as withstanding. It can be seen that the maximum stress is around 54,700 psi on the back side of the transducer plate where the securing bolts are fastened. This stress level can be mitigated by using washers in between the nut and the plate. With the washers in place the maximum stress would be reduced to roughly 27,000 psi which would correspond to an FOS of 2.It should be noted by the reader that Solidworks® Simulation® models bolts in a mathematical fashion. This means that kinematic constraints are automatically introduced into the system based on the user specification of the bolt interface. This method could also be introducing error into the solution which could be correlating to the stress concentrations near the bolt holes.
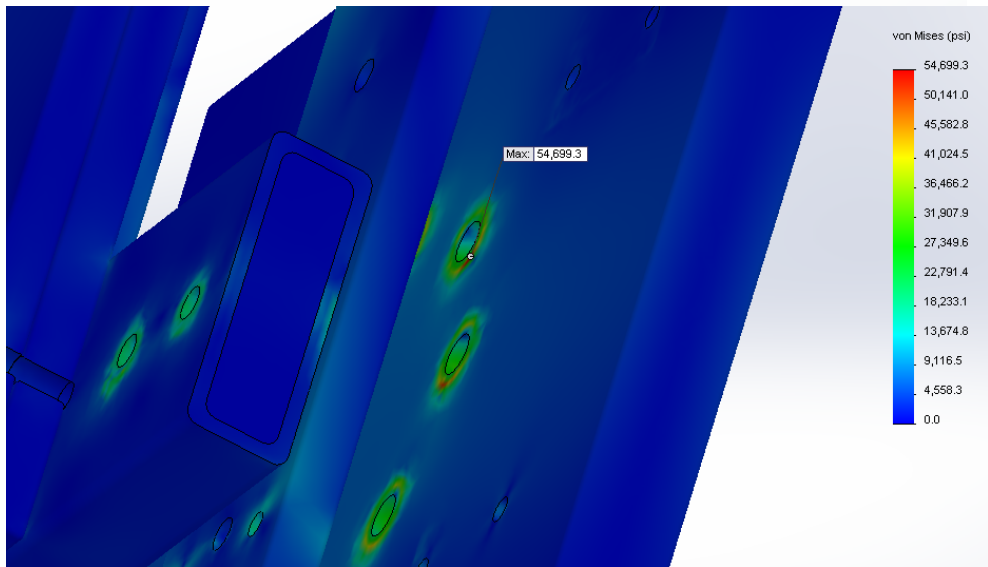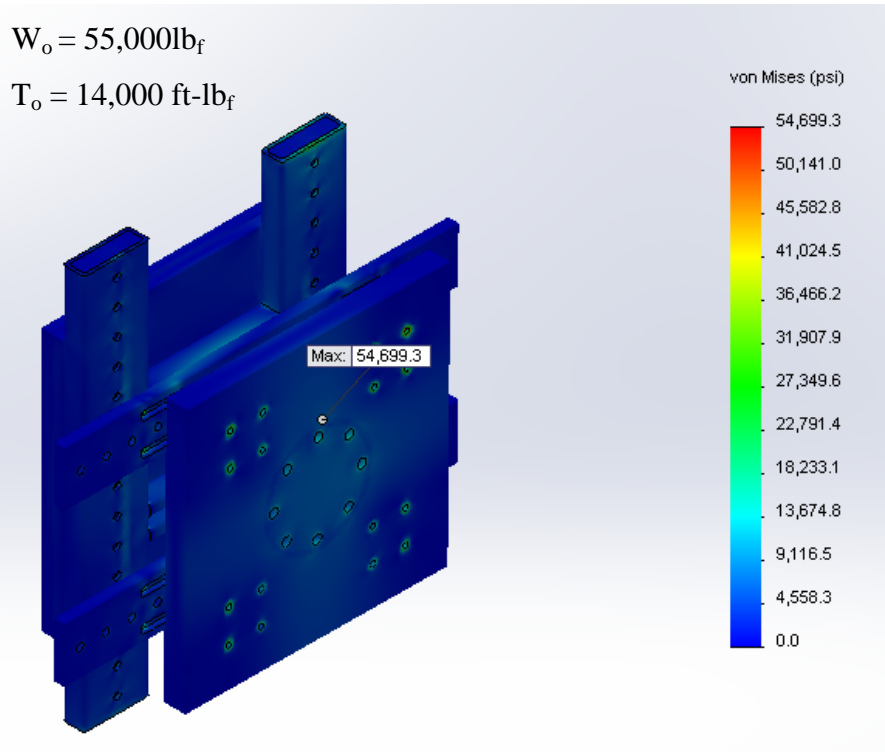
$W_o = 55,000 lb_f$

$T_o = 14,000$ ft-lb$_f$

Figure 3.32:   Maximum Stress on Components of XY Translator Assembly

3.3.3.4.   Hydraulic Pin Support

The hydraulic pin analysis included an analytical comparison as a means to validate Solidworks® Simulation®. Figure 3.33 and Figure 3.34 depict the simulation setup and results of the study. A closer examination of the isolated hydraulic pin is shown in Figure 3.35. Observing the analytical solution to the problem (Appendix H) one can see very similar results, thus suggesting the mush density of the simulation model is appropriate and that Solidworks® Simulation® can in fact be reliable in a structural analysis when used properly.
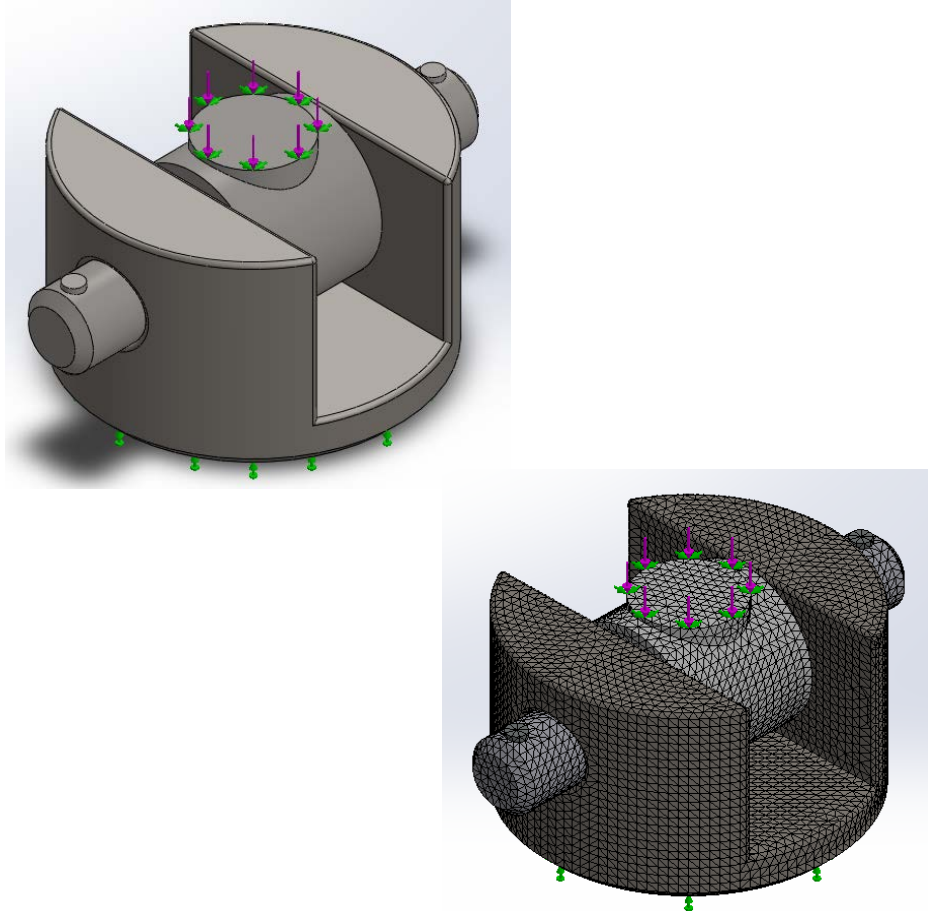

Figure 3.33:   Hydraulic Pin Support CAD Model and Mesh Plot

von Mises (psi)

63,949.5
58,620.7
53,291.8
47,963.0
42,634.2
37,305.4
31,976.5
26,647.7
21,318.9
15,990.0
10,661.2
5,332.4
3.5

Max: 63,949.5

$W_o = 55,000 \text{lb}_f$

FOS

10.00
9.43
8.85
8.28
7.71
7.14
6.56
5.99
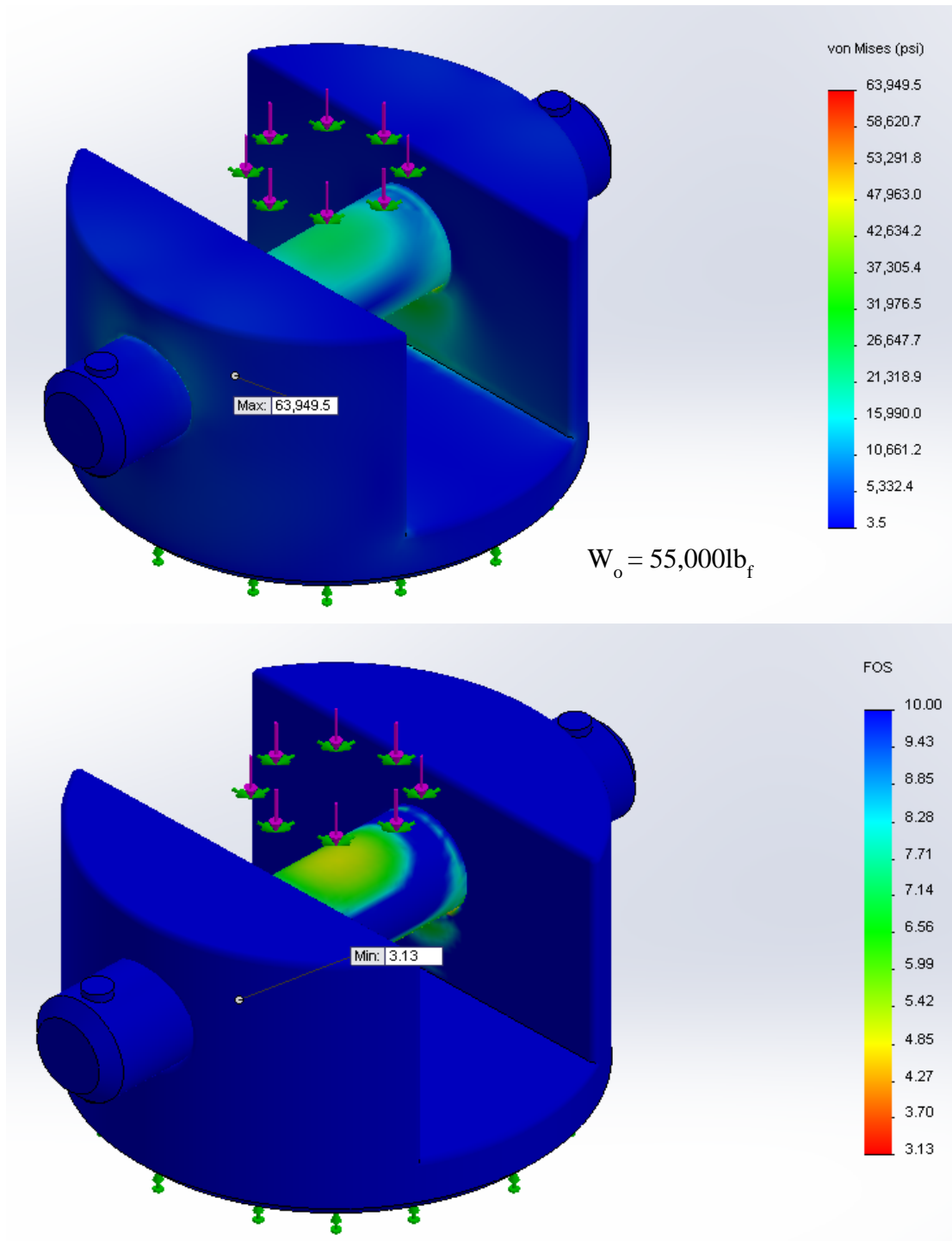5.42
4.85
4.27
3.70
3.13

Min: 3.13

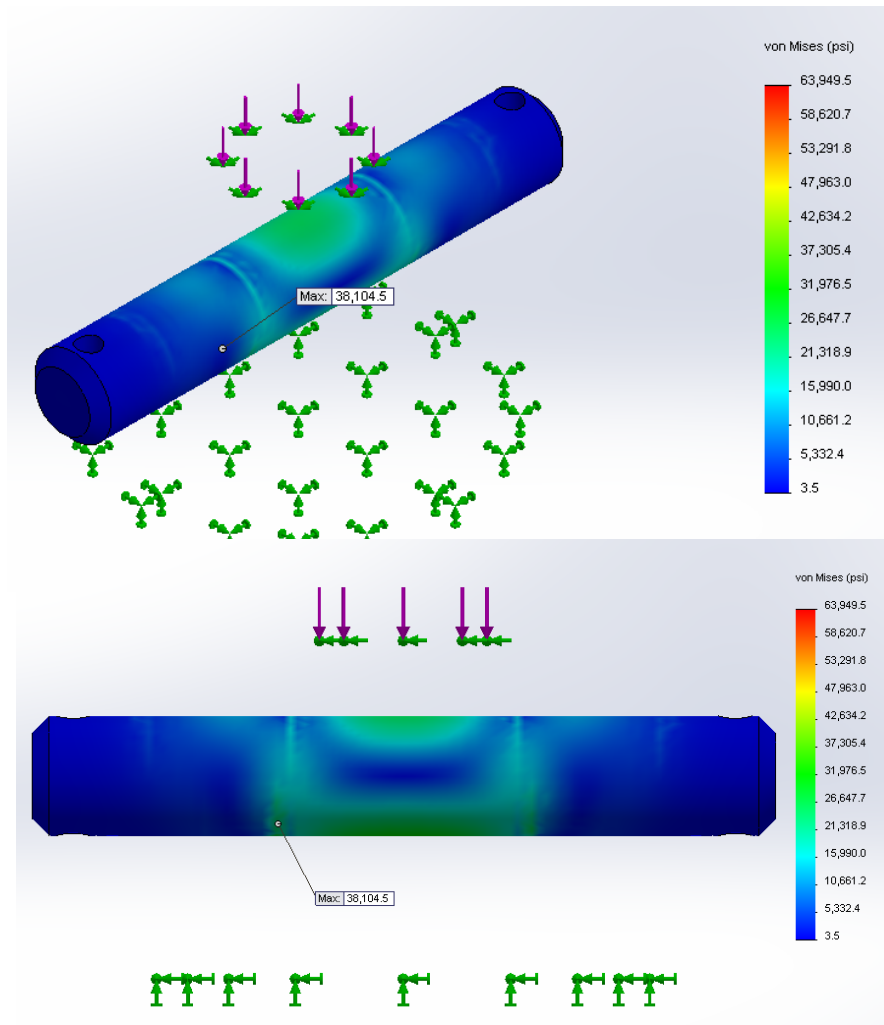**Figure 3.34:   Hydraulic Pin Support Stress and FOS Plots**

Figure 3.35:   Hydraulic Pin Stress Plots

3.3.3.5.   Measurement Frame Structure

The measurement frame structure is the structural support for the sample containment and the measurement system. It is imperative that the frame can support all loading that it will be subjected to. The forces applied in the simulation models are the combined reaction forces calculated from the previous simulations under a "maximum rig loading" condition. The model and the results can be seen in Figure 3.36 and Figure 3.37. It should be noted that the frame must only satisfy the torsional FOS of 1.45 since all axial loading is carried only by the XY-translator.
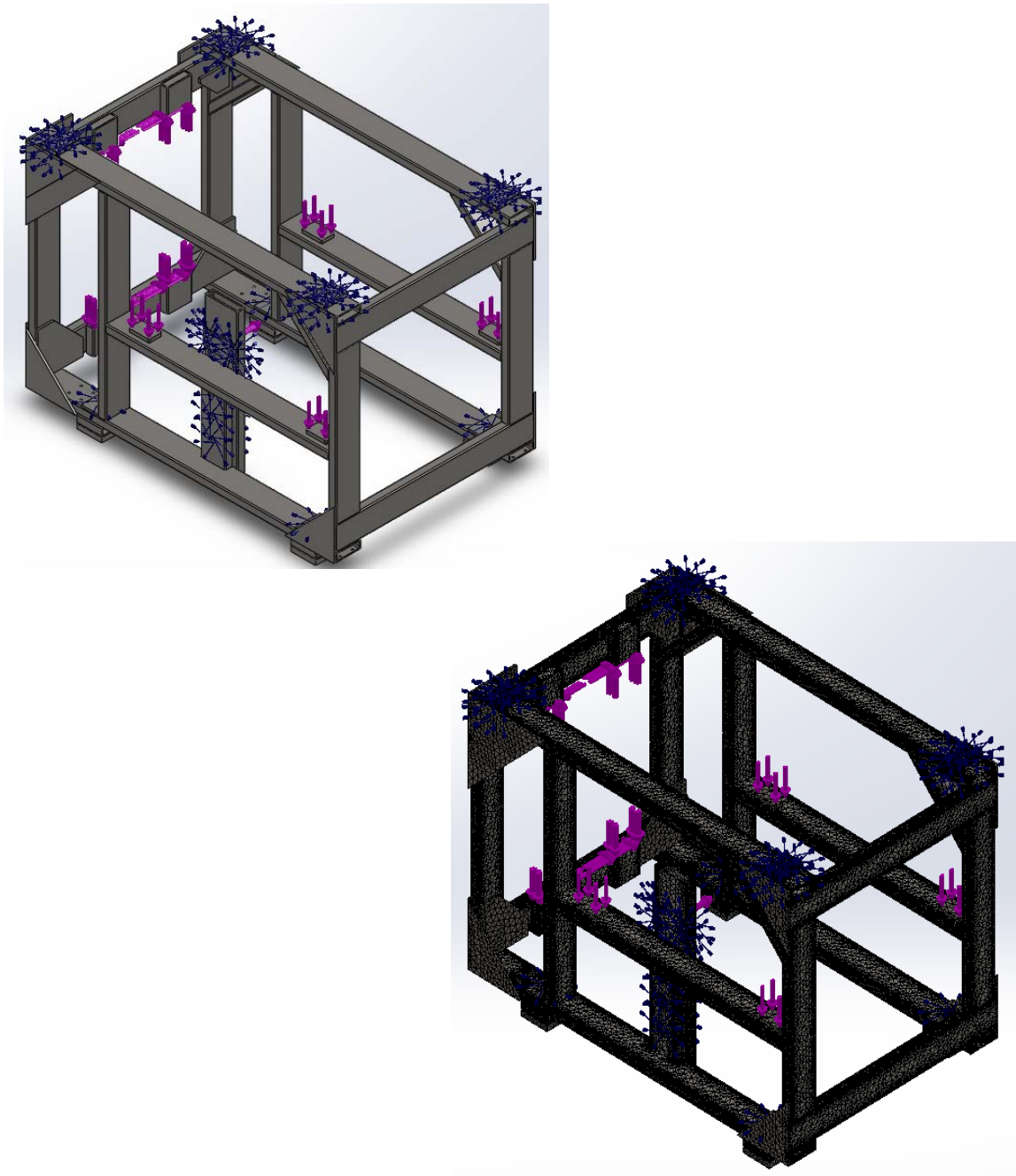
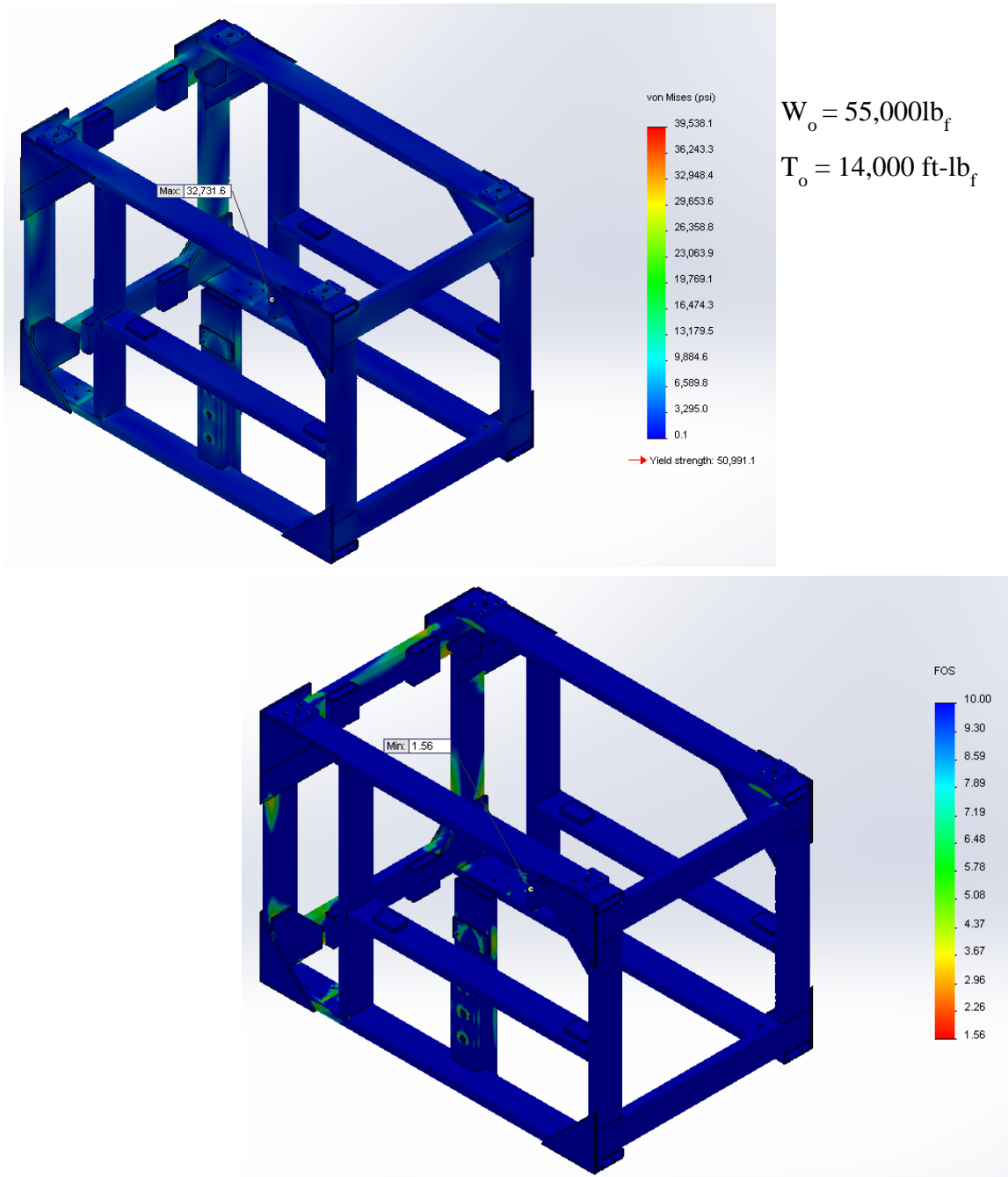**Figure 3.36:   Measurement Frame Structure CAD Model and Mesh Plot**

$W_o = 55,000 lb_f$

$T_o = 14,000 \text{ ft-lb}_f$

Figure 3.37:   Measurement Frame Structure Stress and FOS Plots

3.3.3.6. Side Load Support

The side load support does not have a recommended FOS as the force will be readily controlled. As long as the assembly can adequately manage the determined 4,000 lb$_f$ capacity (See Year 2 Simulations) then it is thought to be safe, since maximum side load occurs under static operation with no bit rotation. The minimum FOS was found to be 1.34 (Figure 3.38) so the side load support is a suitable design.

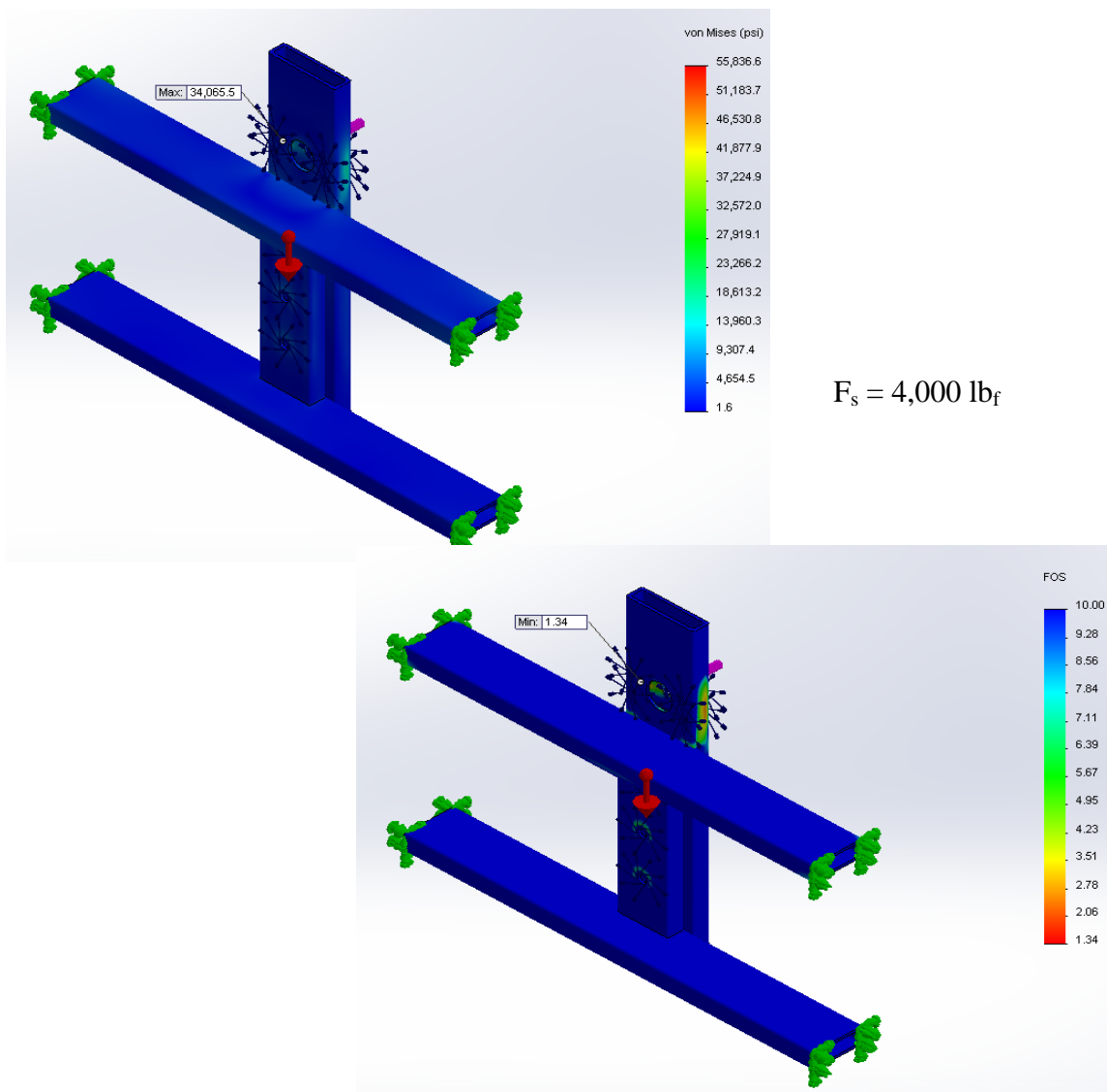$$F_s = 4,000 \text{ lb}_f$$

Figure 3.38:   Side Load Stress and FOS Plot

3.3.3.7. Sliding Structure

The sliding structure allows the sample to be advanced onto the bit while maintaining its direction of motion. The structure is supported by six 3,000 lb$_f$ dynamic capacity wheels. Figure 3.39 depicts the FEA assembly.
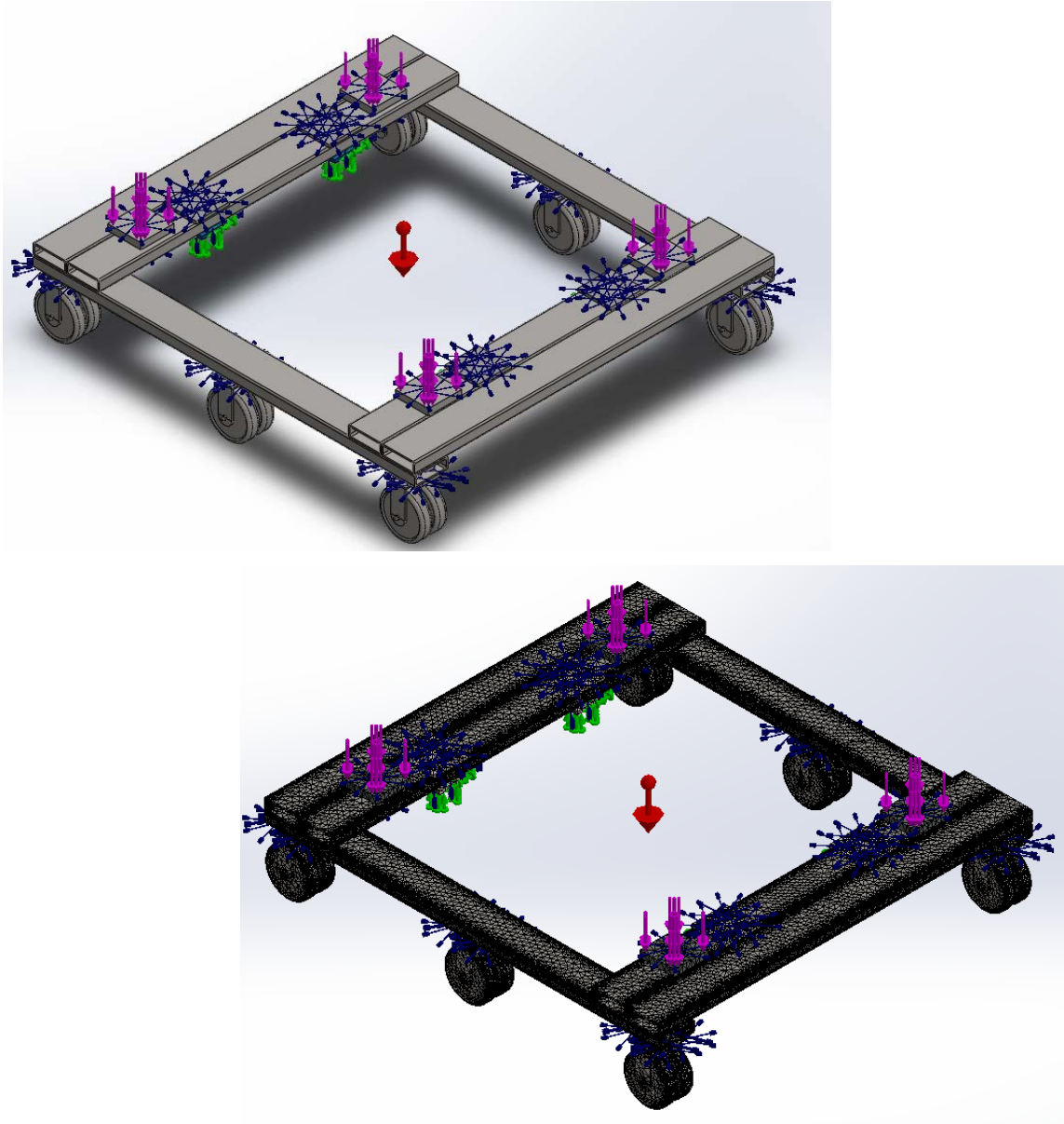

Figure 3.39:   CAD Model and Mesh Plot of Sliding Structure
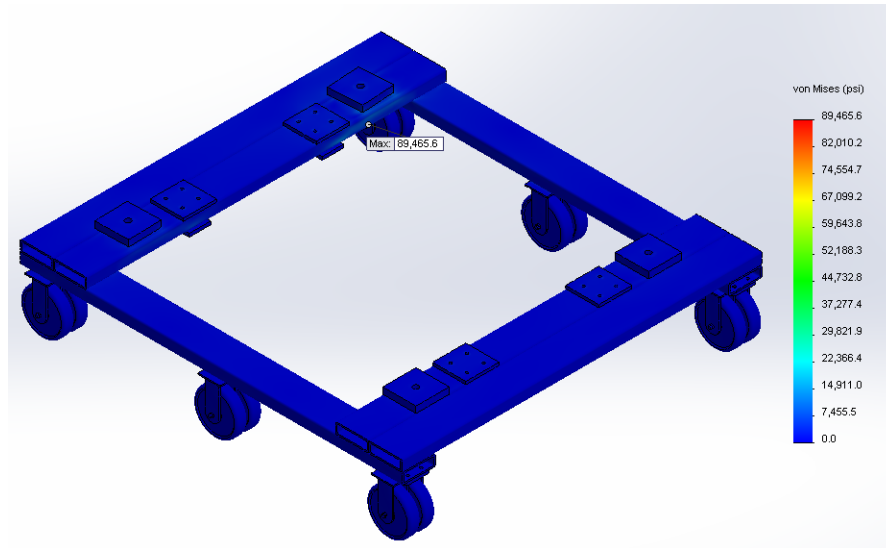
Figure 3.40:   Stress Plot of Sliding Structure

Since the loading on the structure is completely from the torsional loading on the rig, the minimum FOS needs to be 1.45. The stress plot shown in Figure 3.40 suggests that the stresses would exceed the allowable ceiling, but a closer examination reveals that the max stress occurs in the wheels which are not modeled to exact specifications in order to simplify the modeling. By checking the free body forces on the wheels and verifying that the loads do not exceed the capacities of the wheels Figure 3.41 an acceptable design can be determined. Knowing that the wheel capacities have not been exceeded, the remainder of the model can be analyzed. Figure 3.42 depicts the final stress distribution and FOS plot of the sliding structure.
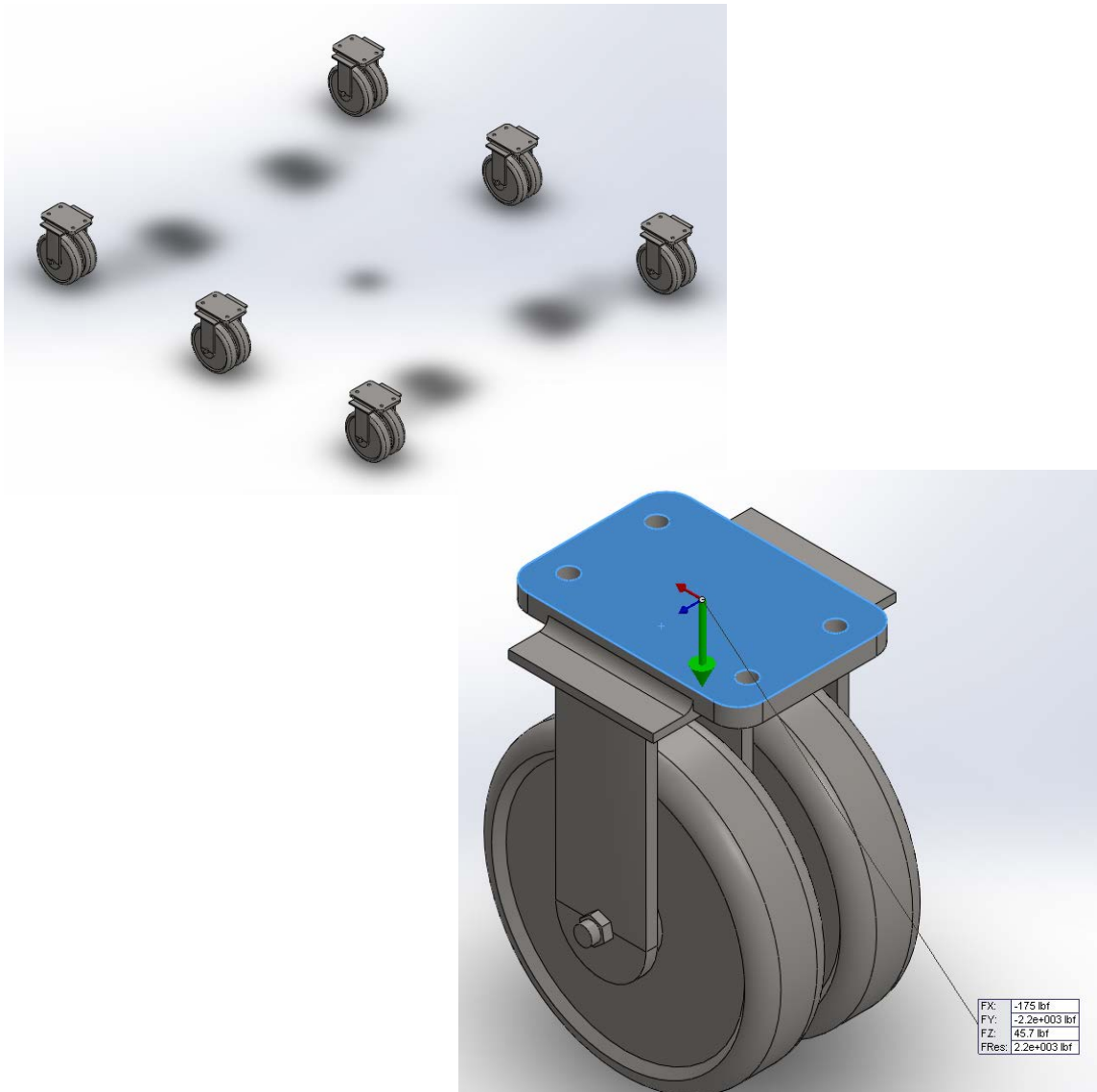
Figure 3.41:   Verification of Wheel Capacities

$$T_o = 14,000 \text{ ft-lb}_f$$
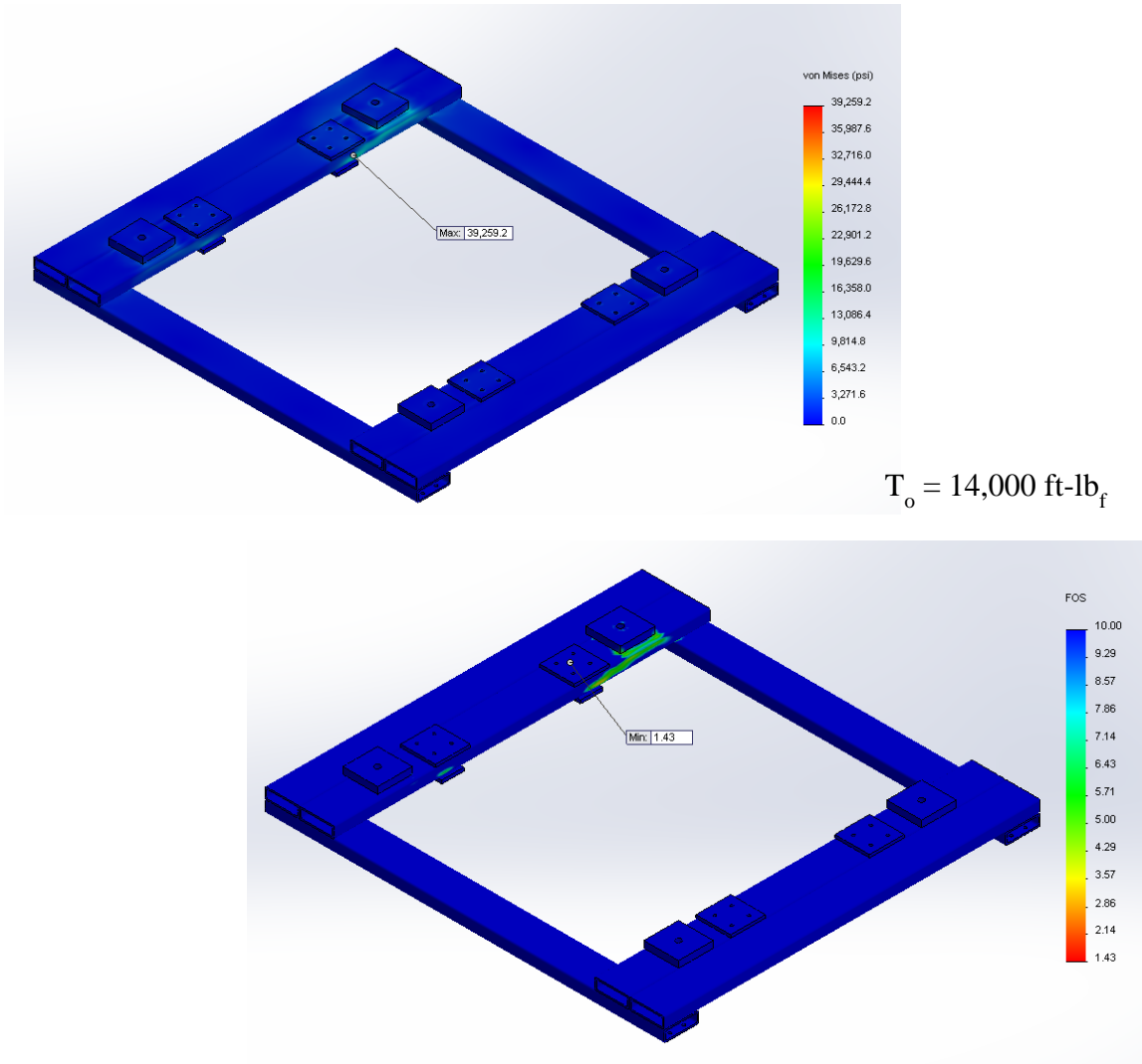
Figure 3.42:   Final Stress and FOS of Sliding Structure

3.3.4. Year 2 Component Simulations
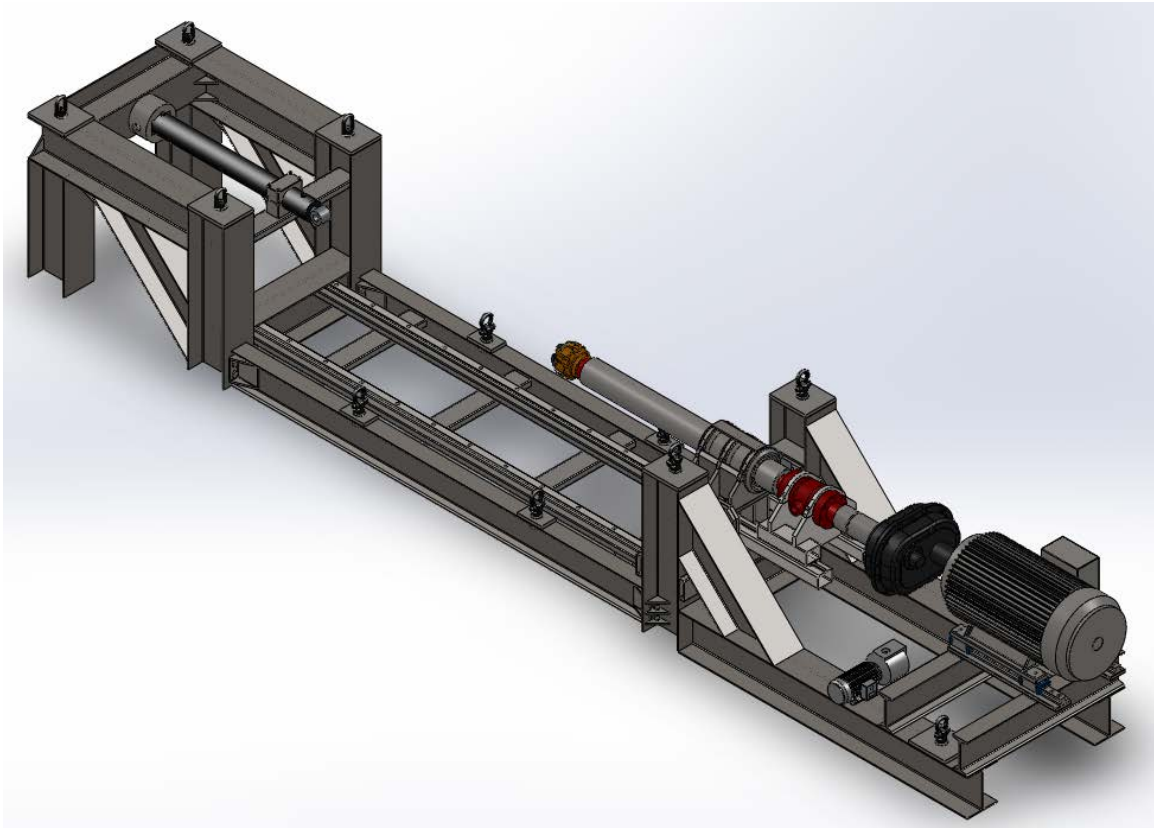
Figure 3.43:   Year 2 Test Rig Frame

Figure 3.43 displays the test rig frame that is to be built in year 2 of the project. The frame is the foundation of the rig and will provide the structural integrity necessary to apply the desired loads to the formation that is to be examined. As mentioned in Section 2, the frame is sectioned into 3 main components: the hydraulic cylinder support (WOB end), the drive system support (TOB end) and the linear guidance support (torsional loading section). Again, due to the size of the assembly, each component was analyzed individually to obtain the best possible results from the simulation software.

3.3.4.1. Rig Frame Piece 1

The first piece of the frame to be analyzed was the WOB end. Figure 3.44 and Figure 3.45 illistrate the solid modeling and simulation results of this part of the rig.
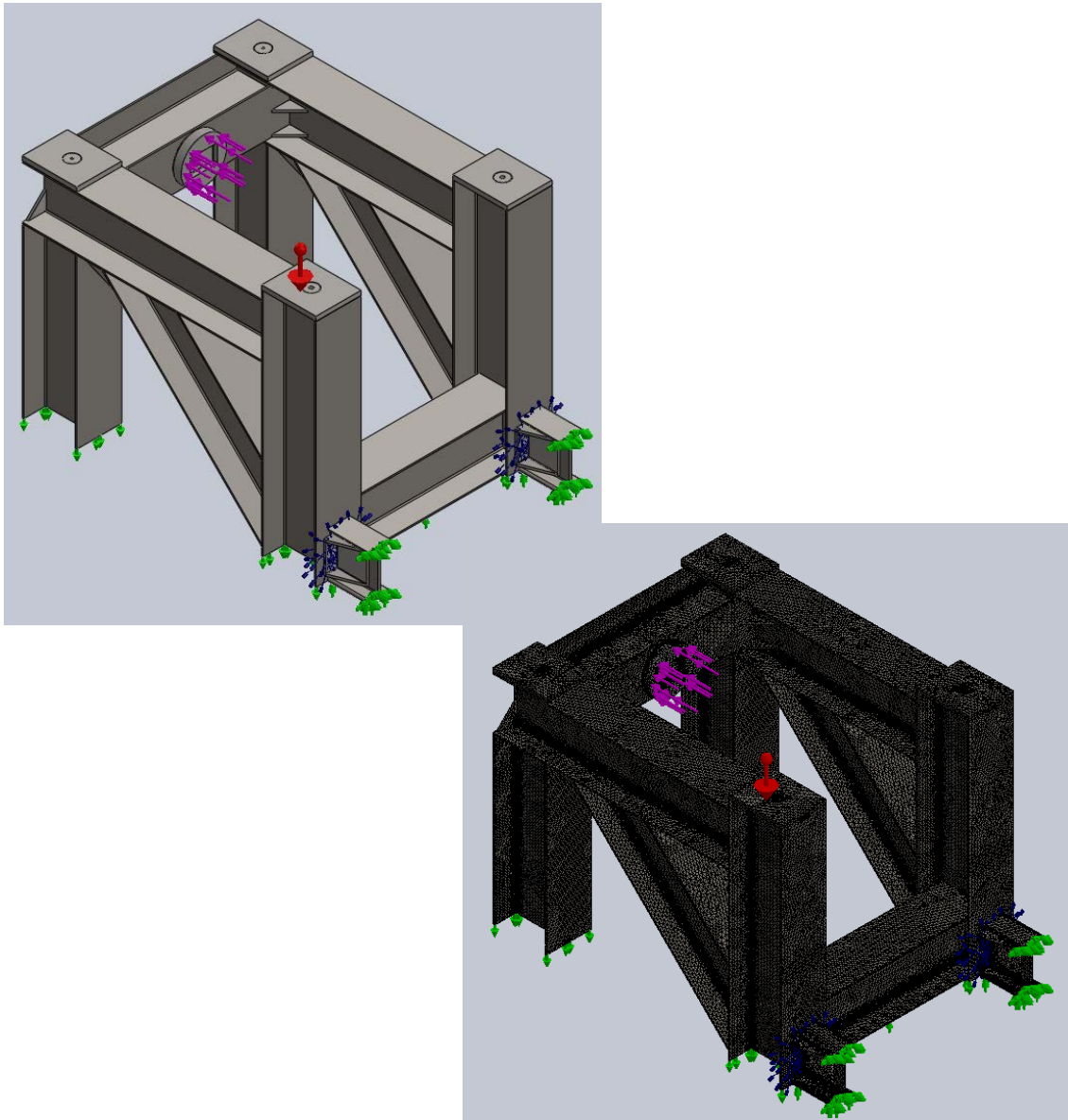
Figure 3.44:   CAD Model and Mesh Plot of the Rig Frame Piece 1

$W_o = 55{,}000 lb_f$
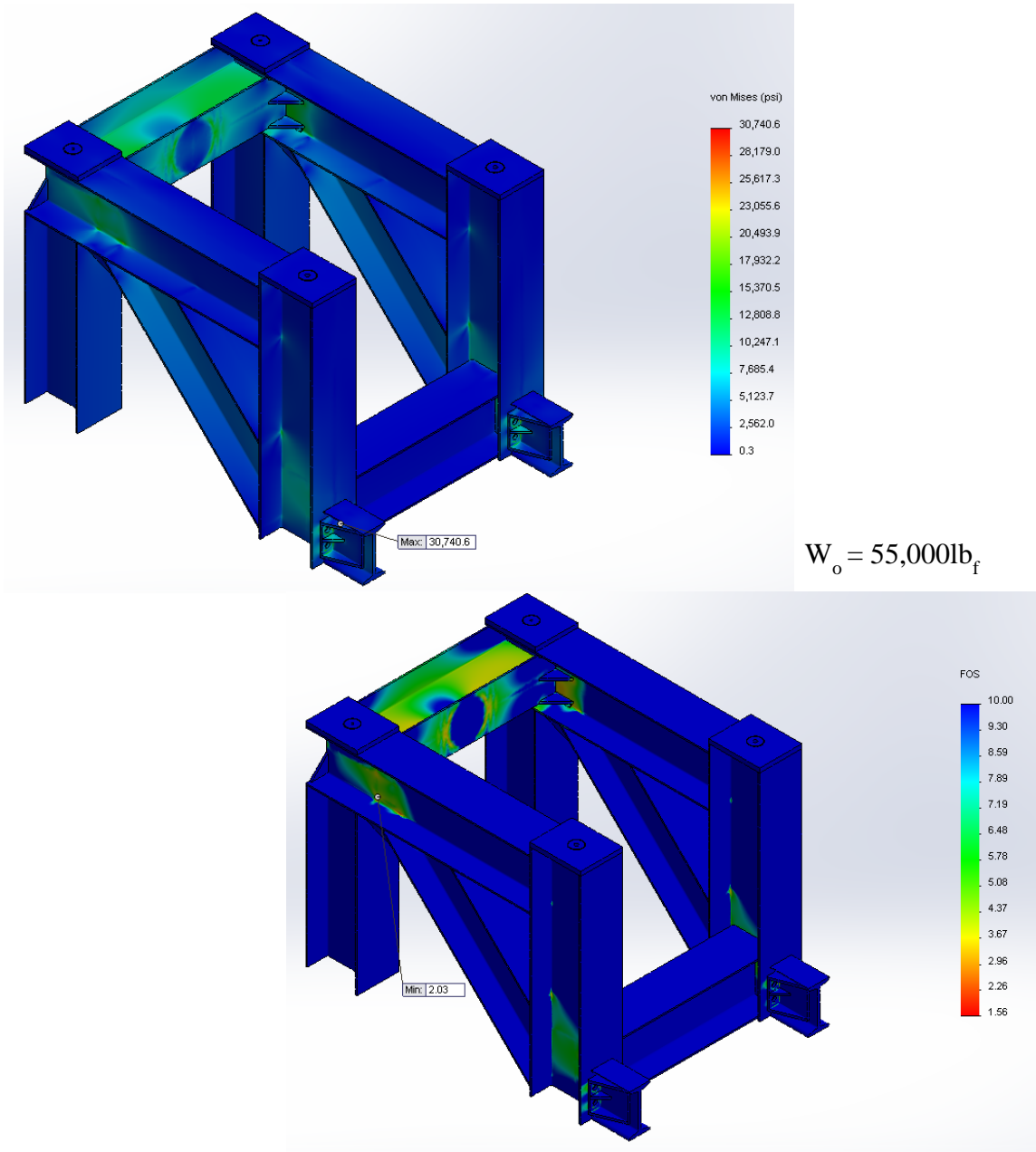
Figure 3.45:   Stress and FOS Plots of the Rig Frame Piece 1

3.3.4.2. Rig Frame Piece 2

Figure 3.46 and Figure 3.47 show the CAD modeling and FEA results for the second piece of the rig frame. It can be seen that the FOS is 1.66; this is acceptable as the primary stresses induced in the model are from torsional loading. The axial members(the long I-beams) can easily withstand the WOB on bit loading of the rig which can be verified from a simple force per area calculation.
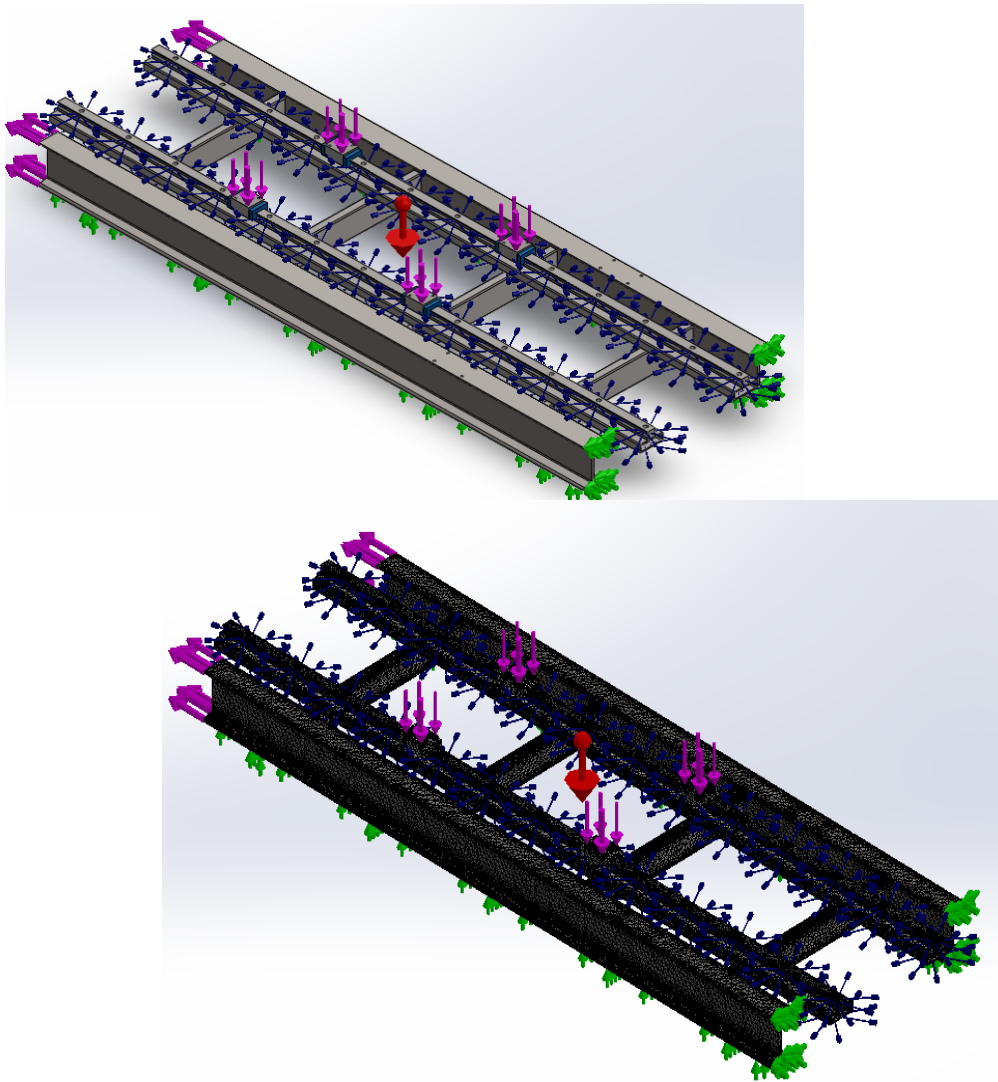
Figure 3.46:   CAD Model and Mesh Plot of Rig Frame Piece 2

$W_o = 55,000 lb_f$

$T_o = 14,000 \text{ ft-lb}_f$
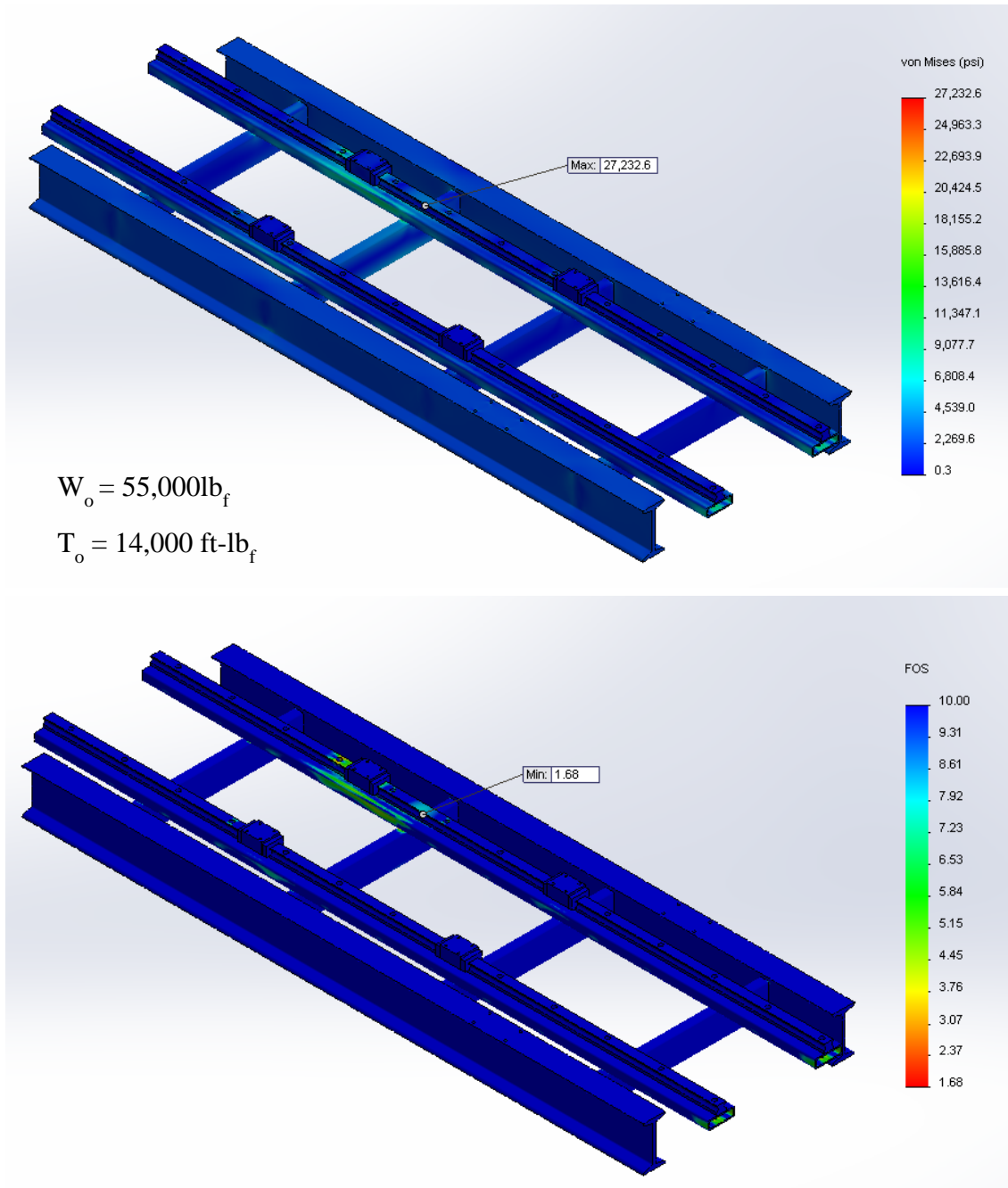
Figure 3.47:   Stress and FOS Plots of Rig Frame Piece 2

3.3.4.3. Rig Frame Piece 3

The third piece of the rig frame is the drive system support. This piece secures the shaft in a stationary position while the formation is advanced onto it. Along with the WOB and TOB loading, there will also be a slide load at the shaft fixture that will need to be supported by the structure. Figure 3.48 and Figure 3.49 display the 3D setup and results of the FEA for the 3rd component of the rig frame.
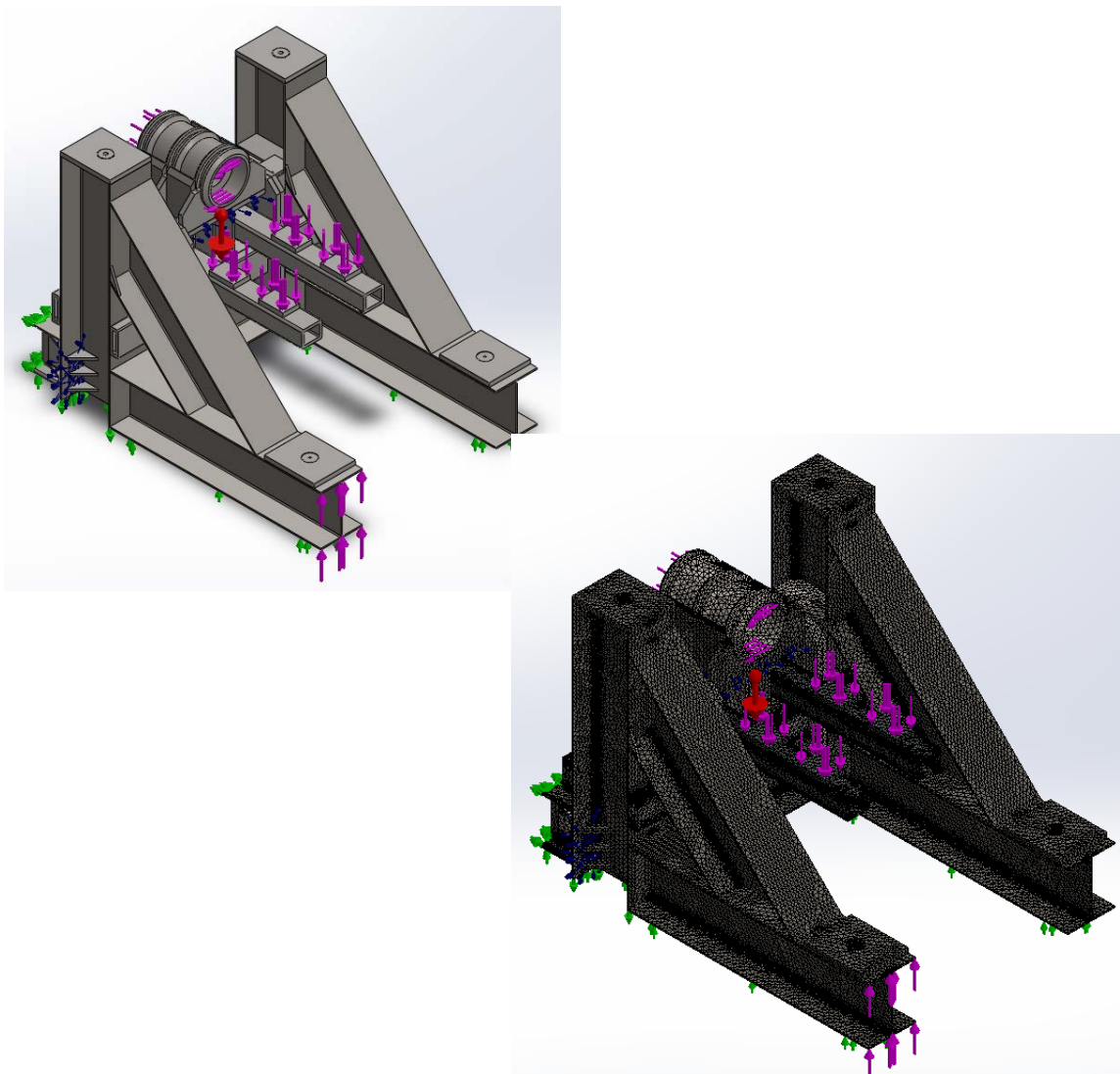
Figure 3.48:   CAD Model and Mesh Plot of Rig Frame Piece 3

$W_o = 55,000 \text{lb}_f$

$T_o = 14,000 \text{ ft-lb}_f$
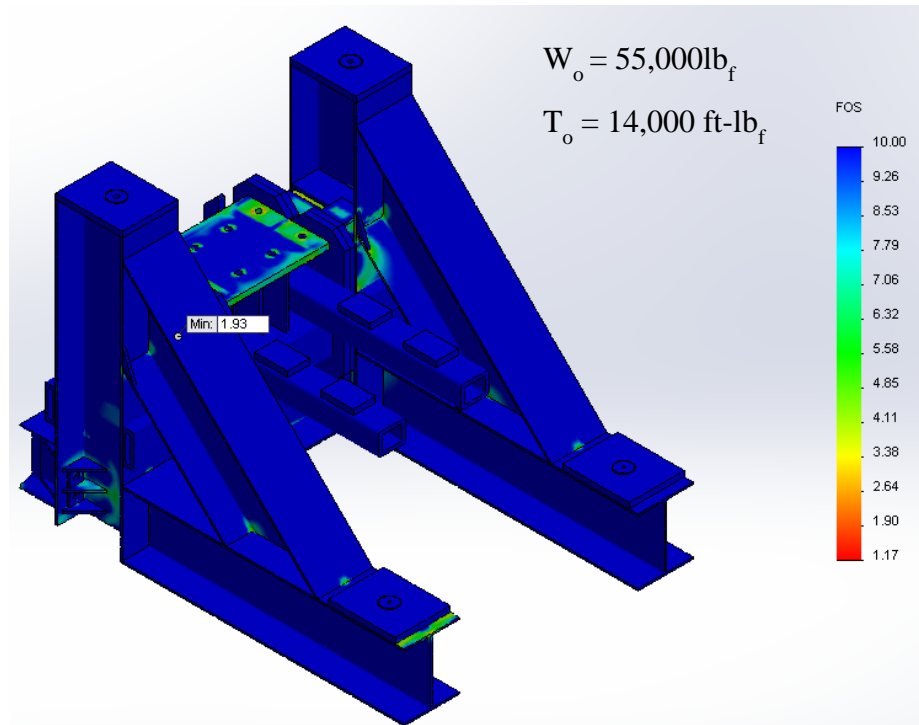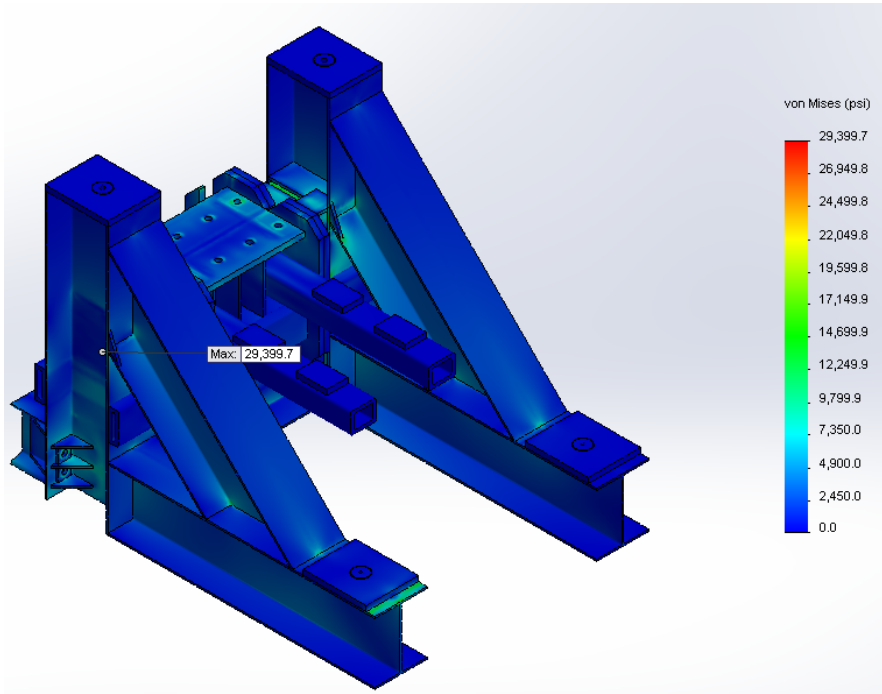
Figure 3.49:   Stress and FOS Plots of the Rig Frame Piece 3

91

3.3.4.4. Hook Loading

When hoisting large machinery, a failure is unacceptable. A failure means severely damaged equipment or injury to a person. For this reason hoisting calculations were purposely over estimated to ensure the safety of everyone, and everything, near the rig. The loading capacities of the hoist rings are calculated and presented in Appendix I. The associated process of FEA for this loading is seen in Figure 3.50.
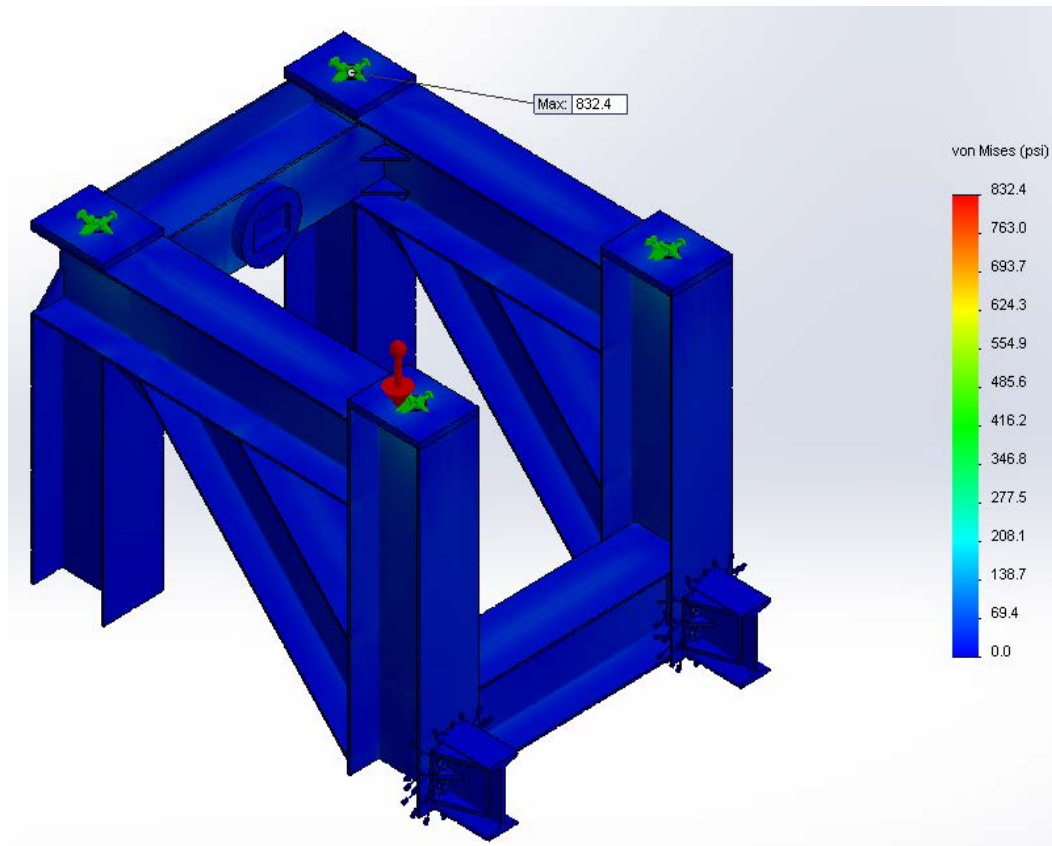
Figure 3.50: Rig Frame Piece 1 Hook Loading

3.3.4.5.   Formation Stiffness Deflection Study

One of the rig's functions is to measure the effective stiffness provided by the wellbore under lateral loading. During this test, the formation will be pushed against the stationary bit while the actuation force and the formation displacement are measured. By plotting the measured displacement against the applied load, an effective stiffness can be determined (See Section 6 for an explanation of measurement). In order to estimate the range of displacements that are to be measured, calculations of the Hertzian contact deflection for a sphere internal to a cylinder and a cylinder internal to a cylinder (Appendix J) are compared against a finite element simulation of the test that is to be done with the rig. Figure 3.51 and Figure 3.52 outline the simulation approach to the problem.

Figure 3.51:   CAD Model of Bit for Side Load Deflection Study
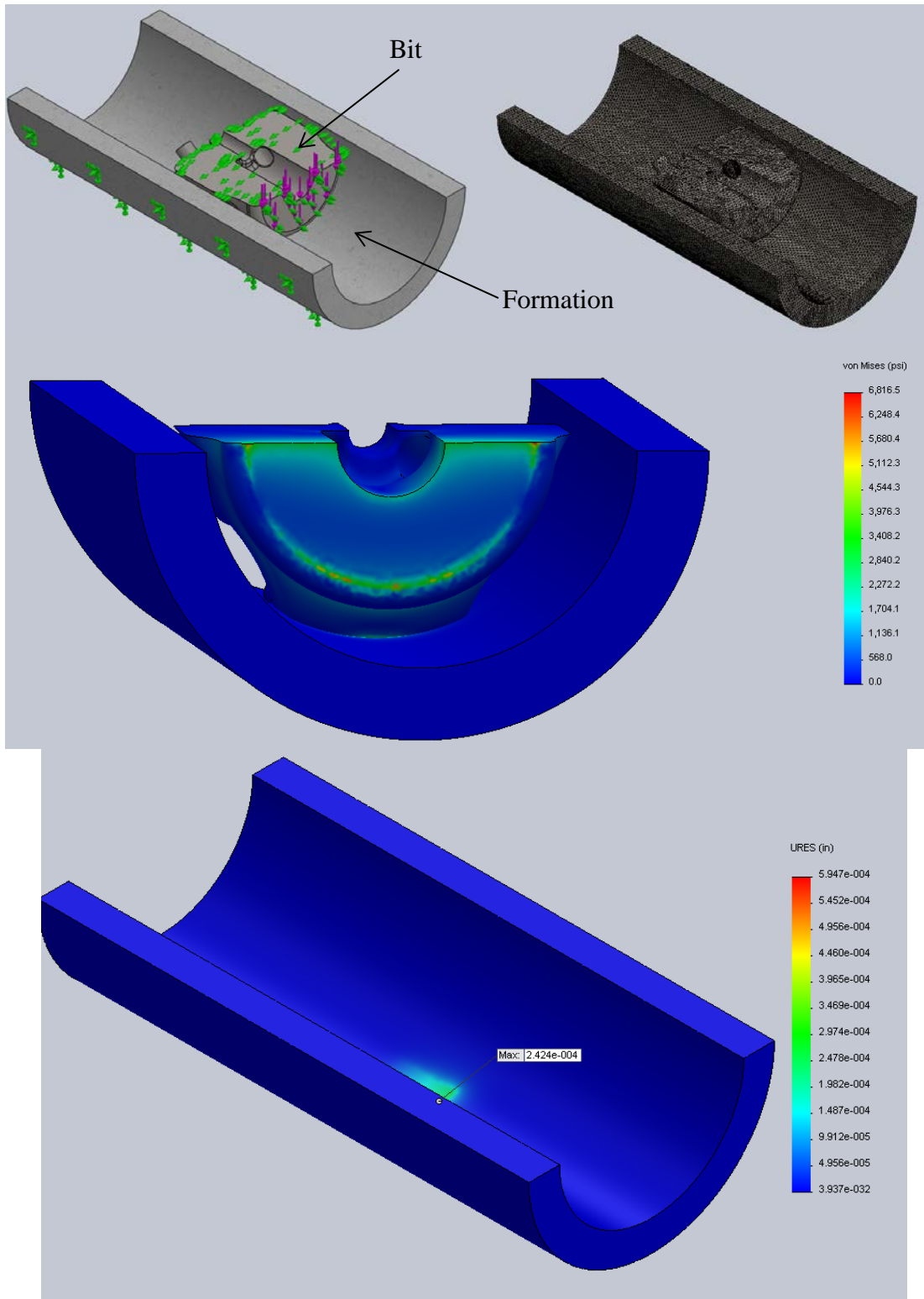
Figure 3.52:   Mesh and Stress Plots for Side Load Deflection Study

Table 3.4 summarizes the results of the deflection study. The data suggests a minimum displacement measurement of 0.0001362 inches and a maximum measurement of 0.0092309 inches.

Table 3.4: Results of Side Load Deflection Study

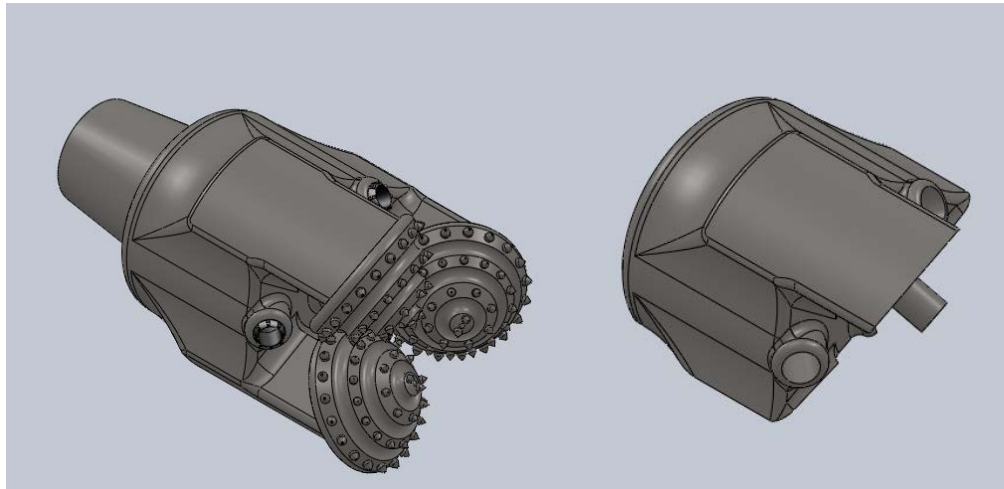|	Analytical (Hertzian Contact)		Simulation (FEA)
Displacements in inches	Sphere in Cylinder	Cylinder in Cylinder	Bit in Cylinder
Quartz	0.0019362	0.0019748	0.0001362
Granite	0.0019878	0.0020446	0.0001402
Dolerite	0.0025190	0.0027915	0.0002023
Limestone (G1)	0.0028519	0.0032886	0.0002424
Shale	0.0063583	0.0092309	0.0006072
Limestone (G2)	0.0033206	0.0040038	0.0002888
Sandstone	0.0030342	0.0035601	0.0002599

3.3.4.6. Shaft Design and Support

The drill shaft is one of the most important components of the rig. It must withstand the entire spectrum of the rig's loading conditions (WOB, TOB and LIL) while maintaining its integrity and functionality. The design and layout of the shaft is a unique configuration in which it is supported by opposing spherical roller thrust bearings. The pre-load for each bearing is provided by 8 Belleville Washer springs. Spherical roller thrust bearings were chosen because they support large axial load as well as some radial loading, and any wobbling of the shaft will not damage the bearings. The bearing literature, provided by Nachi, suggests radial bearing loads to remain below 50% of the applied axial load. The largest anticipated side radial load at the bearing was estimated to be between 3,000 and 4,000 lb_f (determined from FEA). For this reason, the Belleville Washers are needed to apply a minimum preload to the bearings of 8,000 lbf. Each washer is compressed by 0.1110 inches which corresponds to a force output of 1,000 lb_f for each washer in place.
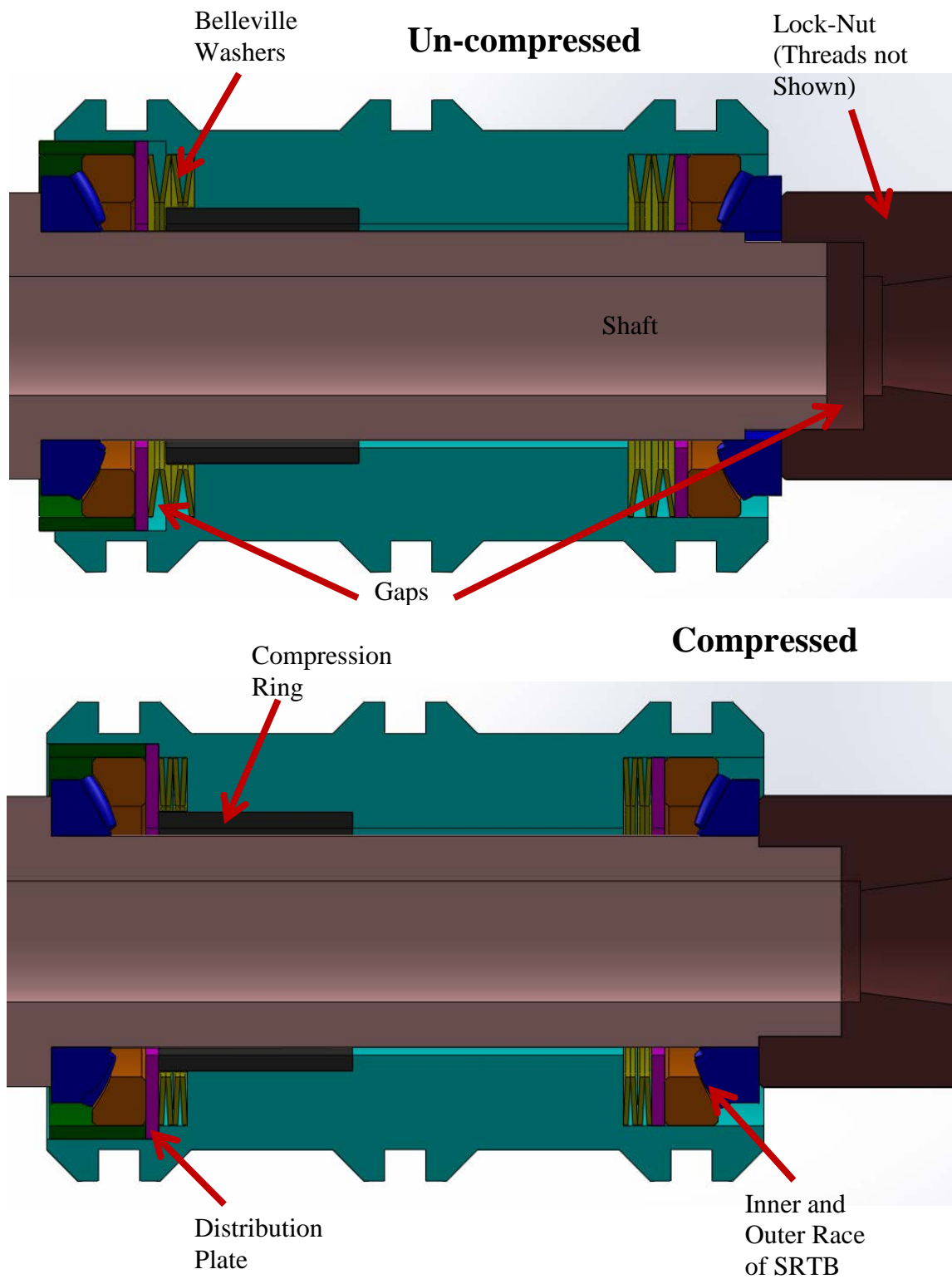
Figure 3.53:   Shaft Support Configuration

Figure 3.53 illustrates the use of the spring washers in conjunction with the shaft support. In the assembly's uncompressed configuration there are two noticeable gaps; one on the left between the compression ring and the distribution plate and the other between the shaft and the lock nut. As the lock nut is screwed onto the shaft, the washers are compressed, thus generating the desired pre-load.

The compression ring prevents further deflection of the washers, beyond their needed limit. There is only need for one compression ring since the axial loading of the shaft is only in one direction. The distribution plates allow for the force generated from the washers to be adequately transferred to the bearings.

3.3.4.6.1. Shaft Analysis

Appendix K provides analytical insight into the shaft's design. A maximum stress was calculated to be nearly 18,000 psi. The FEA (Figure 3.54 through Figure 3.56) suggests a maximum stress that is roughly 3 times that calculated in the appendix. This is due, in part, to the stress concentration factors that were not included in the analytics. The geometry of the shaft includes relatively small fillets at the discontinuities (changes in cross sectional area) which lead to the high stresses that are developed and shown by the simulation results. Calculations also suggest there is no danger of buckling as well.
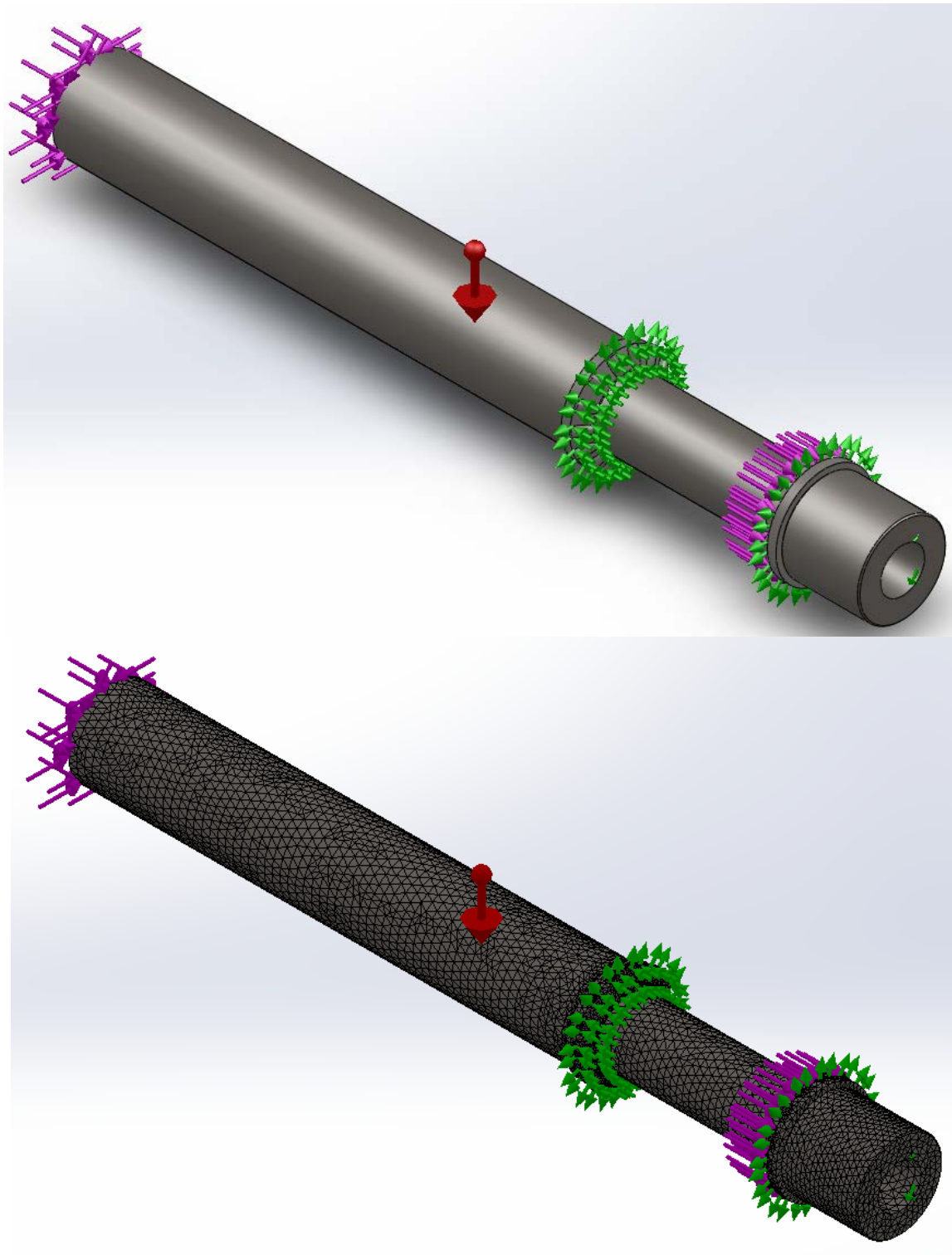
Figure 3.54:   CAD Model and Mesh Plot of Drill Shaft
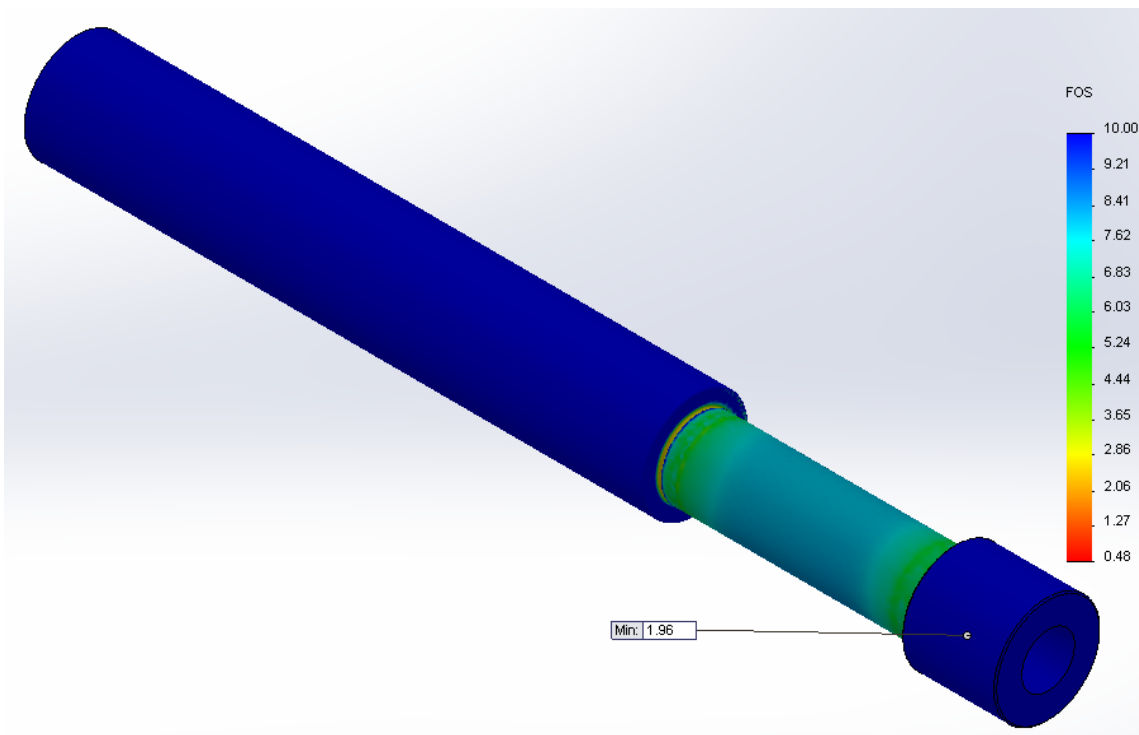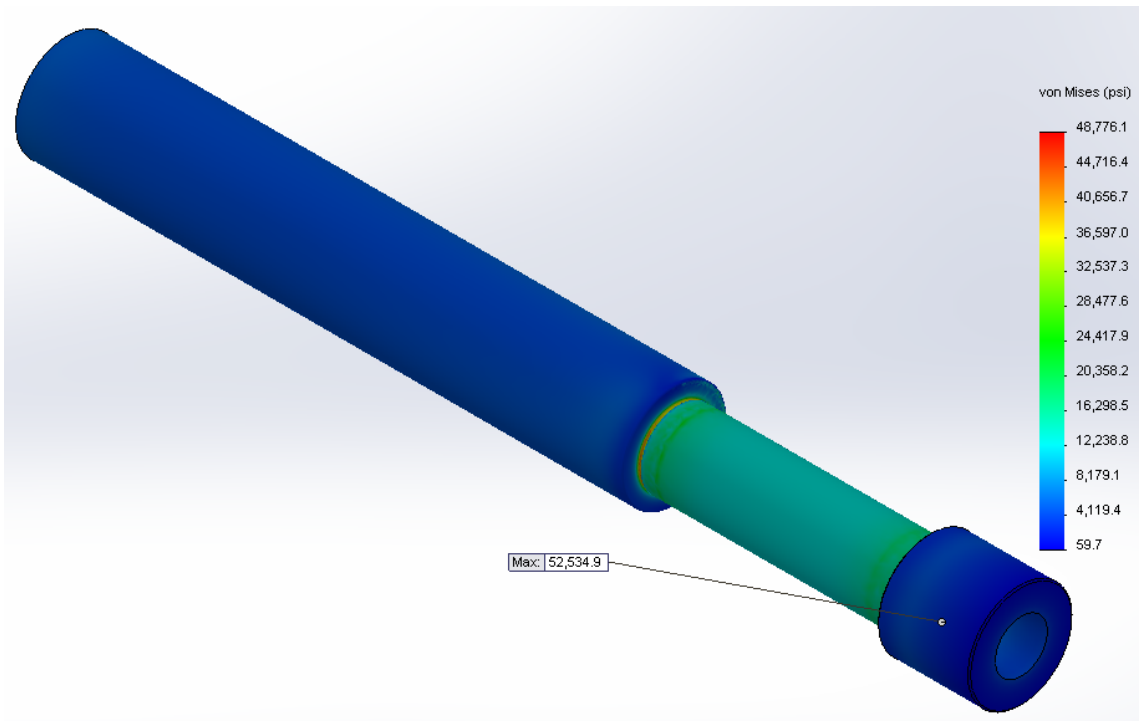
Figure 3.55:   Stress and FOS Plots of Shaft Under Maximum Loading Conditions
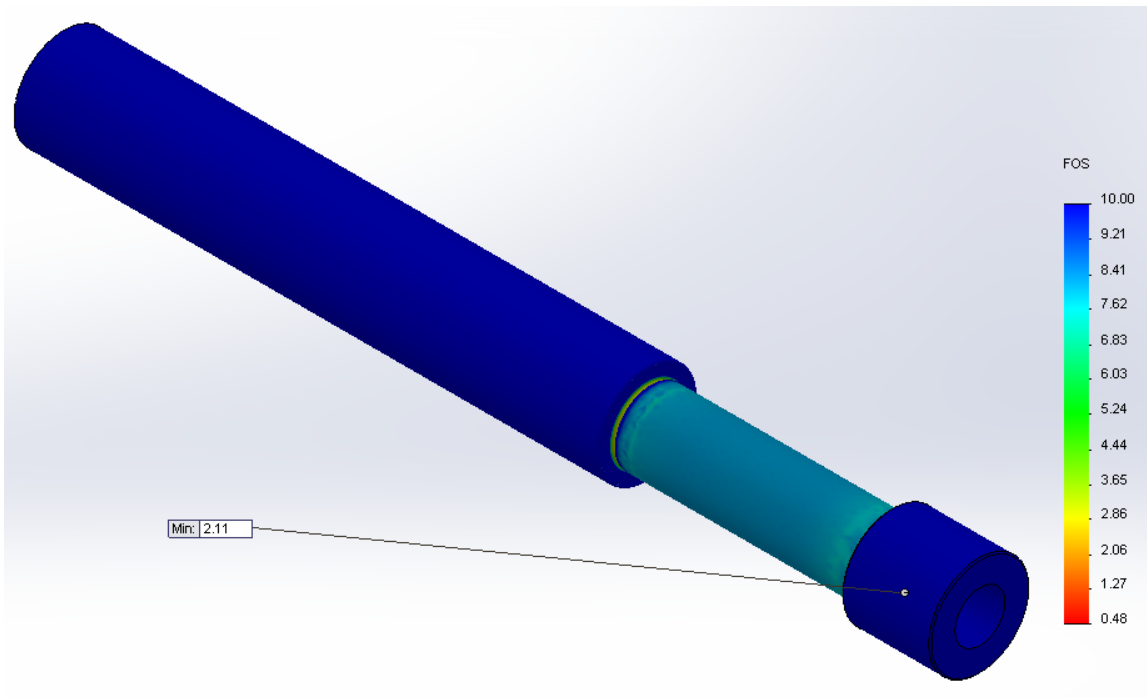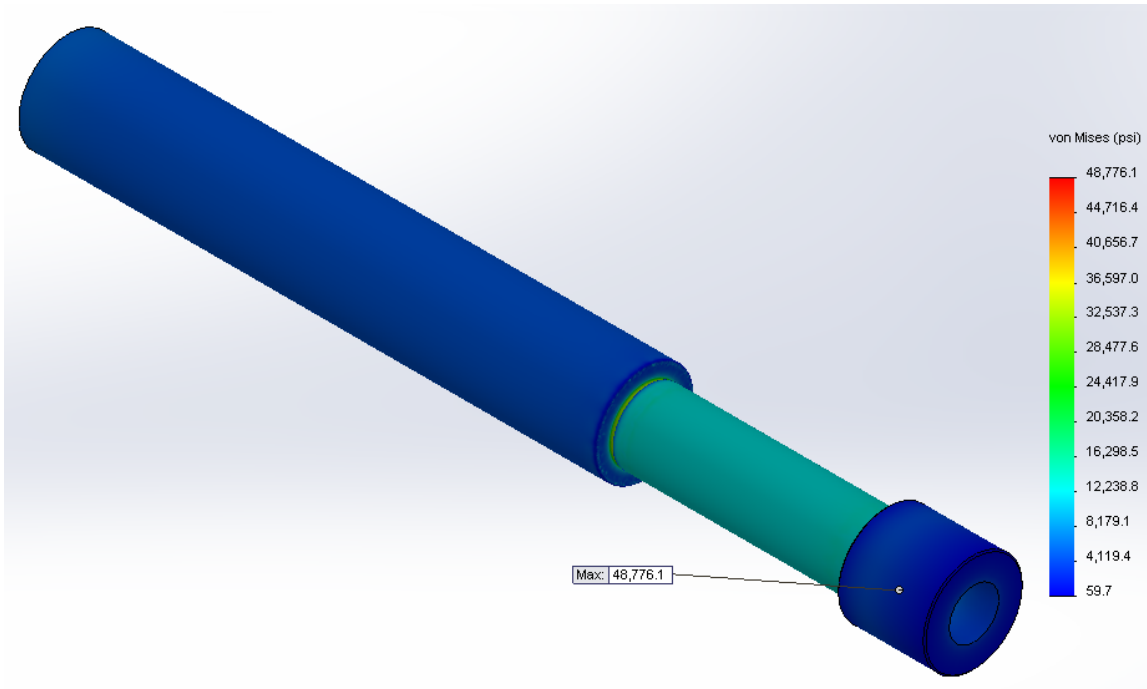
Figure 3.56:   Stress and FOS Plots of Shaft under Maximum WOB and TOB

Vibrations are an area of concern in any rotor dynamics application. In the specific case of the test rig, there is limited vibrational analysis that can be done due to the limitation on the knowledge of spring and damping coefficients. The appropriate course of action was to estimate the coefficients of the simplified shaft model and determine the natural frequency from the available data. If the excitation frequency was found to be relatively small as compared to the natural frequency ($\omega_n = 378$ rad/s), then the shaft was considered stable. Appendix K includes this vibrational investigation.
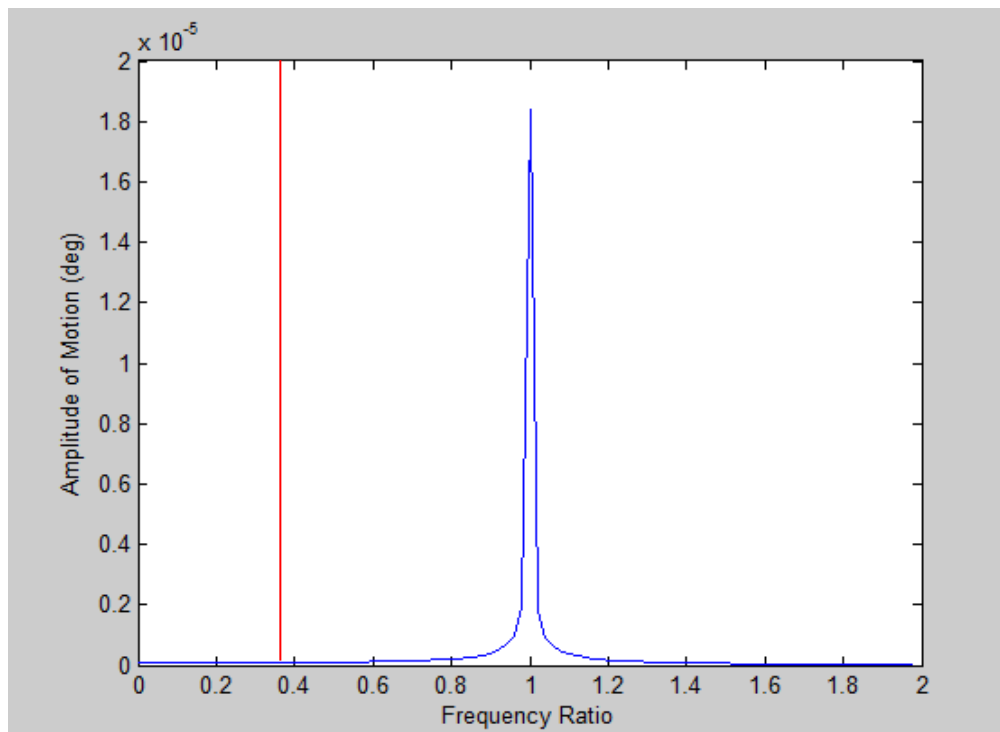
Figure 3.57: Amplitude of Oscillation vs. Frequency Ratio (ω/ω_n)

Figure 3.57 displays the response amplitude as a function of frequency ratio. The red line indicates the maximum anticipated operational frequency ($\omega_{max} = 147$ rad/s) as mentioned in the appendix. From this information it is clearly discernible that the rig's

operation will not reach a critical state. The appendix also addresses the lock nut capacity and buckling considerations of the shaft.

3.3.4.6.2. Shaft Support FEA

The shaft support transfers the WOB loading from the drill shaft to the rig frame. While maintaining its integrity for axial forces, it must also withstand any and all transverse loading that the shaft would be subjected to. From the shaft analysis, it has been determined that a maximum side loading on the support housing could be up to 6,000 lb_f. This force was included with the maximum axial force in the modeling shown in Figure 3.58 and Figure 3.59.

Figure 3.58:   CAD Model and Mesh Plot for Shaft Support
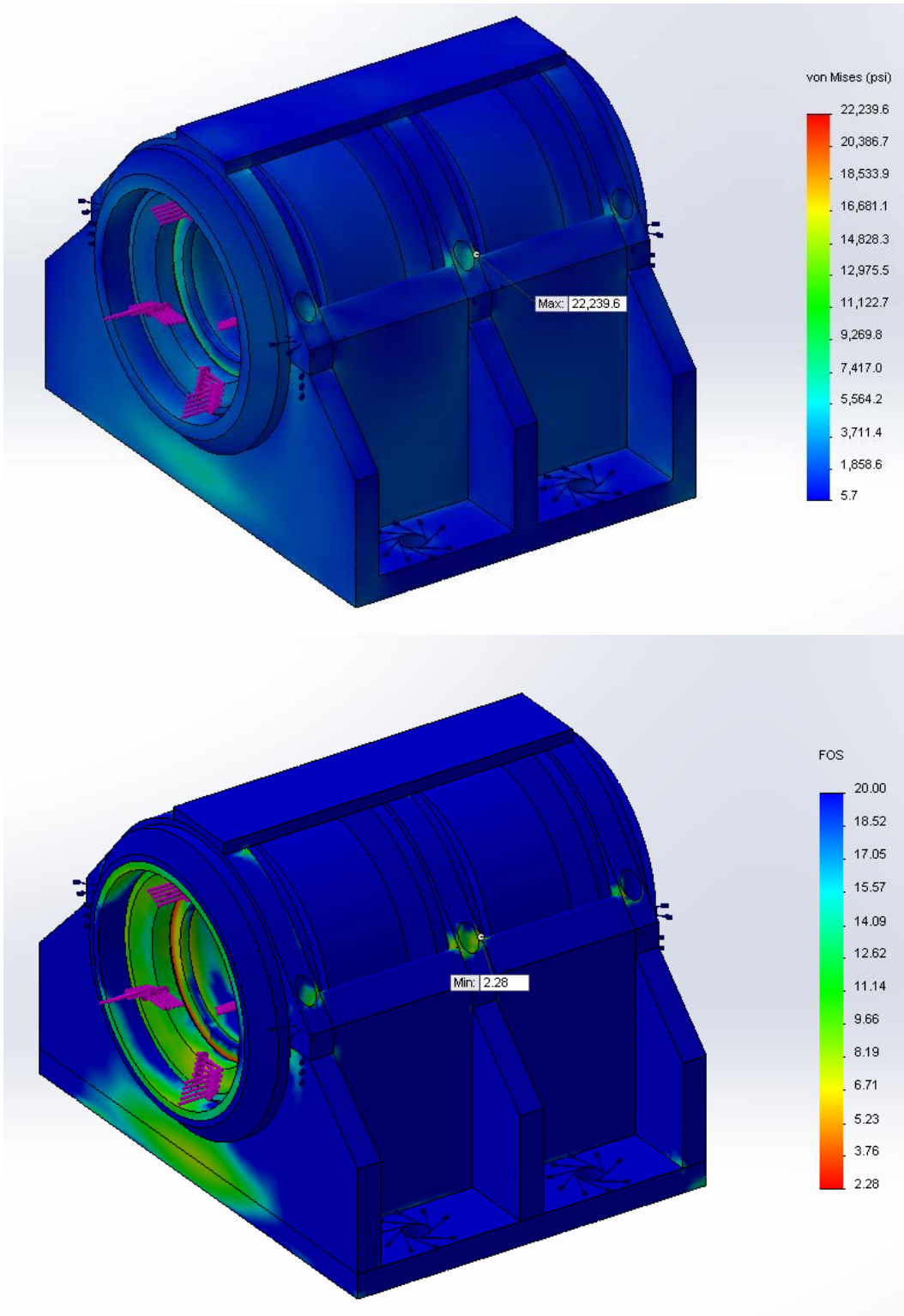
Figure 3.59:   Stress and FOS Plots for Shaft Support

4. FRICTION TESTING (FEASIBILITY OF MEASUREMENT SYSTEM)

The unique test rig design utilizes an XY-translator table mounted to the bottom of the inner sample container (Figure 4.1). By doing this, any transverse loading on the axial-torsional load cell will theoretically be removed, therefore creating a more accurate testing environment.
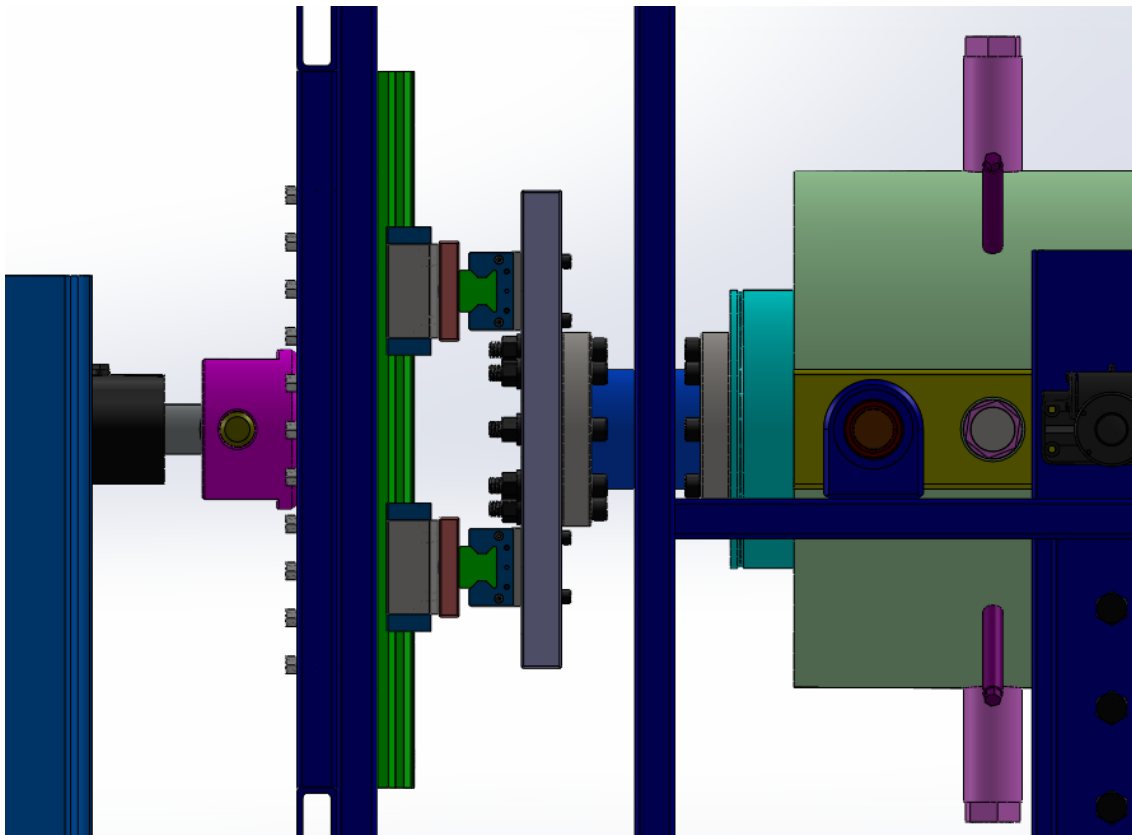
Figure 4.1:   XY-Translator Table on Sample Containment Structure

Of course, as in most cases, theory and practice can greatly differ and in this scenario any source of error would be due to friction within the roller carriages. With the addition

of error, it becomes necessary to determine the magnitude of this uncertainty in order to gauge the accuracy of the measurement system.

4.1. Setup

While planning the experiment, much thought was put into determining how to accurately measure the maximum friction force that would be encountered. An assembly was developed that allowed for the measurement of the frictional force developed by 2 roller carriages simultaneously. Not only does the presented method provide a means of measuring the frictional force under a variable load, but it also accommodates averaging between carriages so as to not narrow the results to a specific roller. As can be seen in Figure 4.2, an assembly of four roller carriages is sandwiched together with a pull plate in-between. This allows for symmetric loading and a the means to measure the frictional force creating by two roller carriages concurrently. Ideally, the force measured by pulling the plate (thus causing two of the roller carriages to move together) will be the force required to move one roller carriage under a specified load, multiplied by two.
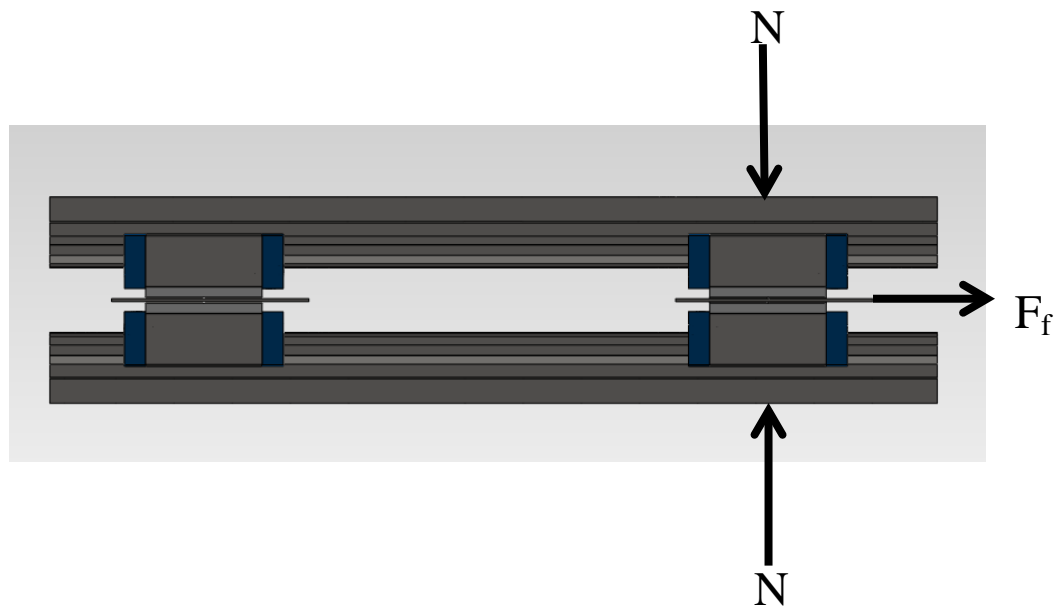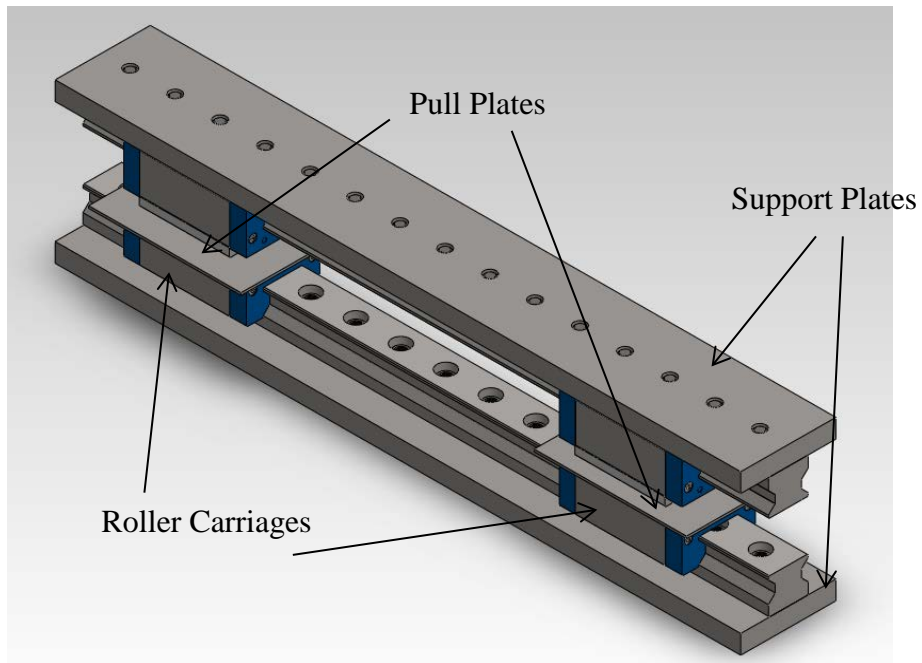
Figure 4.2: CAD Model of Roller Carriage Testing Assembly
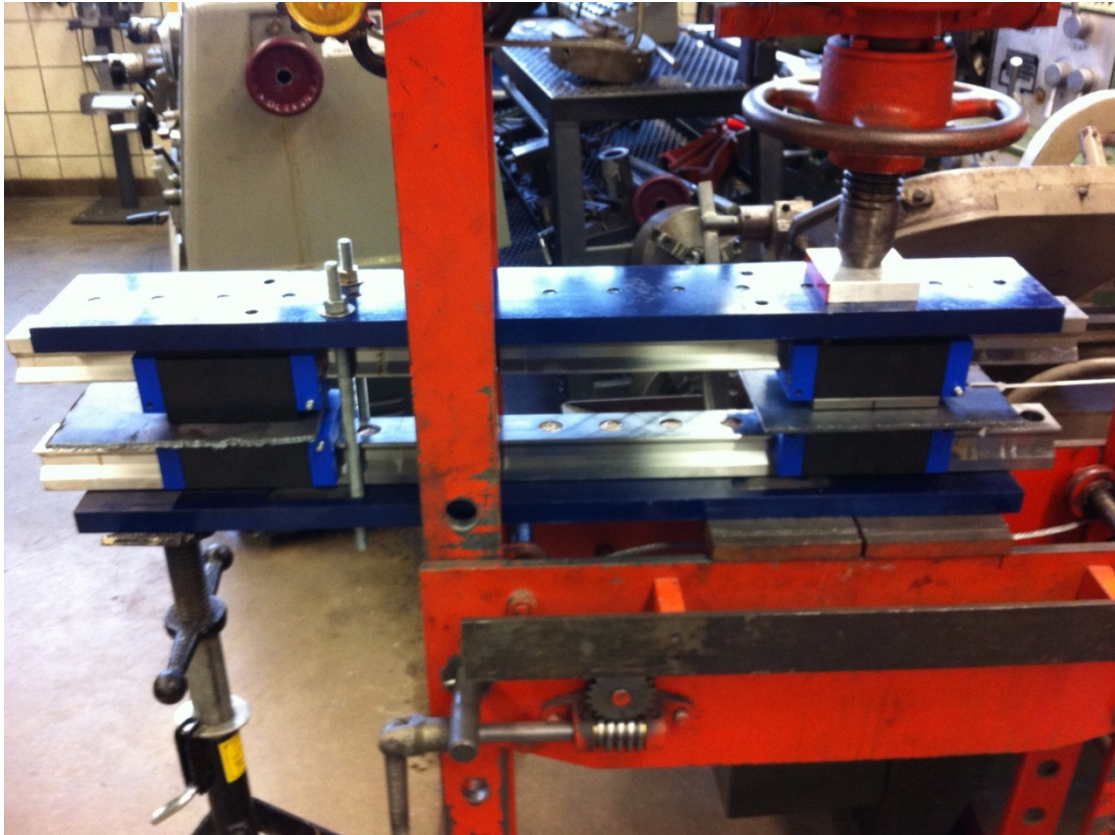
Figure 4.3:   **Experimental Setup for Friction Testing**

The actual experimental setup (Figure 4.3) was done using a 35 metric ton machine press in Texas A&M's Mechanical Engineering Machine Shop. The aligning bolts (Figure 4.4) are put in place to keep the two plates from moving independently from one another, thus isolating the motion to the roller carriages. The pull plate (Figure 4.5) is the mechanism in which the frictional force is applied. The carriages are Thomson 512P55C3 Linear Guides and each roller carriage was lubricated with BioBlend HD#2 grease.
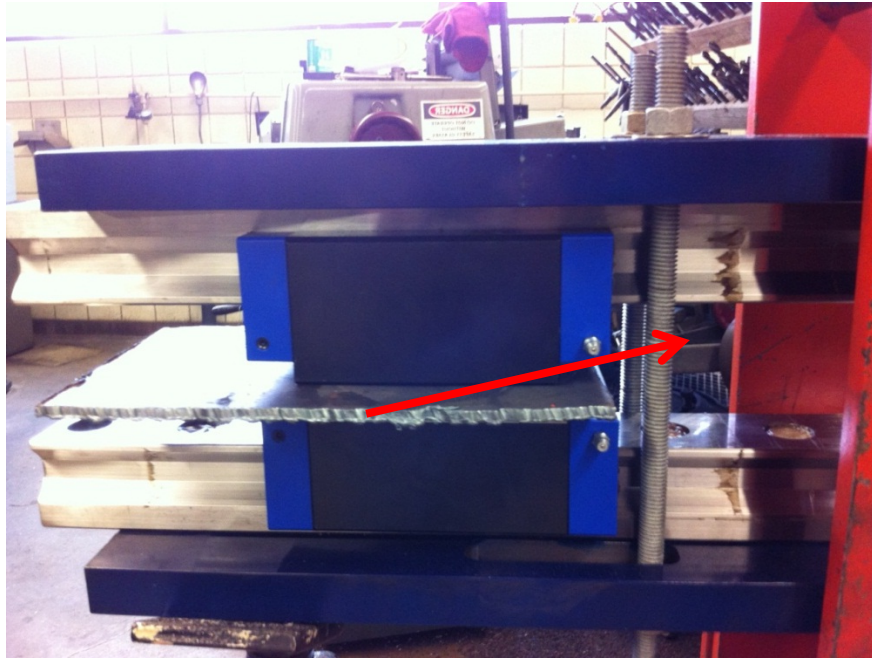
Figure 4.4:   Aligning Bolts
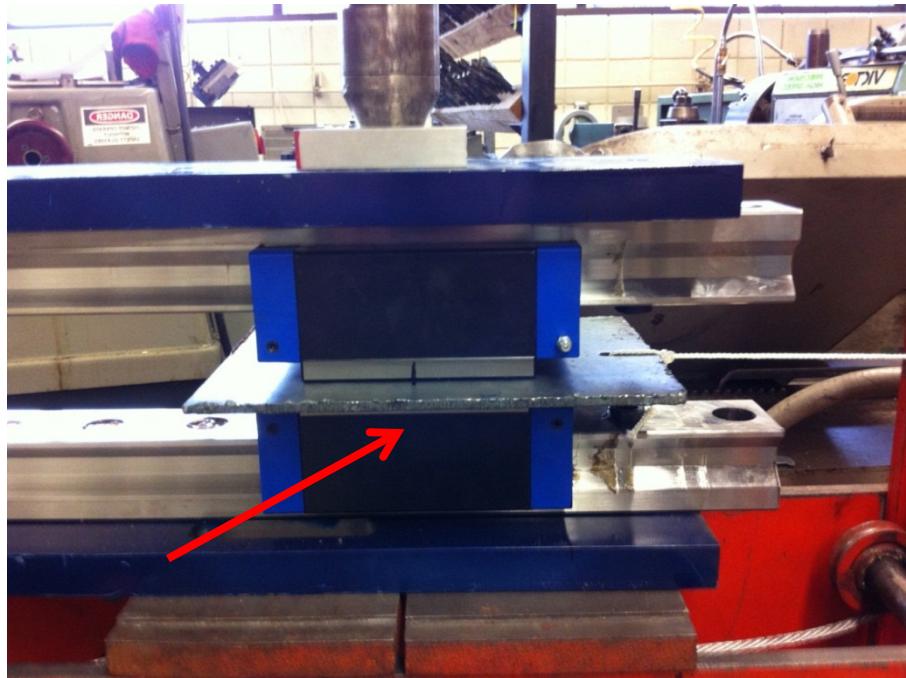
Figure 4.5:   Pull Plate

Figure 4.6:   Axial Load Cell (Interface)

Figure 4.6 shows the Interface load cell used for testing. The transducer is an axial tension/compression load cell with a 200 lb_f capacity. There was no need to obtain a larger capacity as it is assumed that if the force required to pull two roller carriages approached 200 lb_f, then the feasibility of the XY translator would be discredited and the design would then have to be drastically altered.

4.2. Procedure

The testing procedure was as follows:

1. Apply 10VDC excitation to load cell
2. Attach load cell to Pull Plate in a manner such that the force can be measured by pulling the plate.
3. Apply normal load (start with 1 metric ton)

4. Measure force required to instigate roller carriage movement

5. Disengage normal load

6. Re-align roller carriages to initial position

7. Repeat steps 3-4, 5 times for each normal load

8. Repeat steps 3-5, for up to 9 metric tons (19,841.6 lb$_f$)

Since the maximum normal rig loading will be 55,000 lb$_f$ it is only necessary to load each roller carriage by 13,750 lb$_f$. During experimentation, the roller carriages were loaded beyond their anticipated maximum operating load, but below their maximum rated load (29,652 lb$_f$).

4.3. Results

Table 4.1, **Figure 4.7** and **Figure 4.8** summarize the test data.

Table 4.1: Friction Test Data

V_{exc} (V)	σ_V	σ_{VM} (mV)	σ_{LC} (%)	σ_N	σ_R					
10	0.05	0.005	0.013	220.462	0.0000195					
	Metric Tons									
Run #	0	1	2	3	4	5	6	7	8	9
1	2.7088	2.528	2.6546	2.8049	3.1088	3.2899	3.619	3.7983	4.0134	4.0685
2	2.5388	2.5876	2.6055	2.7629	3.0098	3.4809	3.3923	3.7309	4.1059	3.8365
3	2.4988	2.5501	2.5394	2.7692	3.0098	3.1158	3.5622	4.0488	4.1788	4.2689
4	2.5688	2.4676	2.4715	2.7521	3.0622	3.2108	3.5134	3.7176	4.0095	4.1793
5	2.5404	2.4172	2.6453	2.8468	2.8588	3.3589	3.5348	3.472	3.9488	4.1529
AVG (mV)	2.57112	2.5101	2.58326	2.78718	3.00988	3.29126	3.52434	3.75352	4.05128	4.10122
Err$_{AvgmV}$	0.039546903	0.039191492	0.03961728	0.04080129	0.0420984	0.043737	0.045089	0.046431	0.048152	0.048448
N load (lb$_f$)	0	2204.62	4409.24	6613.86	8818.48	11023.1	13227.72	15432.34	17636.96	19841.58
F$_{pull}$ (lb$_f$)	20.75257882	20.26006102	20.8505658	22.4964889	24.293993	26.56513	28.44641	30.29622	32.69957	33.10265
F$_f$ (lb$_f$)	10.37628941	10.13003051	10.4252829	11.2482445	12.146997	13.28256	14.22321	15.14811	16.34978	16.55133
σ_{Ff}	0.159624857	0.158190054	0.15990897	0.16468888	0.1699253	0.176542	0.181997	0.187418	0.194366	0.195559
Force Err (%)	1.538361652	1.561595039	1.53385736	1.46412965	1.3989076	1.329128	1.279579	1.237236	1.188799	1.181533

The propagation of uncertainty (Tabulated in Table 4.1) was calculated with the formulation presented by H.H. Ku [129]. This method is outlined by the following equation

$$\sigma_f^2 = \left(\frac{df}{dx}\right)^2 \sigma_x^2 + \left(\frac{df}{dy}\right)^2 \sigma_y^2 + \left(\frac{df}{dz}\right)^2 \sigma_z^2 + \cdots$$

Where the uncertainty of interest, σ_f, is a combination of partial derivatives and correlating uncertainties. Applying this equation to the present study, the propagation of uncertainty through the experiment can be characterized as

$$\sigma_{VO_i} = \sigma_{VM} + \sigma_{LC}(VO_i) + \sigma_V \qquad \text{Eq. 42}$$
$$VO_{avg} = \frac{VO_1 + VO_2 + VO_3 + VO_4 + VO_5}{5} \qquad \text{Eq. 43}$$
$$\sigma_{Avg}^2 = \frac{1}{25}\left(\sigma_1^2 + \sigma_2^2 + \sigma_3^2 + \sigma_4^2 + \sigma_5^2\right) \qquad \text{Eq. 44}$$
$$F = \frac{A}{2R} \qquad \text{Eq. 45}$$
$$\sigma_F^2 = \left(\frac{1}{2R}\right)^2 \sigma_A^2 + \left(\frac{VO_{avg}}{2R^2}\right)^2 \sigma_R^2 \qquad \text{Eq. 46}$$

where,

σ_v = Uncertainty of the Supply Voltage

σ_{vm} = Uncertainty of the Voltmeter Reading

σ_{LC} = Uncertainty of the Load Cell as a percentage of output voltage

σ_R = Uncertainty of the Voltage to Force Load Cell Ratio

σ_{VO} = Uncertainty of the Load Cell's output voltage

σ_{Avg} = Uncertainty of the Average Load Cell output

VO = Load Cell output Voltage [mV]
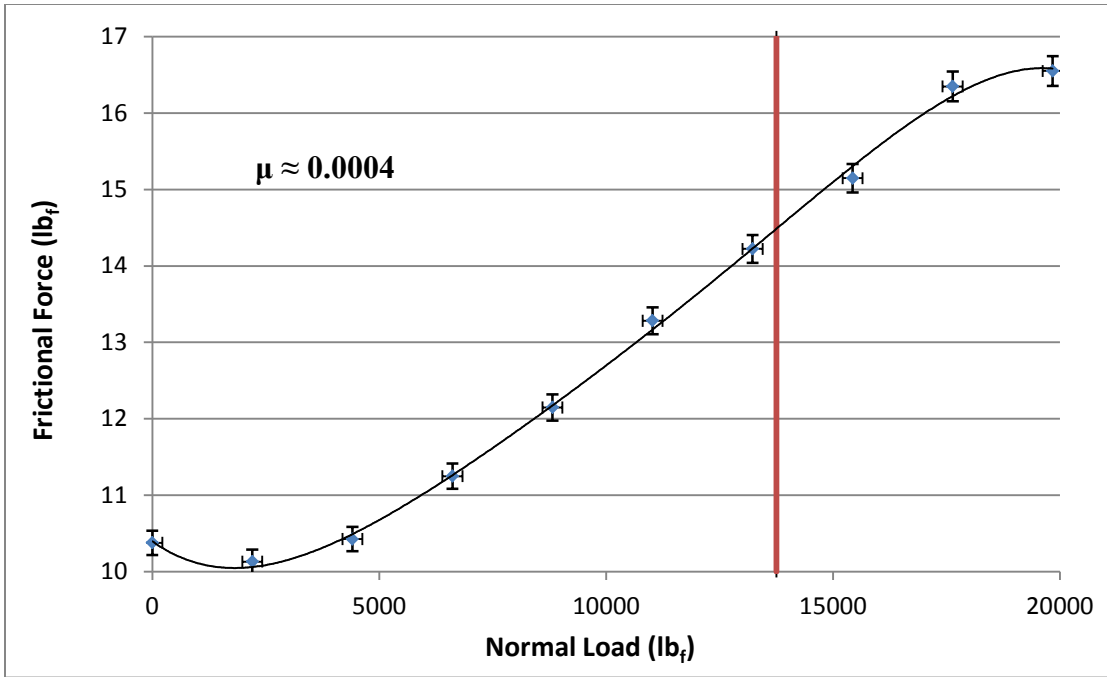
Figure 4.7:   Graphical Friction Test Results
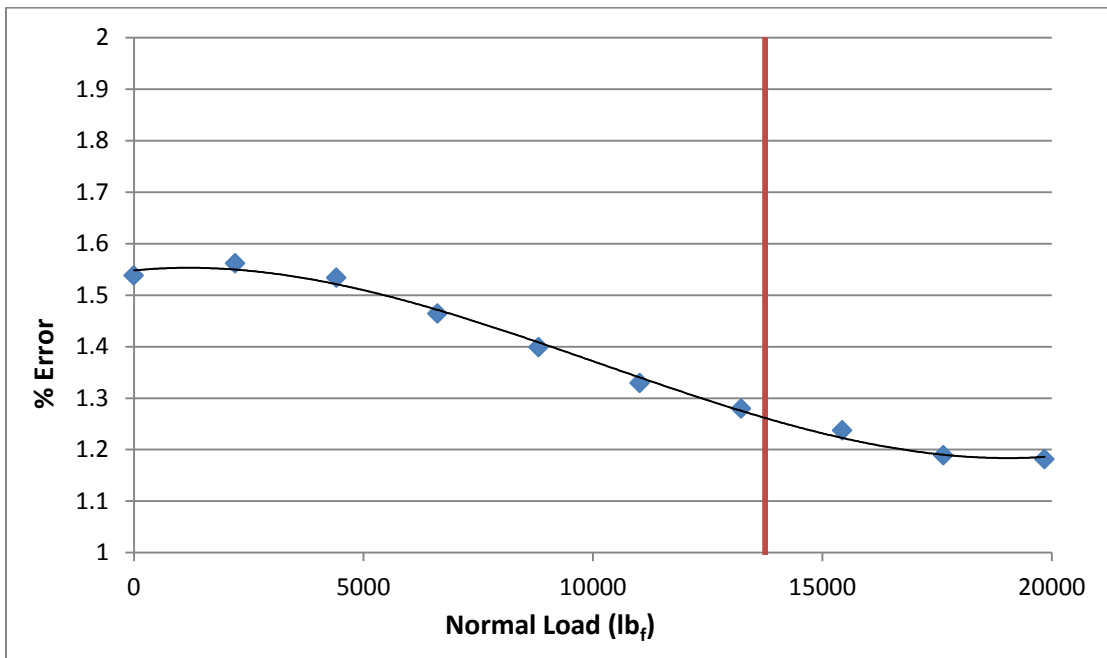
Figure 4.8:   Variation in Error with Normal Loading

112

The red line in the plots represents the maximum applied operating force to each roller carriage. A closer examination of Figure 4.7 reveals a seemingly odd occurrence of the trend in force as the normal load is varied. A dip in the friction force is seen between 0 and 2,200 lb_f as well as at the top of the chart as the normal force approaches 20,000 lb_f. The two situations have their own explanation. First, the dip between 0 and 2,200 lb_f is a result of the internal clearance in the carriage being closed as a reaction to the applied normal load. Second, the taper seen as the normal force approaches 20,000 lb_f is a result of the curve fit. The black line is not an exact representation of the relationship between the normal load and the frictional force, but rather it is there to give an understanding of the trend. Since there is no data point after the last one, the curve fitting algorithm that is built into excel assumes that the data terminates here and provides the curve that fits best to the data presented. In actuality the line would remain linear until the capacity of the carriage has been reached. The results of the test suggest a coefficient of friction for each carriage of about 0.0004. Figure 4.9 is a graphical representation of the total side load measurement error as a function of side load magnitude for varying WOB. If the error stays below 5%, the rig should provide reasonable data; if the side load is not sufficient for the desired WOB, then testing will have to be done without the XY translator assembly by supporting the inner sample container with the measurement rods, with lower strength formations.
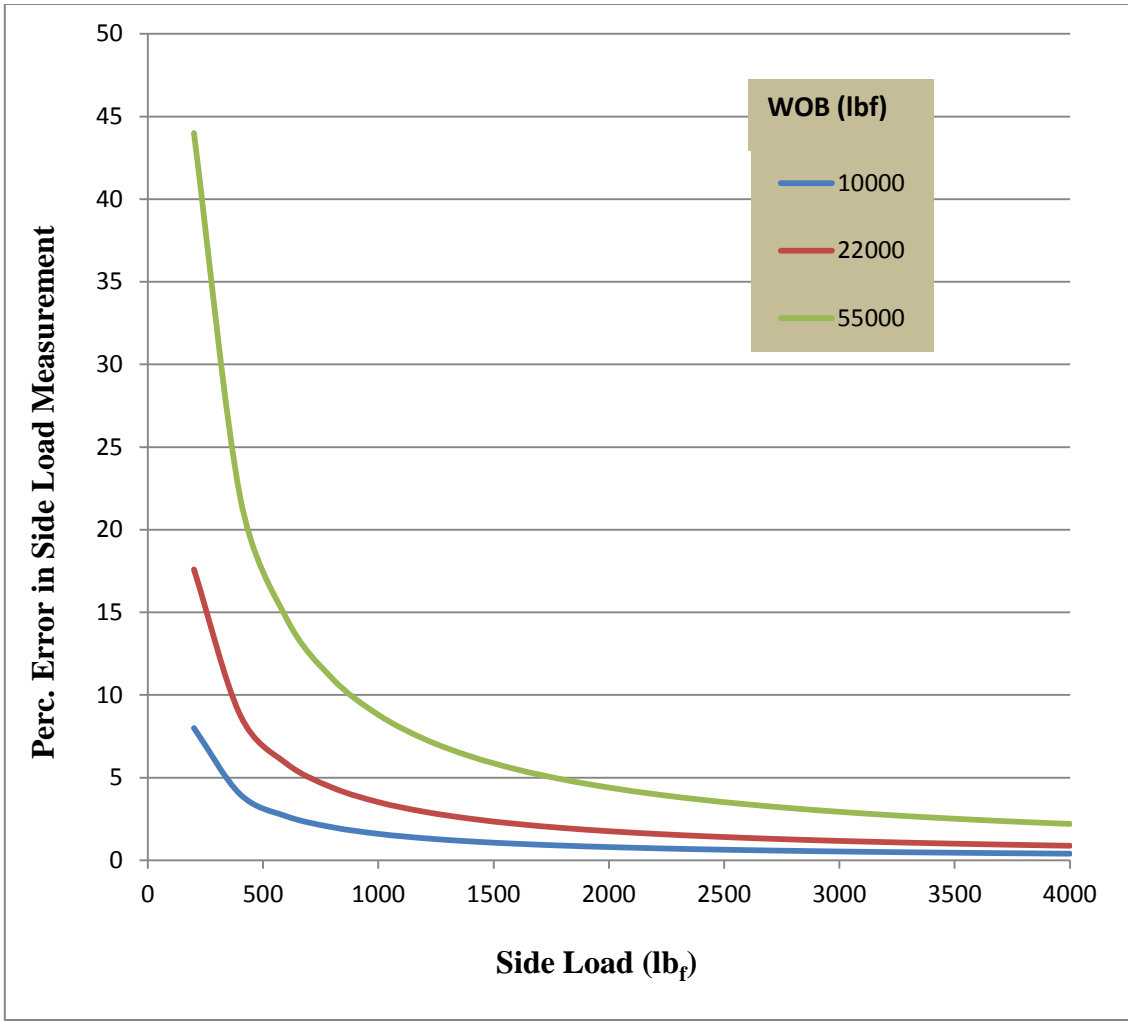
Figure 4.9:   Total Side Load Measurement Error vs. Applied WOB

5. MEASUREMENT ROD CALIBRATION

The later force measurement rods are major components of the force/torque measurement system; they provide a means to measure all load paths on the rig. In order for the rods to provide accurate data when operating as part of the test rig, the strain gauge array must be calibrated. Each rod has been mounted with 6 strain gauges; two for the X - direction, 2 for the Y - Direction and 2 for the Z – direction (Figure 5.1). By mounting the gauges in this fashion, it is possible to isolate each load of the 3 directional loads acting on the rod.
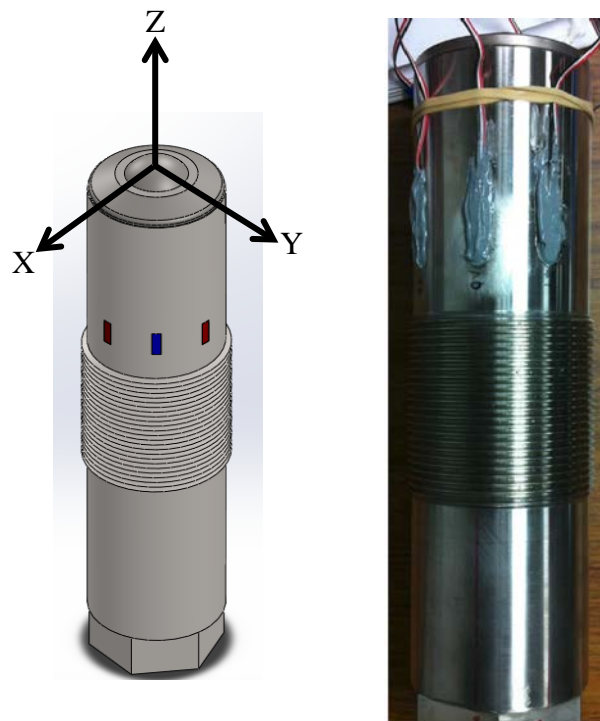
Figure 5.1:   Lateral Force Measurement Rods

5.1. Strain Gauge Setup

It is valuable to understand how the strain gauge configuration is working to give an accurate measurement of the forces and torques on the system. The 2 gauges for each transverse direction (X and Y) are wired in a half bridge configuration as shown in Figure 5.2. This approximately subtracts the two signal outputs (R_1 and R_2) and effectively cancels out any axial output while doubling the signal from the applied cantilevered loading in the associated direction of interest.

Gauge in
Tension, R_1

Gauge in
Compression, R_2

Half-Bridge Strain Gauge Set-up

$$\frac{V_o}{V_{ex}} = -\frac{GF \cdot \epsilon_t}{2}$$

R_D R_1

V_E

V_O

R_D R_2
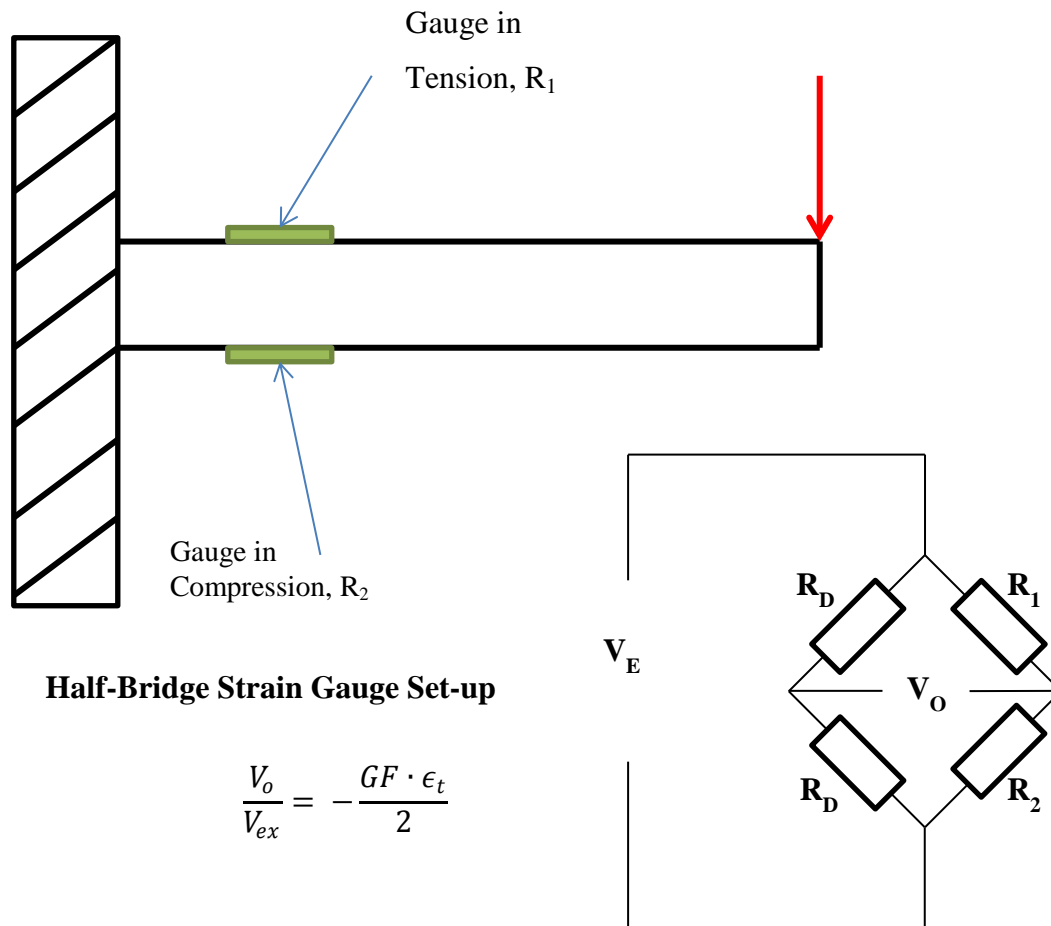
Figure 5.2:   Transverse Rod Loading Strain Gauge Connection

Figure 5.3 depicts the quarter bridge configuration that was used for each of the 2 axial gauges on each rod. In a similar manner as was applied to the transverse gauges, the output from each axial quarter-bridge can be added together, which will cancel any cantilevered loading while the axial signal is doubled. The dummy gauges in the previous figures, denoted by R_D, are internal to the data acquisition system (DAQ); thus, for the measurement rods, only the numbered resistors are needed as gauges. This configuration will not compensate for thermal fluctuations of the rod as significant changes in temperature are not anticipated during the rigs operation. However, if it is found that the current strain gauge configuration is not adequate for the rig's testing, more gauges can be added later to properly compensate for any temperature changes [130].

Gauge in Compression, R_1

Gauge in Compression, R_2

V_E

R_D

$R_{1/2}$

V_O

R_D

R_D

Quarter-Bridge Strain Gauge Set-up

$$\frac{V_o}{V_{ex}} = -\frac{GF \cdot \epsilon_a}{4}\left(\frac{1}{1 + GF\frac{\epsilon_a}{2}}\right)$$
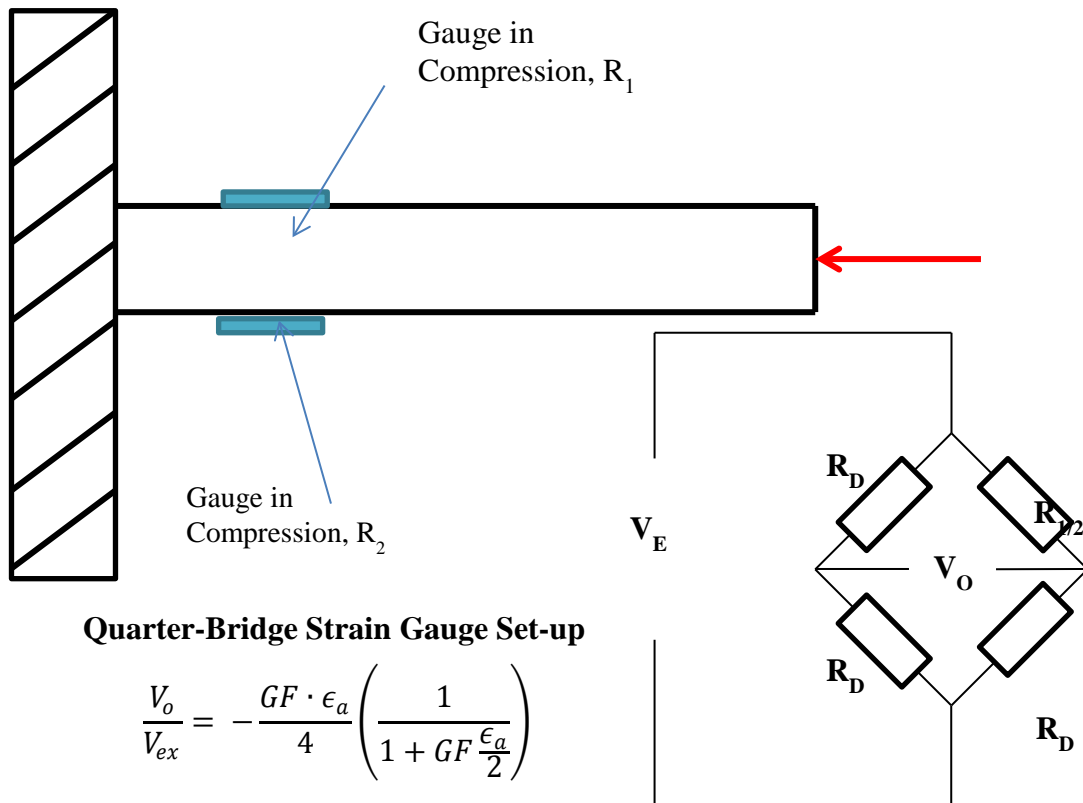
Figure 5.3:   Axial Rod Loading Strain Gauge Connection

117

5.2. Data Acquisition System (DAQ)
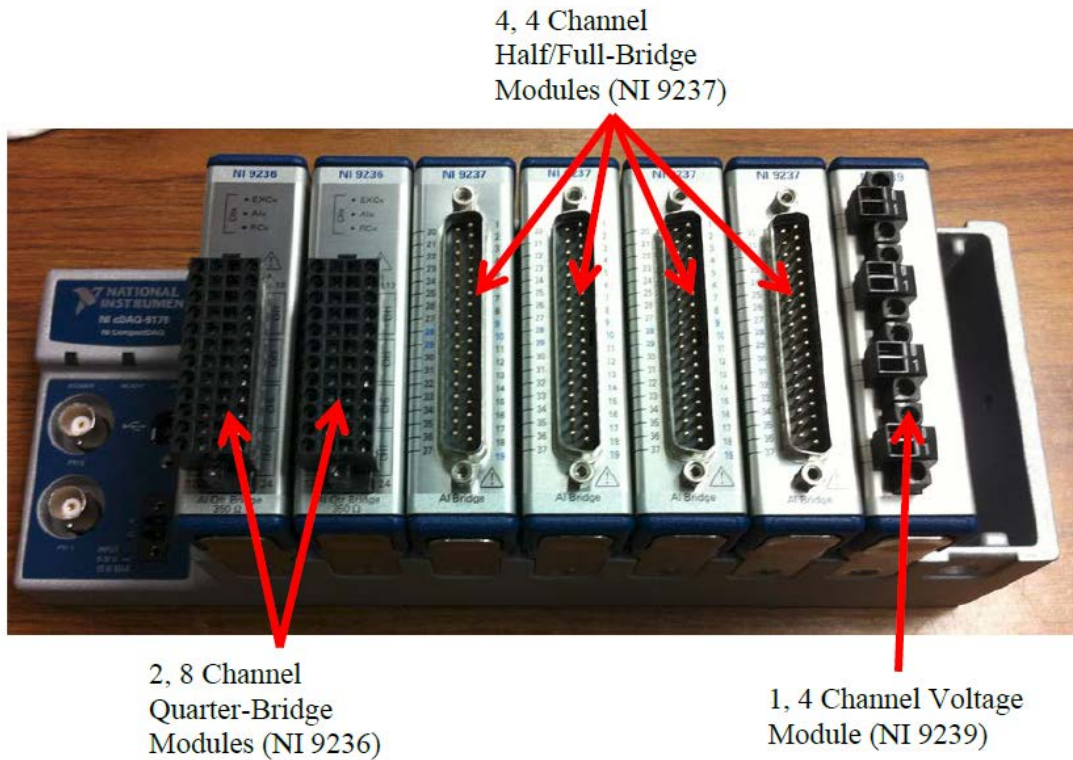
Figure 5.4:   DAQ for the Drilling Test Rig

Figure 5.4 displays the DAQ from national instruments (NI-cDAQ-9178). The DAQ consists of a chassis, two 8-channel quarter-bridge modules (NI 9236), four 4-channel half/full bridge modules (Ni 9237) and one 4-channel voltage module (NI 9239). These are the chassis and modules that will be used on the test rig. While calibrating the measurement rods, each bridge measurement was taken through its own respective channel so as to be able to simulate the exact wiring that would be used in operation.

Rod 1 –
Z1 & Z2

Rod 2 –
Z1 & Z2

Rod 3 –
Z1 & Z2

Rod 4 –
Z1 & Z2

Rod 5 –
Z1 & Z2

Rod 6 –
Z1 & Z2

Rod 7 –
Z1 & Z2

Rod 8 –
Z1 & Z2

Z1 Red

Z1 Black

Z1 White

Z2 Red

Z2 Black
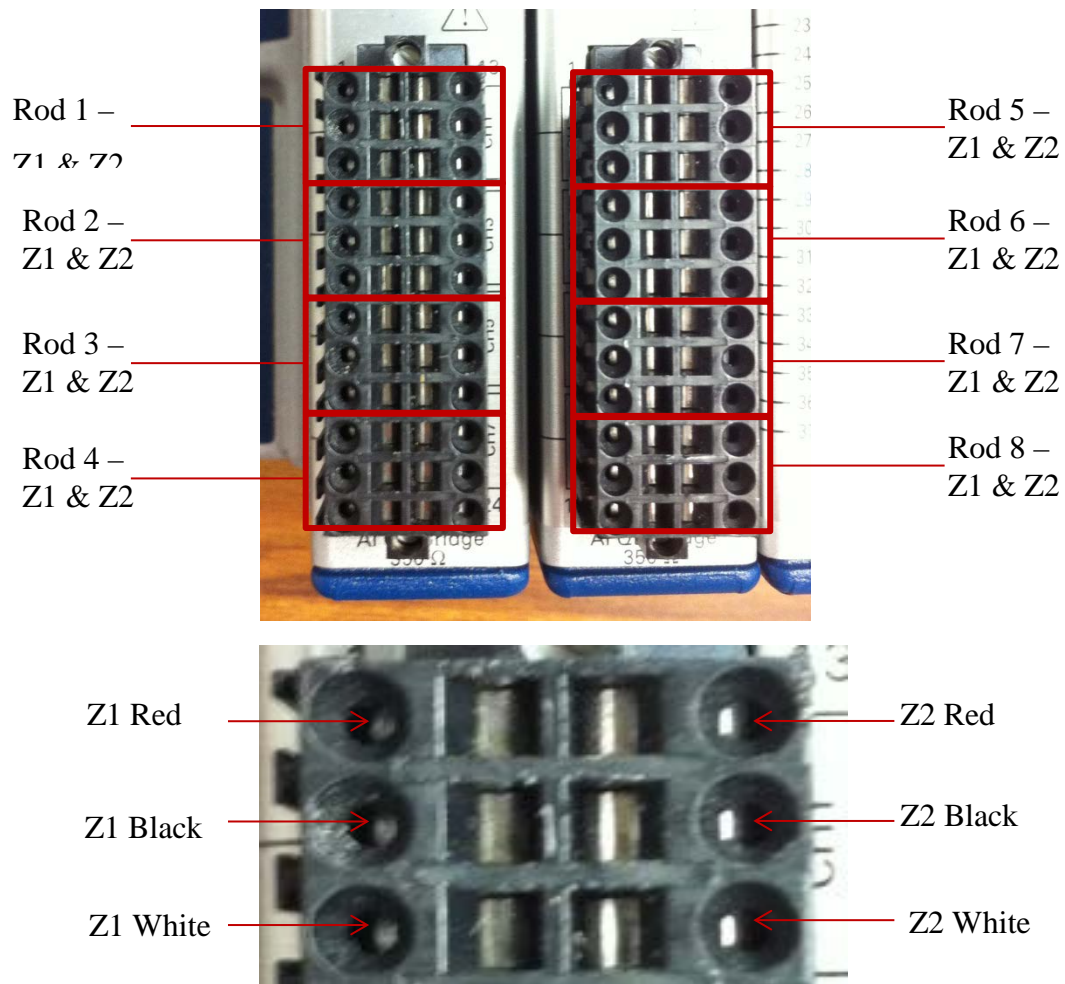
Z2 White

Figure 5.5:   Quarter-Bridge Connection Chart

Figure 5.5 displays the connectivity chart for the quarter-bridge modules (NI 9236). Each rod will have a gauge labeled Z1 and Z2, which will each have 3 wires coming off of them (red, white, black) that need to go in their respective slots on the module.

The transverse sensing strain gauges are connected via a half-bridge circuit as can be seen in Figure 5.6. The illustrations are provided as a wiring reference if future calibration is needed or desired.
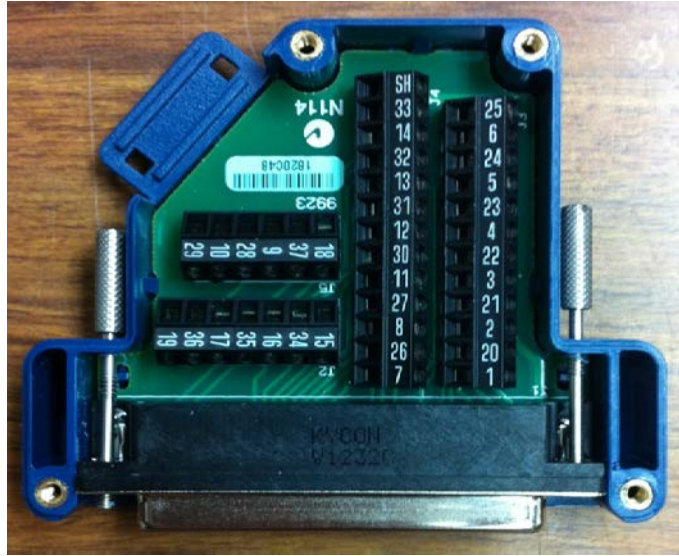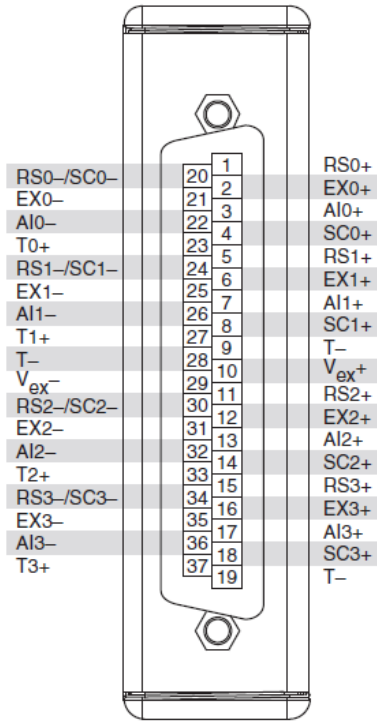
NI 9923
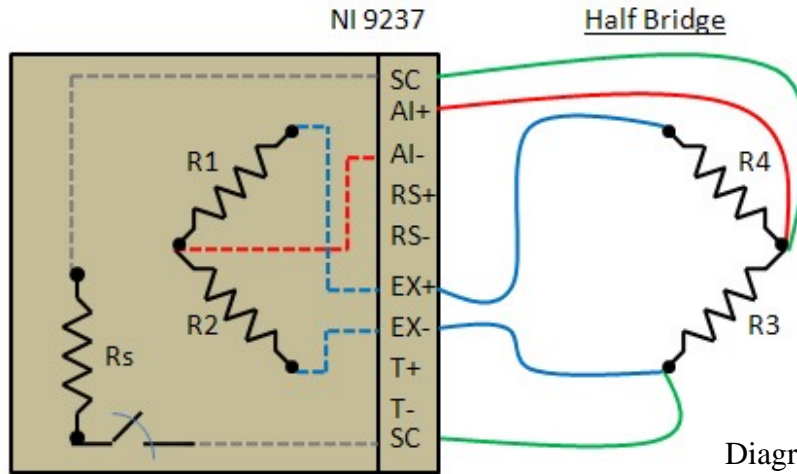
Diagrams courtesy
of NI.com

Figure 5.6: **Half-Bridge Connection Diagram**

5.3. Experimental Setup

5.3.1. Transverse Calibration

The transverse calibration assembly is shown in Figure 5.7 and Figure 5.8. The assembly allows for 2 rods to be tested simultaneously; it consists of a rod support structure, two measurement rods, a load plate and a load cell. The configuration operates under the assumption that the load applied through the load cell is equally distributed between the two rods.

Figure 5.7 is the original CAD model of the assembly, while Figure 5.8 is the actual setup. A difference is clearly noticed between the ways the force is applied. In the CAD model the force is applied via a dimpled plate, however this created a significant non-linear output from the axial sensors due to an axial load developed as the transverse load increased. Because of this occurrence, it was decided to apply the load to the top edge of and in the middle of the two rods (see Figure 5.9). This, in turn, generates the same bending moment at the strain gauge location as if the force where applied at the exact center of the tip of the ball transfer as long as the deflections of the rods are significantly small.

The force applied to the rods is considered a resultant force. The X and Y components of this force are determined by measuring the angle, measured from a specified reference direction, and applying the appropriate sine or cosine multiplier. The angle measurement was possible by marking each rod at the point of applied force as shown in Figure 5.10.

Load Cell

Rod Support
Structure

Rod Lock
Nut

F

The reaction
support forces
(F/2) are supplied
by the machine
press

F/2   F/2
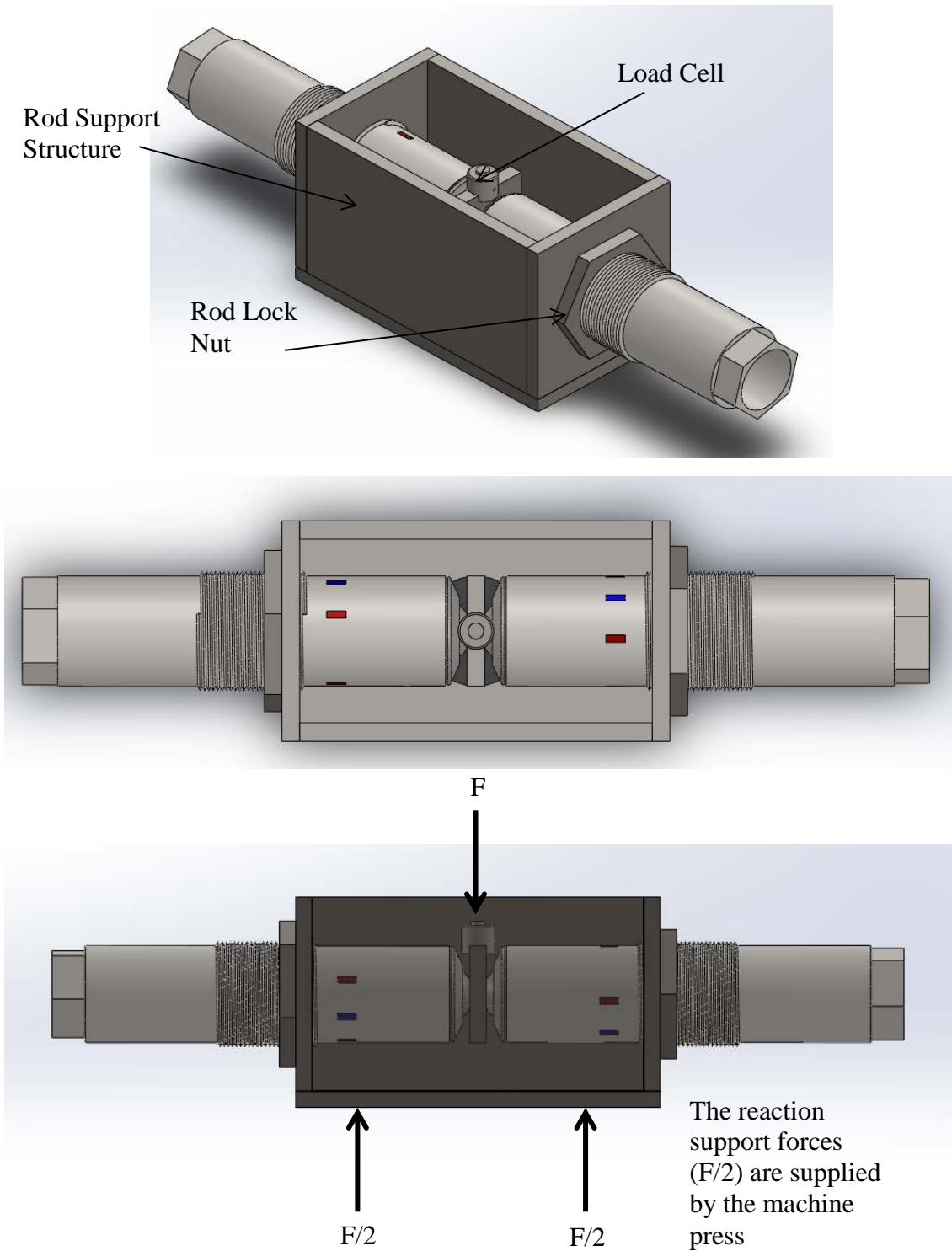
Figure 5.7:   CAD Model of Transverse Calibration Assembly
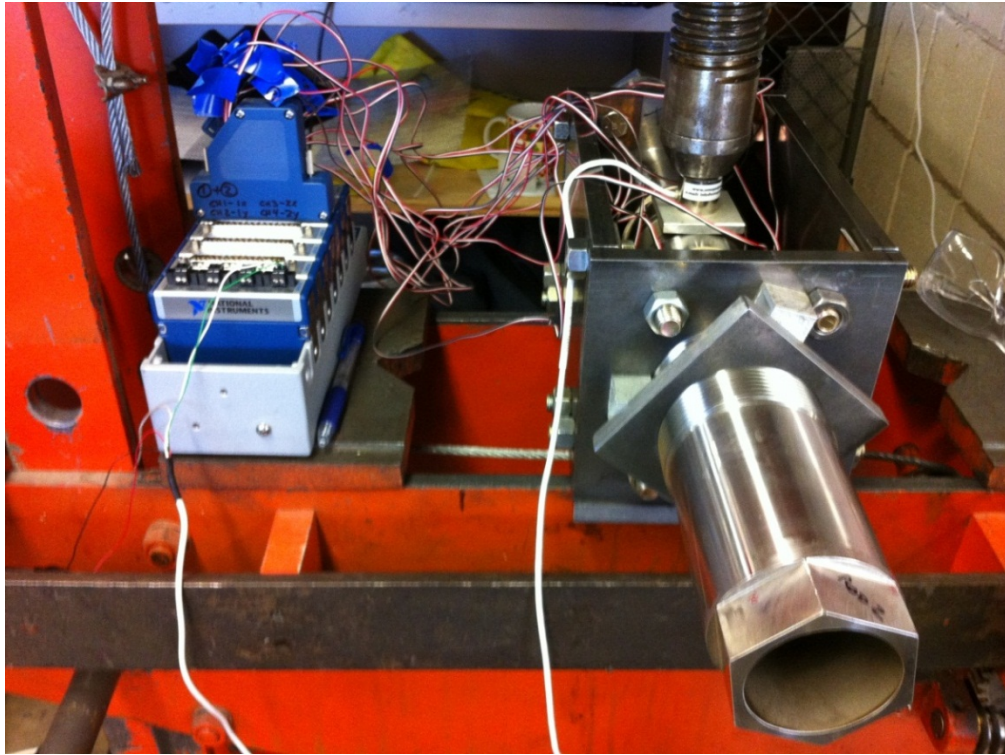
Figure 5.8:   Experimental Transverse Calibration Setup
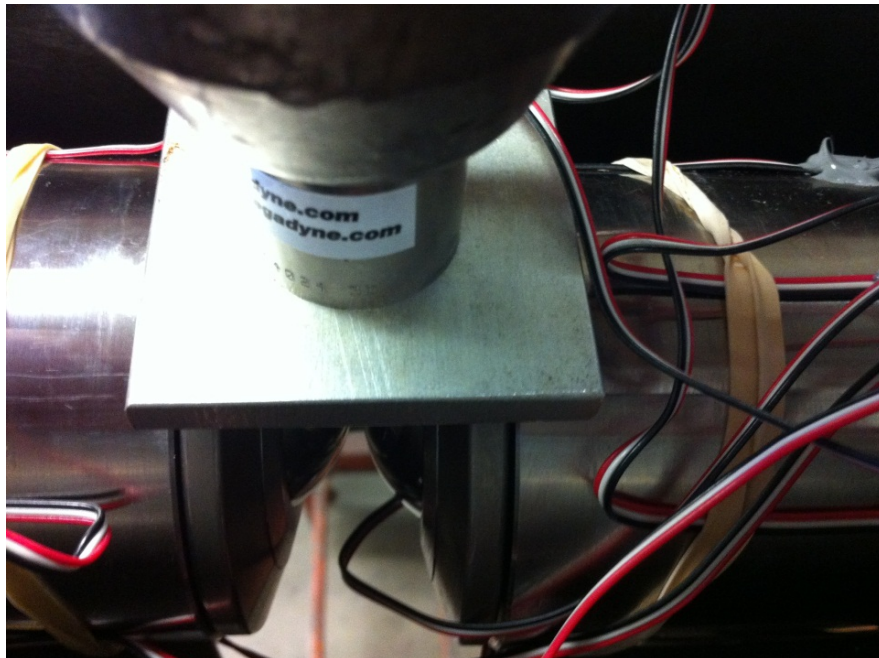
Figure 5.9:   Plate Loading for Transverse Calibration

Figure 5.10:   Angle Marker for Transverse Calibration

5.3.2. Axial Calibration

Axial testing was carried out in a similar fashion, with only one rod being tested at a time. Figure 5.11 and Figure 5.12 illustrate the calibration setup for the axial loading. The load cell in this case is simply sandwiched in between the ball caster and a stationary block. The rod is simply screwed further into the assembly to generate a higher axial load.
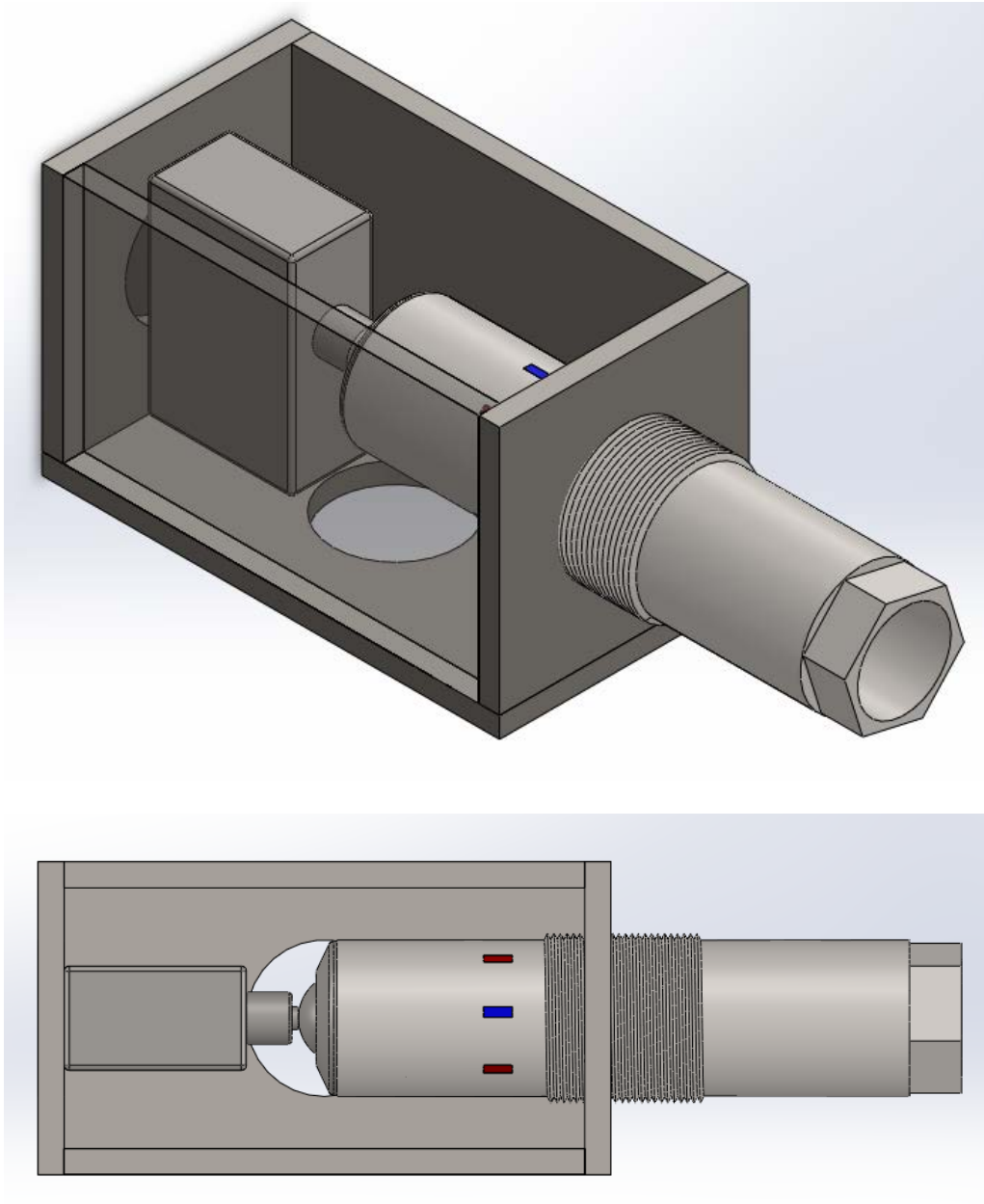
Figure 5.11: CAD Model of Axial Calibration Assembly
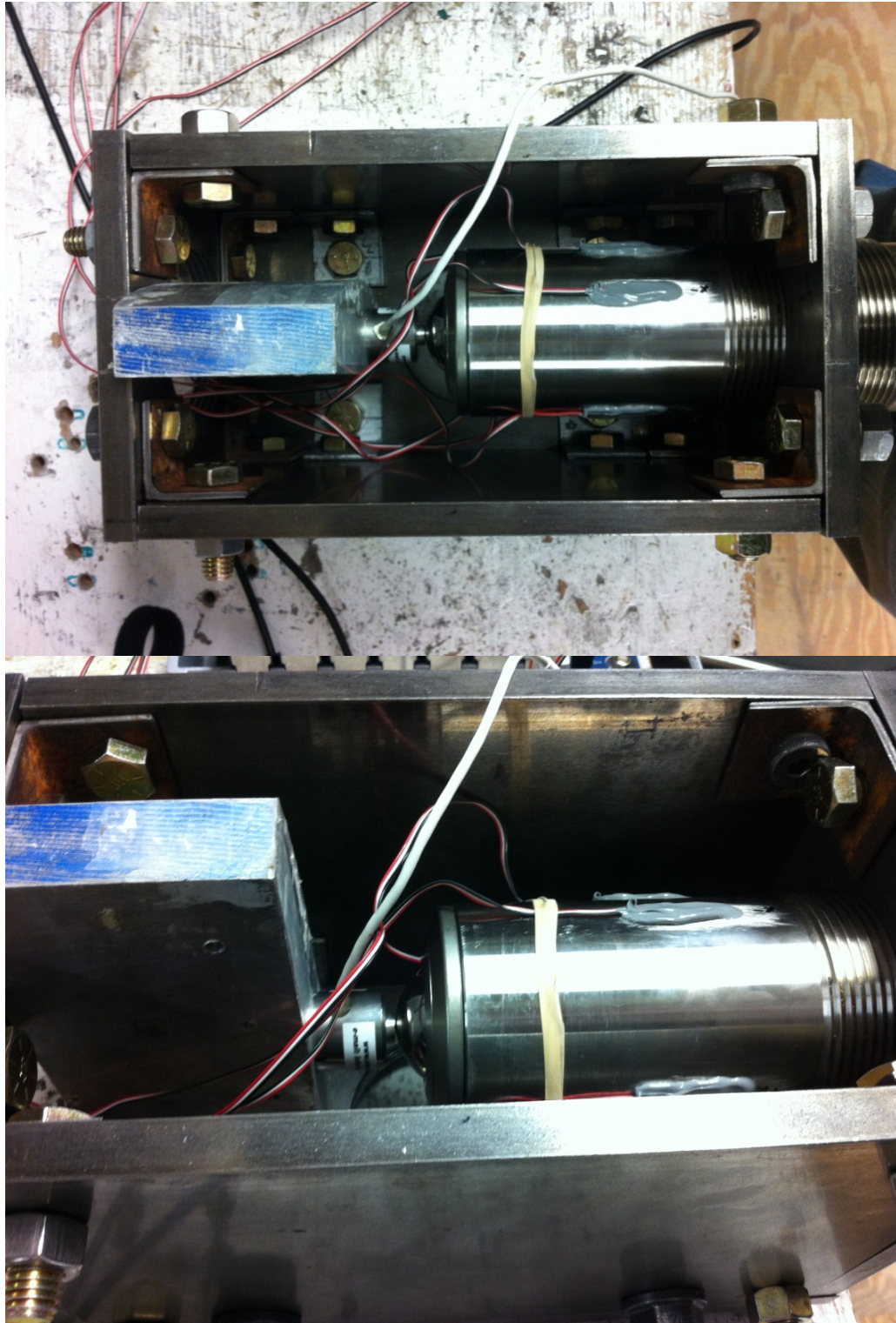
Figure 5.12:   Experimental Axial Calibration Setup

5.4. Testing Procedures

The general calibration procedure can be described as follows:

1. Wire appropriate strain gauges to associated input modules.
2. Wire preferred load cell to appropriate input/output device (In the present case, the load cell was measured via LabView along with the bridge outputs)
3. Adjust DAQ channels to be read in LabView accordingly.
4. Calibrate each bridge to be read.
5. Measure outputs from each bridge for the rod of interest for several, incrementally increasing loads.
6. Process data to obtain a $(mv/V)/lb_f$ reading from each strain gauge configuration.

The proper wiring was outlined in the experimental setup. The LabView processing and respective bridge calibrations are outlined by the following figures.
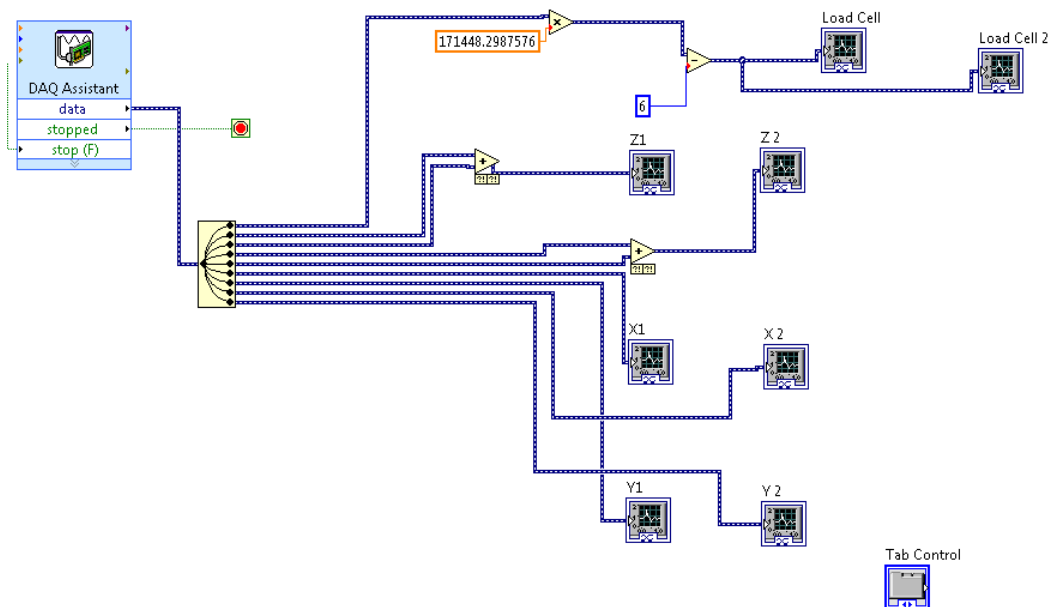
Figure 5.13:   LabView Calibration Code

127

Figure 5.13 depicts the relatively simple LabView calibration program for the transverse loading scenario It can be seen that the two axial (Z1 & Z2) strain gauge signals are added together to give the appropriate output, while the X and Y direction outputs are directly measured due to the fact that their half-bridge configurations act in the same way as subtracting the two signals. The aforementioned LabView code can easily be altered to accommodate the axial calibration tests by merely adjusting which channels are being read from the DAQ.

By double-clicking on the box labeled "DAQ Assistant", the DAQ Assistant Window can be accessed (Figure 5.14). The separate channels that are to be read from the DAQ can be edited and fine-tuned in this window. The colored lines in the plot at the top of the figure are the un-calibrated voltage outputs from each bridge. This, of course needs to be adjusted so that the unloaded output from each bridge is close to zero.
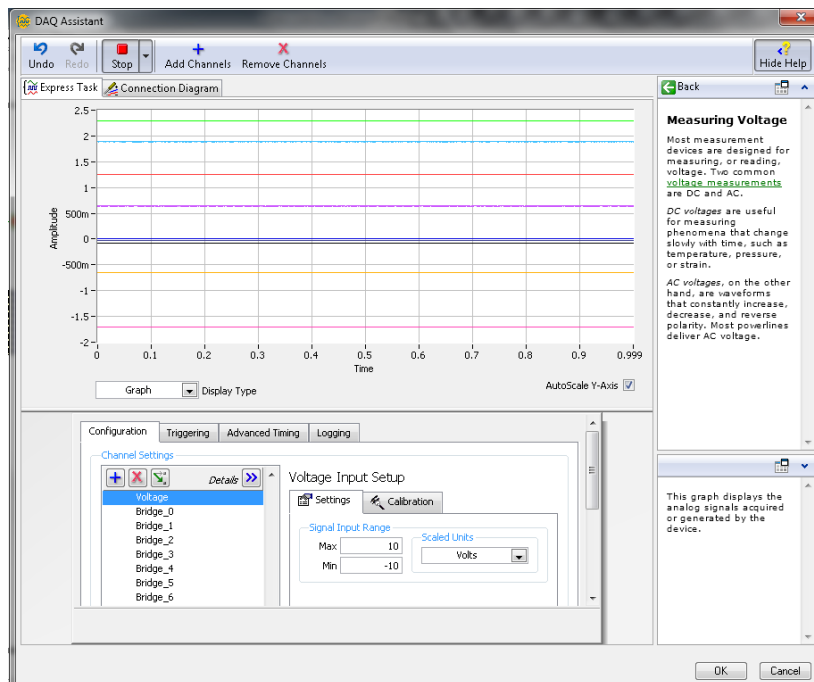
Figure 5.14:   DAQ Assistant Window (Un-calibrated Bridge Outputs)

This bridge calibration can be done automatically through the DAQ Assistant in LabView. By clicking on the "Device" tab for a selected bridge, then clicking on the "Bridge Calibration" button (Figure 5.15) the "Setup Hardware" window is opened (Figure 5.16).
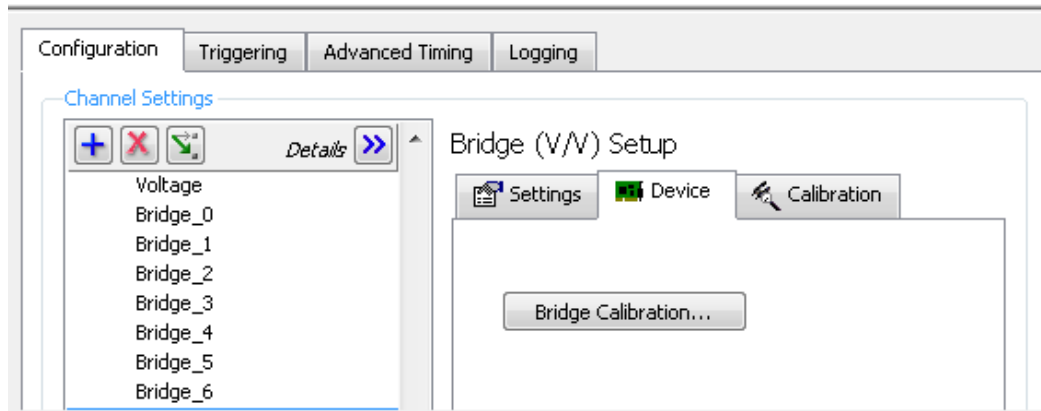
Figure 5.15:   Bridge Calibration Access Button
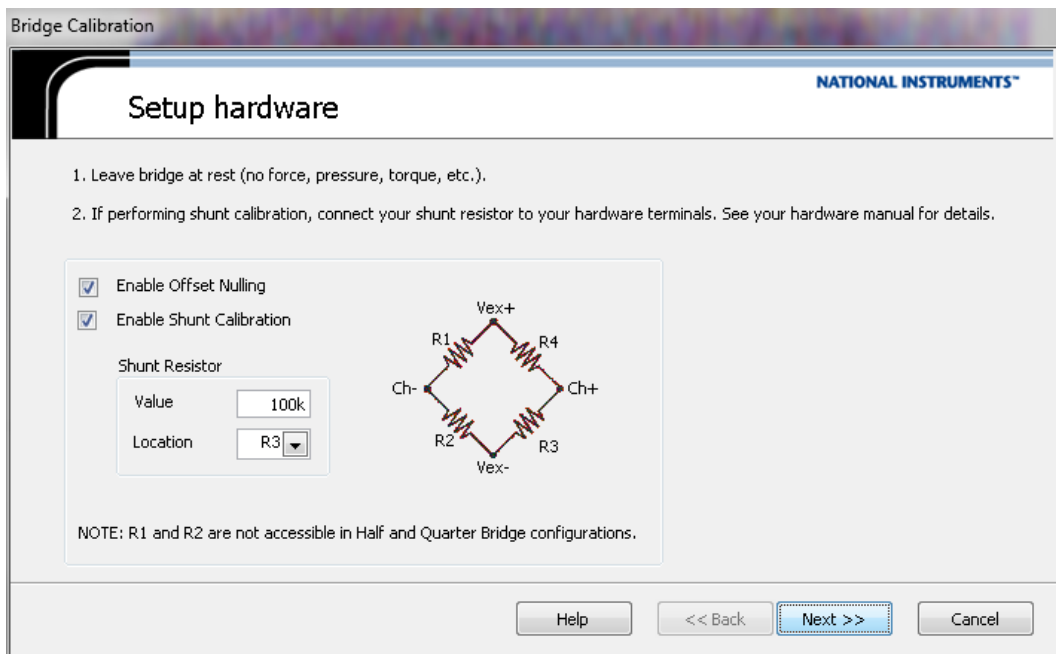
Figure 5.16:   Hardware Setup Window for Bridge Calibration

The built in bridge calibration relies on a shunt calibration method, which essentially replaces the R3 resistor in the Wheatstone bridge with a component of a large, known resistance in order to determine the appropriate adjustment to achieve a zero-voltage output. Clicking the "Next" button the previous figure, leads to the "Measurement and Calibrate" window shown in Figure 5.17. If the system has been connected properly, the only thing to do is for the user to hit the "Calibrate" button and "Finish". The bridge can be calibrated repeatedly until the desired error percentage is achieved.

If the calibration was successful, the resulting outputs from each bridge should resemble the plot shown in Figure 5.18. The bridge calibration is a crucial part to being able to obtain useable data from the measurement rods. The rods may either be re-calibrated before being used on the rig or the (mV/V)/lb$_f$ relations found from this study can be used. Whatever the case may be, some sort of calibration must be applied to the final operating code of the rig for the force measurement system. The program written for purposes of this calibration study was not intended to be used as the final rig program, but merely as a means to show that the measurement rods do function as intended and can be calibrated.
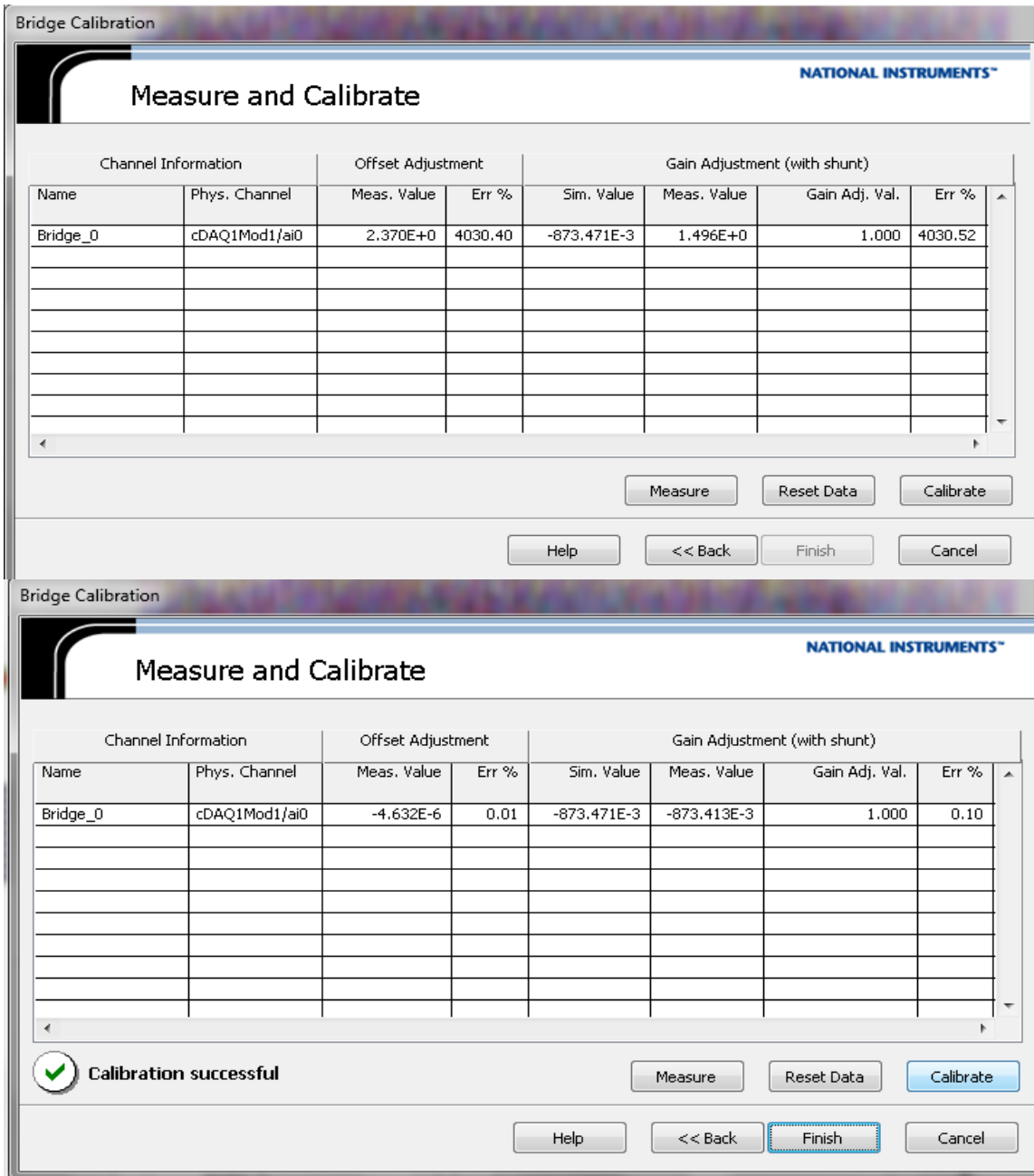
Figure 5.17:   Measurement and Calibration Window for Bridge
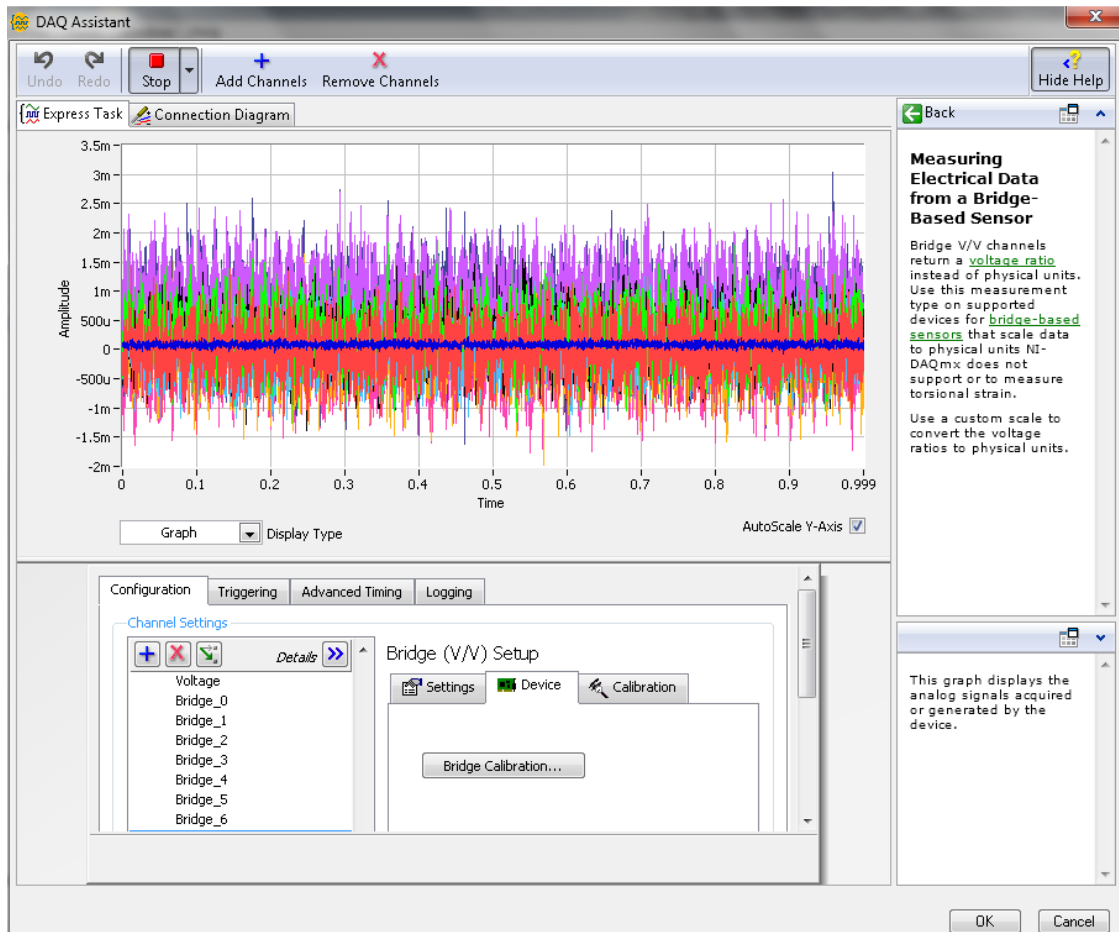
Figure 5.18: Calibrated Bridge Outputs

The output from the LabView code gives an output graph from the load cell and three output graphs from each rod, one for each measured direction. A typical output will look like that shown in Figure 5.19. The outputs are then read with a specified value (represented by the solid red line) and an associated uncertainty (denoted by the dotted lines) as can be seen by Figure 5.20.
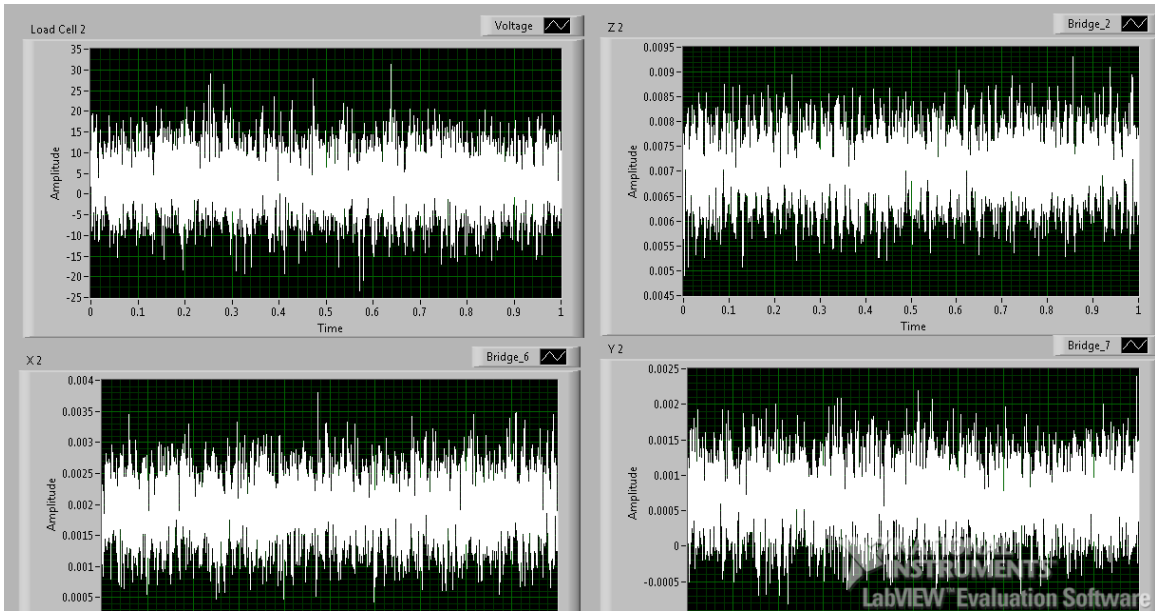
Figure 5.19: Calibration Data Output
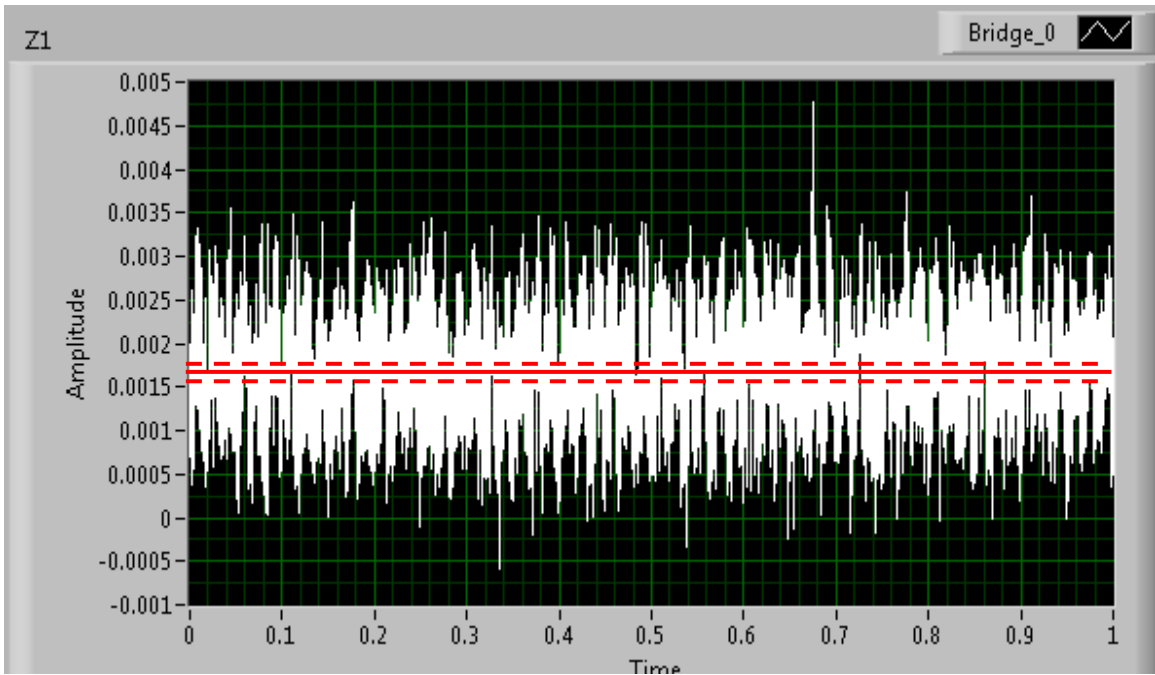
Figure 5.20: Data Extraction Method

133

5.5. Results
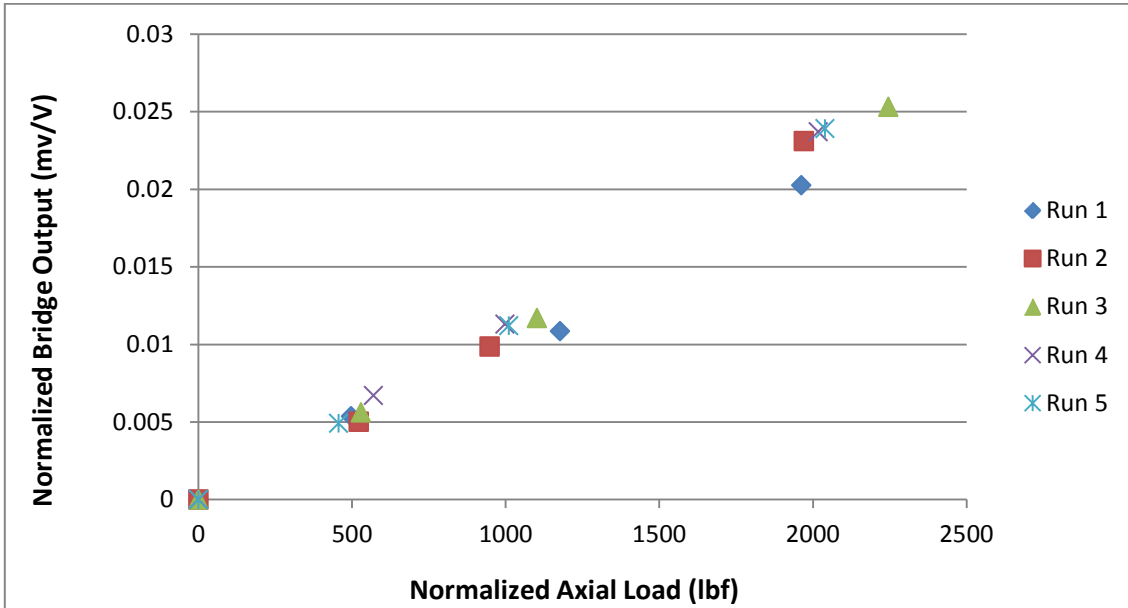
Rod 1

Figure 5.21:   Axial Calibration (Rod 1)
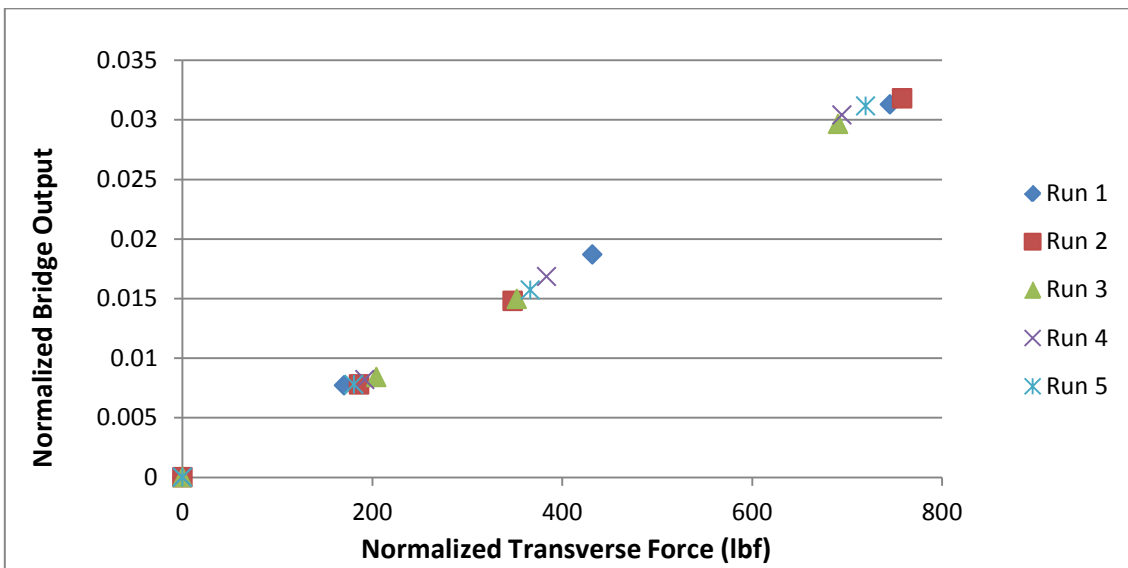
Figure 5.22:   X Calibration (Rod 1)
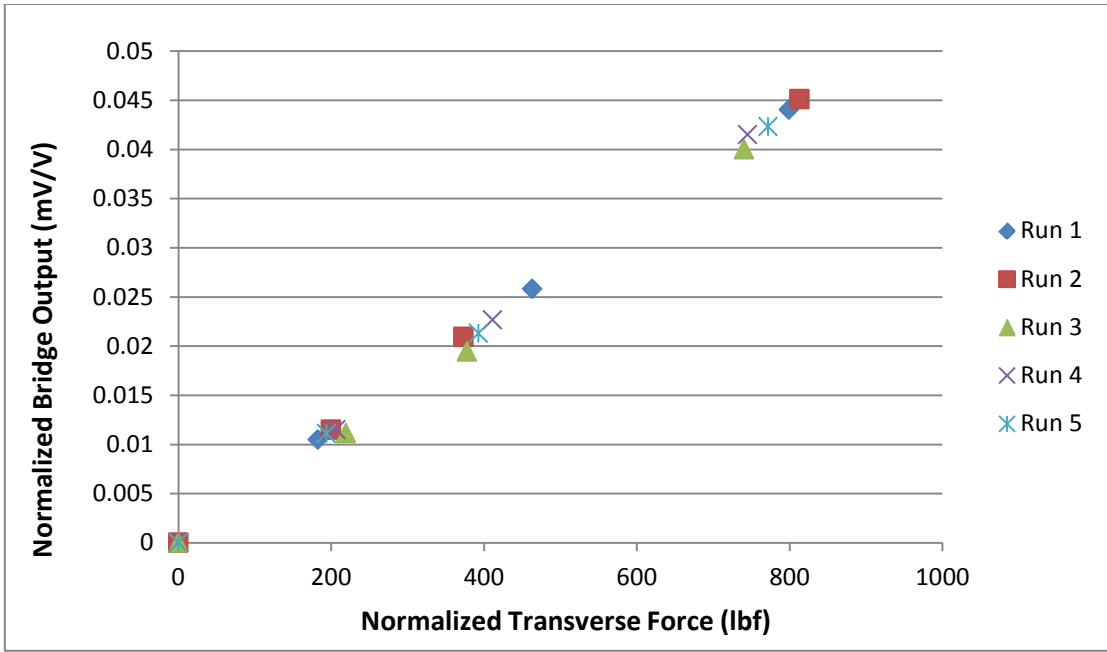
Figure 5.23: Y calibration (Rod 1)
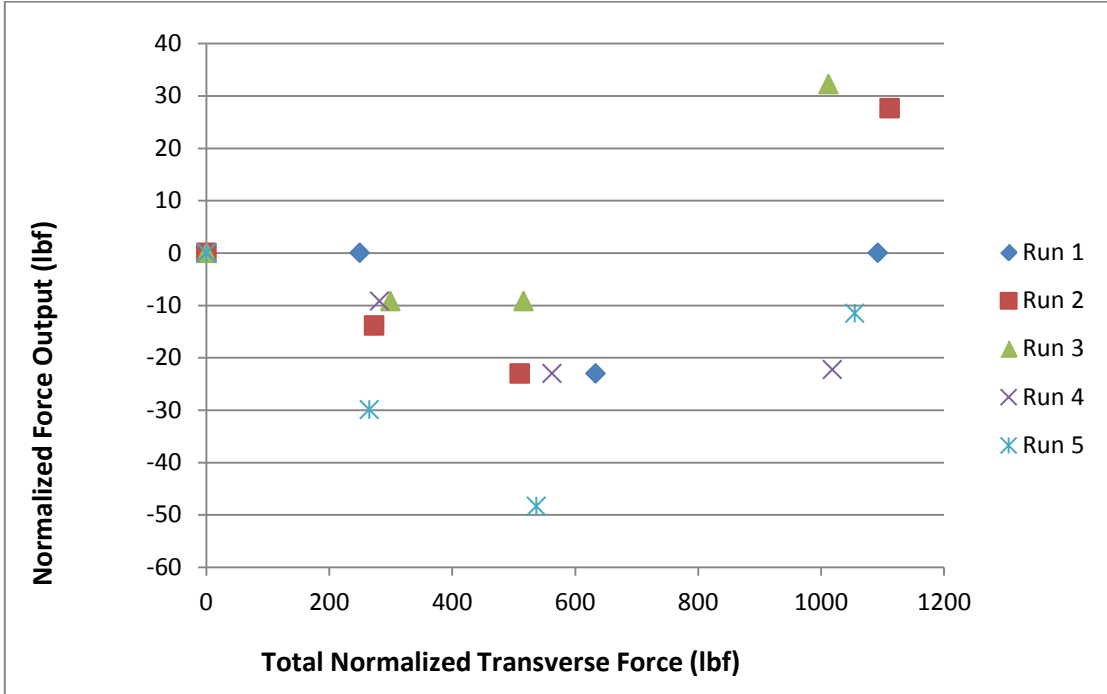
Figure 5.24: Axial Sensitivity to Transverse Load (Rod1)

135
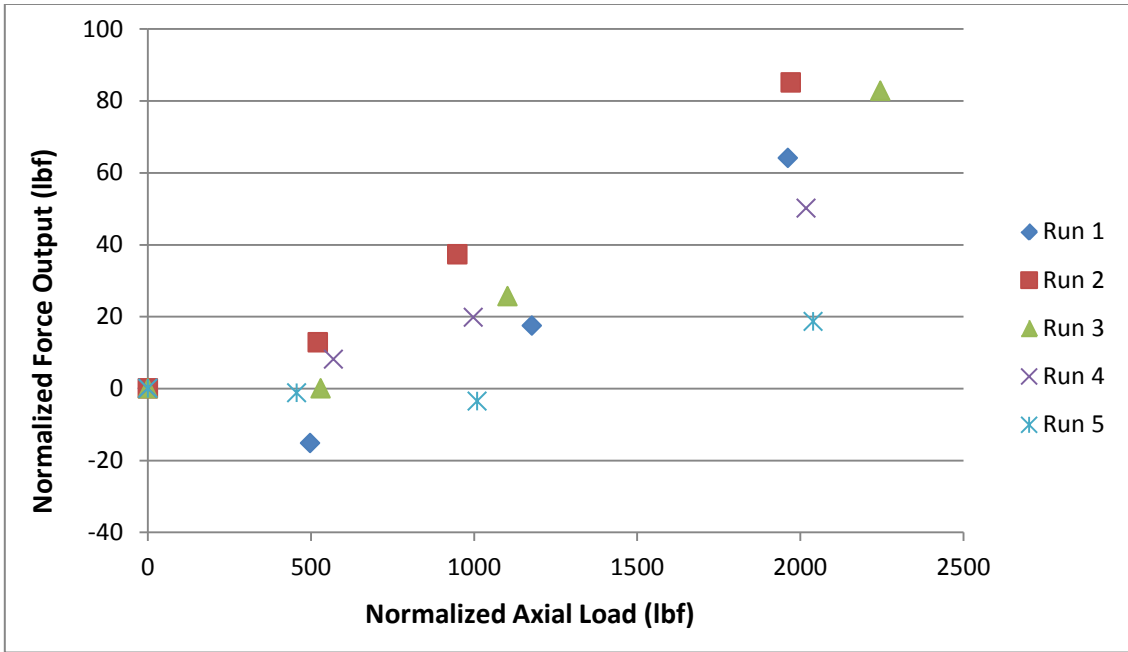
Figure 5.25: X Sensitivity to Axial Load (Rod 1)
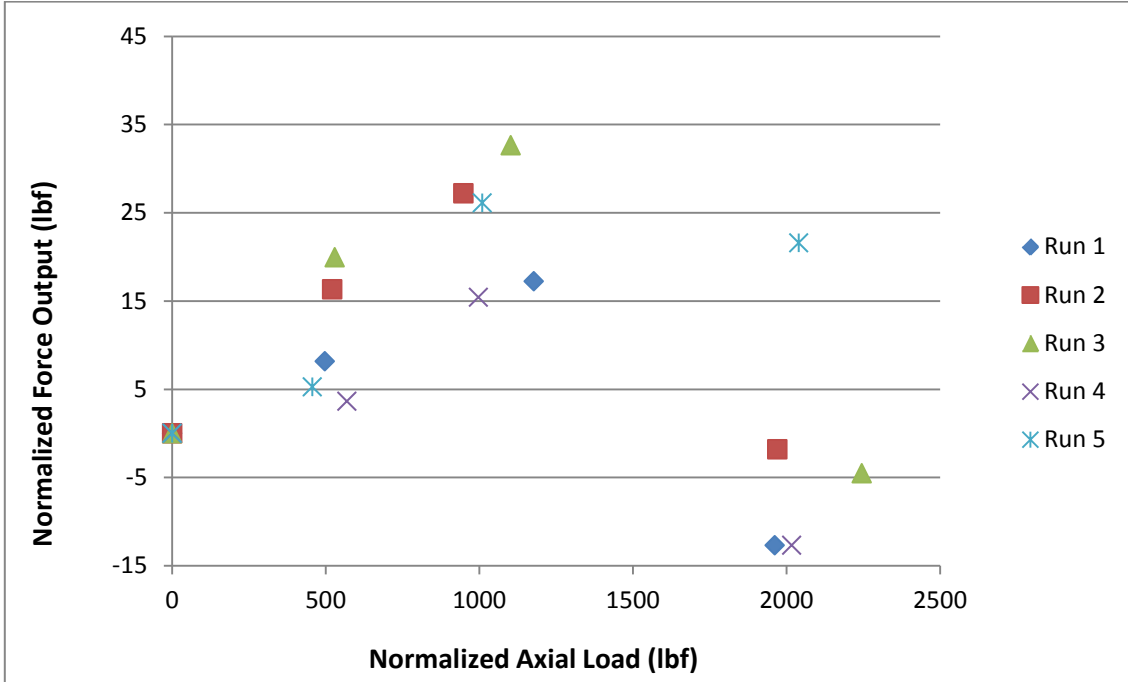
Figure 5.26: Y Sensitivity to Axial Load (Rod 1)

136

Figure 5.21 through Figure 5.23 display results from the calibration tests for Rod 1. It is clear from the graphs that a linear, repeatable, relationship between applied load and bridge output for every load direction is present. The quantification of these $lb_f/(mV/V)$ relationships is summarized in Table 5.1.

Table 5.1: Rod Calibration Results

Rod 1						
	lbf/(mV/V)			Transverse Sensitivity		
	Z	X	Y	Z (% of Trans)	X (% of Axial)	Y (%of Axial)
	92114.85	23323.85	18139.63	-3.3342	1.6438	1.4162
Err (+/-)	539.92	398.15	300.40			
Rod 2						
	lbf/(mV/V)			Transverse Sensitivity		
	Z	X	Y	Z (% of Trans)	X (% of Axial)	Y (%of Axial)
	93942.79	22097.28	17121.22	3.7295	-1.2441	0.6914
Err (+/-)	531.24	22097.28	296.98			
Rod 3						
	lbf/(mV/V)			Transverse Sensitivity		
	Z	X	Y	Z (% of Trans)	X (% of Axial)	Y (%of Axial)
	94312.60	25020.39	18287.13	47.3407	-0.8192	0.2953
Err (+/-)	525.64	336.66	278.28			
Rod 4						
	lbf/(mV/V)			Transverse Sensitivity		
	Z	X	Y	Z (% of Trans)	X (% of Axial)	Y (%of Axial)
	96568.29	20263.25	21664.96	2.0243	0.3748	-0.6293
Err (+/-)	541.86	383.94	475.22			
Rod 5						
	lbf/(mV/V)			Transverse Sensitivity		
	Z	X	Y	Z (% of Trans)	X (% of Axial)	Y (%of Axial)
	88069.59	23681.53	23464.37	-123.8159	-0.8295	-1.3263
Err (+/-)	475.27	256.51	982.37			
Rod 6						
	lbf/(mV/V)			Transverse Sensitivity		
	Z	X	Y	Z (% of Trans)	X (% of Axial)	Y (%of Axial)
	83611.95	17934.47	4644.39	-80.4894	0.1245	1.0453
Err (+/-)	462.25	207.39	2943.50			

The transverse sensitivity of each rod is determined from the linear relationships that are then applied to the sensitivity output (Figure 5.24 through Figure 5.26) for each rod.

Since the sensitivity outputs appear to be sporadic and lacking in from, any error will have to be considered a mean value. Averaging the corresponding forces, the sensitivity of each load direction can then be expressed as a percentage of the associated direction that the bridge is sensitive to.

It is evident from the results presented in the table that there are a few unacceptable discrepancies in the data, particularly the Z-direction sensitivity to transverse loading of rods 3, 5 and 6. Examining the data plots of these rods (see Appendix L) it can be seen that there exists a more repeatable trend in the sensitivity plots of these rods when compared to the same plots for other rods. The significant source of error is thought to be caused by misalignment in the strain gauges. Recalling (Figure 5.2 and Figure 5.3) that the method of measurement is a process of adding and subtracting signals from one another, it can easily be understood how a small misalignment in opposing gauges can lead to significant output errors.
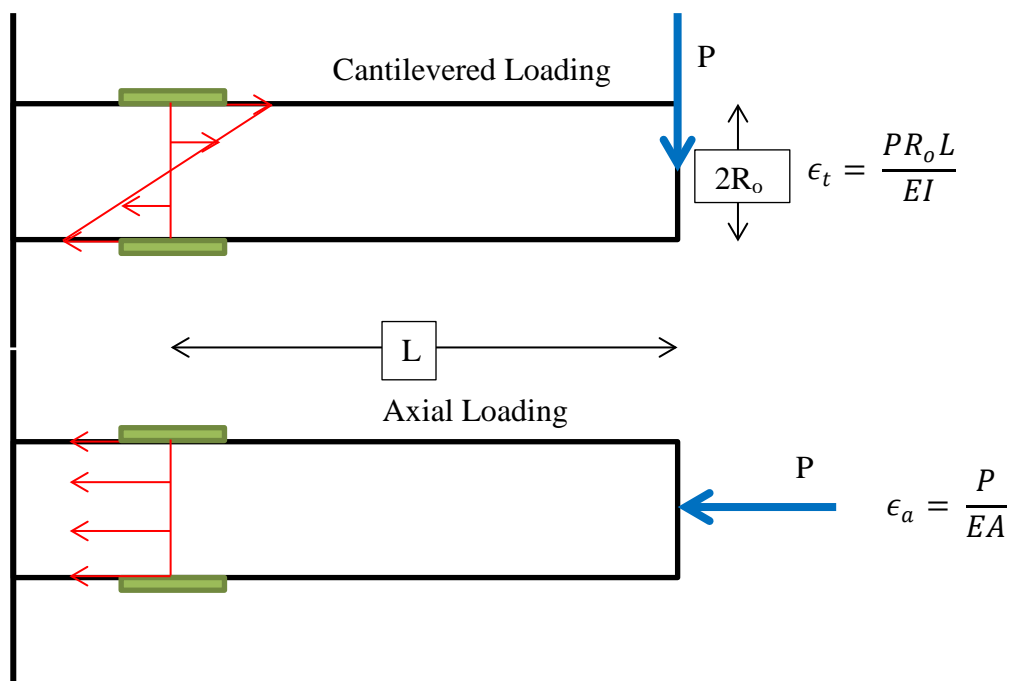
Figure 5.27:   Stress Distributions for Cantilevered and Axial Loading

Figure 5.27 further illustrates this point. In the cantilevered case, it can be seen that the strain at one of the gauges, ϵ_t, is a function of L, and should be equal and opposite to the opposing gauge reading. Therefore, if you add the signals from the gauges together, there should be zero output. However, if the gauges are not at the same distance, L, from the load, P, then adding the two signals will not cancel out the transverse loading. The two gauges would also need to be in the same plane (i.e. opposing each other on the rod by 180°). It is believed that the misalignment along the length of the rod is responsible for the significant error in the axial sensitivity to transverse loading for rods 3, 5 and 6. To fix this error, the gauges will need to be replaced with correctly oriented gauges and recalibrated.

Along the same lines, if the axial case is examined it can be seen why the X and Y sensitivities would be less affected by their distance from the load point. For the X and Y directions, the signals from opposing gauges are subtracted from one another, which effectively cancel out any axial loading. Since the strain equation for axial loading does not depend on L and is relatively uniform over the entire length of the rod, there can be misalignment in L with little error in the results.

In conclusion, the measurement rods have been proven to be a feasible concept. The errors in misalignment of gauges will be corrected for the affected rods and they will be recalibrated. It should be noted that any uncertainty calculated was done so by the method illustrated in Section 4.

6. TESTING RECOMMENDATIONS

In order to obtain the necessary data for an adequate representation of the Bit/Formation Interface Law certain tests are required. This section is devoted to explaining the necessary tests and the results that will be obtained from each. Figure 6.1 is a visualization tool to help the reader understand the goals of the rig's testing.
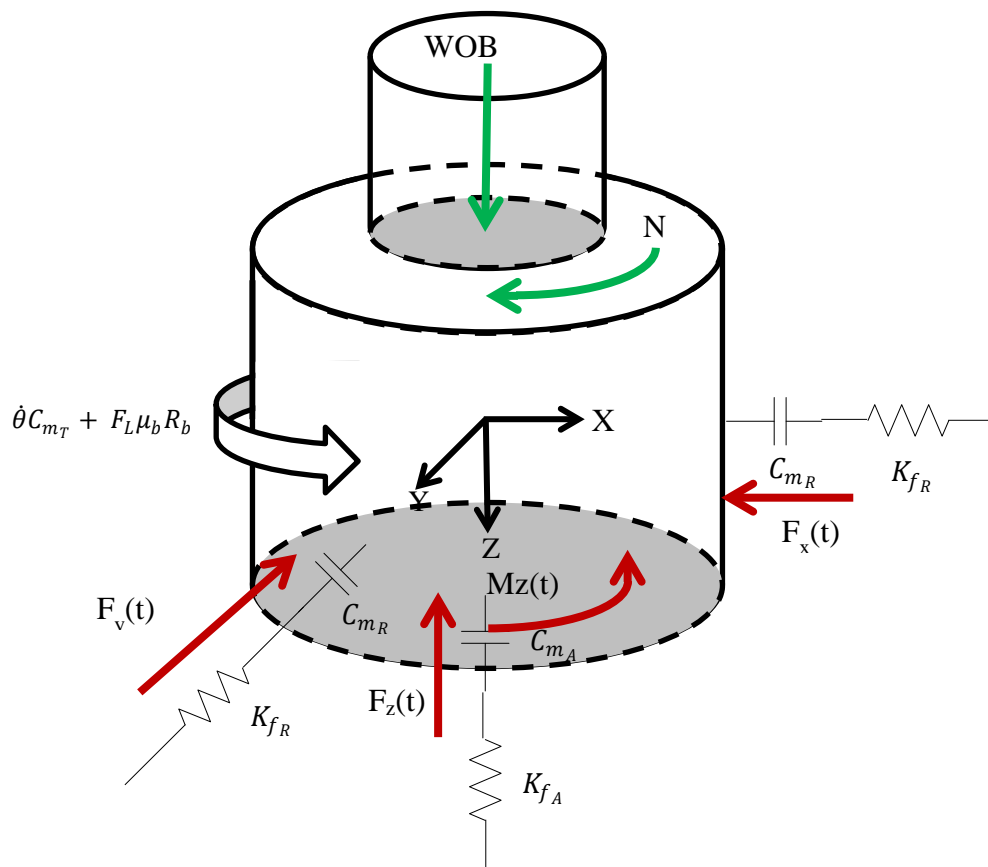
Figure 6.1:   General Vibrational Model of a Drill bit

K_{fR} = Radial formation stiffness

K_{fA} = Axial formation stiffness

C_{mR} = Radial mud damping coefficient

C_{mA} = Axial mud damping coefficient

C_{mT} = Torsional mud damping coefficien

The figure depicts broad representations of the interactions of the bit with the wellbore environment. The objective of testing will be to determine formation stiffness (K_f), fluid damping (C_m), as well as magnitude and direction of the resultant forces and moments (F, M) while the bit is in contact with the formation.

6.1. Normal Drilling
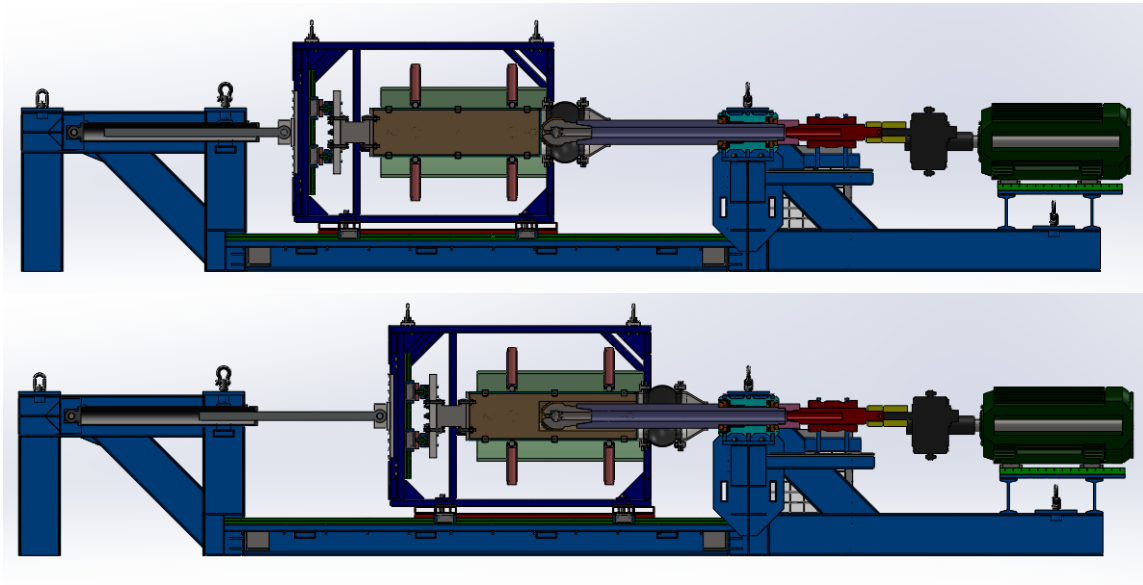
Figure 6.2:   Normal Drilling Mode of Test Rig

The normal drilling mode (Figure 6.2) will allow for an overall measurement of the force and torque on the bit and determine a relationship to rate of penetration. This approach will be able to develop relationships of the form

$$ROP = f(WOB, S, \gamma, \rho_m, Q)$$
$$TOB = f(WOB, S, \gamma, \rho_m, Q)$$
$$F_S = f(WOB, S, \gamma, \rho_m, q_m)$$

for each bit type tested; where **ROP**, **TOB** and $\mathbf{F_S}$ are the rate of penetration, torque on bit and side loading on the bit respectively. The equations would be functions of WOB, formation strength (**S**), bit parameters ($\boldsymbol{\gamma}$), mud density ($\boldsymbol{\rho}_m$) and flow rate (**Q**). This representation is the most general form of the Bit/Formation Interface Law. These will be the governing of equation that will dictate the forces, torques and penetration rates generated at the bit under various operating conditions.

If one wishes to develop an interface law similar to the one presented by Detournay and Defourny (See Sections 1 and 2), it is important to realize where the separation of the friction and cutting components are originating from. Looking back at Figure 3.2, it can be seen that the cutting component is the contribution of the TOB associated with the cutting surface and the formation. Since the cutting area is not changing, this quantity will remain relatively constant throughout a bit's life. The frictional component is associated with contact of the bit with the bottom of the wellbore; typically referring to the sliding of the wear-flat along the formation behind the cutting surface. This contact area will increase as the bit is being used. As the bit drills, the wear-flat is continuously eroded, so at some point it will be impossible to supply enough torque to the bit to adequately drill through the formation. In order to measure the contribution of the frictional component separately from the cutting component, multiple bits with various wear-flat areas must be tested. As previously alluded to, by doing this one should be able to see a trend as the wear-flat area increase; there will be a constant torque component that is always present (due to the cutting), and there will be a frictional torque component that increases with increasing wear-flat area.

6.2. Spinning Bit with no ROP

Rotating the bit without advancing it axially will allow for the determination of the torsional fluid damping measurement. For this test, the axial torsional transducer will be removed and the lateral force measurement rods will be inserted into the inner can's torque dimples (Figure 6.3).
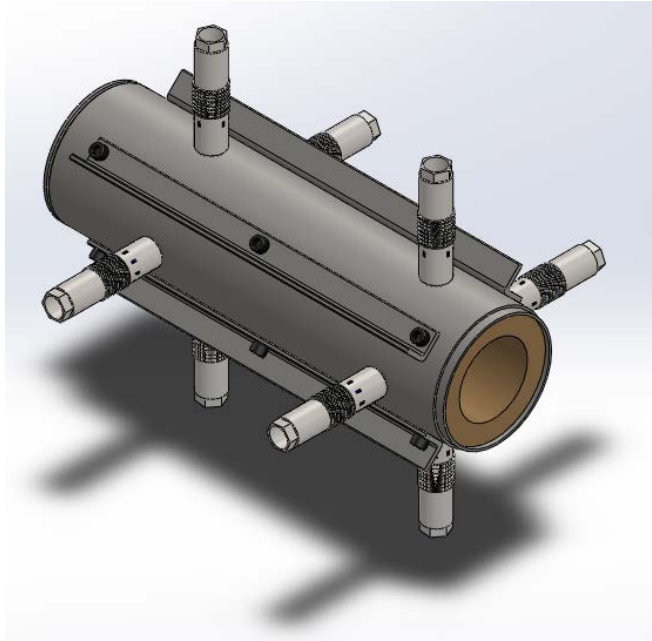
Figure 6.3:   Secondary Measurement Configuration

This test will produce a more sensitive torque reading, as the reaction torque will not be near as large as it would be for the normal drilling mode. This can be shown by following a formulation of the torque induced within a rotational viscometer, as presented by Mitchell and Miska [9], to estimate the torque that will be seen during the fluid damping testing. A rotational viscometer is a made of concentric cylinders; an internal stator and an external rotor. As the external cylinder rotates, the torque on the inner cylinder is measured and a relationship between the generated torque and the rotational speed is used to estimate fluid properties of the drilling fluid. The torsional damping coefficient test will essentially act as a rather large rotational viscometer. Thus, an estimate of the torque generated during testing can be obtained by idealizing the bit as a cylinder rotating within another cylinder (the wellbore). The torque on the bit, T_o, can be written as

$$T_{o_f} = 2\pi R_B^2 L\tau \qquad\qquad\text{Eq. 47}$$

where the fluid shear stress, τ, is a function of the yield stress, τ_y, and the shear rate, $\dot{\gamma}$, given by

$$\tau = \tau_y + \mu_p\dot{\gamma} \qquad\qquad\text{Eq. 48}$$
$$\dot{\gamma} = 4\pi\,\frac{R_w^2}{R_w^2 - R_B^2}\,\Omega \qquad\qquad\text{Eq. 49}$$

Thus, the equation for the torque becomes a function of shear stress (τ_y), plastic viscosity (μ_p), the two concentric radii (R_w and R_B), rotational speed of the bit (Ω) and the contact length (L).

$$T_{o_f} = \left[\tau_y + 4\pi\mu_p\,\frac{R_w^2}{R_w^2 - R_B^2}\,\Omega\right]2\pi R_B^2 L \qquad\qquad\text{Eq. 50}$$

where the fluid properties can be calculated as was shown for the mud pump power requirements. Now, converting for consistent units, Equation 50 becomes

$$T_{o_f} = \left[0.0579\tau_y + 5.0628\cdot 10^{-8}\pi\mu_p\,\frac{R_w^2}{R_w^2 - R_B^2}\,\Omega\right]2\pi R_B^2 L \qquad\qquad\text{Eq. 51}$$

where the yield stress is $lb_f/100ft^2$, μ_p is in cP, Ω is in RPM, and T_o is in ft-lb_f. By taking the radius of the wellbore, $R_w = 4.26$ in, to be slightly greater that the bit radius, $R_B = 4.25$ in , and the contact length to be representative of the length of the bit (10in), the torque is found to be

$$T_{o_f} =$$
$$\left[0.6944(16.2868) + 6.0753\cdot 10^{-7}\pi(33.1955)\,\frac{4.26^2}{4.26^2 - 4.25^2}\,(200)\right]2\pi 4.25^2(10)$$
$$\text{Eq. 52}$$

$$T_{o_f} = 1167.3\ ft\cdot lb_f$$

This is roughly $1/14^{th}$ of the maximum anticipated drilling torque, which is a significant reduction torque that will need to be measured. This test will be done with and without fluid circulation in order to gauge its effects.

The addition of L-beams is also seen in the figure. These are placed on the inner sample container in the event that the container was to break loose from the dimples. The safety catch rods (See Appendix B) will prevent the sample container from freely rotating and the machine can be stopped and adjusted.

6.3. Formation Side Loading

This testing will consist of two parts. The first will be pushing the formation against a stationary bit and measuring the displacement of the formation and the load applied. Doing this will give an estimate of the radial formation stiffness. Figure 6.4 display the side load deflection configuration. The applied side load, $\mathbf{F_s}$, will be measured via the force measurement rods and the relative displacement between the formation and the bit will be measured by an Eddy-Current Displacement Sensor (circled in yellow) that is capable of measuring the displacements outlined in Section 3.
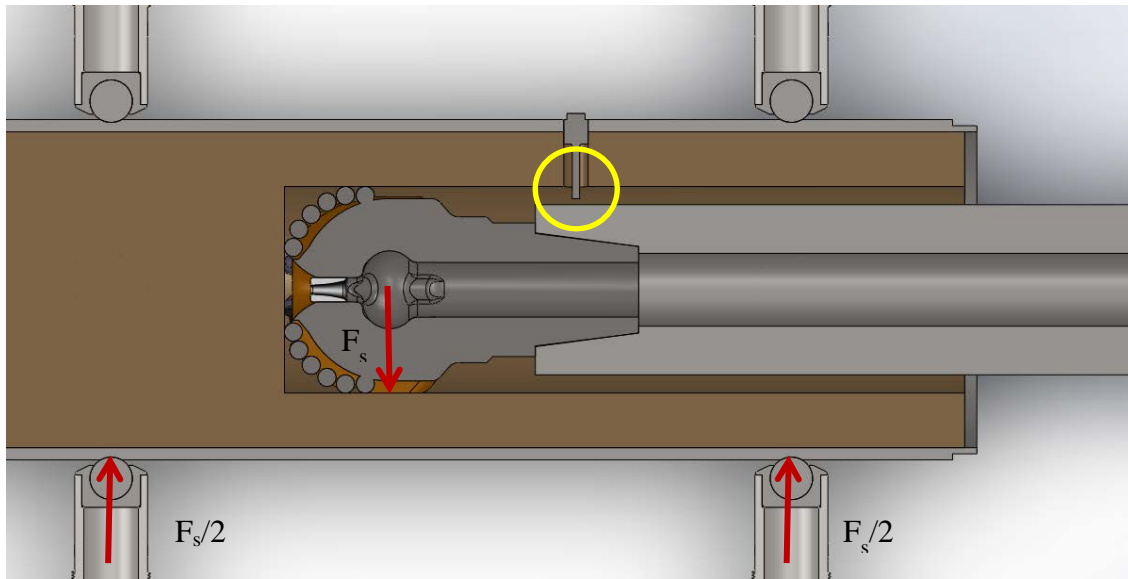
Figure 6.4:   Formation Displacement Measurement Configuration

The second test will be pushing the formation against a spinning bit; while this is done, the torque on the formation can be measure and a value of a coefficient of friction will be determined (See Figure 6.5).
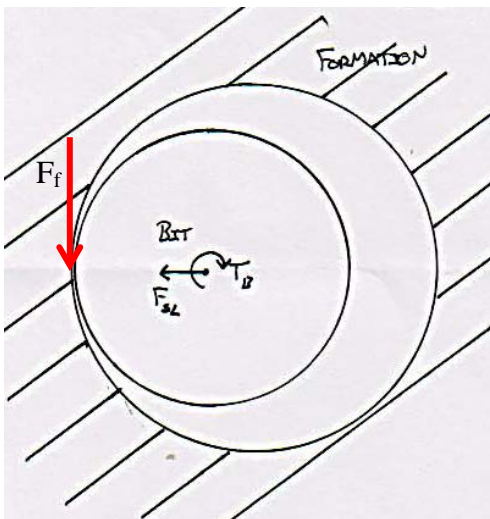
Figure 6.5:   Side Loading of Bit

6.4. Lateral Sample Actuation

The side shaking test will be used to determine the lateral fluid damping effects with and without fluid circulation or drill shaft rotation. This test will be conducted by disconnecting the bit from the shaft and actuating the formation at various frequencies.. The method of measurement will be an indirect one; through measuring the acceleration of the system and the forces on the system, a plot of accelerance (acceleration/force) can be plotted against the known excitation frequency, as shown in Figure 6.6.
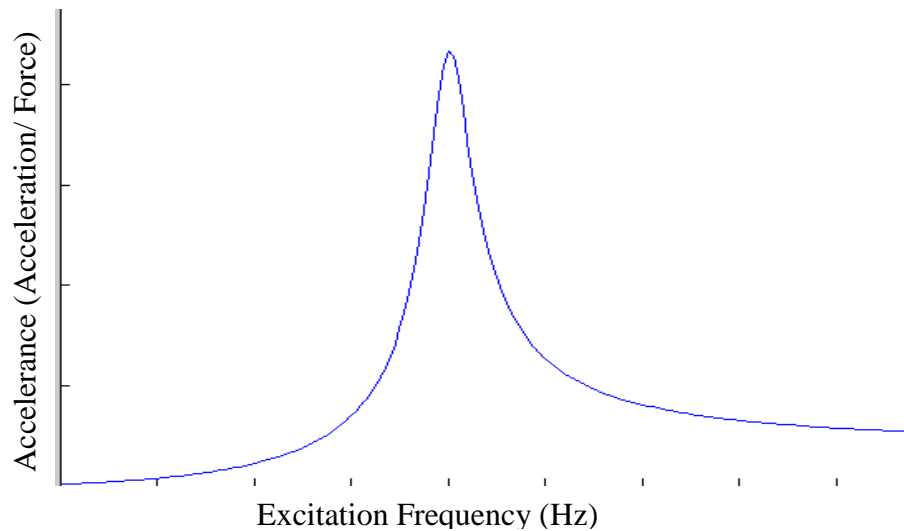
Figure 6.6:   Accelerance vs. Excitation Frequency for Side Actuation Tests

From this plot, system properties such as fluid damping and stiffness can be estimated by using established system response equations that would be typical of a vibrational analysis study.

6.5. Formation Properties

Formation properties will need to be determined for every sample that is drilled. There are two possible ways that this will be done. One would be to send a sample of each core

147

drilled to a testing lab for results, or follow the procedure presented by Adachi et al. [59] and Richard et al. [131] and test each specimen with a scratch test.

7. CONCLUSIONS AND FUTURE WORK

The objectives presented in Section 1 included designing a system that could simulate the drilling process and accurately measure the associated forces and torques on the bit in order to generate a Bit/Formation Interface Law, analyze the respective design in its entirety to confirm the system's integrity, initial testing of the measurement system to validate the feasibility of concept and finally, to propose the necessary tests required of the design to develop an accurate and reliable BFIL. A summary of the conclusions of the research are as follows:

- A test rig concept has been designed and verified through extensive analytical and numerical simulation.
- The design meets the previously laid out requirements that will allow for the proper definition of an adequate BFIL.
- Through friction testing and force measurement calibration, the force/torque measurement system has been determined to be a feasible concept by the fact that the friction coefficients are relatively small and the lateral force measurement rods generate linear outputs for applied loading. However, before the measurement system is deemed a confirmed method of data acquisition, there are more calibration tests needed; particularly, the removal of the severely sensitive gauge bridges and replace them with more accurately placed sensors.
- Methods are outlined as to how to approach the testing of the drilling rig. Proven methods of measuring fluid properties are employed to arrive at reasonable results.

A systematic approach of design was undertaken for the development of the test rig concept. A fully functioning rig design is presented in Section 2. A key feature to the rig is its ability to accommodate bits of up to 8 ½ inches in diameter. In terms of rigs designed for research purposes, this is quite large and more comparable to field

conditions. By designing a larger rig, scaling effects can be bypassed and data obtained are more closely matched to actual bit performance. The design is sectioned into 4 major components: 3 rig frame pieces and the sample containment structure. Each of these components is mounted with hoisting points for easy maneuvering on an open floor, with appropriately sized crane.

Section 3 was devoted to the analysis of the test rig design and a verification of system integrity and reliability. Analytical calculation, coupled with extensive 3D numerical simulation has proven the system to be sustainable and operational. All conceived loading scenarios have been tested and documented with verifiable certainty.

The future work of the rig consists of two paths: immediate needs of the rig and use of the rig beyond the present study. Immediate work includes a confirming calibration study of the force measurement rods in which both an axial and two transverse loads can be applied to each rod and measured. As mentioned in Section 2, due to last minute budget and location changes a reduced power rig will be assembled and used for initial testing on 3 ½ inch bits. The general assembly drawings of the design are shown, in detail, throughout Appendix B. Detailed assembly and fabrication drawings will be the focus of the work immediately following this manuscript. Much detail and thought will be given to the safety of the operator and those around as the rig is being assembled. Electronic safety shutoffs will be included in the programming if the system detects a malfunctioning component.

Giving thought to the rig's use beyond the bounds of the present study, the next course of investigation should be expanding the rig to include in-situ wellbore conditions. While the data obtained from the test rig will be significant to vibrational analysis, it must be understood that the confining pressure surrounding a formation and the pore pressure of the fluids contained within a reservoir can greatly impact the effective

strength of the formation being drilled. The effects of confining and pore pressure typically affect the rock in two ways [132, 133]:

1. Greater confining pressure typically increases the effective strength of the formation, thereby decreasing the rate of penetration.
2. The failure mechanism of the formation has been known to change from a brittle-like behavior to one that exhibits ductile properties, depending on the pressures seen in the formation.

The latter is of less interest as it can be encompassed within the former. The point here is that the formation strength of the sample being drilled with the test rig must encompass the broad spectrum of formation yield strengths. The key to testing will be to test drilling rates based on overall formation strengths; i.e. the interface relations that are developed with the rig should be a function of the drilling strength of the formation. This can be done by using extremely high strength, oil-field cements if formations are unavailable. Alternatively, lover strength materials can be tested with the current rig design and as a later course of study could be the expansion of the rig to verify that the same trends observed previously, hold true for higher formation strengths.

The drilling strength has been commonly thought of as a confined compressive strength of the formation. Caicedo et al. [75] presents an equation that relates the confined compressive strength (**CCS**) to the surrounding formation pressures and the unconfined compressive strength (**UCS**) in the following way.

$$CSS = UCS + DP + \frac{2(DP)\sin(FA)}{1 - \sin(FA)}$$

Eq. 53

Where **DP** = (Equivalent Circulating Density) - (Pore pressure) and **FA** is the internal friction angle of the rock. Ultimately, there exist relations for the **CCS** as functions of pressure for different formations (permeable and impermeable) but it is up to the rig

operator to test formations and/or cements with the appropriate strengths. To give the reader some insight into how formation pressures can affect the yield strength, Figure 7.1 and Figure 7.2 are shown as presented by Robinson.
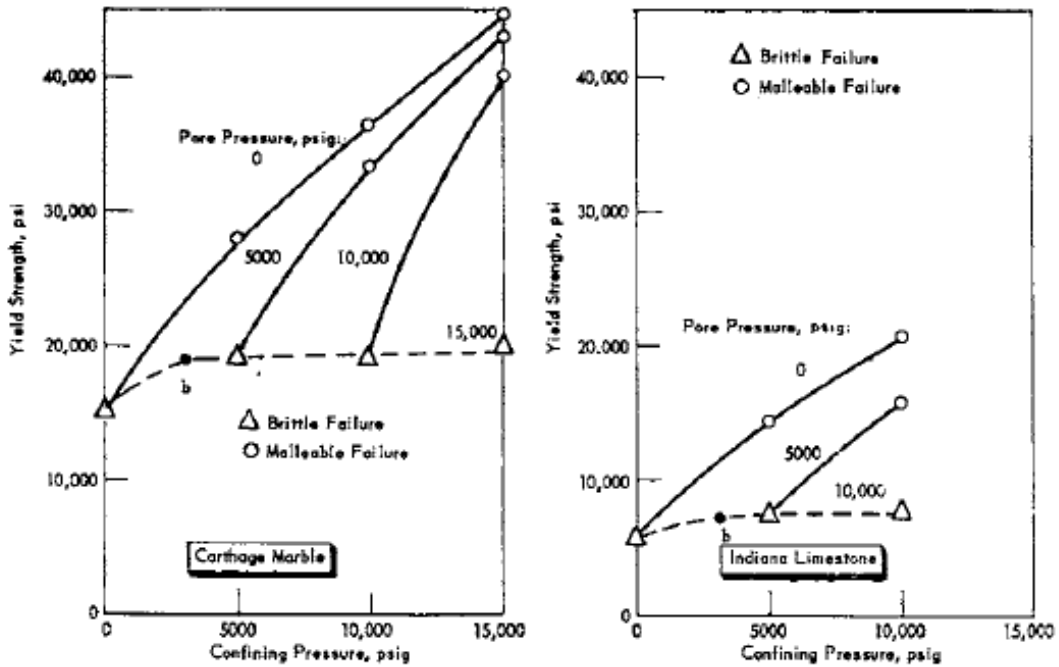

Figure 7.1: **Yield Strength vs. Confining Pressure for Limestone (From [133])**
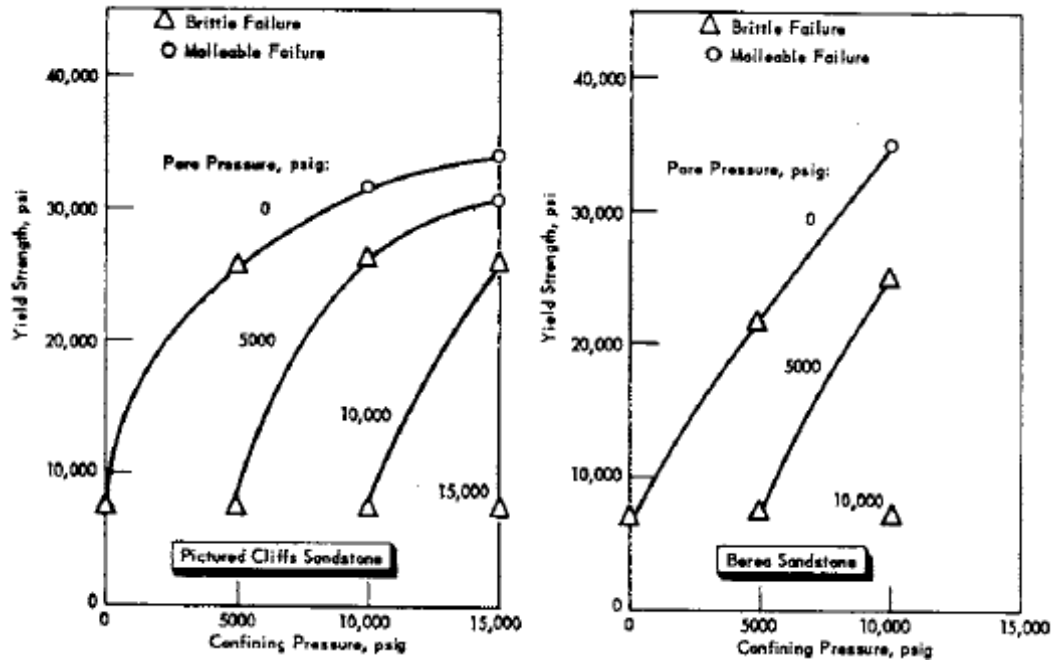
Figure 7.2: **Yield Strength vs. Confining Pressure for Sandstone (From [133])**

REFERENCES

1. Cheng, L.T., D.; Peng, W., *An experimental rig for near-bit force measurement and drillstring acoustic transmission of BHA.* Measurement, 2011. **44**: p. 642-652.

2. Gao, L.F., D.; Gardner, W.; Robbins, C.; Linyaev, E.; Moore, J.; Memarzadeh, M.; Johnson, D., *Acoustic Telemetry Can Deliver More Real-Time Downhole Data in Underbalanced Drilling Operations*, in *IADC/SPE Drilling Conference*2006: Miami, Florida.

3. Freudenrich, C.S., J. *How Oil Drilling Works*. 2001 [cited 2012 Nov 27th]; Available from: http://science.howstuffworks.com/environmental/energy/oil-drilling4.htm.

4. Eastman, H.J. *The Latest Developments and Acheivements of Directional Drilling in the Exploitation of Oil Fields*. in *Proceedings Third World Petroleum Congress - Section II*. 1951. The Hague, The Netherlands.

5. Joshi, S.D., *Cost/Benefits of Horizontal Wells*, in *SPE Wastern Regional/AAPG Pacific Section Joint Meeting,* 2003: Long Beach, CA.

6. Agrawal, A.W., Y.; Holditch, S.A., *A Technical and Economic Study of Completion Techniques in Five Emerging US Gas Shales: A Woodford Shale Example.* SPE Drilling and Completion, 2012. **27**: p. 39-49.

7. Sonowal, K.B., M.; Wong, P.; Isevcan, E., *How Continuous Improvement Lead to the Longest Horizontal Well in the World*, in *SPE/IADC Drilling Conference and Exhibition,* 2009, SPE: Amsterdam, The Netherlands.

8. Jacobsen Plutt, L.A.P., A.L.; Pardo, N.O.; Rodriguez, E.M., *Achieving Improved Performace Through Drilling Optimization and Vibration Management at a GoM Development Project*, in *APE/IADC Drilling Conference and Exhibition,* 2009, SPE/IADC: Amsterdam, The Netherlands.

9.   Mitchell, R.F.M., S. Z., *Fundamentals of Drilling Engineering*. SPE Textbook Series, ed. S.o.P. Engineers. 2011, Richardson, TX: Society of Petroleum Engineers. 696.

10.   Cobern, M.E.W., M.E., *Laboratory Testing of an Active Drilling Vibration Monitoring & Control System*, in *AADE National Technical Conference and Exhibition*2005: Houston, TX.

11.   Esmaeili, A.E., B.; Fruhwirth, R.K.; Thonhauser, G., *Laboratory Scale Control of Drilling Parameters to Enhance Rate of Penetration and Reduce Drill String Vibration*, in *SPE Saudi Arabia Section Technical Symposium and Exhibition*, S.o.P. Engineers, Editor 2012: Al-Khobar, Saudi Arabia.

12.   Yaveri, M.D., K.; Kalbhor, H., *Solution to the Down Hole Vibrations During Drilling*, in *SPE International Conference and Exhibition*2010: Tinapa-Calabar, Nigeria.

13.   Jain, J.R.L., L.W.; Hoffmann, O.J.; Schwefe, T.; Fuselier, D.M., *Mitigation of Torsional Stick-Slip Vibrations in Oil Well Drilling through PDC Bit Design: Putting Theories to the Test*, in *SPE Annual Technical Conference and Exhibition*2011, SPE: Denver, CO, USA.

14.   Brett, J.F., *The Genesis of Torsional Drillstring Vibrations*. SPE Drilling Engineering, 1992. **7**: p. 168-175.

15.   Halsey, G.W.K., A.; Aarrestad, T.V.; Lysne, D., *Drillstring Torsional Vibrations: Comparison Between Theory and Experiment on a FUll-Scale Research Drilling Rig*, in *61st Annual Technical Conference and Exhibition*1986: New Orleans, LA.

16.   Khulief, Y.A.A.-S., F.A.; Bashmal, S., *Vibration Analysis of Drillstrings with Self-Excited Stick-Slip Oscillations*. Journal of Sound and Vibration, 2007. **299**: p. 540-558.

17.   Mihajlovic, N.v.V., A.A.; van de Wouw, N.; Nimeijer, H., *Analysis of Friction-induced Limit Cycling in an Experimental Drill-String System*. Journal of Dynamic Systems, Measurement, and Control, 2004. **126**: p. 709-720.

18.   Richard, T.D., E. *Stick-Slip Vibrations of PDC Bits*. in *Proceedings of the 4rth North American Rock Mechanics Symposium*. 2000. Pacific Rocks.

19.   Dareing, D.T., J.; Zamudio, C., *Self-Excited Vibrations Induced by Drag Bits.* Transactions of the ASME, 1990. **112**: p. 54-61.

20.   Karkoub, M.A.-M., Y.L.; Balachandran, B., *Drill-String Torsional Vibration Suppression Using GA Optimized Controllers.* Journal of Canadian Petroleum Technology, 2009. **48**(12): p. 32-41.

21.   Pavone, D.R.D., J.P., *Application of High Sampling Rate Downhole Measurements for Analysis and Cure of Stick-Slip in Drilling*, in *69th Annual Technical Conference*1994, SPE: New Orleans, LA.

22.   Richard, T.G., C.; Detournay, E., *Self-Excited Stick-Slip Oscillations of Drill bits.* Acadmeie des Sciences, 2004. **332**: p. 619-626.

23.   Richard, T.G., C.; Detournay, E., *A simplified model to explore the root cause of stick-slip vibrations in drilling systems with drag bits.* Journal of Sound and Vibration, 2007. **305**: p. 432-456.

24.   Tucker, R.W.W., C., *On The Effective Control of Torsional Vibrations in Drilling Systems.* Journal of Sound and Vibration, 1999. **224**(1): p. 101-122.

25.   Besselink, B.W., N.; Nijmeijer, H., *A Semi-Analytical Study of Stick Slip Oscillations in Drilling Systems.* Journal of Computational and Nonlinear Dynamics, 2011. **6**: p. 1-9.

26.   Leine, R.I.V.C., D.H.; Keultjes, W.J.G., *Stick-Slip Whirl Interaction in Drillstring Dynamics.* Journal of Vibration and Acoustics, 2002. **124**: p. 209-220.

27.   Spanos, P.D.P., M.L.; Secora, C.K., *Bottom-Hole Assembly Modeling and Dynamic Response Determination.* Journal of Energy Resources Technology, 1997. **119**: p. 153-158.

28.   Yigit, A.S.C., A.P., *Coupled Torsional and Banding Vibrations of Drillstrings Subject to Impact With Friction.* Journal of Sound and Vibration, 1998. **215**(1): p. 167-181.

29.   Dareing, D.L., B.J., *Longitudinal and Angular Drill-String Vibrations With Damping.* Journal of Engineering for Industry, 1968. **90**(4): p. 671-679.

30.   Wu, X.K., V.; Nagaraj, V.; Partin, U.; Machado, M.; Franco, M.; Duvvuru, H., *Identifying the Root Cause of Drilling Vibration and Stick-Slip Enables Fit-for-Purpose Solutions*, in *IADC/SPE Drilling Conference and Exhibition*2012: San Diego, California.

31.   Heisig, G.N., M., *Lateral Drillstring Vibrations in Extended-Reach Wells*, in *2000 IADC/SPE Drilling Conference*2000: New Orleans, LA.

32.   Hsu, F.W., Jr., J.C., *Lateral Vibration of Drill Pipe Including Wall Reaction*, in *Conference on Drilling and Rock Mechanics*1965: Austin, TX. p. 41-48.

33.   Sadiq, T., *Experimental Investigation of Lateral Contact Force in Horizontal and Directional Wells, A Thesis*, in *Petroleum Engineering*1995, Texas A&M University. p. 152.

34.   Gao, G.M., S., *Dynamic Buckling and Snaking Motion of Rotating Drilling Pipe in a Horizontal Well*, in *2008 SPE Annual Technical Conference and Exhibition*, S. International, Editor 2008: Denver, CO.

35.   Kotsonis, S.J., *Effects of axial forces on drillstring lateral vibrations, A Thesis*, in *Mechanical Engineering*1994, Rice University: Houston, TX.

36.   Kotsonis, S.J.S., P.D., *Chaotic and Random Whirling Motion of Drillstrings.* Journal of Energy Resources Technology, 1997. **119**: p. 217-222.

37.   Christforou, A.P.Y., A.S., *Fully Coupled Vibrations of Actively Controlled Drillstrings.* Journal of Sound and Vibration, 2003. **267**: p. 1029-1045.

38.   Liao, C.M.B., B.; Karkoub, M.; Abdel-Magid, Y.L., *Drill-String Dynamics: Reduced-Order Models and Experimental Studies.* Journal of Vibration and Acoustics, 2011. **133**: p. 1-8.

39.   Germay, C.V.d.W., N.; Nijmeijer, H.; Sepulchre, R., *Nonlinear Drillstring Dynamics Analysis.* Journal of Applied Dynamical Systems, 2009. **8**(2): p. 527-553.

40. Zamudio, C.A.T., J.L.; Dareing, D.W., *Self-Excited Vibrations in Drillstrings*, in *62nd Annual Technical Conference*1987, SPE: Dallas, TX.

41. Elsayed, M.A.D., D.W.; Dupay, C.A., *Effect of Downhole Assembly and Polycrystalline Diamond Compact (PDC) Bit Geometry on Stability of Drillstrings.* Journal of Energy Resources Technology, 1997. **119**: p. 159-163.

42. Spanos, P.D.S., A.K.; Cunningham, R.A.; Paslay, P.R., *Modeling of Roller Cone Bit Lift-Off Dynamics in Rotary Drilling.* Journal of Energy Resources Technology, 1995. **117**: p. 197-207.

43. Detournay, E.D., P., *A Phenomenological Model for the Drilling Action of Drag Bits.* International Journal of Rock Mechanics, 1992: p. 13-23.

44. Cheatham, J.B.D., W.H., *A Study of Factors Influencing the Drillability of Shales: Single Cutter Experiments With STRTAPAX Drill Blanks.* Journal of Energy Resources Technology, 1979. **101**: p. 189-195.

45. Gray, K.E.A., F.; Gatlin, Carl, *Two-Dimensional Study of Rock Breakage in Drag-Bit Drilling at Atmosperic Pressure.* Journal of Petroleum Technology, 1962. **14**(1): p. 93-98.

46. Swenson, D.V.W., D.L.; Jones, A.K., *Analytical and Experimental Investigations of Rock Cutting Using Polycrystalline Diamond Compact Drag Cutters*, in *56th Annual Fall Technical Conference and Exhibition*, SPE, Editor 1981: San Antonio, TX.

47. Adams, G.G., *Self-Excited Oscillations of Two Elastic Half Spaces Sliding with Constant Coefficient of Friction.* Journal of Applied Mechanics, 1995. **62**: p. 867-872.

48. Adams, G.G., *Steady Sliding of Two Elastic Half-Spaces With Friction Reduction due to Interface Stick-SLip.* Transactions of the ASME, 1998. **65**: p. 470-475.

49. Moirot, F.N., Q., *An example of stick-slip waves.* Transactions of the [French} Academy of Sciences, 2000. **328**(9): p. 663-669.

50. Moirot, F.N., Q.; Oueslati, A., *An example of stick-slip and stick-slip-seperation waves.* European Journal of Mechanics A/Solids, 2002. **22**: p. 107-118.

51. Simoes, F.M.F.M., J.A.C., *Instability and ill-posedness in some friction problems.* International Journal of Engineering Science, 1998. **36**: p. 1265-1293.

52. Detournay, E.R., T.; Shepherd, M., *Drilling Response of Drag Bits: Theory and Experiment.* International Journal of Rock Mechanics & Mining Sciences, 2008. **45**: p. 1347-1359.

53. Fairhurst, C.L., W.D. *Some Priciples and Developments in Hard Rock Drilling*. in *Sixth Annual Drilling and Blasting Symposium*. 1956. University of Minnesota, Minneapolis, Minnesota: The University of Minnesota.

54. Franca, L.F.P., *Drilling Action of Roller-Cone Bits: Modeling and Experimental Validation.* Journal of Energy Resources Technology, 2010. **132**: p. 1-9.

55. Franca, L.F., *A Bit-Rock Interaction Model for Roatry -Percussive Drilling.* International Journal of Rock Mechanics & Mining Sciences, 2011. **48**: p. 827-835.

56. Weeden, R.W.W., S.; Lugo, F.; Gaduan, P., *Cutting Carbonates - New Technology Delivers Step Changes in Bit Performance*, in *SPE/IADC Drilling Conference and Exhibition*2011: Amsterdam, The Netherlands.

57. Alehossein, H.D., E.; Huang, H., *An Analytical Model for the Indentation of Rocks by Blunt Tools.* Rock Mechanics and Rock Engineering, 2000. **33**(4): p. 267-284.

58. Huang, H.D., B.; Detournay, E., *Normal Wedge Indentation in Rocks with Lateral Confinement.* Rock Mechanics and Rock Engineering, 1998. **31**: p. 81-94.

59. Adachi, J.I.D., E.; Drescher, A., *Determination of rock strength parameters from cutting tests*, in *2nd North American Rock Mechanics Symposium*1996: Montreal, Quebec, Canada. p. 1517-1523.

60. Guo, H.A., N.I.; Schmidt, L.C., *Rock Cutting Study Using Linear Elastic Fracture Mechanics.* Engineering Fracture Mechanics, 1992. **41**(5): p. 771-778.

61. Murphy, D.M., D.; Gilmour, J.;Tetley, N.; Centala, P.; Iwere, E., *Deepwater Drilling in Both Hard and Abrasive Formations: The Continuing Challenge of*

Bit Optimization, in *North Africa Technical Conference and Exhibition*2012: Cairo, Egypt.

62.   Centala, P.B., M.; Burnett, T.; Ford, R.; Sinesi, J., *Unlocking Two-Cone-Bit Potential: Technology, People, and Planning Make it Possible and Lessons Learned*, in *IADC/SPE Drilling Conference*2006: Miami, Florida.

63.   Pessier, R.C.D., M., *Hybrid Bits Offer Distinct Advantages in Sleected Roller Cone and PDC Bit Applications*, in *IADC/SPE Drilling Conference and Exhibition*2010, IADC/SPE: New Orleans, Louisiana.

64.   Franca, L.F.M., A. *Estimation of the Rock Strength While Drilling with Roller-Cone Bits*. in *ISRM International Symposium*. 2008. Tehran, Iran: 5th Asian Rock Mechanics Symposium (ARMS5).

65.   Jaggi, A.U., S.; Chowdhury, A.R., *Succesful PDC/RSS Vibration Management Using Innovative Depth-of-Cut Control Technology: Panna Field, Offshore India*, in *SPE/IADC Drilling Conference*, SPE, Editor 2007: Amsterdam, The Netherlands.

66.   Hareland, G.W., A.; Rashidi, B., *A Drilling Rate Model for Roller Cone Bits and It's Applications*, in *CPS/SPE International Oil & Gas Conference and Exhibition*, SPE, Editor 2010, SPE: Beijing, China.

67.   Hoberock, L.L.B., G.J., *A New Approach for Determining In-Situ Rock Strength While Drilling*. Journal of Energy Resources Technology, 1996. **118**: p. 249-255.

68.   Rampersad, P.R.H., G.; Boonyapaluk, P., *Drilling Optimization Using Drilling Data and Available Technology*, in *Latin American/Caribean Petroleum Engineering Conference*1994: Buenos Aires, Argentina.

69.   Rashidi, B.H., G.; Wu, A., *New Approach in Mechanical Modeling of inserts of the Rollercone Bits*, in *46th US Rock Mechanics/Geomechanics Symposium*2010: Chicago, IL.

70.   Warren, T.M., *Factors Affecting Torque for a Roller Cone Bit.* Journal of Petroleum Technology, 1984. **36**(9): p. 1500-1508.

71. Warren, T.M., *Penetration-Rate Performance of Roller-Cone Bits.* SPE Drilling Engineering, 1987. **2**(1): p. 9-18.

72. Winters, W.J.W., T.M.; Onyia, E.C., *Roller Bit Model With Rock Ductility and Cone Offset*, in *62nd Annual Technical Conference and Exhibition of the Society of Petroleum Engineers*1987: Dallas, TX.

73. Black, A.D.W., B.H.; Tibbitts, G.A.; Sandstrom, J.L., *PDC Bit Performance for Rotary, Mud Motor, and Turbine Drilling Applications.* SPE Drilling Engineering, 1986. **1**(6): p. 409-416.

74. Mensa-Wilmot, G.K., T.; Stephan, I., *Dual Torque Concept Enhances PDC Bit Efficiency in Directional and Horizontal Drilling Programs*, in *SPE/IADC Drilling Conference*1999: Amsterdam, Holland.

75. Caicedo, H., W. Calhoun, and R. Ewy. *Unique ROP Predictor Using Bit-Specific Coefficient of sliding Friction and Mechanical Efficiency as a Function of Confined Compressive Strength Impacts Drilling Performance*. in *SPE/IADC Drilling Conference*. 2005. Amsterdam: SPE/IADC.

76. Kelessidis, V.C.M., R.; Tsamantaki, C.; Aspirtakis, Y., *Optimal determination of rheological parameters for Herschel-Bulkley drilling fluids and impact on pressure drop, velocity profiles and penetration rates during drilling.* Journal of Petroleum Science and Engineering, 2006. **53**: p. 203-224.

77. Mohan, K.A., F.; Samuel, R., *Tracking Drilling Efficiency Using Hydro-Mechanical Specific Energy*, in *SPE/IADC Drilling Conference and Exhibition*2009: Amsterdam, The Netherlands.

78. Mostofi, M.R., V., *An Estimation of Rock Strength Using a Drilling Performance Model: A Case Study in Blacktip Field, Austrailia.* Rock Mechanics and Rock Engineering, 2011. **44**: p. 305-316.

79. Pessier, R.C. and M.J. Fear. *Quantifying Common Drilling Problems with Mechanical Specific Energy and a Bit-Specific Coefficient of Sliding Friction*. in *67th Annual Technical Conference and Exhibition of the Society of Petroleum Engineers*. 1992. Washington, D.C.: SPE Inc.

80.   Pessier, R.W., S.; Oueslati, H., *Drilling Performance is a Function of Power at the Bit and Drilling Efficiency*, in *IADC/SPE Drilling Conference and Exhibition*2012: San Diego, California.

81.   Xu, H.H., T.; Yonezawa, T.;Suzuki, A., *Evaluation of Bit Performance Using an Advanced Drilling-Test-System*, in *IADC/SPE Asia Pacific Drilling Conference*1998, SPE: Jakarta, Indonesia.

82.   Teale, R., *The Concept of Specific Energy in Rock Drilling.* International Journal of Rock Mechanics and Mining, 1964. **2**: p. 57-73.

83.   Lubinski, A.W., H.B., *Factors Affecting the Angle of Inclination and Dog-Legging in Rotary Bore Holes.* Drilling and Production Practice - American Petroleum Institute, 1953: p. 222-250.

84.   Bai, C.X., Q., *Stability analysis of liquid hydrogen turbopump-seal rotor system with internal damping.* Aircraft Engineering and Aerospace Technology: An International Journal, 2011. **83**(1): p. 8-13.

85.   Fritz, R.J., *The Effects of an Annular Fluid on the Vibrations of a Long Rotor, Part 1-Theory.* Journal of Basic Engineering, 1970. **92**(4): p. 923-929.

86.   Fritz, R.J., *The Effects of an Annular Fluid on the Vibrations of a Long Rotor, Part 2-Test.* Journal of Basic Engineering, 1970. **92**(4): p. 930-937.

87.   Muszynska, A., *Stability and Whip in Rotor/Bearing Systems.* Journal of Sound and Vibration, 1988. **127**(1): p. 49-64.

88.   Muszynska, A.B., D.E., *Frequency-Swept Rotating Input Perturbation Techniques and Identification of the Fluid Force Models in Rotor/Bearing/Seal Systems and FLuid Handling Machines.* Journal of Sound and Vibration, 1990. **143**: p. 103-124.

89.   Cunningham, R.A., *Analysis of Downhole Measurements of Drill String Forces and Motions.* Transactions of the ASME, 1968. **90**(2): p. 208-216.

90.   Bailey, J.R.B., E.A.O.; Gupta, V., *Drilling Vibrations Modeling and Field Validation*, in *IADC/SPE Drilling Conference*2008: Orlando, Florida.

91.   Bailey, J.R.R., S.M., *Managing Drilling Vibrations Through BHA Design Optimization*, in *International Petroleum Technical Conference*2009: Doha, Qatar. p. 458-471.

92.   Bailey, J.R.W., L.; Tenny, M.J.; Armstrong, M.; Zook, J.R.; Elks, W.C., *Design Tools and Workflows to Mitigate Drilling Vibrations*, in *SPE Annual Technical Conference and Exhibition*, SPE, Editor 2010: Florence, Italy.

93.   D'Ambrosio, P.B., R.R.; Clarke, A.; Laird, J.; McKay, J.; Edwards, S.T., *Distributed Dynamics Feasibility Study*, in *IADC/SPE Drilling Conference and Exhibition*2012: San Diego, CA.

94.   Davis, J.E.S., G.F.; Bolivar, N.; Pastusek, P.E., *Eliminating Stick-Slip by Managing Bit Depth of Cut and Minimizing Variable Torque in the Drillstring*, in *SPE/IADC Drilling Conference and Exhibition*2012: San Diego, California.

95.   Mensa-Wilmot, G.J., B.; Aggarwal, L.; Van Luu, H.; Rueda, F., *Gage Design - Effects of Gage Pad Length, Geometry and Activity (Side Cutting) on PDC Bit Stability, Steerability, and Borehole Quality in Rotary Steerable Drilling Applications*, in *IADC/SPE Drilling Conference*2006: Miami, Florida.

96.   Mensa-Wilmot, G.M., B.; Al-Saeedi, M.; Sounderrajan, M.; Al-Enezi, D.; Al-Khaldi, M., *Innovative Design Processes and Technologies Improve PDC Bit Performance in Harsh Drilling Enviornments*, in *IADC/SPE Asia Pacific Drilling Technology Conference and Exhibition*2006: Bangkok, Thailand.

97.   Perrin, V.P.M.-W., G.; Alexander, W.L., *Drilling Index - A New Approach to bit Performance Evaluation*, in *SPE/IADC Drilling Conference*1997, SPE: Amsterdam, the Netherlands.

98.   Macini, P.M., M.; Da Dalt, G.; Valente, P., *Bit Performance Evaluation Revisited by Means of Bit Index and Formation Drillability Catalogue*, in *SPE/IADC Middle East Drilling Technolgy Conference and Exhibition*2007: Cairo, Eqypt.

99.   Barton, S.C., K.; Nwachukwu, D.; Cozon, B.; Marinho, C.; Solarin, A., *Bit Selection Using Mathematically Modeled Indices Deliver Significant*

Improvement in Directional Drilling Performance, in *Offshore Technology Conference*2009: Houston, Texas.

100.   Clegg, J.B., S., *Improved Optimisation of Bit Selection Using Mathematically Modelled Bit-Performance Indices*, in *Asia Pacific Drilling Technology Conference and Exhibition*2006: Bangkok, Thailand.

101.   Macini, P.M., M.; Valente, P., *Drill-Bit Catalog and Bit Index: A New Method for bit Performance Evaluation*, in *SPE Latin American and Caribbean Petroleum Engineering Conference*2005: Rio de Janeiro, Brazil.

102.   Gray, K.E., *Some Current Rock-Mechanics Research Related to Oil-well Drilling*, in *Spring Meeting of the Southwestern District, API Division Production*1967. p. 82-99.

103.   Andreev, G.E., *Brittle Failure of Rock Materials: Test Results and Contitutive Models*. 1995, Rotterdam, Brookfield: A.A. Balkema.

104.   Yasar, E.R., P.G.; Viete, D.R., *An Experimental investigation into the Drilling and Physio-Mechanical Properties of a Rock-like Brittle Material.* Journal of Petroleum Science and Engineering, 2011. **76**: p. 185-193.

105.   McCormick, J.L., G., *Torque and Drag Modeling Advanced Techniques and Troubleshooting*, in *SPE Annual Technical Conference and Exhibition*2012: San Antonia, TX.

106.   Judzis, A.B., R.G.; Curry, D.A.; Black, A.D.; Robertson, H.A.; Meiners, M.J.; Grant, T.C., *Optimization of Deep Drilling Performance : Benchmark Testing Drives ROP Improvements for Bits and Drilling Fluids*, in *SPE/IADC Drilling Conference*2007: Amsterdam, The Netherlands.

107.   January 2, 2012]; Available from: http://ffden-2.phys.uaf.edu/211_fall2010.web.dir/Jared_Boerger/Technique.html.

108.   Banabihakir, K.U.R.M., *Priciples of Rock Drilling*. 1998, Rotterdam; Brookfield, Vt.: Balkema.

109.   Lama, R.D.V., V.S., *Handbook on Mechanical Properties of Rocks - Testing Techniques and Results - Volume II*. 1978, Clausthal, Germany: Trans Tech Publications.

110.   Lama, R.D.V., V.S., *Handbook on Mechanical Properties of Rocks - Testing Techniques and Results - Volume III*. 1978, Clausthal, Garmany: Trans Tech Publications.

111.   Lama, R.D.V., V.S., *Handbook on Mechanical Properties of Rocks - Testing Techniques and Results - Volume IV*. 1978, Clausthal, Germany: Trans Tech Publications.

112.   Vutukuri, V.S.L., R.D.; Saluja, S.S, *Handbook on Mechanical Properties of Rocks - Testing Techniques and Results - Volume I*. Vol. 1. 1974, Clausthal, Germany: Trans Tech Publications.

113.   Galle, E.M.W., H.B., *Best Constant Weight and Rotary Speed for Rotary Rock Bits*. Drilling and Production Practice, 1963: p. 48-73.

114.   Kennedy, J.L., *Fundamental of Drilling - Technology and Economics*. 1983, Tulsa, oklahoma: Penn Well Publishing Company.

115.   Nguyen, J.P., *Drilling - Oil and Gas Field Development Techniques*. 1996, Paris, France: Editions Technip.

116.   Cooper, B.G., T.F., *North Sea Oil - The Great Gamble*. 1966, London, England: William Heinemann Ltd., London, England.

117.   Caldwell, D.H.B., H.E., *Flow of Muds, Sludges, and Suspensions in Circular Pipe*. Industrial and Engineering Chemistry, 1941. **33**(2): p. 249-256.

118.   Demirdal, B. and J.C. Cunha. *Rheological and Volumetric Characterization to Plan and Optimize Managed Pressure Drilling Operations*. in *Petroleum Society's 7th Canadian International Petroleum Conference*. 2006. Calgary, Alberta, Canada: Canadian International Petroleum Conference.

119.   Fredrickson, A.G.B., R.B., *Non-Newtonian Flow in Annuli*. Industrial and Engineering Chemistry, 1958. **50**(3): p. 347-352.

120.   Laird, W.M., *Slurry and Suspension Transport, Basic Flow Studies on Bingham Plastic Fluids.* Industrial and Engineering Chemistry, 1957. **49**(1): p. 138-141.

121.   White, F.M., *Fluid Mechanics, Fourth Edition*. 1999, Singapore: WCD/McGraw-Hill.

122.   Colebrook, C.F., *Turbulent Flow in Pipe, with Particular Reference to the Transition Region Between the Smooth and Rough Pipe Laws.* Instituion Journal, 1939. **11**(4): p. 133-161.

123.   Economides, M.J.H., D.A.; Ehlig-Economides, C.; Zhu, D., *Petroleum Production Systems, 2nd Edition*. 2012: Prentice Hall.

124.   Hanks, R.W., *The Laminar-Turbulent Transition for Flow in Pipes, Concentric Annuli, and Parallel Plates.* A.I.Ch.E. Journal, 1963. **9**(1): p. 45-48.

125.   Hanks, R.W.P., D.R., *On the Flow of Bingham Plastic Slurries in Pipes and Between Parallel Plates.* Society of Petroleum Engineers Journal, 1967. **7**(4): p. 342-346.

126.   Robinson, L. *Drill Bit Nozzle Pressure [Exploitation of Finagle Factor Technology]*. in *AADE Fluids Conference and Exhibition*. 2010. Houston, TX: AADE.

127.   Kurowski, P.M., *Engineering Analysis with Solidworks Simulation 2011*. 2011: Stephen Schroff.

128.   Reddy, J.N., *An Introduction to the Finite Element Method*. 2006, New York, NY: McGraw-Hill Higher Education.

129.   Ku, H.H., *Notes on the Use of Propogation of Error Formulas.* Journal of Research of the National Bureau of Standards - C. Engineering and Instrumentation, 1966. **70C**(4): p. 263-273.

130.   Perry, C.C.H.R.L., *The Strain Gauge Primer*. 1955, York, PA: McGraw-Hill Book Company.

131.   Richard, T.D., F.; Poyol, E.; Detournay, E., *Rock strength determination from scratch tests.* Engineering Geology, 2012. **147**: p. 91-100.

132. Kolle, J.J., *The Effects of Pressure and Rotary Speed on the Drag Bit Drilling Strength of Deep Formations*, in *SPE Annual Technical Conference and Exhibition*1996: Denver, Colorado.

133. Robinson, J., L.H., *Effects of Pore and Confining Pressures on Failure Characteristics of Sedimentary Rocks.* Petroleum Transactions, AIME, 1959. **216**: p. 26-32.

134. Burgess, T.M.L., W.G., *Measuring the Wear of Milled Tooth Bits Using MWD Torque and Weight-on-Bit*, in *SPE/IADC 1985 Drilling Conference*, SPE/IADC, Editor 1985: New Orleans, LA.

135. Puttock, M.J.T., E.G., *Elastic Compression of Spheres and Cylinders at Point and Line Contact*, in *National Standards Laboratory Technical Paper*1969, Commonwealth Scientific and Industrial Research Organization: Australia.

136. Roark, R.J.Y., W.C., *Formulas for Stress and Strain, 5th Edition*. 1965, New York, NY: McGraw-Hill, Inc.

137. Timoshenko, S.P.G.J.N., *Theory of Elasticity*. 1970, Singapore: McGraw Hill.

138. Whittemore, H.L.P., S.N., *Friction and Carrying Capacity of Ball and Roller Bearings.* Paper No. 201 - Technologiv Papers of the Bureau of Standards, 1921.

139. Hartog, J.P.D., *Advanced Strength of Materials*. 1952, Mineola, New York: The McGraw Hill Company.

140. Budynas, R.G.N., J. Keith, *Shigley's Mechanical Engineering Design, Eighth Edition*. 2008, New York, NY: The McGraw-Hill Companies.

141. Jansen, J.D., *Whirl and Chaotic Motion of Stabilized Drill Collars.* SPE Drilling Engineering, 1992. **7**(2): p. 107-114.

APPENDIX A – INTERFACE LAWS

- **Burgess and Lesso, Jr. [134]**

$$M = a_1 + a_2 \sqrt{R/Nd}$$

a_1, a_2 = dimensionless bit constant

R = rate of penetration

N = bit rotation speed

D = bit diameter

- **Dareing et al. [19]**

$$F(t) = m\frac{d}{2}Kh(t)$$

m = number of cutter edge

d = bit diameter

K = force per unit area of material being removed

$h(t)$ = time-dependent depth of cut

- **Detournay and Defourny [43]**

$$T = T_c + T_f$$
$$W = W_c + W_f$$
$$T_c = \frac{1}{2}\epsilon\delta a^2$$

$$W_f = \frac{a^2 e\mu\sigma k_2}{2}$$
$$W_c = \zeta\epsilon\delta a$$
$$W_f = ae\sigma k_1$$

T = total torque of bit

T_c = cutting component of torque

T_f = frictional component of torque

W = total weight on bit

W_c = cutting component of weight

W_f = frictional component of weight

ϵ = intrinsic specific energy of formation

δ = depth of cut per revolution

a = bit radius

e = representative contact length

μ = coefficient of friction at rock/wear flat interface

σ = normal contact stress

k_1, k_2 = calculated coefficients

ζ = ratio of drilling strength over rock strength

- **Franca and Mahjoob [64]**

$$T = T_d + T_c$$
$$W = W_d + W_c$$
$$T_d = \frac{1}{2}\epsilon a^2 d$$

$$T_c = \frac{\mu W_c a}{2}$$
$$W_d = \zeta\epsilon ad$$
$$W_c = \sigma al$$

T = total torque on bit

W = total weight on bit

T_c = contact contribution to torque (friction)

T_d = drilling component of torque

W_c = contact component of weight

W_d = drilling component of weight

ϵ = intrinsic specific energy of the rock

a = bit radius

d = depth of cut per revolution

l = contact length

σ = normal stress acting across the contact interface

ζ = ratio relating T_d to W_d

- **Germay et al. [39]**

$$F_{CS} = \varepsilon wd$$
$$F_{Cn} = \zeta F_{cs}$$

$$F_{fs} = \mu F_{fn}$$
$$F_{fn} = \sigma wl$$

F_{cs} = cutting force in the horizontal direction

F_{cn} = cutting force in the vertical direction

$\mathbf{F_{fs}}$ = frictional force in the horizontal direction

$\mathbf{F_{fn}}$ = frictional force in the vertical direction

ε = intrinsic specific energy

ζ = number characterizing cutting force

σ = wearflat parameter

$\mathbf{w}$ = cutter width

μ = coefficient of friction

$\mathbf{l}$ = wearflat length

$\mathbf{d}$ = depth of cut

- **Hareland et al. [66]**

$$ROP = K \frac{80 n_t m RPM^a}{D_b^2 \tan^2 \psi} \left(\frac{1}{C_2} \left(\frac{WOB}{100 n_t l \sigma_P} - C_1 w \right) \right)^b \left(1 - d \left(\frac{DG}{8} \right)^c \right)$$

ROP = rate of penetration

K = comprehensive coefficient

$\mathbf{n_t}$ = number of inserts in contact with the rock bottom

m = number of insert penetrations per revolution

RPM = bit rotational speed

a, b, c, d = coefficients

ψ = chip formation angle

$\mathbf{D_b}$ = bit diameter

WOB = weight on bit

$\mathbf{C_1, C_2}$ = calculated coeffieicnts

l = length of insert flat

σ_p = ultimate strength of rock at differential pressure

w = width of insert flat

DG = tooth dull grade

- **Hoberock and Bratcher [67]**

$$R^{-1} = \frac{af_c(P_e)D^3\sigma^2}{NW^2} + \frac{bf_c(P_e)}{ND} + \frac{c\rho\mu D}{I_m}$$

$\boldsymbol{\sigma}$ = in-situ effective compressive rock strength

$\mathbf{N}$ = rotary speed

$\mathbf{W}$ = weight on bit

$\mathbf{f_c\ (P_e)}$ = chip hold-down function

$\mathbf{R}$ = rate of penetration

$\mathbf{D}$ = bit diameter

$\boldsymbol{\rho}$ = mud density

$\mathbf{M}$ = mud viscosity

$\mathbf{I_m}$ = modified impact force

$\mathbf{a, b, c}$ = bit coefficients

- **Mostofi et al. [78]**

$$S = \sqrt{\frac{1}{af_c(P_e)}\left(\frac{NW^2W_f}{D^3R} - \frac{c\rho\mu NW^2}{F_{jm}D^2}\right) - \frac{bW^2}{aD^4}}$$

$\mathbf{a, b, c}$ = bit constants

$\mathbf{f_c\ (P_e)}$ = chip hold-down function

$\mathbf{R}$ = rate of penetration

$\mathbf{N}$ = rotary speed

$\mathbf{W}$ = weight on bit

$\mathbf{S}$ = formation type parameter

$\mathbf{D}$ = wellbore diameter

$\mathbf{F_{jm}}$ = modified jet impact force

$\boldsymbol{\rho}$ = mud density

$\boldsymbol{\mu}$ = mud viscosity

$\mathbf{W_f}$ = bit wear function

- **Rashidi et al. [69]**

$$F = k * Offset^a * h^b * RPM^c * \sigma^d + e$$
$$V = e^{(a_1*Offset+b_1*h+c_1*RPM+d_1*\sigma+c_1)}$$

$\mathbf{F}$ = force

$\mathbf{V}$ = generated crater volume

$\mathbf{Offset}$ = offset of the cone axis

$\mathbf{h}$ = indentation depth

$\mathbf{RPM}$ = rotary speed

$\boldsymbol{\sigma}$ = rock strength

$\mathbf{a, a_1, b, b_1, c, c_1, d, d_1, e, e_1}$ = constants

171

- **Spanos et al. [42]**

$$T = W \cos\frac{\gamma}{2}\left[\frac{4}{3}\sqrt{\frac{r_h \delta_c}{\sin\gamma}} - sign(\dot{\theta})\frac{\partial S}{\partial\varphi}\right]$$

$$\frac{\partial S}{\partial\varphi} = 3S_o \cos(3\varphi)$$

T = torque on bit

W = weight on bit

γ = basic cone angle

r_h = wellbore radius

δ_c = depth of cut per bit revolution

θ = rotation angle

$S(r,\varphi)$ = formation surface elevation variable

S_o = lobe amplitude

- **Warren [71]**

$$R = \left(\frac{aS^2 d_b^3}{N^b W^2} + \frac{c}{N d_b}\right)^{-1}$$

a, b, c = bit constants

R = penetration rate

N = bit rotation speed

W = weight on bit

d_b = bit diameter

S = Rock strength

- **Winters et al. [72]**

$$\frac{1}{R} = \frac{\sigma D^2}{NW}\left(\frac{a\sigma D\varepsilon}{W} + \frac{\varphi}{\varepsilon}\right) + \frac{b}{ND} + \frac{c\rho\mu D}{I_m}$$

R = penetration rate

σ = rock compressive strength

D = bit diameter

a, b, c = bit constants

N = bit rotation speed

W = weight on bit

ε = rock ductility

φ = cone offset coefficient

APPENDIX B – GENERAL RIG ASSEMBLY DRAWINGS

The following appendix is provided to aid in the understanding of how the rig is configured. Detailed engineering drawings of the complete rig are too numerous to include in this manuscript.
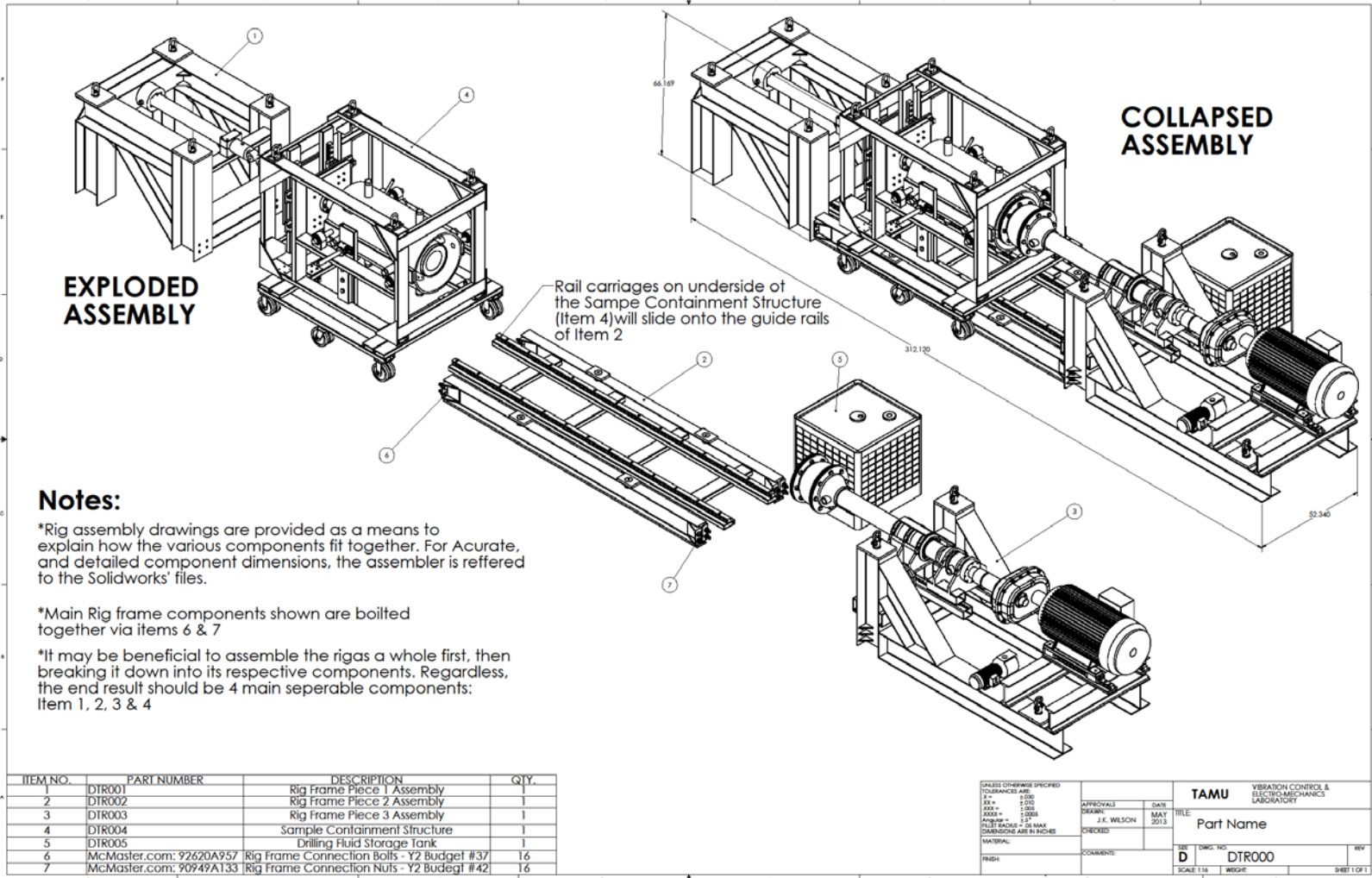
EXPLODED ASSEMBLY

COLLAPSED ASSEMBLY

Rail carriages on underside ot the Sampe Containment Structure (Item 4)will slide onto the guide rails of Item 2

Notes:

*Rig assembly drawings are provided as a means to explain how the various components fit together. For Acurate, and detailed component dimensions, the assembler is reffered to the Solidworks' files.

*Main Rig frame components shown are boilted together via items 6 & 7

*It may be beneficial to assemble the rigas a whole first, then breaking it down into its respective components. Regardless, the end result should be 4 main seperable components: Item 1, 2, 3 & 4

ITEM NO.	PART NUMBER	DESCRIPTION	QTY.
1	DTR001	Rig Frame Piece 1 Assembly	1
2	DTR002	Rig Frame Piece 2 Assembly	1
3	DTR003	Rig Frame Piece 3 Assembly	1
4	DTR004	Sample Containment Structure	1
5	DTR005	Drilling Fluid Storage Tank	1
6	McMaster.com: 92620A957	Rig Frame Connection Bolts - Y2 Budget #37	16
7	McMaster.com: 90949A133	Rig Frame Connection Nuts - Y2 Budegt #42	16

UNLESS OTHERWISE SPECIFIED
TOLERANCES ARE:
X = ±.030
.XX = ±.010
.XXX = ±.005
.XXXX = ±.0005
Angular = ±.5°
FILLET RADIUS = .05 MAX
DIMENSIONS ARE IN INCHES

MATERIAL:

FINISH:

APPROVALS   DATE
DRAWN: J.K. WILSON   MAY 2013
CHECKED:
COMMENTS:

TAMU   VIBRATION CONTROL & ELECTRO-MECHANICS LABORATORY

TITLE: Part Name

SIZE D   DWG. NO. DTR000   REV

SCALE: 1:56   WEIGHT: SHEET 1 OF 1
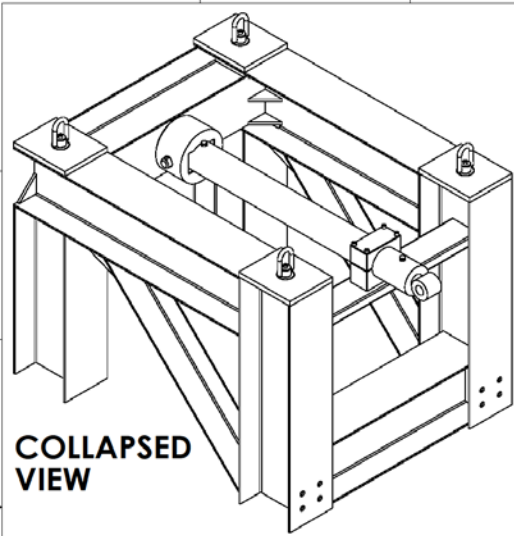
EXPLODED VIEW

The hydraulic cylinder pin must be secured with cotter pins during operation

The hydraulic cylinder latch prevents the cylinder from buckling as the axial force is applied to the sample.

The hydraulic cylinder is powered by a 3,000 psi hydraulic pump that is not shown here. It is the decision of the operator to dictate proper placement.

COLLAPSED VIEW

NOTES:

*This component of the rig is designed to handle the stresses of axial loading. The maximum operating force from the hydraulic cylinder should not exceed 55,000lbf. The design is able to withstand a 100,000 lbf load, but this is to compensate for any impact loading on the rig while drilling.

ITEM NO.	PART NUMBER	DESCRIPTION	QTY.
8	IMW-5040	Hydraulic Cylinder - Y2 Budget #1	1
12	DTR009	Hydraulic Cylinder Pin - Y2 Budget #34	1
13	DTR010	Hydraulic Cylinder Latch	1
15	DTR006	Welded Frame Piece 1	4
18	McMaster.com: 91251A015	Hydraulic Cylinder Latch Screws - Y2 Budget #49	4
19	McMaster.com: 2994T65	Hoist Rings - Y2 Budget #20	4

UNLESS OTHERWISE SPECIFIED
TOLERANCES ARE:
X = ±.030
XX = ±.010
XXX = ±.005
XXXX = ±.0005
Angular = ±.5°
FILLET RADIUS = .05 MAX
DIMENSIONS ARE IN INCHES

APPROVALS   DATE
DRAWN: J.K. WILSON   MAY 2013
CHECKED:

MATERIAL:

FINISH:

COMMENTS:

TAMU   VIBRATION CONTROL & ELECTRO-MECHANICS LABORATORY

TITLE: Rig Frame Piece 1 Assembly

SIZE: D   DWG. NO. DTR001   REV

SCALE: 1:6   WEIGH: SHEET 1 OF 1

COLLAPSED
VIEW
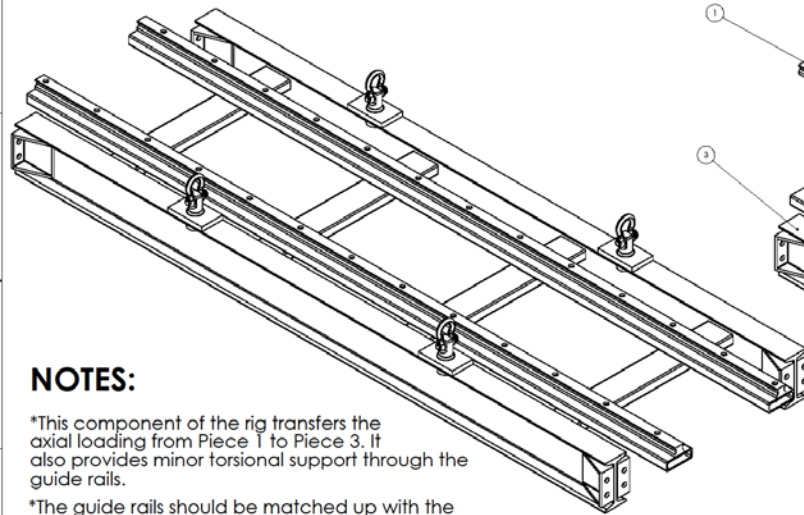
NOTES:

*This component of the rig transfers the
axial loading from Piece 1 to Piece 3. It
also provides minor torsional support through the
guide rails.

*The guide rails should be matched up with the
roller carriages on the under side of the Sample
Containment Structure before they are permanently
welded in place (tac-welding would be useful).

EXPLODED
VIEW
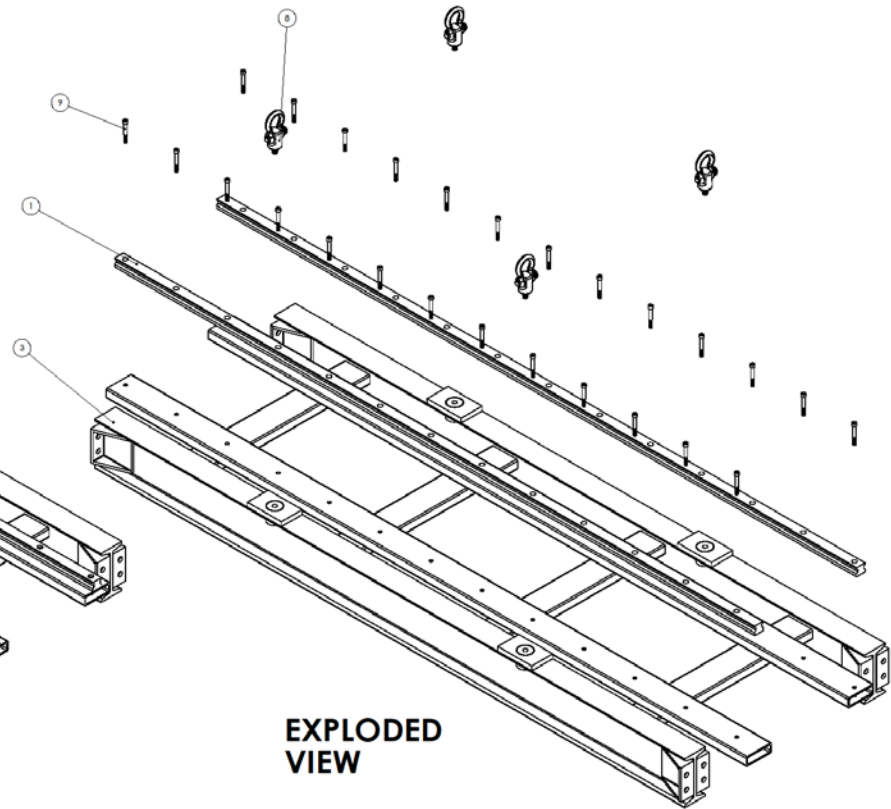
ITEM NO.	PART NUMBER	DESCRIPTION	QTY.
1	512P55C2	Guide Rail (Thomson 512P55C2) 153.45 in. - Y2 Budget #9	2
3	DTR007	Welded Frame Piece 2	2
8	McMaster.com: 3026T44	Hoist Rings - Y2 Budget #20	4
9	McMaster.com: 91290A769	Guide Rail Bolts - Y2 #39; Corresponding Nuts - y2 Budget #45	26

UNLESS OTHERWISE SPECIFIED
TOLERANCES ARE:
X =   ± .030
XX =   ± .010
XXX =   ± .005
XXXX =   ± .0005
Angular = ± .5°
FILLET RADIUS = .05 MAX
DIMENSIONS ARE IN INCHES.

MATERIAL:

FINISH:

APPROVALS   DATE
DRAWN: MAY
J.K. WILSON   2013
CHECKED:

COMMENTS:

TAMU   VIBRATION CONTROL &
          ELECTRO-MECHANICS
          LABORATORY

TITLE:
Rig Frame Piece 2 Assembly

SIZE   DWG. NO.   REV
D   DTR002

SCALE: 1:8   WEIGH: SHEET 1 OF 1
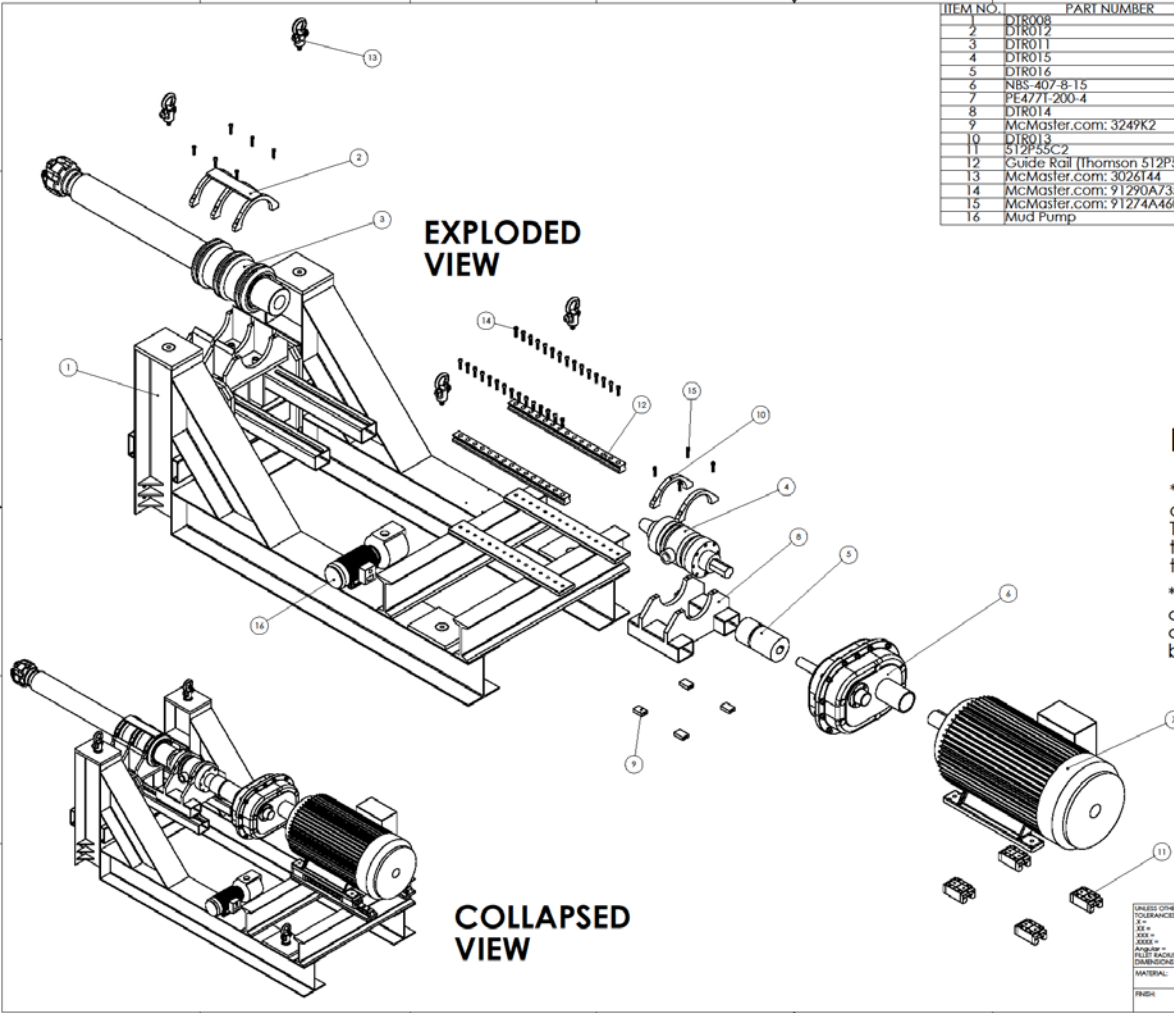
ITEM NO.	PART NUMBER	DESCRIPTION	QTY.
1	DTR008	Welded Frame Piece 3	2
2	DTR012	Shaft Housing Latch	1
3	DTR011	Shaft Assembly	1
4	DTR015	Side Inlet Swivel - Y1 Budget #6	1
5	DTR016	Torque Coupling	1
6	NBS-407-8-15	Speed Reducing Gearbox - Y2 Budget #55	1
7	PE477T-200-4	Drive Motor - Y2 Budget #53	1
8	DTR014	Swivel Support	1
9	McMaster.com: 3249K2	Roller Carriage for Swivel Mount - Y2 Budget #10	4
10	DTR013	Swivel Latch	2
11	512P55C2	Roller Carriage - Y1 budget #7	4
12	Guide Rail (Thomson 512P55C2)	Guide Rail - Y2 Budget #12	2
13	McMaster.com: 3026T44	Hoist Rings - Y2 Budget #19	4
14	McMaster.com: 91290A735	Guide Rail Screws - Y2 Budget #52	30
15	McMaster.com: 91274A460	Swivel/Shaft Latch Screws - Y2 Budget #46	10
16	Mud Pump	Y2 Budget - #3-7	1

EXPLODED VIEW

COLLAPSED VIEW

NOTES:

*The speed reducing gearbox will be attached to the frame via a torque arm. This will have to be accounted for during the assembly as the exact dimensions of the gearbox are unkown

*The mud pump dimensions are not exact and its connection to the rig will have to be determined as this part of the rig frame is being constructed.

UNLESS OTHERWISE SPECIFIED
TOLERANCES ARE:
X = ±.030
XX = ±.010
.XXX = ±.006
.XXXX = ±.0005
Angular ±.5°
FILLET RADIUS = .06 MAX
DIMENSIONS ARE IN INCHES
MATERIAL:
FINISH:

APPROVALS / DATE
DRAWN: J.K. WILSON / MAY 2013
CHECKED:
COMMENTS:

TAMU VIBRATION CONTROL & ELECTRO-MECHANICS LABORATORY

TITLE: Rig Frame Piece 3 Assembly

SIZE: D   DWG. NO. DTR003   REV

SCALE: 1:11   WEIGH: SHEET 1 OF 1

The inner sample container will be fitted with dimpled grooves that the lateral force measurement rods can be inserted into in the event that the XY-translator table produces too much friction for accurate results.
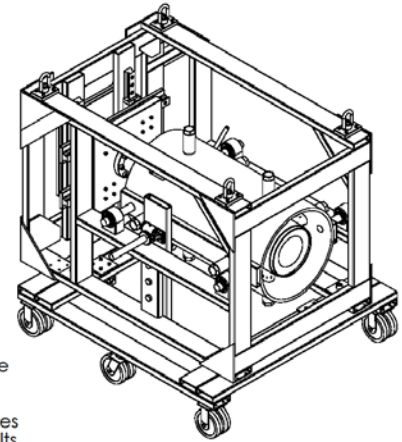
SCALE 1:12

NOTES:

*The sample containment structre is pre-assembled. These drwaings are to aid in the understanding of how the assembly functions. It is also provided as reference if the structure is dismantled.

*The formation will either be a solid core of material, or a mixture of cement and concrete.

The caster wheels should be welded securely on the bottom of the structure

UNLESS OTHERWISE SPECIFIED			TAMU	VIBRATION CONTROL & ELECTRO-MECHANICS LABORATORY
TOLERANCES ARE:	APPROVALS	DATE		
.X = ± .030	DRAWN:		TITLE:	
.XX = ± .010	J.K. WILSON	MAY 2013	Sample Containment Structure	
.XXX = ± .005				
.XXXX = ± .0005	CHECKED:			
Angular = ± .5°				
FILLET RADIUS = .05 MAX				
DIMENSIONS ARE IN INCHES				
MATERIAL:	COMMENTS:		SIZE DWG. NO.	REV
FINISH:			D DTR004	
			SCALE: 1:6 WEIGHT:	SHEET 1 OF 2

SCALE 1:12

FRONT VIEW

ITEM NO.	PART NUMBER	DESCRIPTION	QTY
1	DTR025	Sample Containment Welded Frame	1
2	DTR024	Sliding Structure	1
3	DTR030	Outer Sample Container Assembly	1
4	DTR029	Inner Sample Container Assembly	1
5	DTR028	Lateral Force Measurement Rod	8
6	DTR031	Transducer Plate Assembly	1
7	DTR027	Guide Rail Plate Assembly (XY-Translator)	2
8	DTR026	Hydraulic Plate Assembly	1

UNLESS OTHERWISE SPECIFIED
TOLERANCES ARE:
.X = ±.030
.XX = ±.010
.XXX = ±.005
ANGULAR = ±.5°
FILLET RADIUS = .06 MAX
DIMENSIONS ARE IN INCHES

APPROVALS DATE
DRAWN: J.K. WILSON MAY 2013
CHECKED:

MATERIAL:

FINISH:

COMMENTS:

TAMU VIBRATION CONTROL & ELECTRO-MECHANICS LABORATORY

TITLE: Sample Containment Structure
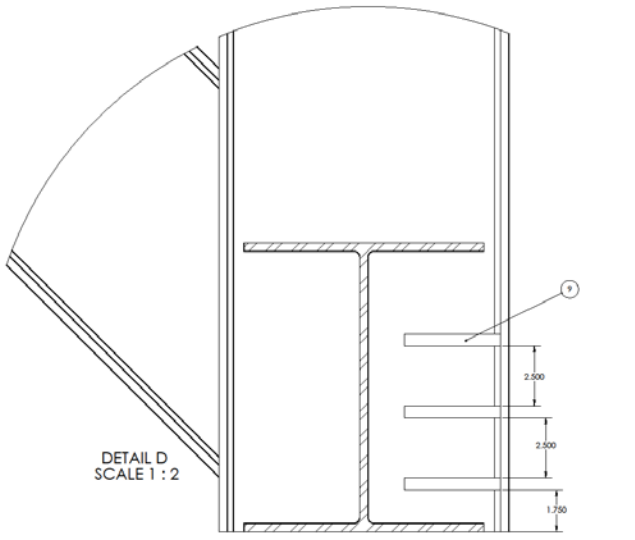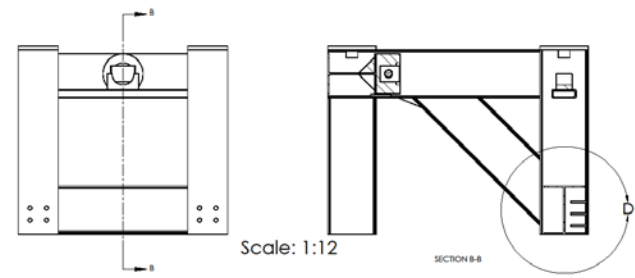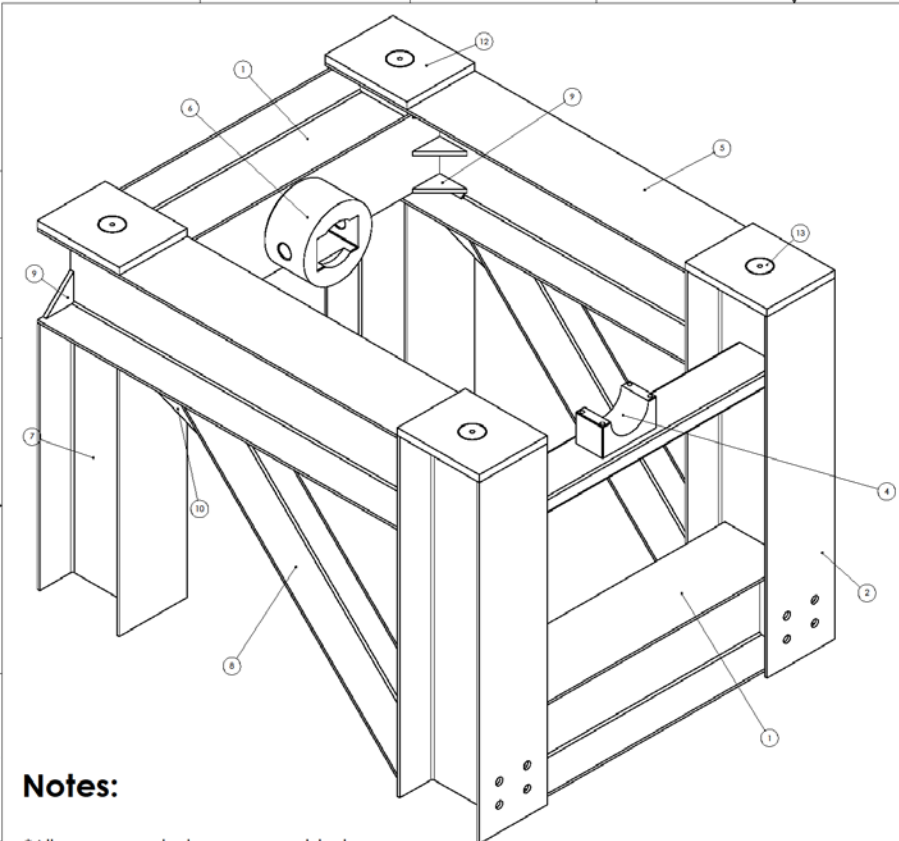
SIZE: D DWG. NO.: DTR004 REV:

SCALE: 1:4 WEIGHT: SHEET 2 OF 2

Notes:

*All components shown are welded together. Multiple views are given to fully describe how the structure should be assembled.

*If more detail is needed, please consult the Solidworks files

*IThe frame structure has several web connections that are to be welded in place. Each one of these connections has a critical roll in supporting the stresses generated during operation. It is the responsibility of the assembler to verify each web is in its intended position. Refer to the Solidworks' files for clarity if needed.

Scale: 1:12

SECTION B-B

DETAIL D
SCALE 1 : 2

2.500

2.500

1.750

ITEM NO.	PART NUMBER	DESCRIPTION	QTY.
1	DTR032	I-Beam (W12x53) 42in	2
2	DTR033	I-Beam (W12x53) 45-155in	2
3	DTR034	Tube-Rec-6x2x5-16-(42in)	1
4	DTR035	Hydraulic Cylinder Buckle Support	1
5	DTR036	I-Beam (W12x53) 55in	2
6	DTR037	Hydraulic Cylinder Pin Support	1
7	DTR038	I-Beam (W12x53) 34-095	2
8	DTR039	I-Beam (W12x53) 60in w slants	2
9	DTR040	I-Beam Web (W12x53)	30
10	DTR041	I-Beam Web 2 (W12x53)	6
12	DTR042	Hoist Ring Mount Plate (Rig Frame P1)	4
13	DTR043	Hoist Ring Mount Cylinder - (Piece 1)	4

19.420

2.750
2.750
2.750
2.750

2.500
2.500
1.750

12.175

34.125

Bottom View

Scale: 1:12

SECTION E-E

DETAIL F
SCALE 1 : 2

UNLESS OTHERWISE SPECIFIED						TAMU	VIBRATION CONTROL & ELECTRO-MECHANICS LABORATORY
TOLERANCES ARE		APPROVALS	DATE				
.X = ±.030							
.XX = ±.010		DRAWN	J.K. WILSON	MAY 2013		TITLE:	
.XXX = ±.005						Welded Frame - Piece 1	
.XXXX = ±.0005		CHECKED:					
Angular = ±.5°							
FILLET RADIUS = .25 MAX							
DIMENSIONS ARE IN INCHES							
MATERIAL:		COMMENTS:				SIZE: D	DWG. NO. DTR006	REV
FINISH:						SCALE: 1:4	WEIGHT:	SHEET 3 OF 3

NOTES:

* All components shown are welded together.

* Before the IpBeam connections are welded to the assembly, it would be a good idea to verify that they match up with the bolt holes on the other two rig frame pieces.

UNLESS OTHERWISE SPECIFIED TOLERANCES ARE: X = ±.030 XX = ±.010 XXX = ±.005 XXXX = ±.0005 Angular = ±.5° FILLET RADIUS = .06 MAX DIMENSIONS ARE IN INCHES			TAMU	VIBRATION CONTROL & ELECTRO-MECHANICS LABORATORY
	APPROVALS	DATE	TITLE:	
	DRAWN: J.K. WILSON	MAY 2013	Welded Frame - Piece 2	
MATERIAL:	CHECKED:			
	COMMENTS:		SIZE **D**	DWG. NO. DTR007	REV
FINISH:			SCALE: 1:24	WEIGH:	SHEET 1 OF 2

ITEM NO.	PART NUMBER	DESCRIPTION	QTY.
1	DTR044	Rectangular Tube - 6"x2"x5/16" -(153.45in)	2
2	DTR045	I-Beam (S10x35) - 139in	2
3	DTR046	I-Beam Connection Bracket	8
4	DTR047	Rectangular Tubing - 6"x2"x5/16" - 41-751in	4
5	DTR048	Small Hoist Ring Plate	4
6	DTR043	Hoist Ring Mount Cylinder	4

TAMU
VIBRATION CONTROL &
ELECTRO-MECHANICS
LABORATORY

TITLE:
Welded Frame - Piece 2

DWG. NO.
DTR007

DRAWN
J.K. WILSON

DATE
MAY 2013

NOTES:

*All components shown are welded together. Multiple views are given to fully describe how the structure should be assembled. Refer to the solidworks files if more detail is needed.

*The frame structure has several web connections that are to be welded in place. Each one of these connections has a critical role in supporting the stresses generated during operation. It is the responsibility of the assembler to verify each web is in its intended position. Refer to the Solidworks files for clarity if needed.

DETAIL F
SCALE 1 : 1

F

UNLESS OTHERWISE SPECIFIED
TOLERANCES ARE:
X =   ±.030
.XX =   ±.010
.XXX =   ±.005
.XXXX =   ±.0005
ANGULAR =   ±.5°
FILLET RADIUS = .06 MAX
DIMENSIONS ARE IN INCHES
MATERIAL:
FINISH:

APPROVALS   DATE
DRAWN   MAY
   J.K. WILSON   2013
CHECKED:

COMMENTS:

TAMU   VIBRATION CONTROL &
              ELECTRO-MECHANICS
              LABORATORY

TITLE:
Welded Frame - Piece 3

SIZE   DWG. NO.   REV
D   DTR008

SCALE: 1:7   WEIGHT: SHEET 2 OF 3

SECTION C-C

DETAIL D
SCALE 1 : 2

ITEM NO.	PART NUMBER	DESCRIPTION	QTY
1	DTR033	I-Beam (W12x53) 46-155in	2
2	DTR034	I-Beam (W12x53) 42in	1
3	DTR049	I-Beam (W12x53) 42in Shaft Support	1
4	DTR050	I-Beam (W12x53) 96in	2
5	DTR042	Hoist Ring Mount Plate (Rig Frame P1)	4
6	DTR051	Large Hoist Ring Mount Cylinder	4
7	DTR052	Large Shaft Support Plate (TOB)	8
8	DTR053	Shaft Support I Beam Web	14
9	DTR054	Shaft Support Plate Short (TOB)	2
10	DTR055	I-Beam (W12x53) 45in with slants	2
11	McMaster.com: 3249K2	Roller Carriages for Swivel Support - Y2 Budget #10	2
12	DTR056	Swivel Support leg (Blank)	2
13	DTR040	I-Beam Weld Web (W12x53)	28
14	DTR057	Guide Rail Support Plate (Motor)	2
15	DTR058	I-Beam (S10x35) 52-34in	2
16	DTR059	Motor Support Plate	4
17	DTR060	Tube-Rec-(6x2x5-16) 52-34in	2
18	McMaster.com: 91251A916	Shaft Support Structure Bolt - Y2 Budget #40	8
19	McMaster.com: 90949A133	Shaft Support Structure Nut - Y2 Budget #44	8
20	DTR061	Shaft Base Support Plate	1
21	DTR062	Shaft Tube Bottom Support Plate	3
22	DTR063	Shaft Tube Support Web Plate	4

UNLESS OTHERWISE SPECIFIED
TOLERANCES ARE:

APPROVALS | DATE
DRAWN: J.K. WILSON
CHECKED:
MATERIAL:
FINISH:
COMMENTS:

TAMU — VIBRATION CONTROL & ELECTRO-MECHANICS LABORATORY

TITLE: Welded Frame - Piece 3

SIZE D | DWG. NO. DTR008 | REV
SCALE 1:5 | WEIGHT: | SHEET 3 OF 3

APPENDIX C – ALTERNATIVE RIG ANALYSIS

This appendix is provided to show that analysis of an alternative, reduced power, rig was conducted and proven to work. The altered components were the Rig Frame Piece1 and Rig Frame Piece 3. The remainder of the rig remains the same.
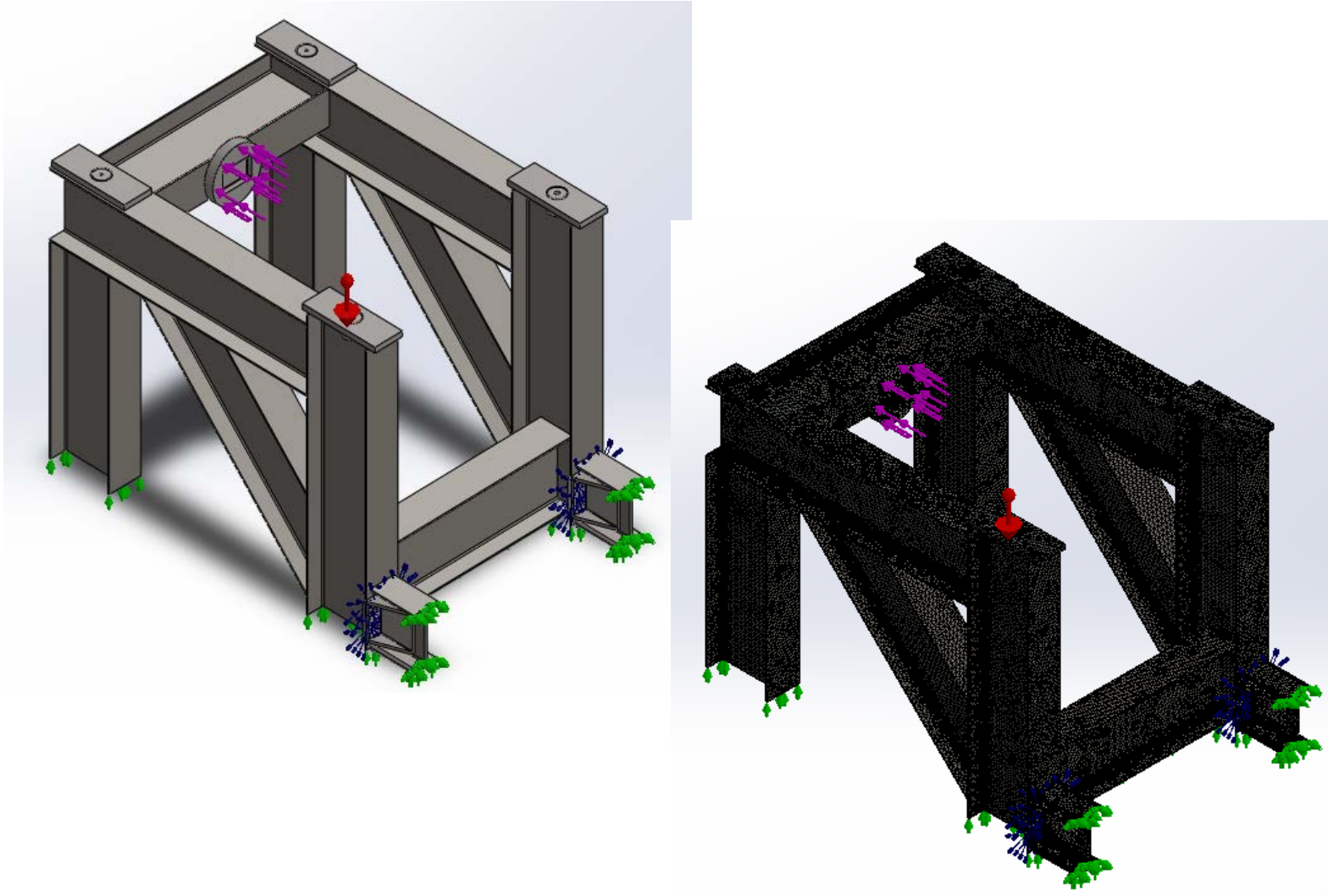
Figure C.1 – CAD Model and Mesh Plot of Alternative Rig Frame Piece 1
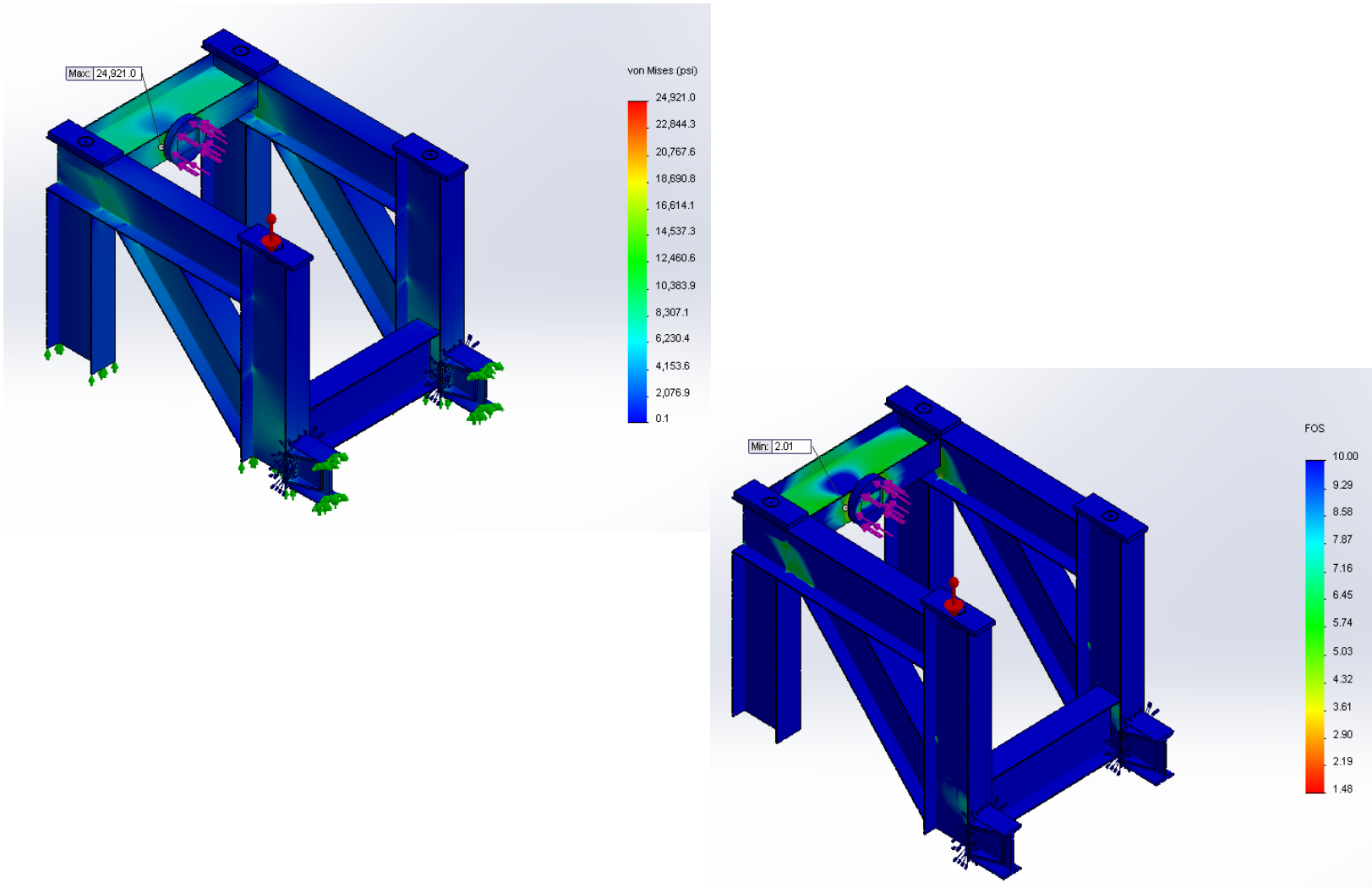
Figure C.2 – Stress and FOS Plots of Alternative Rig Frame Piece 1
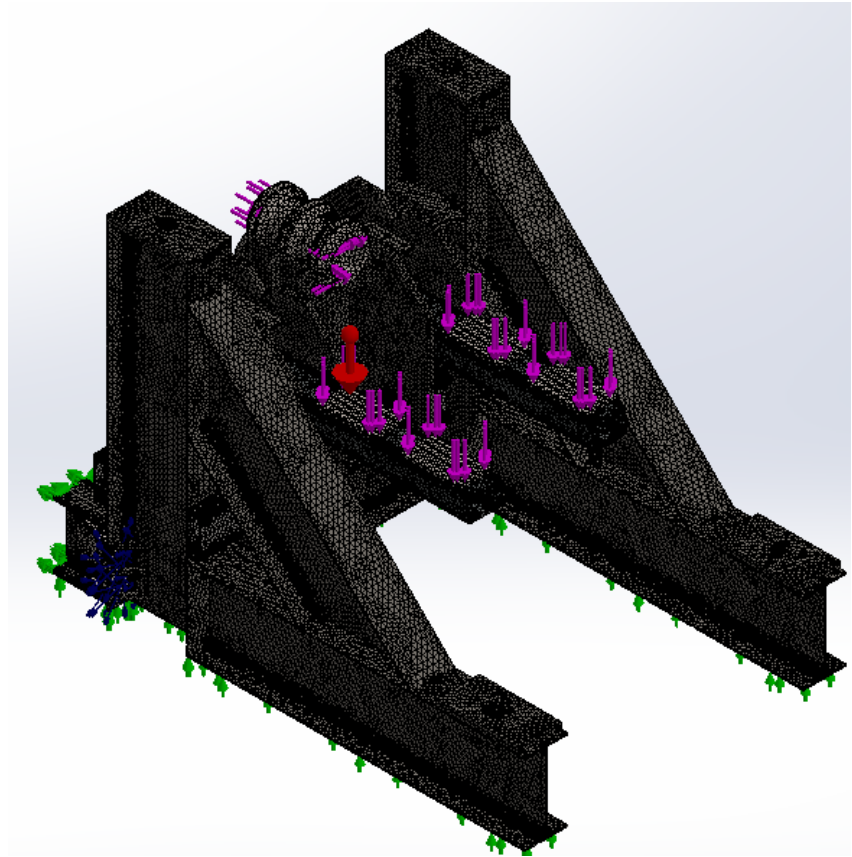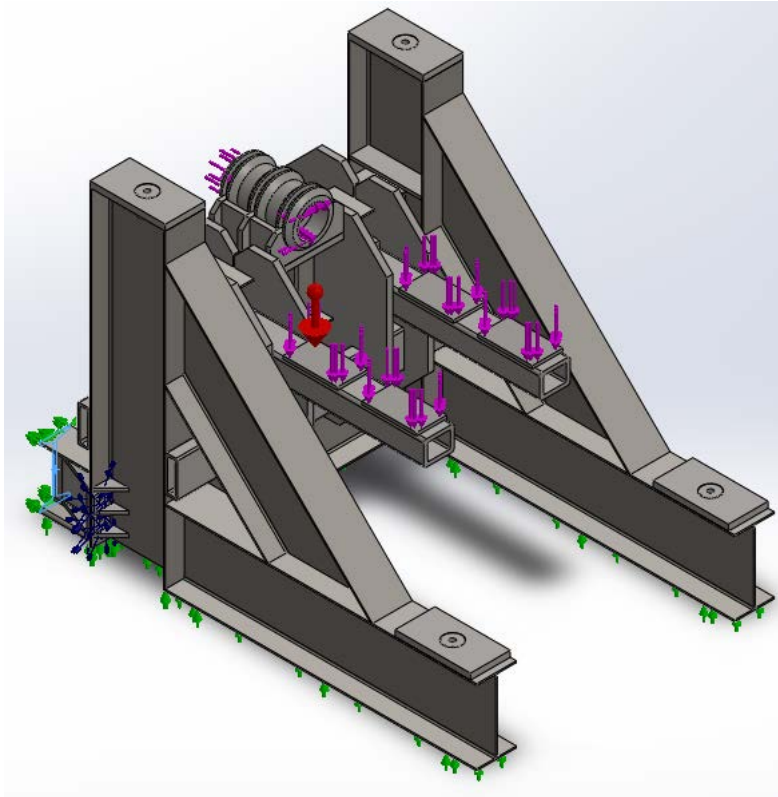
Figure C.3 – CAD Model and Mesh Plot of Alternative Rig Frame Piece 3
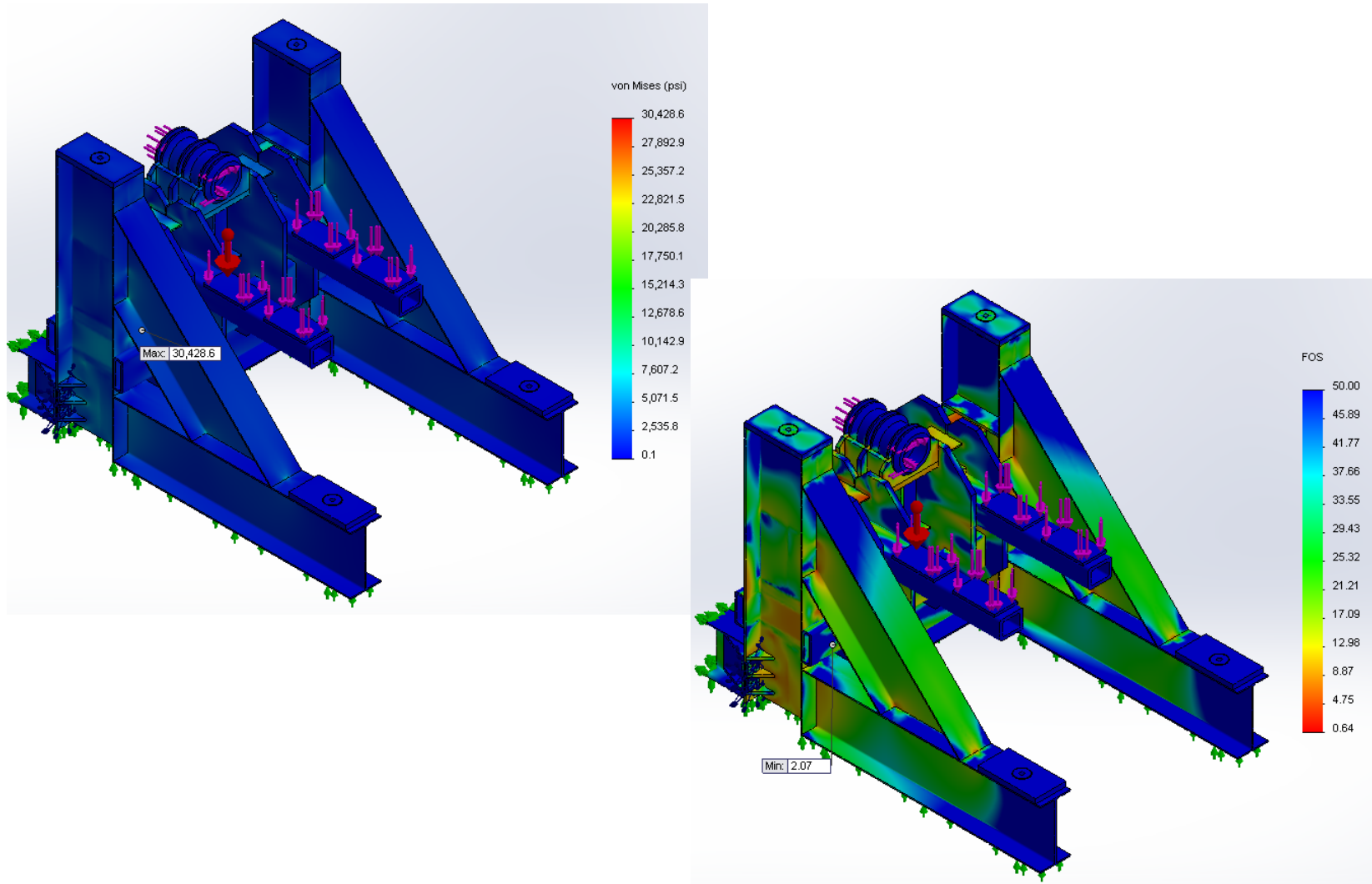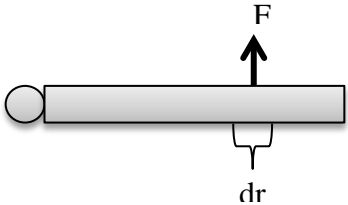
Figure C.4 – Stress and FOS Plots of Alternative Rig Frame Piece 3

APPENDIX D – BIT TORQUE DERIVATION

One "blade" of PDC bit

$$F = \mu N$$

$$N = \frac{2W_f}{nD_B}$$ n = number of "blades"

Total Frictional Bit Torque

$$T_f = n \int_0^{D_B/2} \frac{2W_f}{nD_B} \mu r dr$$

Converting to foot pounds

$$T_f = \frac{W_f D_B \mu}{4} \left[in * lb_f \right]$$

$$T_f = \frac{W_f D_B \mu}{48} \left[ft * lb_f \right]$$

$\boldsymbol{\mu}$ = coefficient of friction

$\mathbf{F}$ = force required at "blade" to rotate bit

$\mathbf{N}$ = Normal force component from WOB

$\mathbf{dr}$ = incremental radial component

$\mathbf{W_f}$ = frictional weight component

$\mathbf{D_B}$ = bit diameter

$\mathbf{T_f}$ = frictional torque component

$\mathbf{n}$ = number of blades

> *restart* :

Mud Pump Requirements (Bingham Plastic)

Assumptions

1) Bingham Plastic Fluid Model

2) Incompressible

3) Change in hydrostatic pressure is negligible

Input Variables

Annular Flow Velocity at "Surface" (ft/s)

> $v := 3.0$:

Ambient Pressure (psi)

> $P := 14.7$:

Ambient Temperature (deg F)

> $T := 70$:

Bit Diameter (in)

> $DB := 8.5$:

Inner Pipe Diameter (in)

> $IPD := 3.0$:

Outer Pipe Diameter (in)

> $OPD := 7.0$:

Length of Drill Shaft (ft)

> $H := 4.6458$:

Nozzle Area (in^2)

> $A_{Nozzle} := 3.14159265359 \left(\dfrac{13}{64} \right)^2$:

Number of Nozzles

> $N_{Nozzles} := 4$:

Nozzle Coefficient

> $C_d := .95 :$

Material Roughness

> $\epsilon_{pipe} := .126 :$

Calculated Values

Plastic Viscosity of Fluid (cp)

> $\mu_p := 2750 * \exp(1.9 * 10^{\wedge}(-4) * P) * T^{\wedge}(-1.04 * \exp(2.0 * 10^{\wedge}(-5) * P));$

$$\mu_p := 33.1955200\text{?}$$

Density of Fluid (ppg)

> $rhoi := (-5.357 * 10^{\wedge}(-6)) * (T^{\wedge}2) + (-1.267 * 10^{\wedge}(-3)) * T + 8.717 :$

> $X := 9.452 * 10^{\wedge}(-11) * T^{\wedge}2 + (-1.530 * 10^{\wedge}(-8)) * T + 4.192 * 10^{\wedge}(-6) :$

> $\rho := rhoi * \exp(X * P);$

$$\rho := 8.60251392\text{?}$$

Yeild Point (lbf/100ft^2)

> $\tau_y := (-1.494 * 10^{\wedge}(-13) * P^{\wedge}5 + 2.751 * 10^{\wedge}(-9) * P^{\wedge}4 - 1.315 * 10^{\wedge}(-5) * P^{\wedge}3 + 2.075 * 10^{\wedge}(-2) * P^{\wedge}2 - 6.511 * P + 797.8) * T^{\wedge}(2.234 * 10^{\wedge}(-8) * P^{\wedge}2 - 3.66 * 10^{\wedge}(-4) * P - .882);$

$$\tau_y := 16.2868227\text{?}$$

Flow Rate (gpm)

> $Q := \dfrac{3.14 \cdot 60 \cdot 12}{4 \cdot 231} \cdot (DB^2 - OPD^2) \cdot v;$

$$Q := 170.661039\text{?}$$

Down Flow (Pipe Flow)

> $v_{Down} := \dfrac{4 \cdot Q \cdot (.002228) \cdot 144}{3.14 \cdot IPD^2} :$

> $R_{Down} := \dfrac{\rho \cdot 0.000135 \, v_{Down} \cdot 12 \cdot IPD}{\mu_p \cdot (1.740452853562310^{-6})} :$

196

> $He_{Down} := \dfrac{37138.811006256\rho \cdot \tau_y \cdot IPD}{\mu_p^2}$:

> $g := He_{Down} * (1 - Ratio)^\wedge 3 / (16800) - Ratio$:

> $Shear := fsolve(g = 0, Ratio)$:

> $R_{critDown} := He_{Down} \cdot (1 - (4/3) * Shear + (1/3) * Shear^\wedge 4) / (8 * Shear)$:

>
if $R_{Down} < R_{critDown}$ **then**

$\quad \alpha := \dfrac{2 \cdot \tau_y \cdot .00095202773263888}{s \cdot \left(\dfrac{IPD}{2}\right)}$:

$\quad k := Q - \dfrac{3.14 \cdot \left(\dfrac{IPD}{2}\right)^4 \cdot s}{8 \cdot .0000039406006899\mu_p} \cdot \left(1 - \dfrac{4}{3} \cdot \alpha + \dfrac{1}{3} \cdot \alpha^4\right)$:

$\quad \Delta P_{Pipe} := fsolve(k = 0, s)$:

else

$\quad g := -2.0 \log_{10}\left(\dfrac{\left(\dfrac{\epsilon_{pipe}}{IPD}\right)}{3.7} + \dfrac{2.51}{R_{Down} \cdot \sqrt{y}}\right) - \dfrac{1}{\sqrt{y}}$:

$\quad f_{DF} := fsolve(g = 0, y)$:

$\quad \Delta P_{Pipe} := \dfrac{f_{DF} \cdot (H \cdot 12) \cdot \left(v_{Down}\right)^2 \cdot (\rho \cdot .000135) \cdot 12}{2 \cdot IPD}$:

end if:

> $\Delta P_{Pipe} := \Delta P_{Pipe}$;

$$\Delta P_{Pipe} := 0.547333821$$

Bit Flow (Nozzle Flow)

> $\Delta P_{Nozzle} := \dfrac{\rho \cdot Q^2}{12032 \cdot \left(C_d\right)^2 \cdot \left(N_{Nozzles} \cdot A_{Nozzle}\right)^2}$;

$$\Delta P_{Nozzle} := 85.8293611$$

Flow Back (Concentric Anulus Flow)

> $v_{Up} := \dfrac{4 \cdot Q \cdot (.002228) \cdot 144}{3.14 \cdot \left(DB^2 - OPD^2\right)}$:

> $R_{Up} := \dfrac{\rho \cdot 0.000135 \cdot v_{Up} \cdot 12 \cdot (DB - OPD)}{\mu_p \cdot \left(1.7405 \cdot 10^{-6}\right)}$:

> $He_{Up} := \dfrac{37138.811006256 \rho \cdot \tau_y \cdot (DB - OPD)}{\mu_p^2}$:

> $g := He_{Up} * (1 - Ratio)^{\wedge}3 / (16800) - Ratio$:

> $ShearU := fsolve(g = 0, Ratio)$:

> $R_{critUp} := He_{Up} \cdot (1 - (4/3) * ShearU + (1/3) * ShearU^{\wedge}4) / (8 * ShearU)$:

>

if $R_{Up} < R_{critUp}$ **then**

$$r_o := \sqrt{\frac{\left(\left(\frac{DB}{2}\right)^2 - \left(\frac{OPD}{2}\right)^2\right)}{2 \cdot \ln\left(\frac{DB}{OPD}\right)}} \ :$$

$$\Delta P_{Annulus} := \left(H \cdot 12 \cdot \left(\frac{8 \cdot \mu_p \cdot 1.74045 \cdot 10^{-6} \cdot Q \cdot 3.85}{3.14} + \frac{8}{3} \cdot \tau_y \right.\right.$$

$$\left.\left. \cdot .000833 \cdot \left(\left(\left(\frac{DB}{2}\right)^3 + \left(\frac{OPD}{2}\right)^3 \right) + 4 \cdot r_o^3 - 3 \cdot r_o^2 \cdot \left(\frac{DB}{2} \right.\right.\right.\right.$$

$$\left.\left.\left.\left. + \frac{OPD}{2} \right)\right)\right)\right) \Bigg/ \Bigg(\left(\left(\frac{DB}{2}\right)^4 - \left(\frac{OPD}{2}\right)^4 \right)$$

$$- \frac{\left(\left(\frac{DB}{2}\right)^2 - \left(\frac{OPD}{2}\right)^2 \right)^2}{\ln\left(\frac{DB}{OPD}\right)} \Bigg) \ :$$

else

$$a := \frac{DB}{2} \ :$$

$$b := \frac{OPD}{2} \ :$$

$$Z := \frac{(a - b)^2 \cdot \left(a^2 - b^2\right)}{a^4 - b^4 - \dfrac{\left(a^2 - b^2\right)^2}{\ln\left(\frac{a}{b}\right)}} \ :$$

$$DH := 2 \cdot (a - b) \ :$$

$$DEFF := \frac{DH}{Z} \ :$$

$$j := -2.0 \log_{10}\left(\frac{\left(\frac{\epsilon_{pipe}}{DEFF}\right)}{3.7} + \frac{2.51}{R_{Up} \cdot \sqrt{w}} \right) - \frac{1}{\sqrt{w}} \ :$$

$$f_{UP} := fsolve\,(j = 0, w) \ :$$

$$\Delta P_{Annulus} := \frac{f_{UP} \cdot (H \cdot 12) \cdot \left(v_{Down}\right)^2 \cdot (\rho \cdot .000135) \cdot 12}{2 \cdot (DB - OPD)};$$

end if:

> $\Delta P_{Annulus} := \Delta P_{Annulus};$

$$\Delta P_{Annulus} := 5.496428672$$

Total Pressure Loss

> $\Delta P_{Total} := \Delta P_{Pipe} + \Delta P_{Nozzle} + \Delta P_{Annulus};$

$$\Delta P_{Total} := 91.8731236$$

Power Required

> $hp := \dfrac{Q \cdot \Delta P_{Total} \cdot 144 \cdot 231}{1728 \cdot 60 \cdot 550};$

$$hp := 9.14617825\text{?}$$

APPENDIX F – AXIAL FACTOR OF SAFETY CALCULATION

Assumptions

1. The drilling action causes the bit to "bounce". The Sample containment structure effectively pushes off the bit 1 in.
2. The bit has "bounced" the sample containment structure under full WOB loading conditions (55,000 lb$_f$).
3. Mass of the year 1 structure is 4,500 lb$_m$.
4. No friction in the wheels or rail carriages (Leads to conservative design in this case)

It is presumed that the formation has lifted away from the bit by a distance, x

$$x = 1\ in = \ 0.0833\ ft$$

The formation container starts at rest with an applied WOB of 55,000 lb$_f$ and using Newton's 2nd law the acceleration, a, can be written as

$$WOB = ma$$

$$a = \frac{55,000\ lb_f}{4,500\ lb_m} = 12.22\ ft/s^2$$

where **m** is the mass of the formation and sample containment structure. The position of the sample formation structure can be written as

$$x = \ x_o + v_o t + \frac{1}{2}at^2 \hspace{3cm} \textbf{Eq. 54}$$

Since x$_o$ and v$_o$ both equal 0, the time, **t**, to close the 1 inch gap is found to be

$$t = \sqrt{\frac{2x}{a}} = .1168 \, s$$

The force of impact is equal to the change in momentum, **mv**, during the time of impact

$$F_{imp} = \frac{d(mv)}{t_{imp}}$$

Time of impact, t_{imp}, is estimated by determining how long it takes the system to travel a characteristic distance (in this case it would be 1 in, or .0833 ft)

$$v_{imp} = at = 1.43 \, ft/s$$

$$t_{imp} = \frac{x}{v_{imp}} = 0.0584 \, s$$

Therefore the impact force is given as

$$F_{imp} = \frac{4,500 \, lb_m (1.43 \, ft/s)}{0.0584 \, s} = 110,000 \, lb_f \qquad \text{Eq. 55}$$

Which implies an axial **FOS of 2.**

APPENDIX G – MATERIAL PROPERTIES FOR ANALYSIS

Material	E (psi)	ν	σ_Y (psi)	σ_{UT} (psi)	ρ (lb/in^3)	Components
Plain Carbon Steel	30,457,925	0.28	31,994	57,990	0.2818	Inner Can Support Rods, Hydraulic Pin Support, Sample Containers
304 Stainless Steel	27,557,170	0.29	29,995	74,987	0.2890	Ball Transfers
ASTM 564 Steel (AL 17-4 Alloy, H 1150)	28,500,000	0.27	125,000	145,000	0.2840	Hydraulic Support Pin
ASTM A500 Grade B Steel	29,232,000	0.26	45,700	58,000	0.2840	Rectangular Steel Tubing
ASTM A992 Steel	29,000,000	0.39	50,000	65,000	0.2840	I Beams
AISI 4340 Steel	29,732,736	0.32	102,977	160,992	0.2836	Drill Shaft
AISI 1018	29,007,548	0.29	50,991	60,989	0.2854	Plates

APPENDIX H – HYDRAULIC PIN CALCULATION
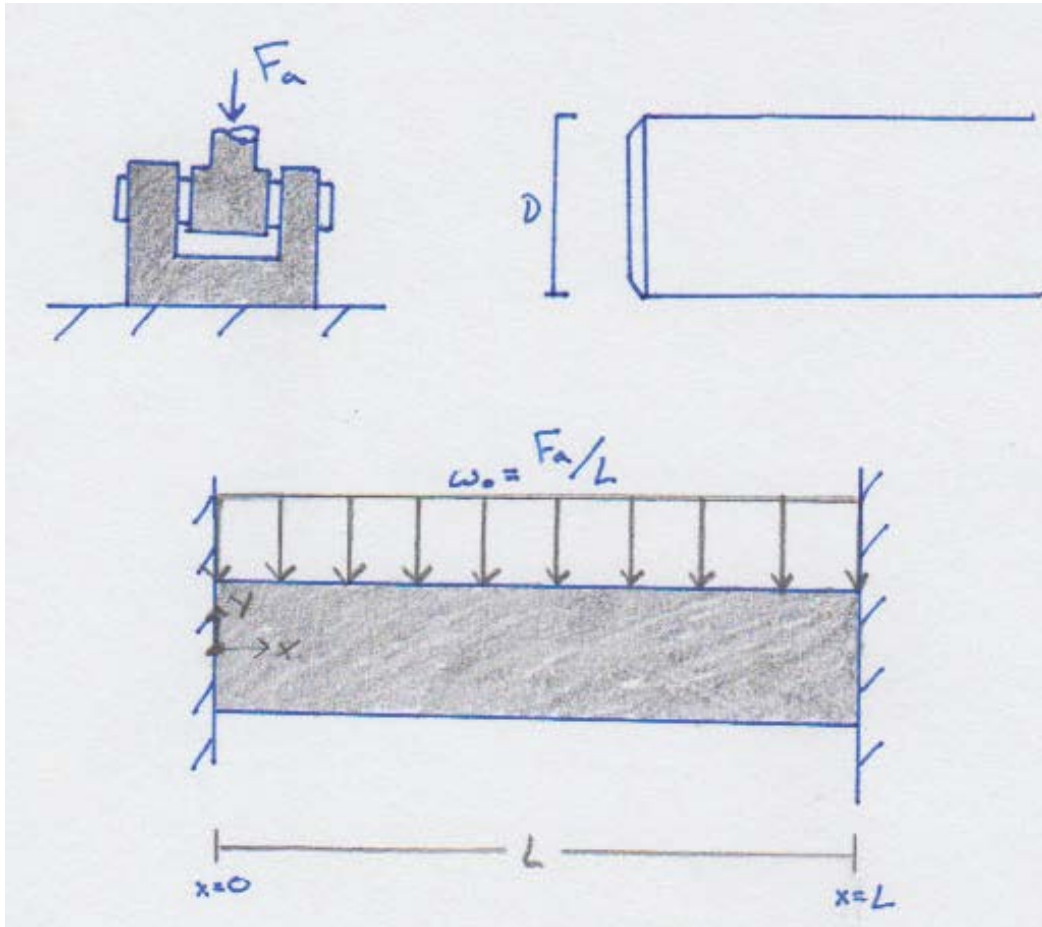
Figure AH.1: Analytical Model of Hydraulic Pin

$F_a = 55,000$ lb$_f$ $W_o = 16,923$ lb$_f$/in

$D = 1.77$ in $A = 2.46057$ in^2

$E = 28.5 \times 10^6$ psi $I = 0.481796$ in^4

$L = 3.25$ in

F_a is the axial load applied to the beam, D is the diameter of the pin, E is the Young's Modulus, L is the length of the pin, A is the cross sectional area, I is the area moment of inertia and W_o is the force per unit length applied to the pin.

Using the 4rth order beam equation for vertical deflection (v),

$$\frac{d^4v}{dx^4} = \frac{w_o}{EI}$$

Eq. 56

And integrating leads to Equation 57,

$$\frac{d^3v}{dx^3} = \frac{w_o}{EI}x + A$$

$$\frac{d^2v}{dx^2} = \frac{w_o}{2EI}x^2 + Ax + B$$

$$\frac{dv}{dx} = \frac{w_o}{6EI}x^3 + \frac{A}{2}x^2 + Bx + C$$

$$\frac{dv}{dx} = \frac{w_o}{6EI}x^3 + \frac{A}{2}x^2 + Bx + C$$

$$v = \frac{w_o}{24EI}x^4 + \frac{A}{6}x^3 + \frac{B}{2}x^2 + Cx + D$$

Eq. 57

Where A, B, C and D are constants of integration. Using the following boundary conditions,

@ x = 0

v = 0,   dv/dx = 0

@ x = L

v = 0,   dv/dx = 0

And solving for the coefficients, a formula for beam deflection is found

$$v = \frac{w_o}{24EI}x^4 - \frac{w_oL}{12EI}x^3 + \frac{w_oL^2}{24EI}x^2$$

Eq. 58

Equation 58 is the displacement formula for the beam depicted in Figure AH.1. Now, understanding that,

$$-M = EI\frac{d^2y}{dx^2}$$

$$-V = EI\frac{d^3y}{dx^3}$$

We arrive at equations for bending moment (**M**) and shear force (**V**) as functions of x,

$$M = -\frac{w_o}{2}x^2 + \frac{w_oL}{2}x - \frac{w_oL^2}{12} \qquad \qquad \textbf{Eq. 59}$$

$$V = -w_ox + \frac{w_oL}{2} \qquad \qquad \textbf{Eq. 60}$$

Realizing that the maximum bending moment and the maximum shear occur @ x=0 and x=L,

$$M_{max} = -\frac{w_oL^2}{12} = 14,896 \left[in * lb_f\right]$$

$$V_{max} = \frac{w_oL}{2} = 27,500 \left[lb_f\right]$$
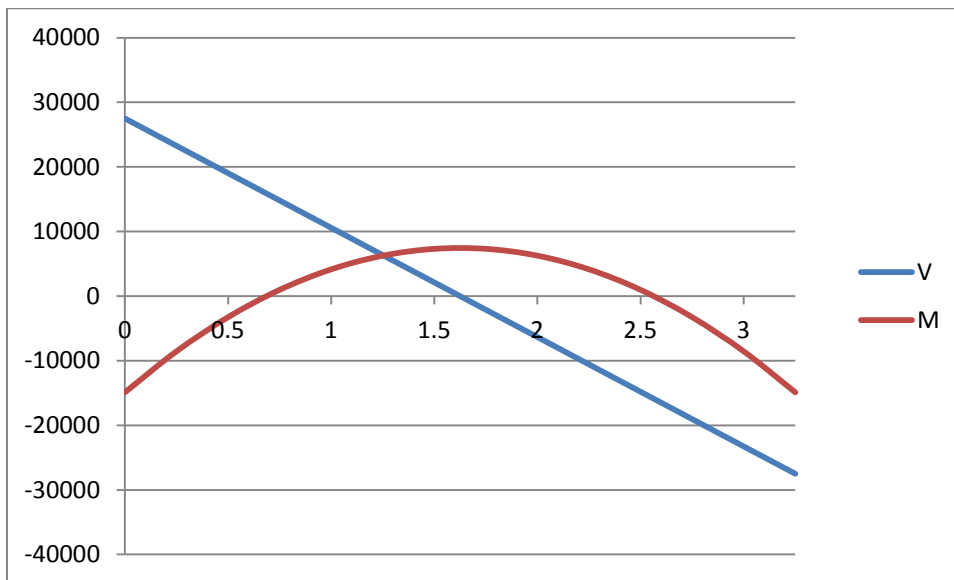
Figure AH.2: Shear and Bending Moment Diagram for Hydraulic Pin

Figure AH.2 illustrates the distribution of the shear and moment values along the length of the beam. The max shear stress is found by,

$$\tau_{max} = \frac{4}{3}\frac{V_{max}}{A} = 14,902 \; psi \qquad \qquad \text{Eq. 61}$$

Maximum bending moment stress occurs at the top and bottom surface of the pin @ y = D/2 in in the x-direction (σ_{xmax}).

$$\sigma_{x_{max}} = \frac{M_{max}D}{2I} = 27,362 \; psi \qquad \qquad \text{Eq. 62}$$

And there will be a stress at the surface in the y-direction (σ_y) from the actuator applying the distributed load

$$\sigma_y = \frac{w_o}{D} = 9,561 \; psi \qquad \qquad \text{Eq. 63}$$

While the maximum shear stress will occur at the center of the support pin, it will be assumed that the maximum shear is at the surface. This is done in order to overcome the underestimated surface stress from the actuator. In reality, the actuator will create a stress concentration on the pin's surface at the discontinuity shown in Figure AH.3.
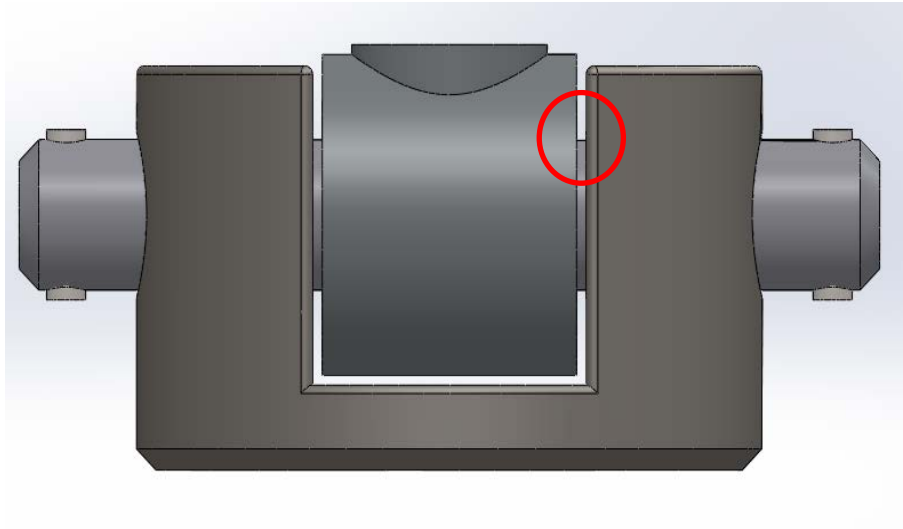
Figure AH.3: Location of Stress Concentration on Hydraulic Pin

Using a Von Mises stress (**σ**_{max}) formula, the maximum stress is found

$$\sigma_{max} = \frac{\sigma_x + \sigma_y}{2} + \sqrt{\left(\frac{\sigma_x - \sigma_y}{2}\right)^2 + \tau_{xy}^2} = 35,819 \ psi \qquad \text{Eq. 64}$$

APPENDIX I – HOOK LOADING

Sample Containment Structure

$$W = 5435.84 \text{ lb}_f$$
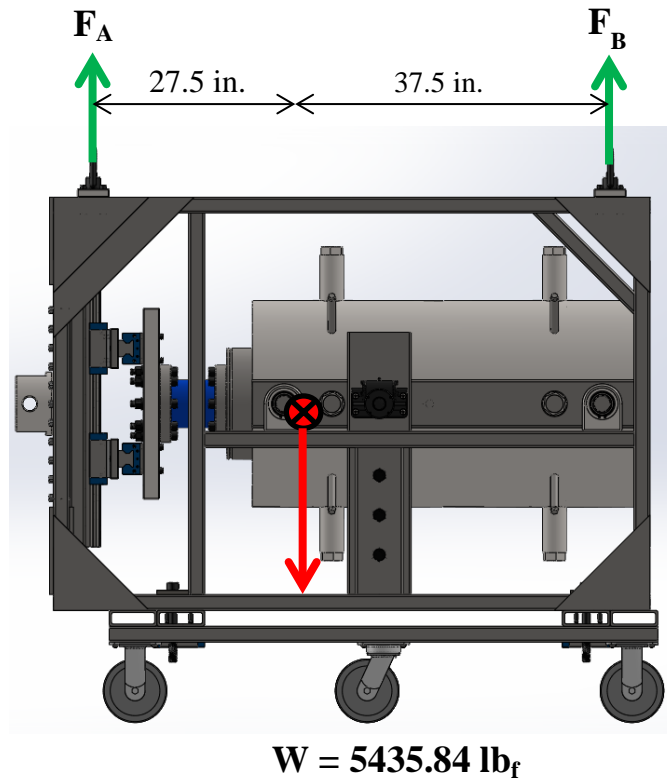
Figure AI.1: Sample Containment Structure

Assumptions

1. Weight is distributed between only 1 set of hoist hooks as shown in the figure
2. Total weight of component is 6,000lb$_f$

F_A, F_B, θ_A, and θ_B represent the corresponding hoisting loads and directions required to lift the component for each of the following calculations.

$$F_A + F_B = 6,000 \; lb_f$$

$$27.5F_A = 37.5F_B$$

$$F_A = 1.36F_B$$

$$(1 + 1.36)F_B = 6,000lb_f$$

$$F_B = 2,542.37\ lb_f$$

$$F_A = 3,457.63\ lb_f$$
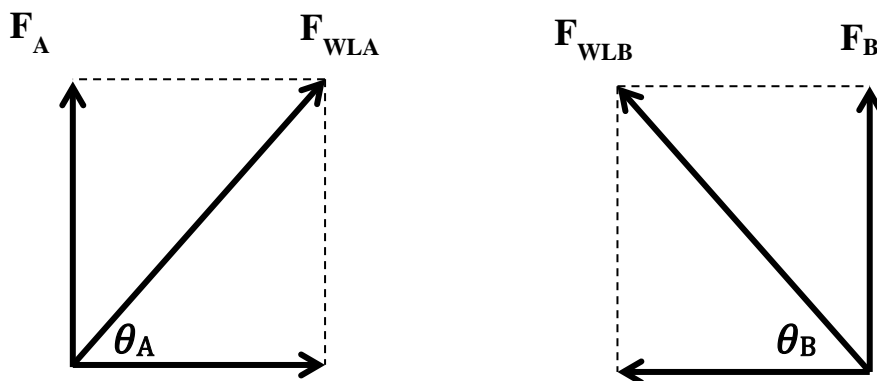
Figure AI.2: Force Balance Diagram for Hoist Rings

Assumption

3. θ_B is 45°

4. Point of hoisting is directly over the C_G

5. The hoisting point is above the center of gravity

$$F_{WL_B} = \frac{F_B}{\sin\theta_B} = 3,595.45\ lb_f$$

For θ_B to be 45°, θ_A must be 53.75°.

$$F_{WL_A} = \frac{F_A}{\sin \theta_A} = 4,287.5 \; lb_f$$

Rig Frame Piece 1

$$W = 1,840 \; lb_f$$
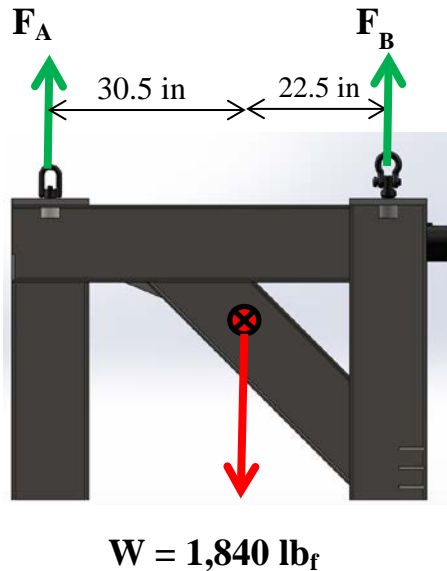
Figure AI.3: Rig Frame Piece 1

Assumptions

1. Weight is distributed between only 1 set of hoist hooks as shown in the figure
2. Total weight of component is 2,000lb$_f$

$$F_A + F_B = 2,000 \; lb_f$$
$$30.5F_A = 22.5F_B$$
$$F_A = 0.74F_B$$
$$(1 + 0.74)F_B = 2,000lb_f$$
$$F_B = 1150.94 \; lb_f$$
$$F_A = 849.06 \; lb_f$$
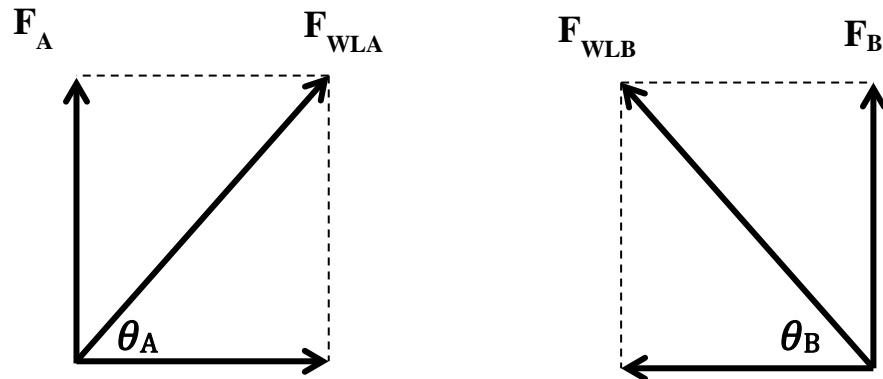
Figure AI.4: Force Balance Diagram for Hoist Rings

Assumption

3. θ_A is 45°

4. Point of hoisting is directly over the C_G

5. The Hoisting Point is above the center of gravity

$$F_{WL_A} = \frac{F_A}{\sin \theta_A} = 1,200.75 \; lb_f$$

Now for θ_A to be 45°,$_B$ must be 53.58°.

$$F_{WL_B} = \frac{F_B}{\sin \theta_B} = 1,430.23 \; lb_f$$

Rig Frame Piece 2
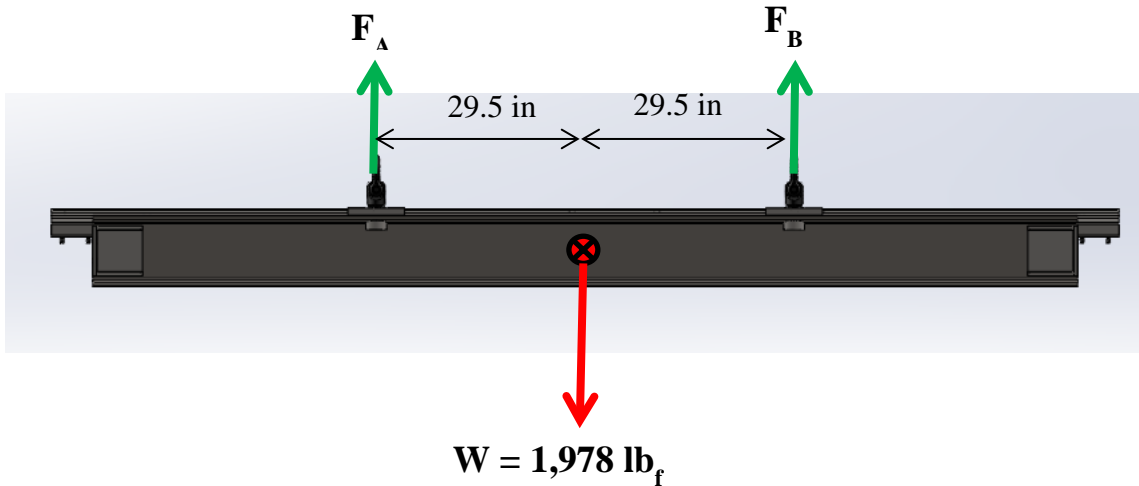
Figure AI.5: Rig Frame Piece 2

Assumptions

1. Weight is distributed between only 1 set of hoist hooks as shown in the figure
2. Total weight of component is 2,000lb$_f$

$$F_A + F_B = 2,000 \ lb_f$$

$$29.5F_A = 29.5F_B$$

$$F_A = F_B$$

$$(2)F_B = 2,000lb_f$$

$$F_B = 1,000 \ lb_f$$

$$F_A = 1,000 \ lb_f$$
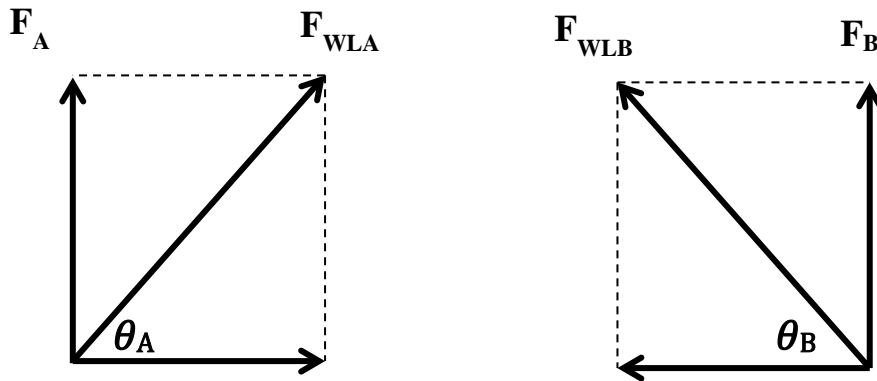
Figure AI.6: Force Balance Diagram for Hoist Rings

Assumption

3. $\theta_A = \theta_B = 45°$

4. Point of hoisting is directly over the C_G

5. The Hoisting Point is above the center of gravity

$$F_{WL_A} = F_{WL_B} = \frac{F_A}{\sin \theta_A} = 1,414 \; lb_f$$

Rig Frame Piece 3

$$F_A$$

40.5 in   48.03 in

$$F_B$$

$$W = 7{,}406\ lb_f$$
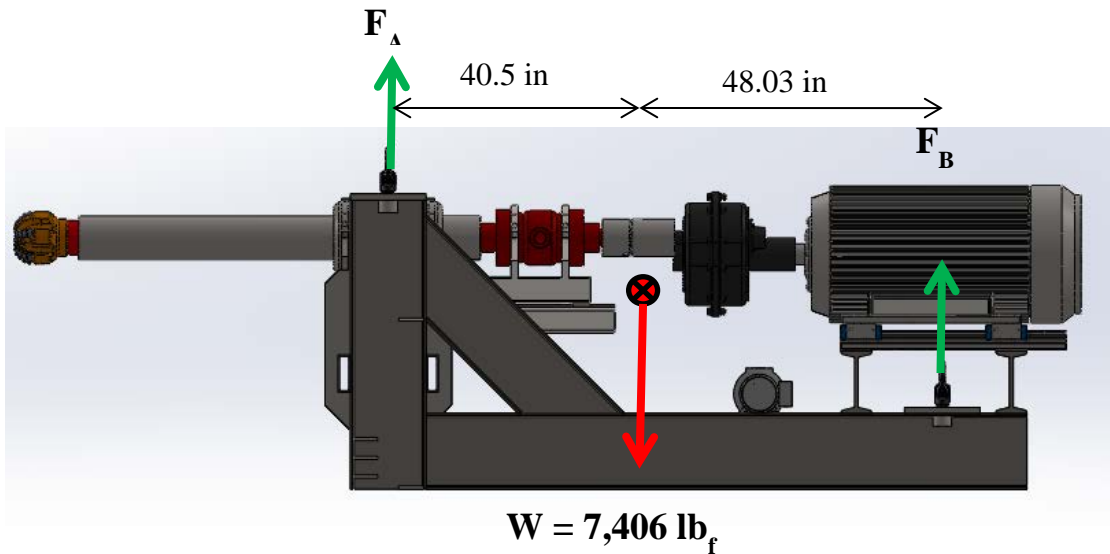
Figure AI.7: Rig Frame Piece 3

Assumptions

1. Weight is distributed between only 1 set of hoist hooks as shown in the figure
2. Total weight of component is 8,000lb$_f$

$$F_A + F_B = 8{,}000\ lb_f$$
$$40.5F_A = 48.03F_B$$
$$F_A = 1.19F_B$$
$$(1 + 1.19)F_B = 8{,}000lb_f$$
$$F_B = 3{,}659.78\ lb_f$$
$$F_A = 4{,}340.22\ lb_f$$
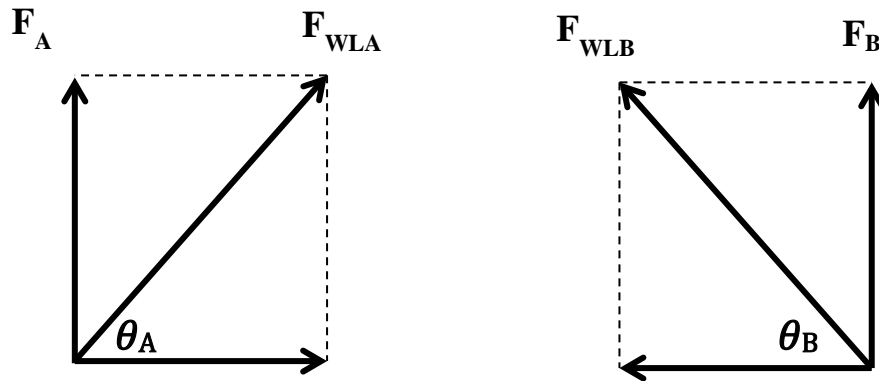
Figure AI.8: Force Balance Diagram for Hoist Rings

Assumption

3. θ_B is 45°

4. Point of hoisting is directly over the C_G

5. The Hoisting Point is above the center of gravity

$$F_{WL_B} = \frac{F_B}{\sin \theta_B} = 5,175.71 \; lb_f$$

For θ_B to be 45°, θ_A must be 49.86°.

$$F_{WL_A} = \frac{F_A}{\sin \theta_A} = 5,677.28 \; lb_f$$

APPENDIX J – FORMATION DEFLECTION/CONTACT STRESS

Puttock and Thwaite [135] present an analytical method for determining the deflection produced by pressing a sphere against the internal wall of a cylinder. Figure AJ.1 illustrates the simplified model.
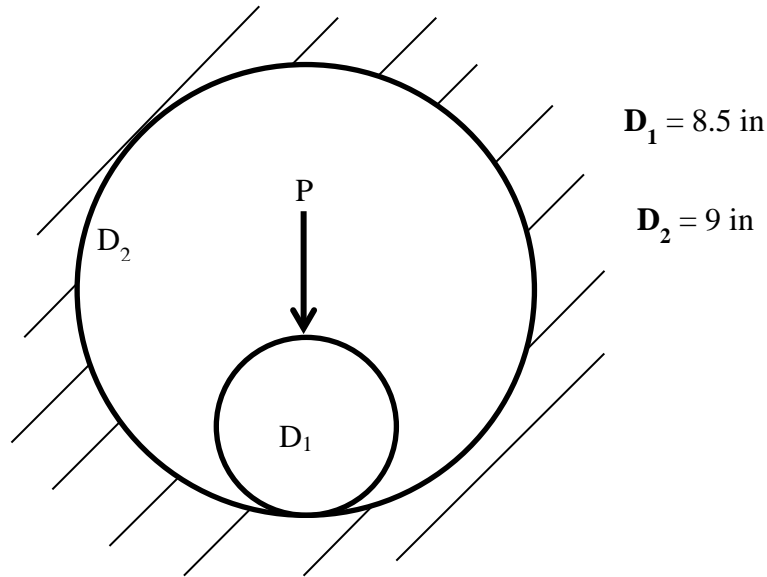
Figure AJ.1: Sphere/Cylinder Inside a Cylinder

In order to determine the deflection of the two bodies, **δ**, the following equations are presented.

$$\frac{A}{B} = \frac{\frac{1}{D_1} - \frac{1}{D_2}}{\frac{1}{D_1}} = 0.0556 \tag{Eq. 65}$$

$$\frac{1}{A} = \frac{1}{\frac{1}{D_1} - \frac{1}{D_2}} = 153 \tag{Eq. 66}$$

$$a = \sqrt[3]{\frac{2QPe}{A}} = 0.3010 \tag{Eq. 67}$$

$$Q = \frac{3}{4\pi}\left[\frac{1-v_1^2}{E_1} + \frac{1-v_2^2}{E_2}\right] = 2.2270 * 10^{-8} \qquad \text{Eq. 68}$$

$$\delta = \frac{2QP}{a}K = 0.0019 \; in \qquad \text{Eq. 69}$$

Where **K** and **e** are constant determined from data tables from Puttock and Thwaite.

$$K = 3.27064$$

$$e = 2.29207$$

P is the applied load, **E** are respective Young's Moduli and **v** are the respective Poisson's ratios.

Roark and Young [136] outline a similar calculation of the displacement, δ, for a cylinder within a cylinder.

$$K_D = \frac{D_1 D_2}{D_1 + D_2} \qquad \text{Eq. 70}$$

$$C_E = \frac{1-v_1^2}{E_1} + \frac{1-v_2^2}{E_2} \qquad \text{Eq. 71}$$

$$b = 1.6\sqrt{PK_D C_E} \qquad \text{Eq. 72}$$

$$\delta = \frac{2P}{\pi}C_E\left(\frac{2}{3} + ln\left(\frac{2D_1}{b}\right) + ln\left(\frac{2D_2}{b}\right)\right) \qquad \text{Eq. 73}$$

Contact stress was calculated using the following method as presented by Timoshenko and Goddier [137]. As an example, the calculation of the contact stress between the Lateral Force Measurement Rods and the Inner Sample Container (Figure AJ.2) is presented here with the following material properties.

$E_1 = 30\text{x}10^6\text{psi}$ \qquad\qquad $R_1 = 7 \text{ in}$

$v_1 = .3$ \qquad\qquad $E_2 = 28.5\text{x}10^6\text{psi}$

$$v_2 = .29 \qquad\qquad\qquad R_1 = 0.875 \text{ in}$$
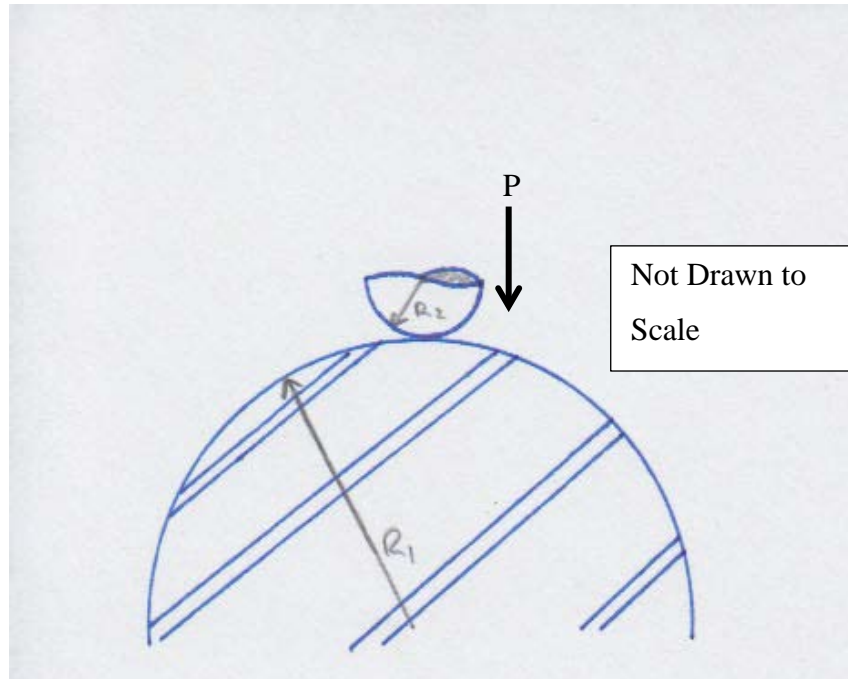
Figure AJ.2: Sphere on Cylinder Contact

$$K_E = \frac{1}{\pi}\left[\frac{1-v_1^2}{E_1} + \frac{1-v_2^2}{E_2}\right] = \frac{1}{\pi}\left[\frac{1-.3^2}{30x10^6} + \frac{1-.29^2}{28.5x10^6}\right] = 1.9885 * 10^{-8} \qquad \text{Eq. 74}$$

$$a = m\sqrt[3]{\frac{3\pi}{4}\frac{PK_E}{\alpha}} \qquad\qquad \text{Eq. 75}$$

$$b = n\sqrt[3]{\frac{3\pi}{4}\frac{PK_E}{A}} \qquad\qquad \text{Eq. 76}$$

$$q_o = \frac{3}{2}\frac{P}{\pi ab} \qquad\qquad \text{Eq. 77}$$

The coefficients **a** and **b** represent the elliptical dimensions of the contact area between the two bodies. The coefficients **m**, **n**, and **A** are determined in the following way.

$$\cos \theta = \frac{B}{A} \qquad\qquad \text{Eq. 78}$$

$$A = \frac{1}{2}\left(\frac{1}{R_1} + \frac{1}{R_1'} + \frac{1}{R_2} + \frac{1}{R_2'}\right) \qquad\qquad \text{Eq. 79}$$

$$B = \frac{1}{2}\sqrt{\left(\frac{1}{R_1} - \frac{1}{R_1'}\right)^2 + \left(\frac{1}{R_2} - \frac{1}{R_2'}\right)^2 + 2\left(\frac{1}{R_1} - \frac{1}{R_1'}\right)\left(\frac{1}{R_1} - \frac{1}{R_1'}\right)\cos 2\psi} \qquad\qquad \text{Eq. 80}$$

In which ψ is the angle of the normal plane between the two bodies while R_1, R_1', R_2, and R_2' represent the corresponding radii of each body in two directions (i.e. R_1 and R_2 would be the in plane curvatures in Figure AJ.2 while R_1' and R_2' would be the respective out-of-plane curvatures of the two bodies).

Whittemore and Petrenko [138] provide empirical data relating the angle θ to m and n, which has been plotted in order to extract a curve fit analytical expression for each (See Figure AJ.3).
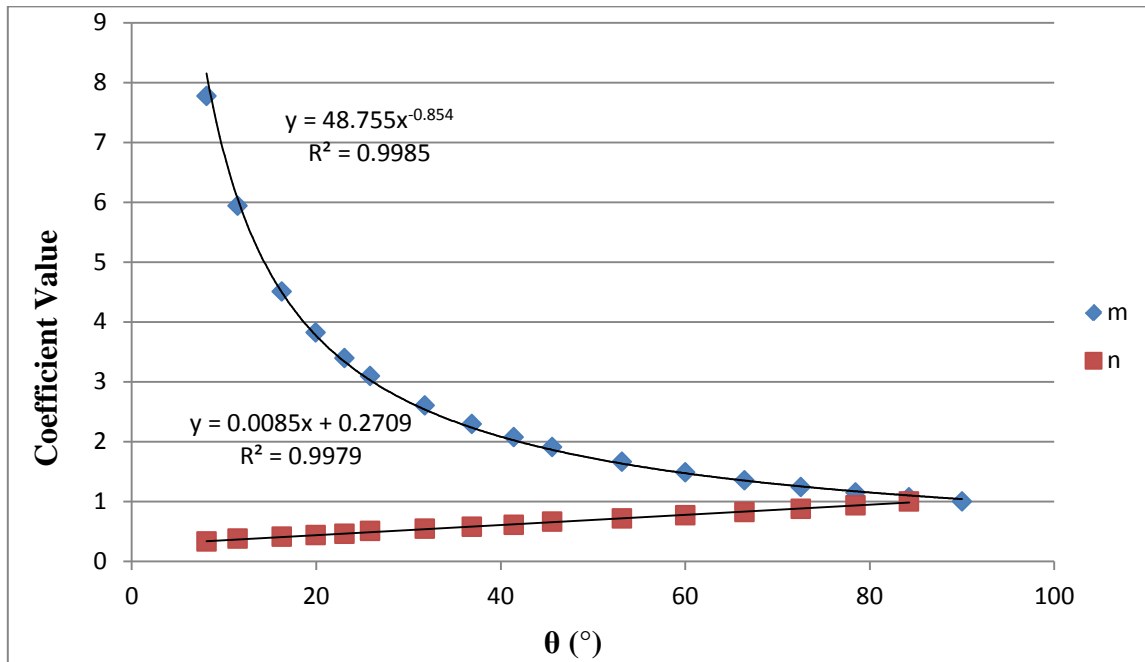
Figure AJ.3: Contact Coefficient Curve Fitting

The analytical expressions matched to the data are listed as follows

$$m = 48.755\theta^{-0.854}$$ **Eq. 81**

$$n = 0.0085\theta + 0.2709$$ **Eq. 82**

APPENDIX K – SHAFT CALCULATIONS

Torsional Stress (Pure Shear)
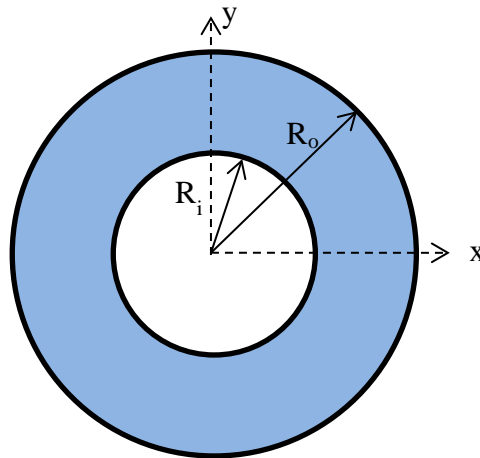
Figure AK.1: Cross Section Geometry of Drill Shaft

The dimensions of the shaft at its minimum diameters are

R_o = 2.56 in

R_i = 1.5 in

Following the method presented by Timoshenko and Goodier [137] the stress function ,Φ, of the shaft's cross section (Figure AK.1) is found by assuming it is equal to

$$\Phi = m(x^2 + y^2 - R^2)$$
Eq. 83

for an arbitrary circle in which **R** is the outer radius of the circle and **x** and **y** are coordinates within the cross section. This would hold true for the above hollow shape along its boundaries at R_o and R_i. And that the condition

$$\nabla^2 \Phi = -2\mu\alpha \qquad\qquad\qquad \text{Eq. 84}$$

holds true within the solid region bounded by outer radius for each circle. Where **μ** is the shear modulus of the material and **α** is the rotation per unit length of the shaft. Therefore, the general stress function for a circle is found by the following

$$\frac{d^2\Phi}{dx^2} + \frac{d^2\Phi}{dy^2} = -2\,\mu\alpha \qquad\qquad\qquad \text{Eq. 85}$$

$$4m = -2\,\mu\alpha \qquad\qquad\qquad \text{Eq. 86}$$

$$m = \frac{-\mu\alpha}{2} \qquad\qquad\qquad \text{Eq. 87}$$

to arrive at

$$\Phi = \frac{-\mu\alpha}{2}\,(x^2 + y^2 - R^2) \qquad\qquad\qquad \text{Eq. 88}$$

The torque supported by a cross section is represented by the following relation

$$T = 2\iint \Phi dA \qquad\qquad\qquad \text{Eq. 89}$$

So for each circular area, this equation must hold true. Thus the torque supported by the outer circle is given as

$$T_o = -\mu\alpha\iint (x^2 + y^2 - R_o^2)\,dA \qquad\qquad\qquad \text{Eq. 90}$$

$$T_o = -\mu\alpha[\iint x^2 dA + \iint y^2\,dA - \iint R_o^2\,dA] \qquad\qquad\qquad \text{Eq. 91}$$

$$T_o = -\mu\alpha\left[\frac{\pi}{4}R_o^4 + \frac{\pi}{4}R_o^4 - \pi R_o^4\right] \qquad\qquad\qquad \text{Eq. 92}$$

$$T_o = \frac{\mu\alpha\pi}{2}R_o^4 \qquad\qquad\qquad \text{Eq. 93}$$

and realizing that the inner radius can be written as

$$R_i = kR_o \qquad\qquad \text{Eq. 94}$$

where k is a constant less than one. The torque supported by the inner circle can be written as

$$T_i = -\mu\alpha \iint (x^2 + y^2 - kR_o^2)\, dA \qquad\qquad \text{Eq. 95}$$

$$T_i = -\mu\alpha [\iint x^2 dA + \iint y^2\, dA - \iint kR_o^2\, dA] \qquad\qquad \text{Eq. 96}$$

$$T_i = -\mu\alpha \left[\frac{\pi}{4} R_o^4 + \frac{\pi}{4} R_o^4 - \pi k^4 R_o^4\right] \qquad\qquad \text{Eq. 97}$$

$$T_i = \frac{\mu\alpha\pi}{2} k^4 R_o^4 \qquad\qquad \text{Eq. 98}$$

The total torque of the cross section can then be interpreted as being the difference in the torque capacities of the outer and inner circles

$$T = \frac{\mu\alpha\pi}{2} R_o^4 (1 - k^4) \qquad\qquad \text{Eq. 99}$$

which agrees with the formula presented from any undergraduate "Strength of Materials" course. The angle of twist per unit length can be written as

$$\alpha = \frac{2T}{\pi\mu R_o^4(1-k^4)} \qquad\qquad \text{Eq. 100}$$

The shear stress components of the cross section can be expressed as derivatives of the total stress function which can be found by plugging Equation 100 into Equation 88.

$$\Phi = \frac{-T}{\pi R_o^4(1-k^4)} (x^2 + y^2 - R^2) \qquad\qquad \text{Eq. 101}$$

$$\tau_{xz} = \frac{d\Phi}{dy} = \frac{-2T}{\pi R_o^4(1-k^4)} y \qquad\qquad \text{Eq. 102}$$

$$\tau_{yz} = -\frac{d\Phi}{dx} = \frac{2T}{\pi R_o^4(1-k^4)} x \qquad\qquad \text{Eq. 103}$$

The total shear stress is written as a sum of 2 squares

$$\tau_{tot} = \sqrt{\tau_{xz}^2 + \tau_{yz}^2}$$

Eq. 104

Noting that the maximum shear will occur at the outer boundary of the cross section and assuming the maximum torque is applied (168,000 ft-lb$_f$) a maximum shear stress is found to be

$$\tau_{tot} = 10,233 \, psi$$

Axial Stress

The axial stress in the shaft is dues to the WOB (σ_{Zaxial}) and the bending moment in the shaft ($\sigma_{Zbending}$).

$$\sigma_{z_{axial}} = \frac{F}{A} = \frac{WOB}{\pi R_o^4(1-k^4)} = \frac{55,000 \, lb_f}{\pi(2.56in)^4(1-0.5862^4)} = 463 \, psi \qquad \text{**Eq. 105**}$$

$$\sigma_{z_{bending}} = \frac{M}{I}y = \frac{F_{sb}L_f}{I}R_o = \frac{4,000lb_f*41in}{\frac{\pi}{4}((2.56in)^4-(1.5in)^4)}2.56in = 14,109 \, psi \qquad \text{**Eq. 106**}$$

Maximum Von Mises Stress

$$\sigma_{max} = \frac{\sigma_z+\sigma_y}{2} + \sqrt{\left(\frac{\sigma_z-\sigma_y}{2}\right)^2 + \tau_{tot}^2} \qquad \text{**Eq. 107**}$$

Using the values from Equations 105 and 106 in Equation 107, the maximum stress is found to be

$$\sigma_{max} = 17,520 \, psi$$

Buckling

Hartog [139], p.296, presents a formulation for the buckling tendency of a column subjected to axial and torsional loading, which would be the case for the rig's drill shaft. Equation 108 summarizes his findings

$$\frac{T_o^2}{(2\pi EI/L)^2} + \frac{W_o}{\pi^2 EI/L^2} = 1 \qquad \text{Eq. 108}$$

where **L** represents the length of the shaft, in this case **L** = 48 in . If the applied torque, T_o, is taken to be 200,000 in-lb$_f$ then, assuming that **E** is assumed to be 30,000,000 psi, the WOB (**W_o**) required to instigate buckling in the shaft would be near 1 billion lb$_f$. From this rough calculation which is also supported by the FEA results, the shaft will yield long before any buckling occurs.

Thread Capacity

In the shaft's design, it is important to verify that the lock nut will be able to support the 8,000 lb$_f$ that will be generated by the spring washers. The nut's ability to withstand the force is a question of thread capacity. Budynas and Nisbett [140] provide relations for estimating the thread capacities of power screws, which can readily be applied to the lock nut for this particular application. The equations below represent the stresses in the principal directions of the threads.

$$\sigma_{x_t} = \frac{6F}{\pi d_r n_t p} \qquad \text{Eq. 109}$$

$$\sigma_{y_t} = -\frac{4F}{\pi d_r^2} \qquad \text{Eq. 110}$$

$$\tau_t = \frac{3F}{\pi d_r n_t p} \qquad \text{Eq. 111}$$

Where **F** is the axial loading (8,000 lb$_f$ in this case), p is pitch, n_t is the number of engaged threads and d_r is the inner most diameter. The calculated values are found to be:

$$\sigma_{x_t} = \frac{6(8,000lb_f)}{\pi(4.6181\ in)(6.4)(0.25\ in)} = 2,067.79\ psi$$

$$\sigma_{y_t} = -\frac{4(8,000lb_f)}{\pi(4.6181\ in)^2} = -477.61\ psi$$

$$\tau_t = \frac{3(8,000lb_f)}{\pi(4.6181\ in)(6.4)(0.25\ in)} = 1,033.9\ psi$$

Again, Equation 106 can be employed again to find the maximum thread stress

$$\sigma_{max} = \frac{2,067.79 \pm 477.61}{2} + \sqrt{\left(\frac{2,067.79 + 477.61}{2}\right)^2 + 1,033.9^2}\ [psi]$$

$$\sigma_{max} = 2,912.43\ psi$$

This maximum calculated value is well below the yield stress of the shaft material (σ_y = 100,000 psi).
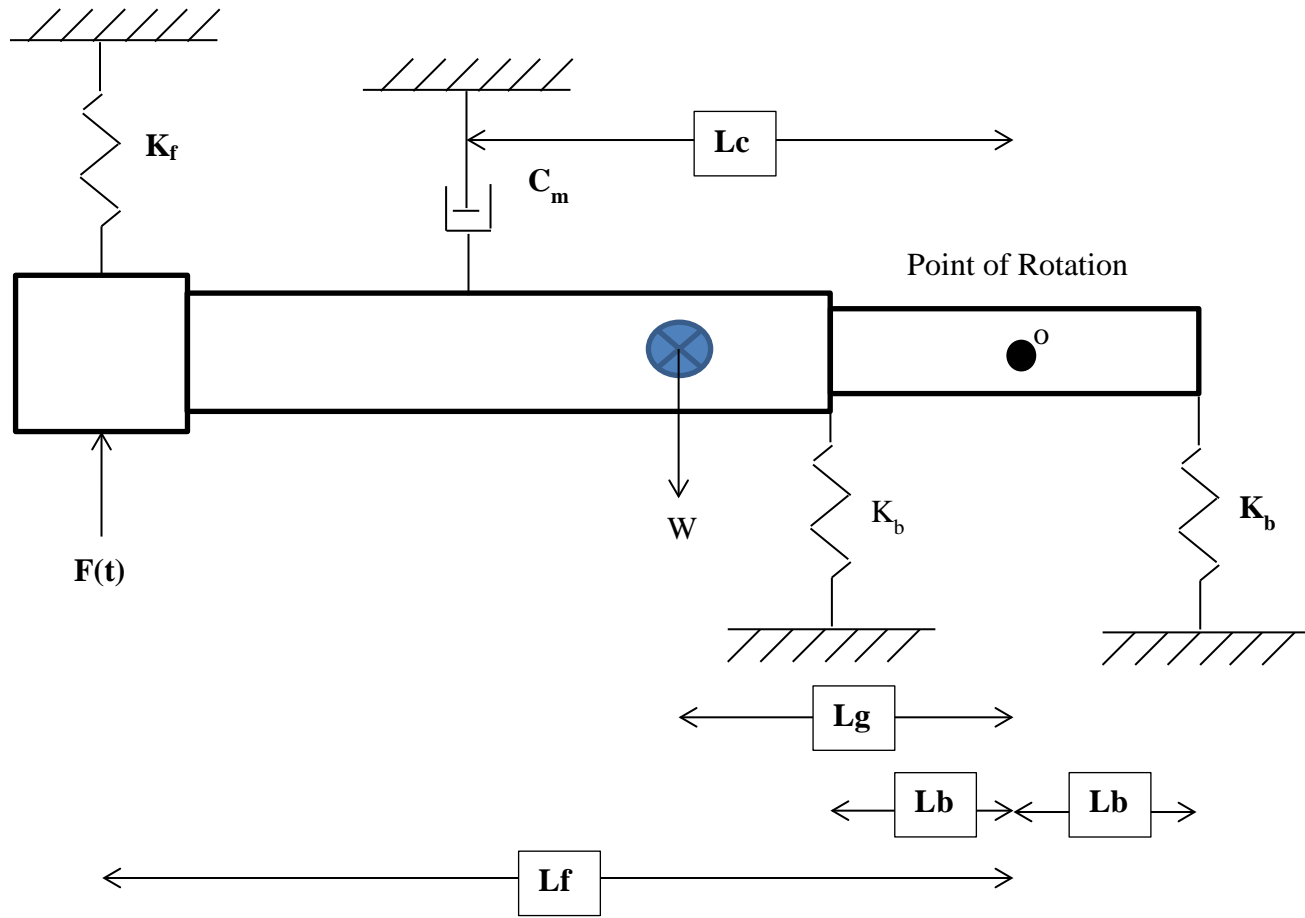
Figure AK.3: Drill Shaft Vibration Model

The drill shaft is a dynamic rotor system that has the potential to vibrate (Figure AK.3). For this reason, it is imperative to recognize the impact of these vibrations on the system. First the equilibrium configuration of the shaft must be determined, and then oscillations about that position can be investigated.
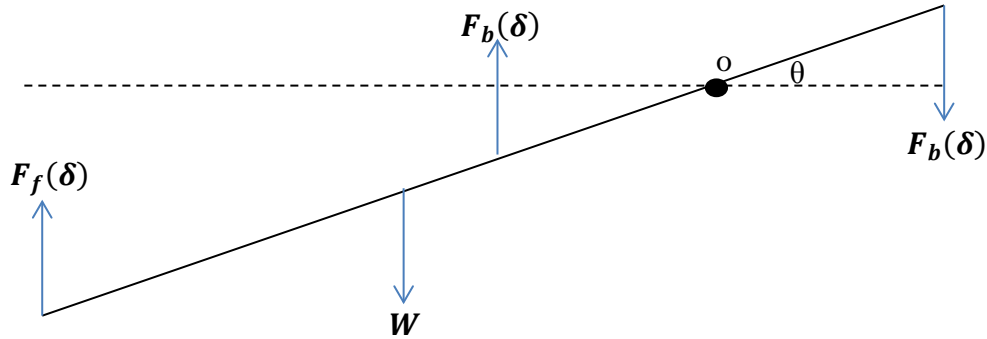
Figure AK.4: Static FBD of Drill Shaft

Figure AK.4 depicts the forces acting on the shaft in its static equilibrium position. Writing a moment balance about point o, an expression for equilibrium is obtained

$$WL_g = F_f(\delta)L_f + 2F_b(\delta)L_b \hspace{4cm} \text{Eq. 112}$$

Where $\mathbf{F_f}(\delta)$ and $\mathbf{F_b}(\delta)$ represent the forces generated by the "springs" at the equilibrium displacement angle, δ. Now the dynamic displacement must be accounted for by assuming small rotations from the equilibrium. Figure AK.5 displays the forces acting on the shaft in a dynamic configuration. Notice that the forces from the spring elements are summations of the static displacement force and the dynamic displacement force.
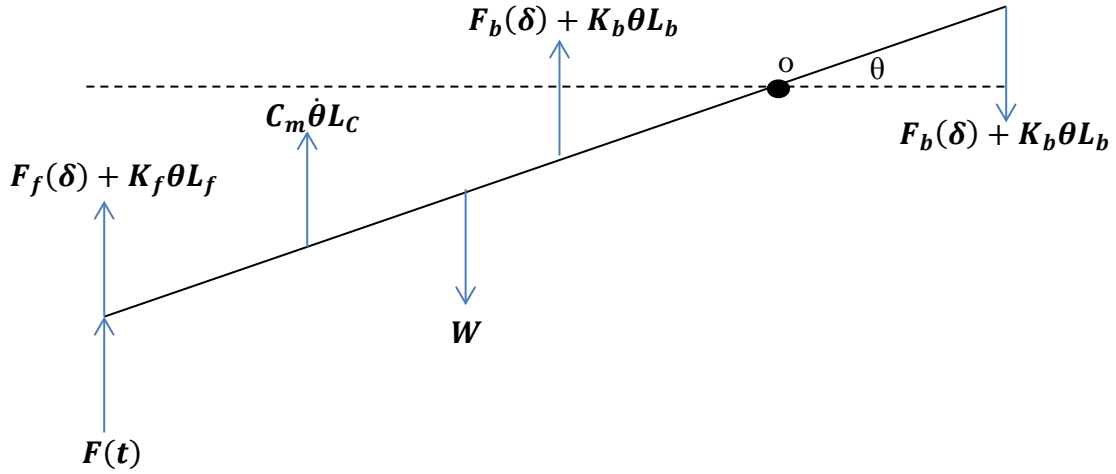
Figure AK.5: Dynamic FBD of Drill Shaft

Summing the moments about the point of rotation, an equation of motion can be written as

$$\ddot{\theta}I_o = -\big[F(t) + F_f(\delta) + K_f\theta L_f\big]L_f - 2\big[F_b(\delta) + K_b\theta L_b\big]L_b - C_m\dot{\theta}L_C^2 + WL_g$$

Eq. 113

Combining Equation 112 and 113, the EOM is reduced to

$$I_o\ddot{\theta} + C_mL_C^2\dot{\theta} + \big[K_fL_f^2 + K_bL_b^2\big]\theta = -F(t)L_f \qquad \text{**Eq. 114**}$$

Where $\mathbf{K_f}$ is the effective formation stiffness, $\mathbf{K_b}$ is the radial bearing stiffness, $\mathbf{C_m}$ viscous damping coefficient from the drilling fluid and L* are the associated lengths.

The quantification of this stiffness is determined from the formation displacement study whose results are shown in Section 3. By averaging the displacements of the formations under a 4,000 lb$_f$ load the formation stiffness can be estimated.

$$K_f = \frac{4{,}000}{\delta_{ang}} \qquad\qquad \textbf{Eq. 115}$$

$$\delta_{ang} = 0.000268 \; in \qquad\qquad \textbf{Eq. 116}$$

$$K_f \cong 14917421.45 \; \frac{lb_f}{in}$$

The bearing stiffness, **K$_b$**, is approximated from limited manufacturer data. From the bearing designer a plot of axial deflection vs. axial load for the Spherical Roller Thrust Bearing is shown.
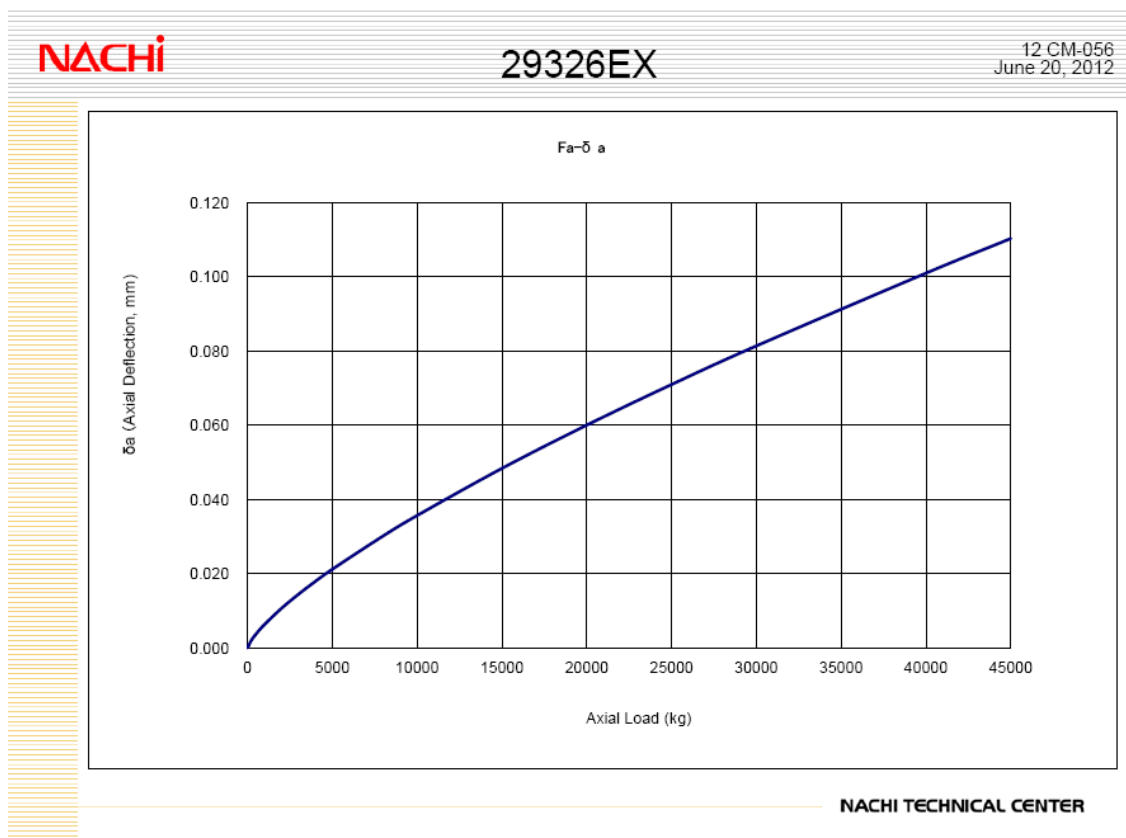
Figure AK.6: Axial Stiffness of Spherical Roller Thrust Bearing

It is obvious from Figure AK.6 that the bearing acts as a non-linear spring. From this data it can be assumed that the radial deflection of the bearing would be non-linear as well. However, the only data that could be obtained from the manufacturer in regards to radial deflection is the following figure.
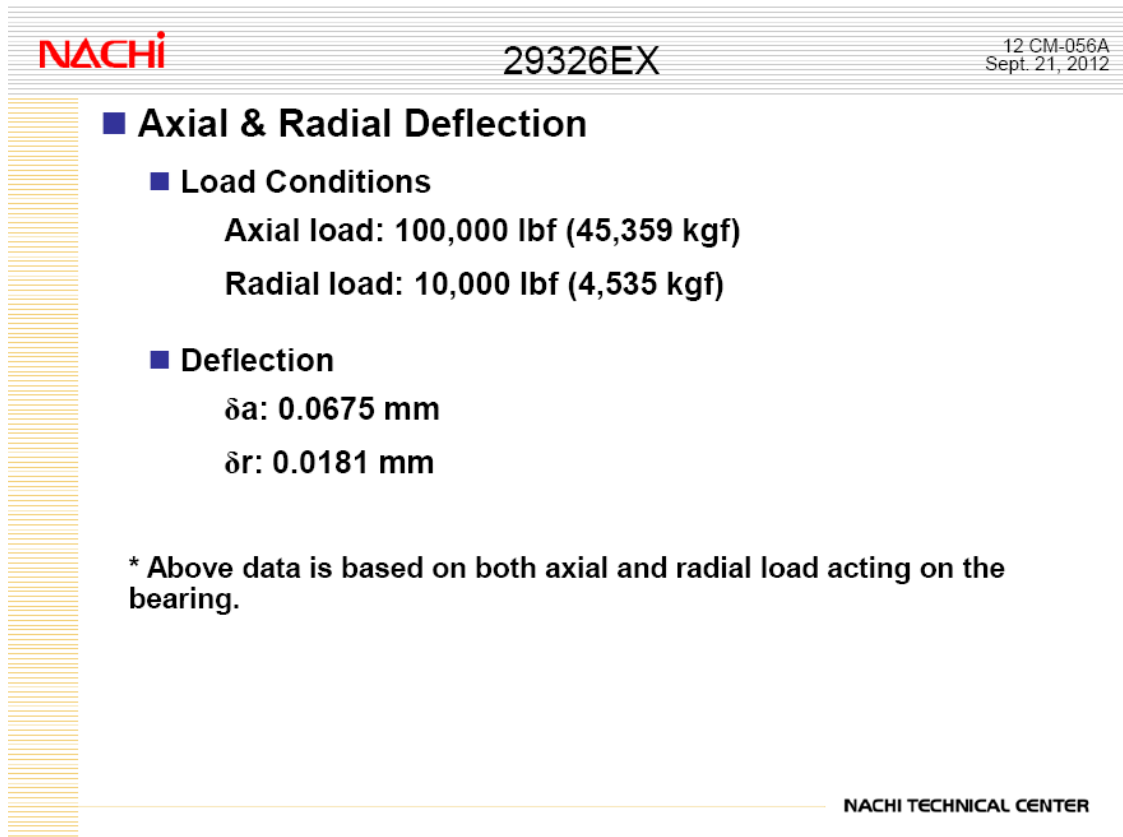
Figure AK.7: Radial Stiffness of Spherical Roller Thrust Bearing

Therefore the only assumption about the bearing Stiffness that can be made from Figure AK.7 is that it is a linear relationship between load and deflection given as the following

$$10,000 = \left(\frac{0.0181}{25.4}\right) K_b \qquad \text{Eq. 117}$$

$$K_b \cong 14033149.17 \frac{lb_f}{in}$$

The damping coefficient, C_m, was estimated following Jansen [141].

$$C_m = \frac{4}{3\pi} c_f L \qquad \text{Eq. 118}$$

$$c_f = \rho_m C_d \frac{OD_p}{2} \qquad \text{Eq. 119}$$

Where L is the length of contact between the fluid and the pipe, ρ_m is the density of the drilling fluid, C_d is the drag coefficient of the cylindrical pipe which is assumed to be 1, and OD_p is the outer diameter of the drill shaft.

The quantity of interest for the shaft's design in the natural frequency, given by

$$\omega_n = \sqrt{\frac{K}{I_o}} \qquad \text{Eq. 120}$$

Where K is equal to

$$K = K_f L_f^2 + 2K_b L_b^2 \qquad \text{Eq. 121}$$

And I_o is calculated in Solidworks as 535600 lb_f*in^2. Using the following dimensions

L_c = 40 in $\qquad\qquad\qquad\qquad$ L_g = 22.75 in

L_f = 70.75 in $\qquad\qquad\qquad\qquad$ L_b = 8 in

The natural frequency of the system is estimated to be

$$\omega_n = 378 \frac{rad}{s}$$

If it is assumed that the bit rotates at it maximum RPM (200 rpm) and the largest number of "blades" of a bit will be 7, then the maximum excitation frequency can be written as

$$\omega_{max} = 7\frac{200\ rot}{min}\frac{2\pi\ rad}{1\ rot}\frac{1\ min}{60\ s} = 147\ \frac{rad}{s} \qquad \textbf{Eq. 122}$$

The largest anticipated operational frequency is found to be 2 ½ times less than the natural frequency, thus the drill shaft is assumed to never reach resonance at any operating regime of bit rotation.

Recalling that the bearing stiffness was a very rough estimate, it is important to determine the effect of the value of this stiffness on the systems response.
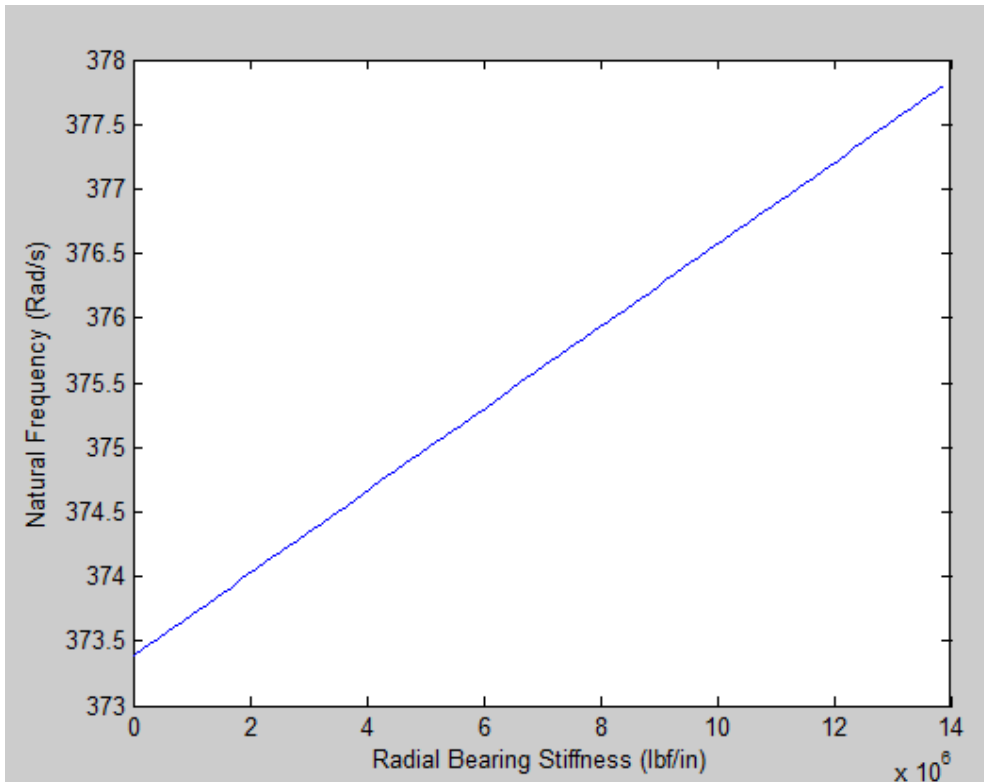
Figure AK.8: Variation of System Natural Frequency vs. Radial Bearing Stiffness

As can be seen from Figure AK.8, adjusting the bearing stiffness significantly does not greatly affect the natural frequency, so whether the bearing stiffness is the previously indicated value or if it is much less, the system should maintain a response that does not approach resonance.

Knowing that the natural frequency will never be reached, it is still important to investigate how large the magnitudes of oscillations could be and the associated forces. Utilizing Maple and taking a "worst case scenario" approach, in which a 4,000 lb$_f$ side load is instantaneously applied to the bit, we find that maximum rotation angles are on the order of 0.0002 degrees and radial forces at the bearings are near 800 lb$_f$ (see the following Maple Worksheet). The first plot that is shown is Rotation Angle (deg) vs. Time and the second plot is the Radial Bearing Force vs. Time.

> $restart$;
> $IN := 535600$:
> $T := Fo \cdot \sin(\omega \cdot t)$:
> $\omega := \dfrac{2 \cdot 3.14159265359}{60} \cdot 200 \cdot 7$;

$$\omega := 146.607657$$

> $W := 570$:
> $Fo := 100$:
> $Cm := 515.153$:
> $Kf := 14917421.42$:
> $Kb := 14033149$:
> $Lc := 40$:
> $Lf := 70.75$:
> $Lg := 22.75$:
> $Lb := 8$:

> $C := Cm \cdot Lc^2$;

$$C := 8.242448001 0^5$$

> $K := Kf \cdot (Lf)^2 + 2 \cdot Kb \cdot Lb^2$;

$$K := 7.646632833 10^{10}$$

> $de := IN \cdot diff(y(t), t\$2) + C \cdot diff(y(t), t\$1) + K \cdot y(t) = -T + 4000$
> $\cdot Lf$;

$$de := 535600\left(\frac{d^2}{dt^2}\,y(t)\right) + 8.242448001\,10^5\left(\frac{d}{dt}\,y(t)\right)$$
$$+ 7.646632833\,10^{10}\,y(t) = -100\sin(146.6076571t)$$
$$+ 2.83000001\,10^5$$

> $\theta := rhs(dsolve(\{de, y(0) = 0, D(y)(0) = 0\}, y(t)));$

$$\theta := -3539626000322362373368107746586123855533314114625209\!\!\!\!/$$
$$1290315409760041925537143247048849244639316781172711299\!\!\!\!$$
$$69280905609653\,e^{-\frac{515153}{669500}\,t}\sin\!\left(\frac{1}{669500}\,\sqrt{63992493138555341}t\right)$$
$$\sqrt{63992493138555341}$$
$$-\,7462483566274031160054466539851243554059342488\!\!\!\!/300$$
$$2016354335447245820365098021003401503132253664361367 4\!\!\!\!3$$
$$e^{-\frac{515153}{669500}\,t}\cos\!\left(\frac{1}{669500}\,\sqrt{63992493138555341}t\right)$$
$$+\,\frac{28300}{7646632833}$$
$$+\,\frac{7552537437803630000000000000000000000}{263691794739433099751279508179231220991496201}$$
$$\cos\!\left(\frac{1466076571}{10000000}\Big/t\right)$$
$$-\,\frac{40596403942212442357752500000000000000}{263691794739433099751279508179231220991496201}$$
$$\sin\!\left(\frac{1466076571}{10000000}\Big/t\right)$$

> $\omega_n := \sqrt{\dfrac{K}{IN}}\,;$

$$\omega_n := 377.846004'$$

> $DR := \dfrac{C \cdot \omega_n}{2 \cdot K};$

$$DR := 0.00203643624$$

> $with(plots):$
> $plot\!\left(\dfrac{\theta \cdot 180}{3.14159265359}, t = 0..10\right);$

236

> $plot\big(\theta \cdot (Lb) \cdot Kb, t = 0..10\big);$

237
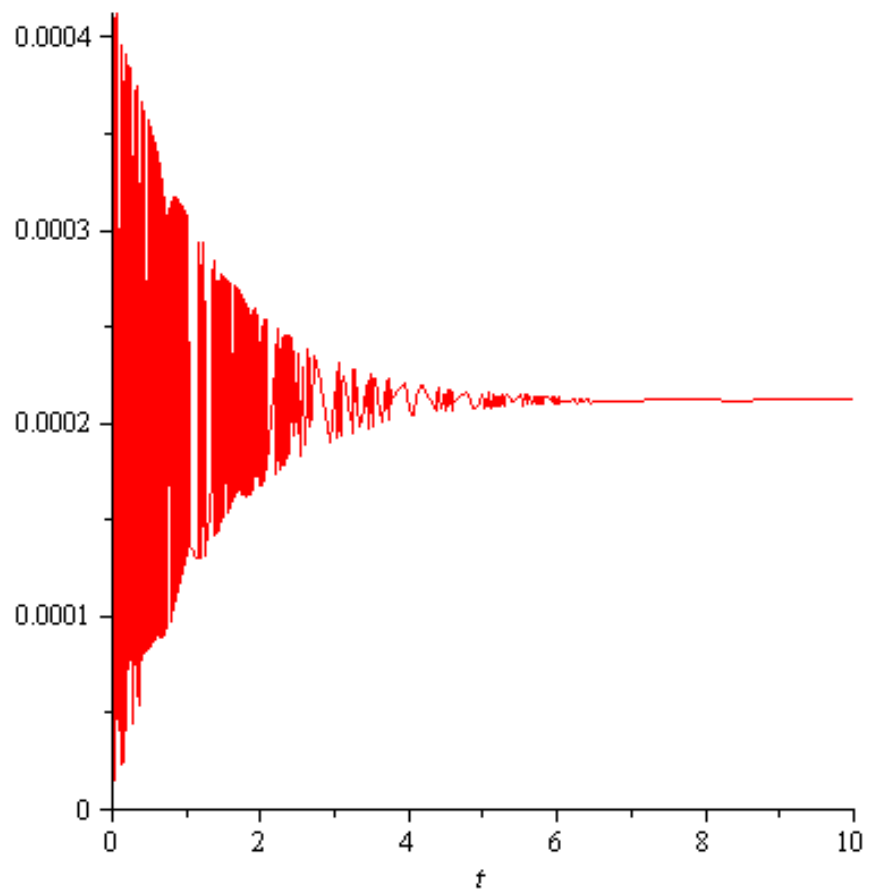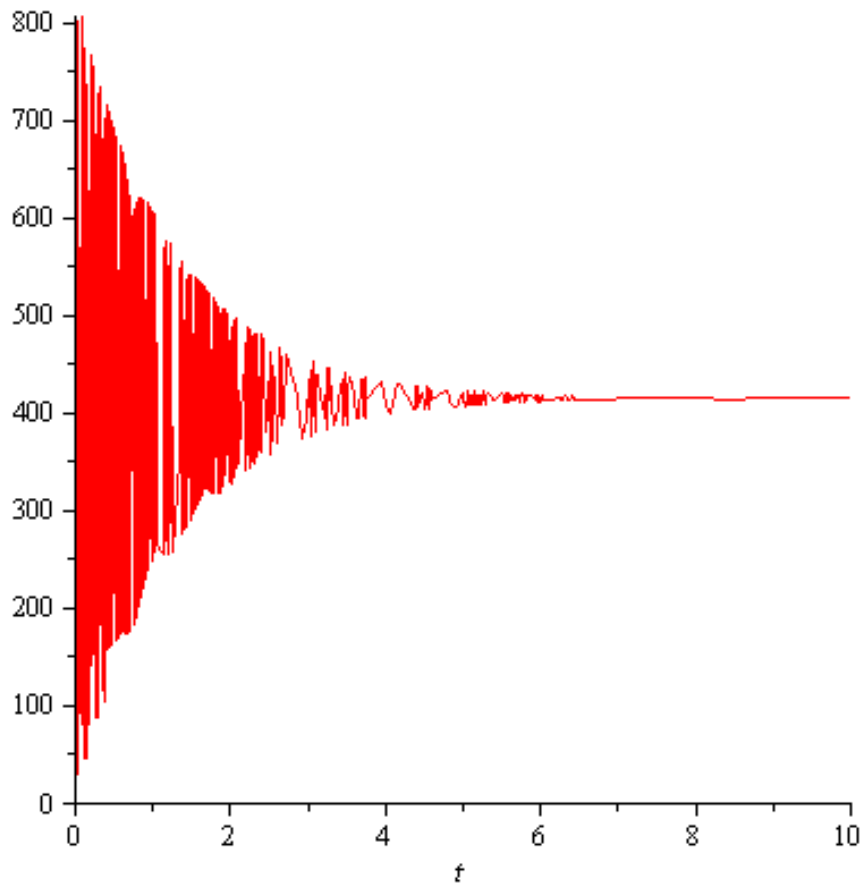
Again, it is important to look at a "worst case scenario" due to the uncertainty in the radial bearing stiffness. So, taking K_b to be zero it can be shown that, while the system appears to oscillate for a lightly longer period of time, the displacement is roughly the same (See Figure AK.9).
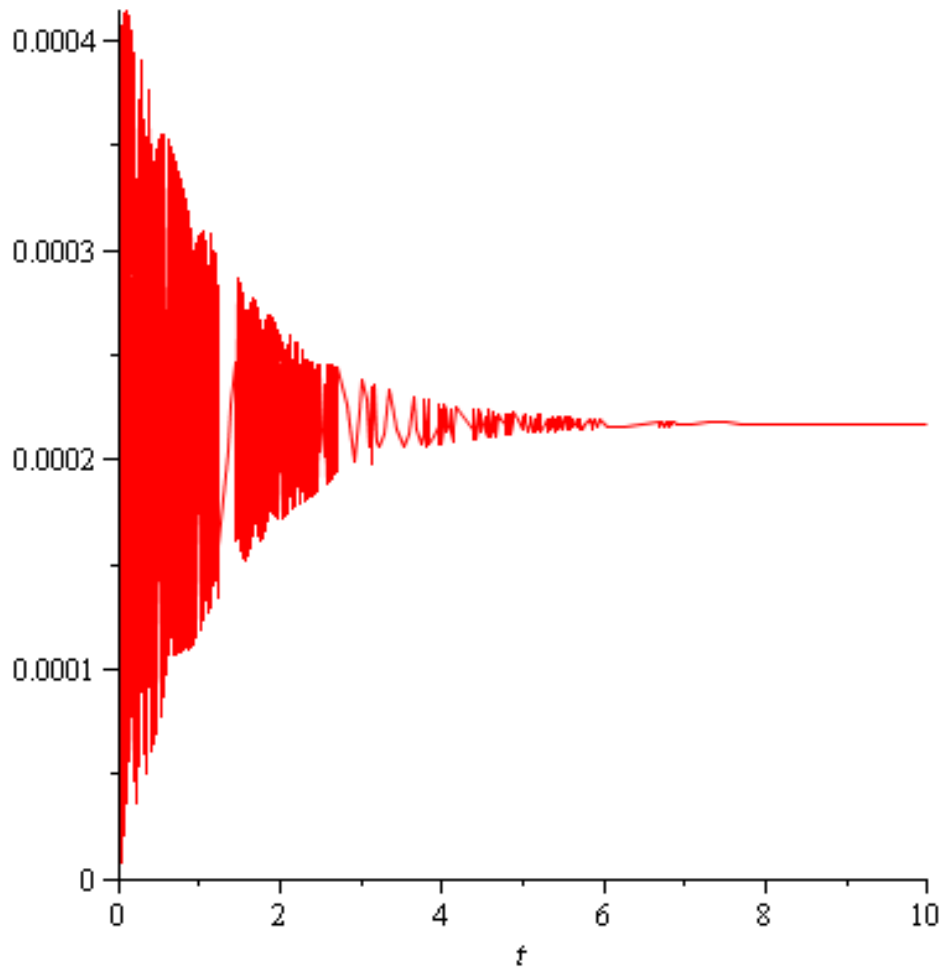
Figure AK.9: Amplitude vs. Time for K_b = 0

APPENDIX L – ROD CALIBRATION DATA
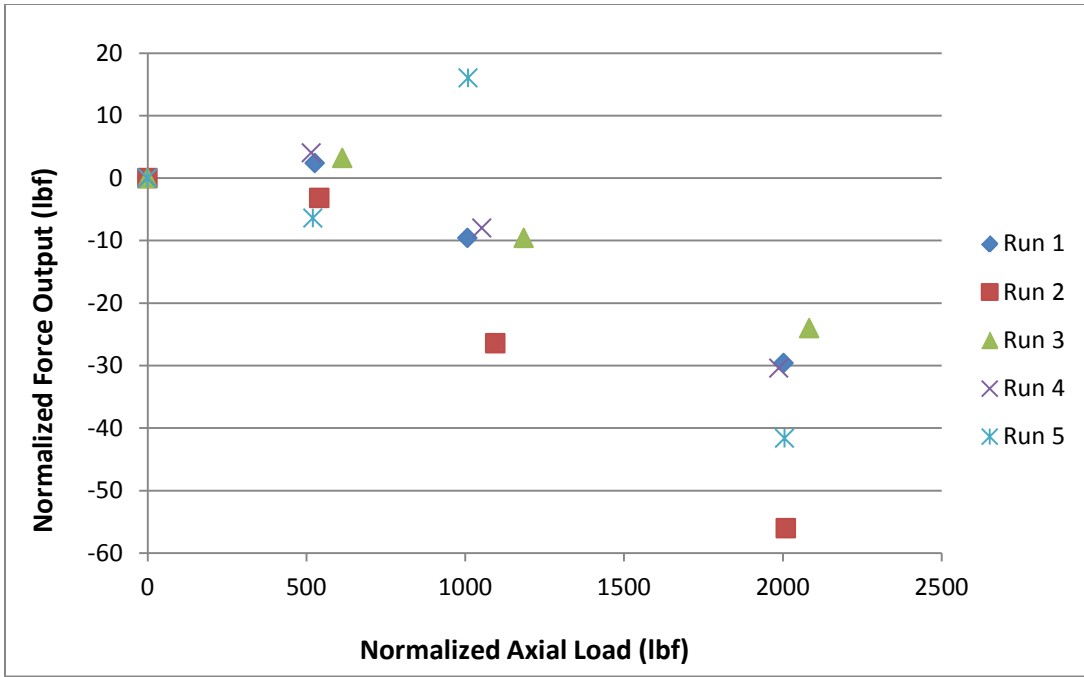
Rod 2
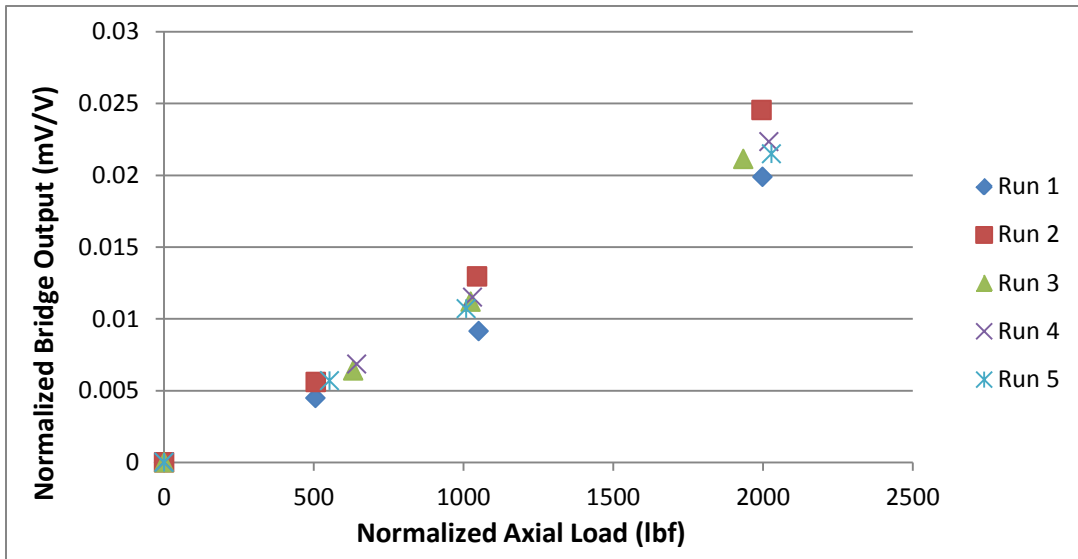
L1 – Axial Calibration (Rod 2)
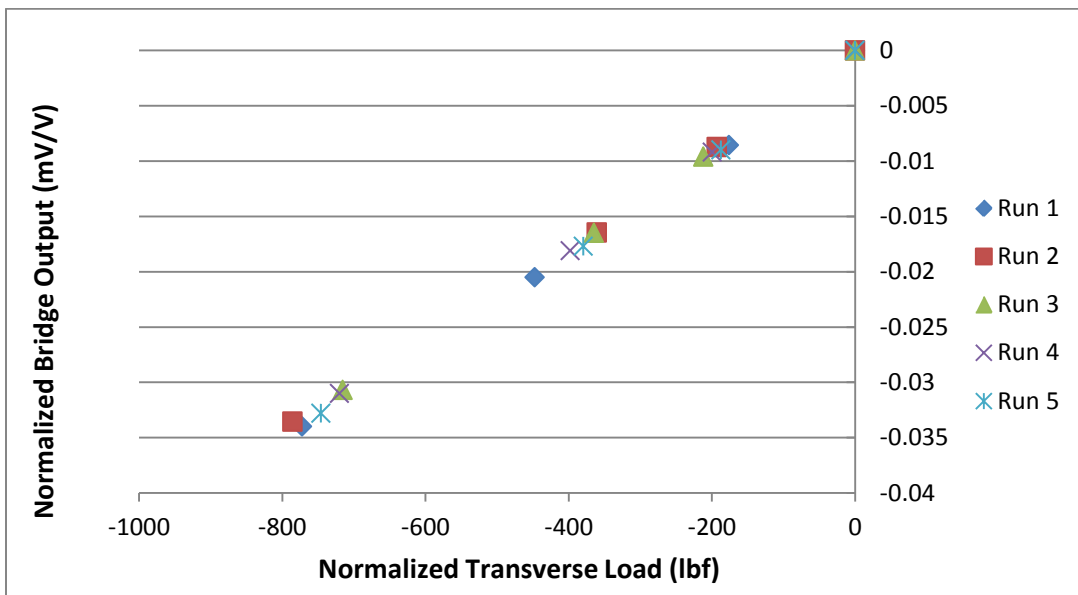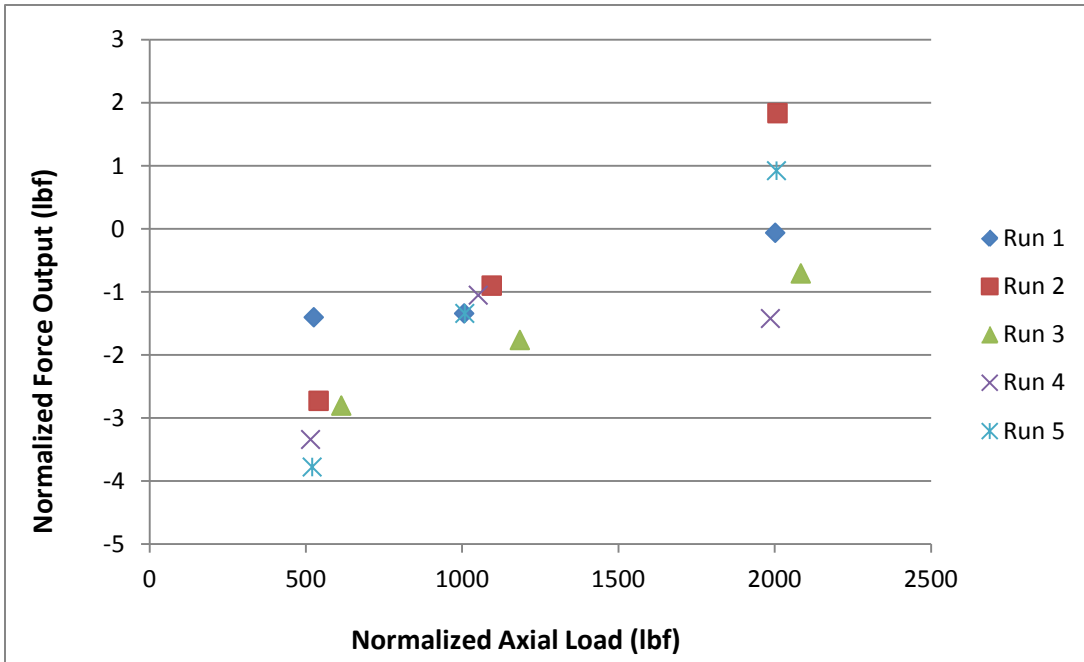

L2 – X Calibration (Rod 2)
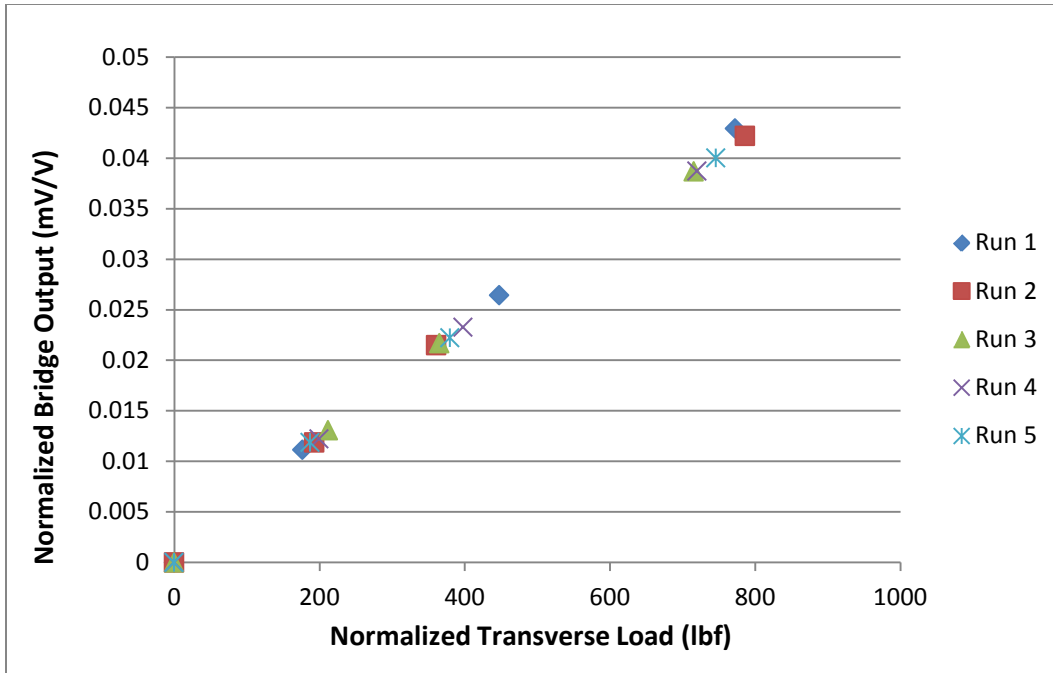
L3 – Y Calibration (Rod 2)
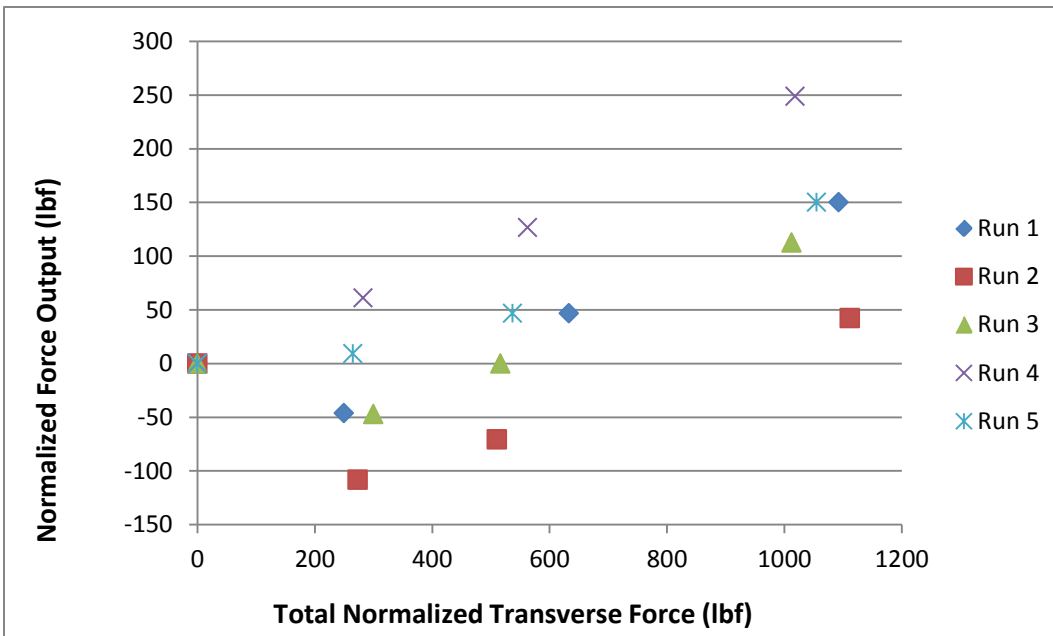
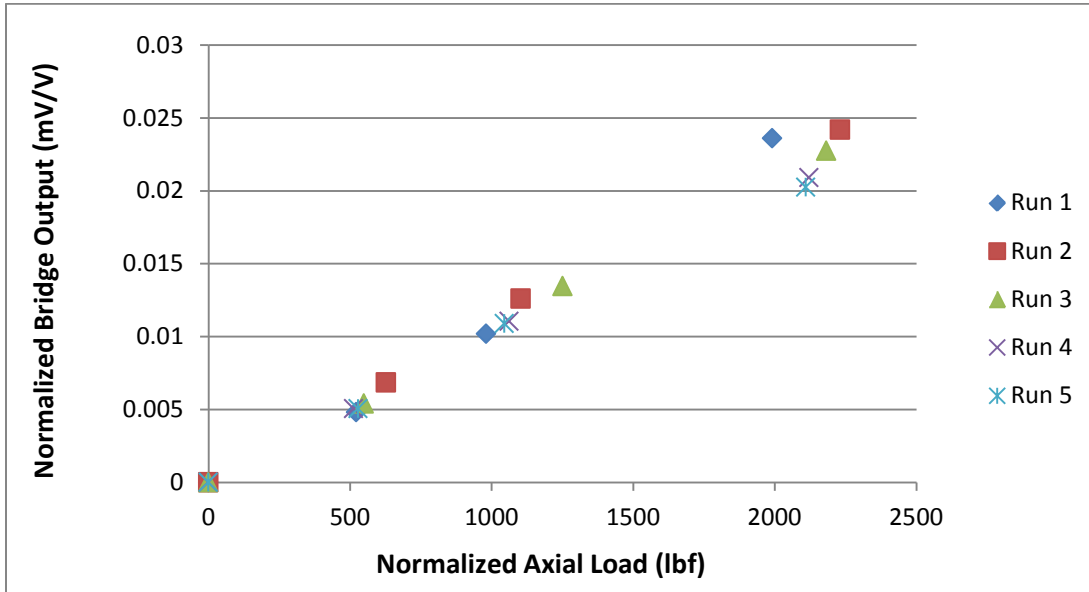**L4 – Axial Sensitivity to Transverse Loading (Rod 2)**
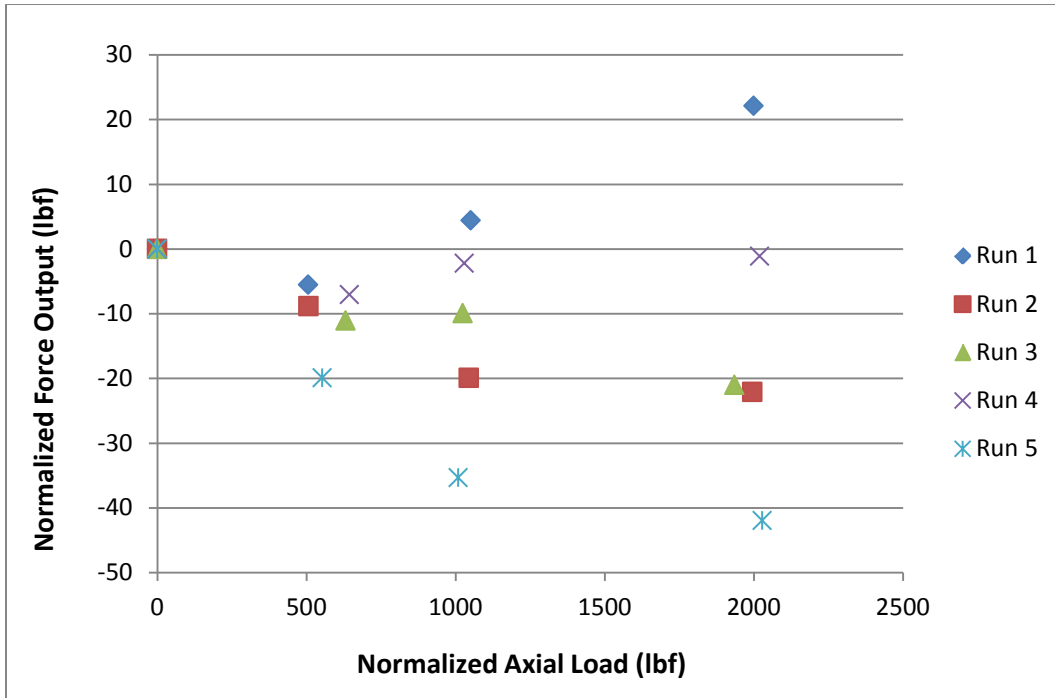
L5 – X Sensitivity to Axial Loading (Rod 2)
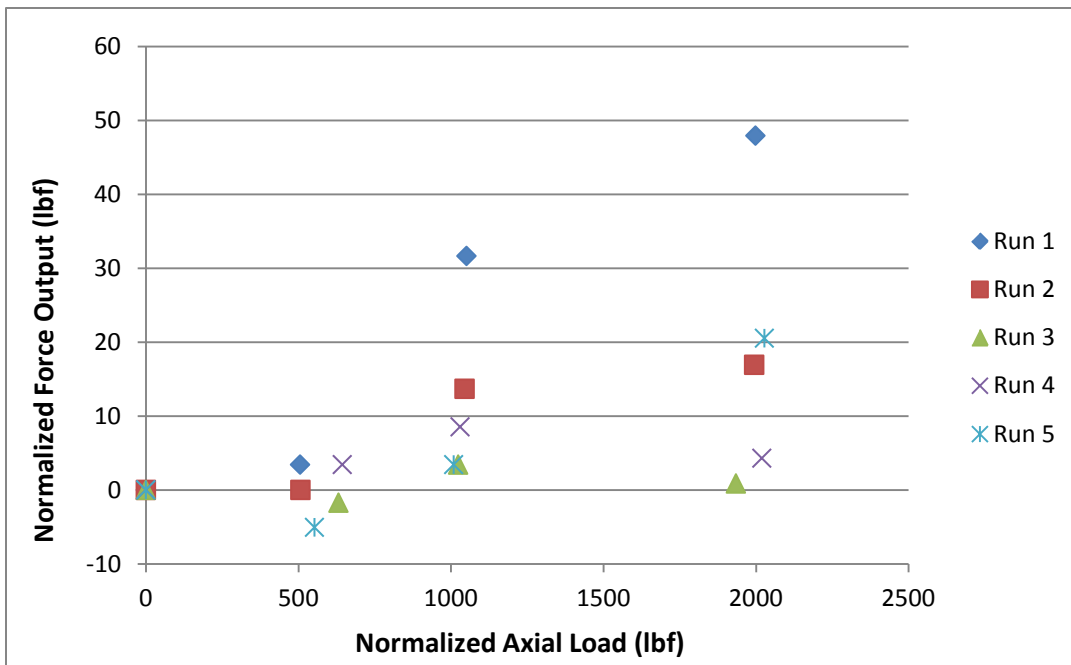
L6 – Y Sensitivity to Axial Loading (Rod 2)

242
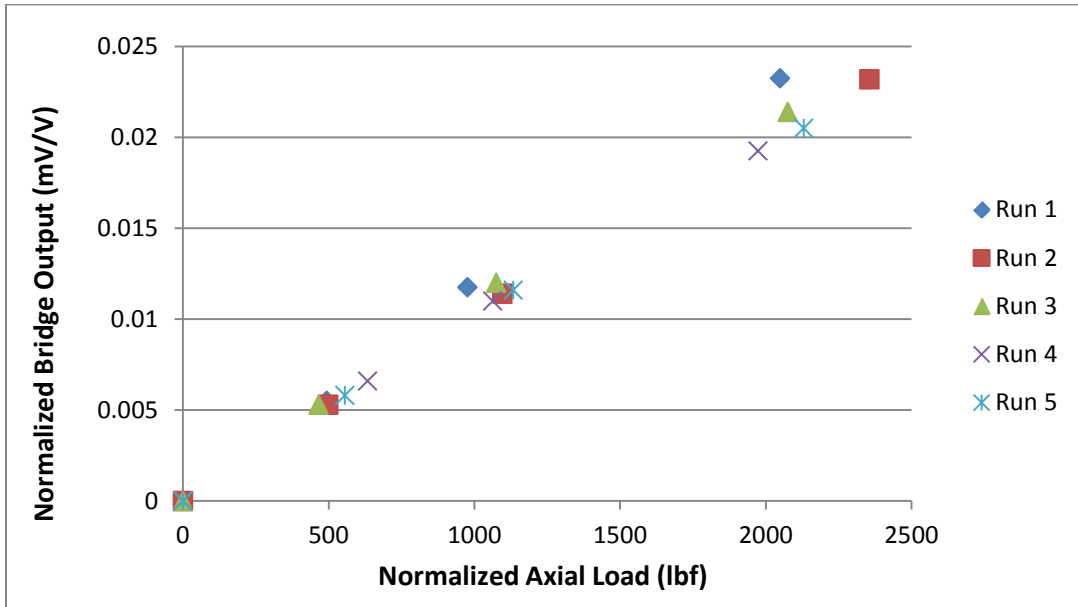
Rod 3

L7 – Axial Calibration (Rod 3)
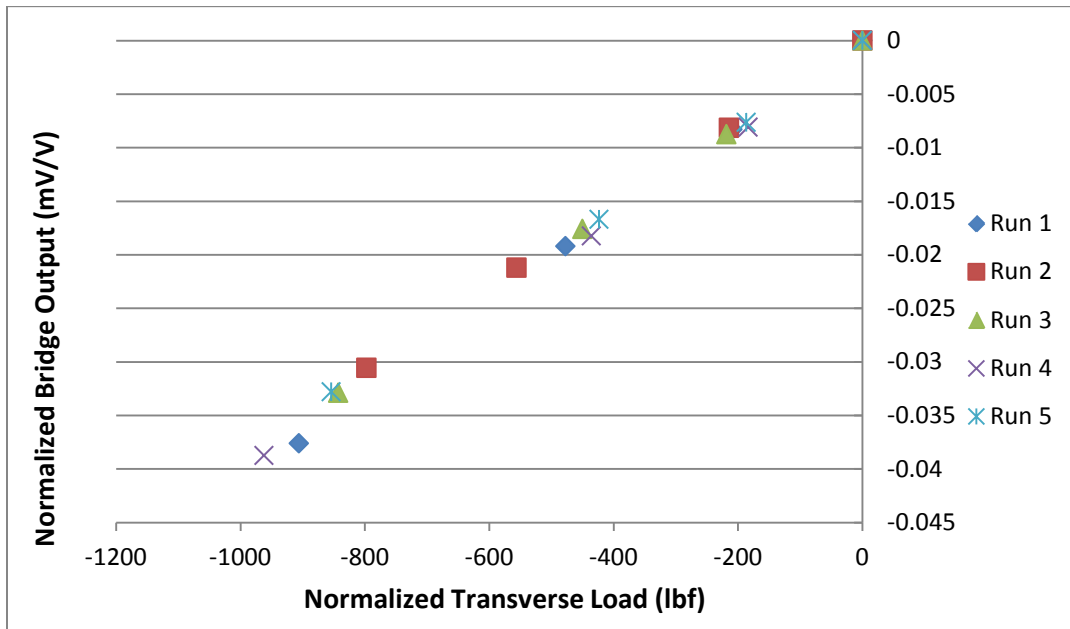
L8 – X Calibration (Rod 3)

243
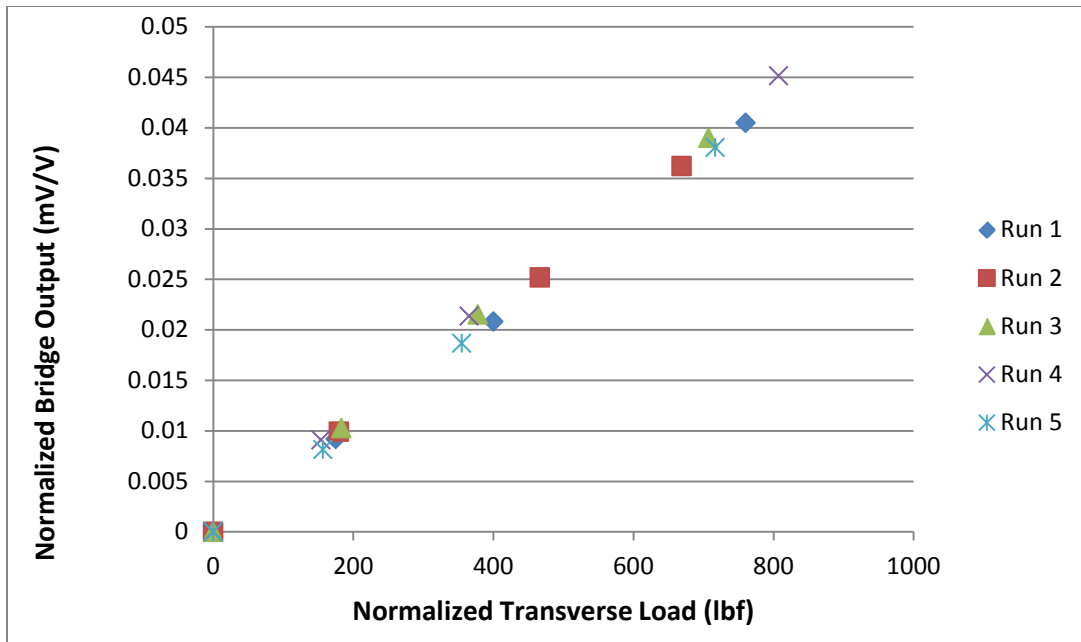
L9 – Y Calibration (Rod 3)
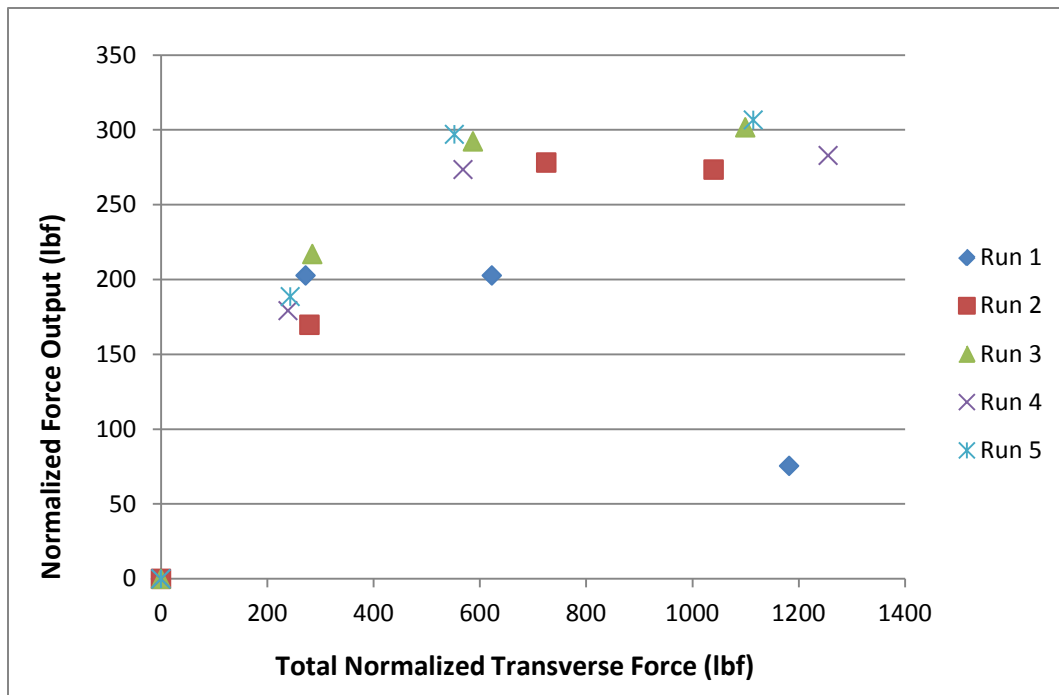
L10 – Axial Sensitivity to Transverse Loading (Rod 3)

244
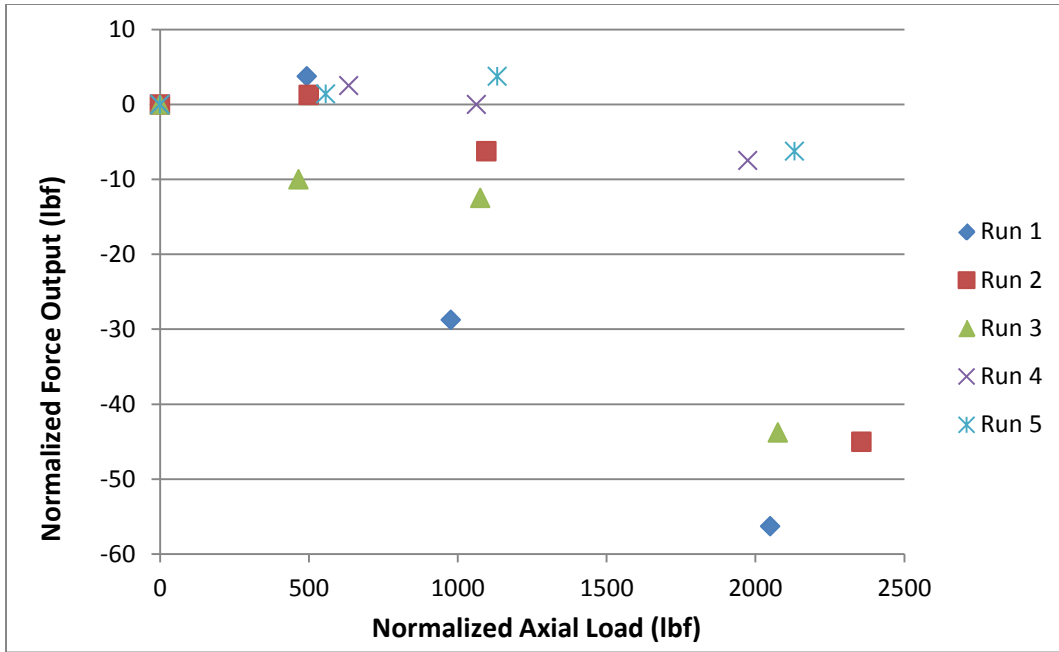
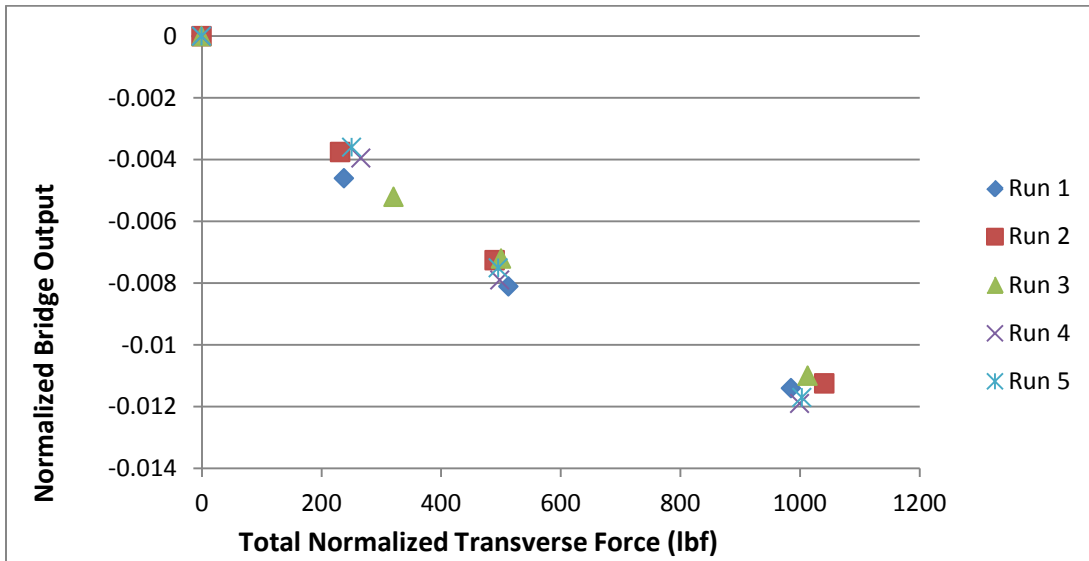**L11 – X Sensitivity to Axial Loading (Rod 3)**
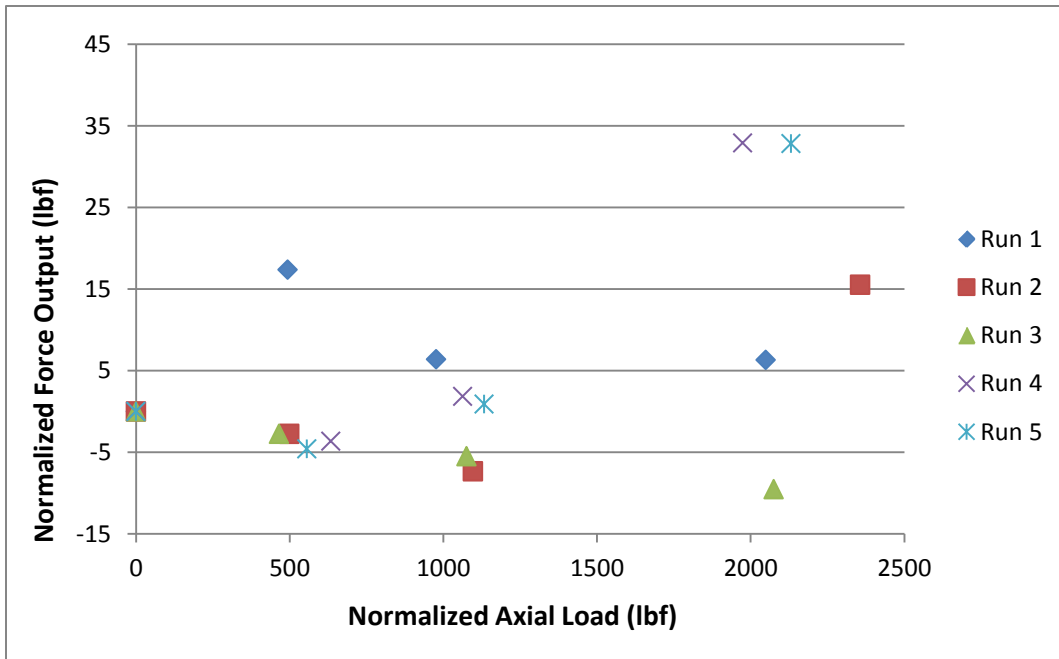
L12 – Y Sensitivity to Axial Loading (Rod 3)

Rod 4
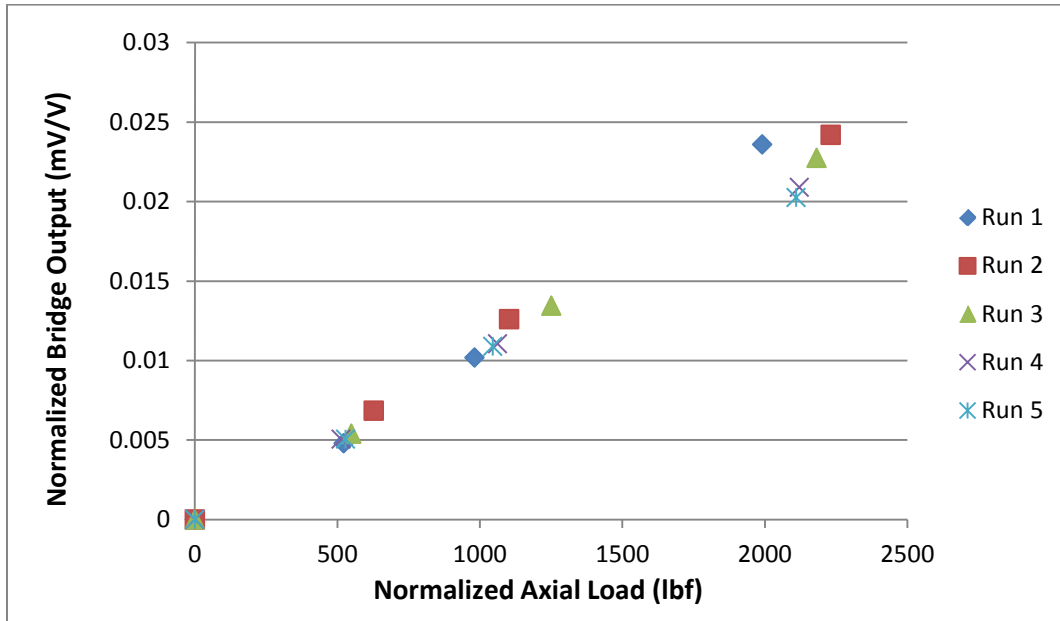
L13 – Axial Calibration (Rod 4)
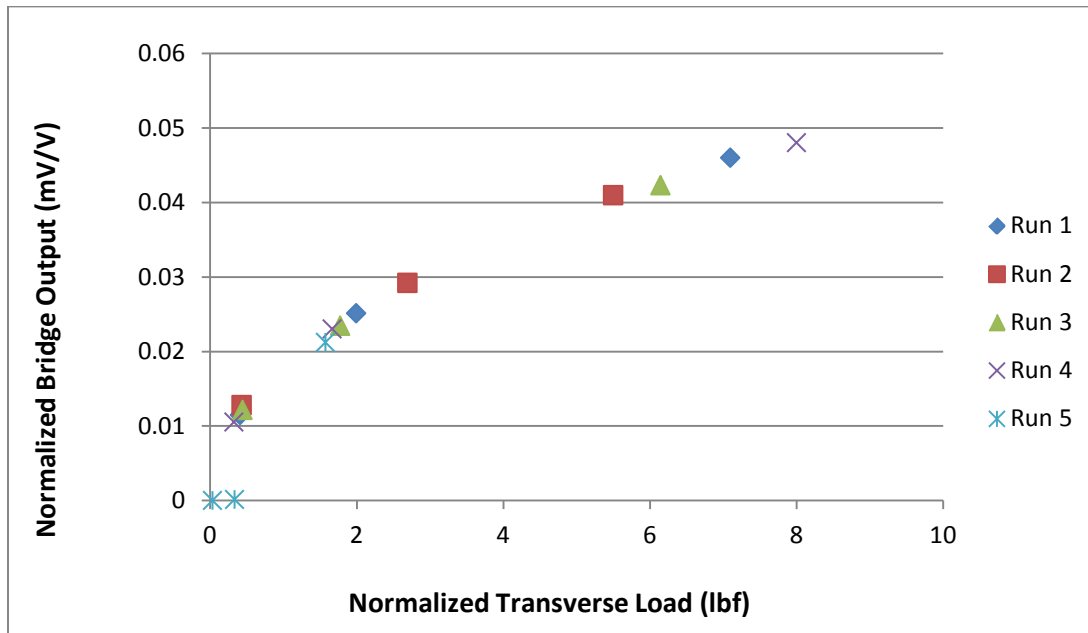
L14 – X Calibration (Rod 4)
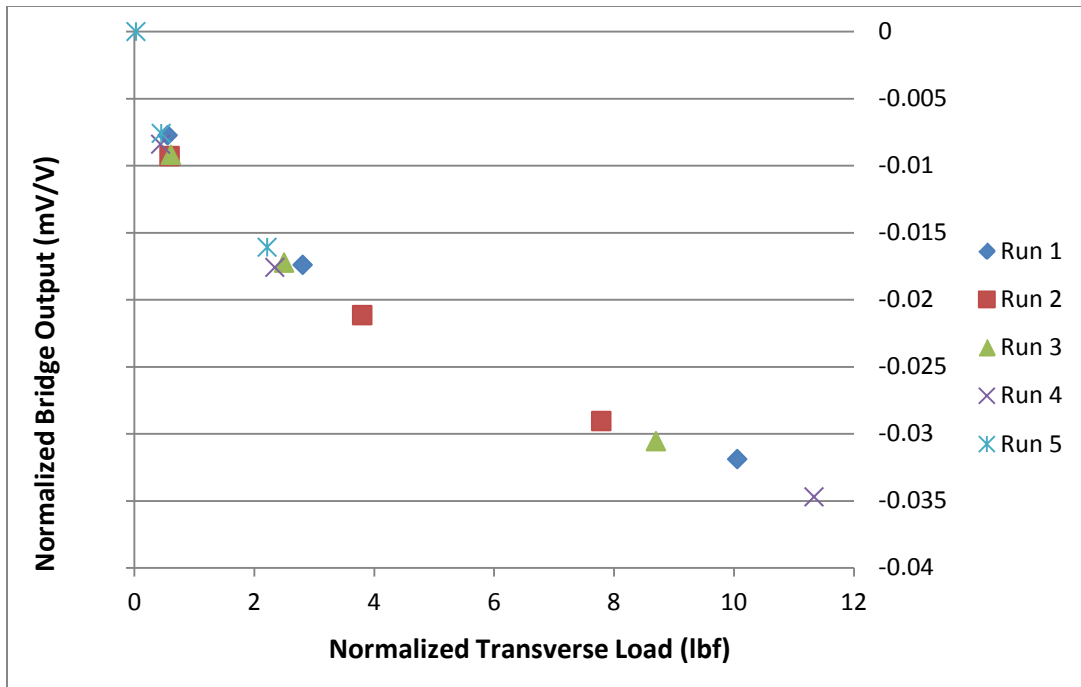
L15 – Y Calibration (Rod 4)
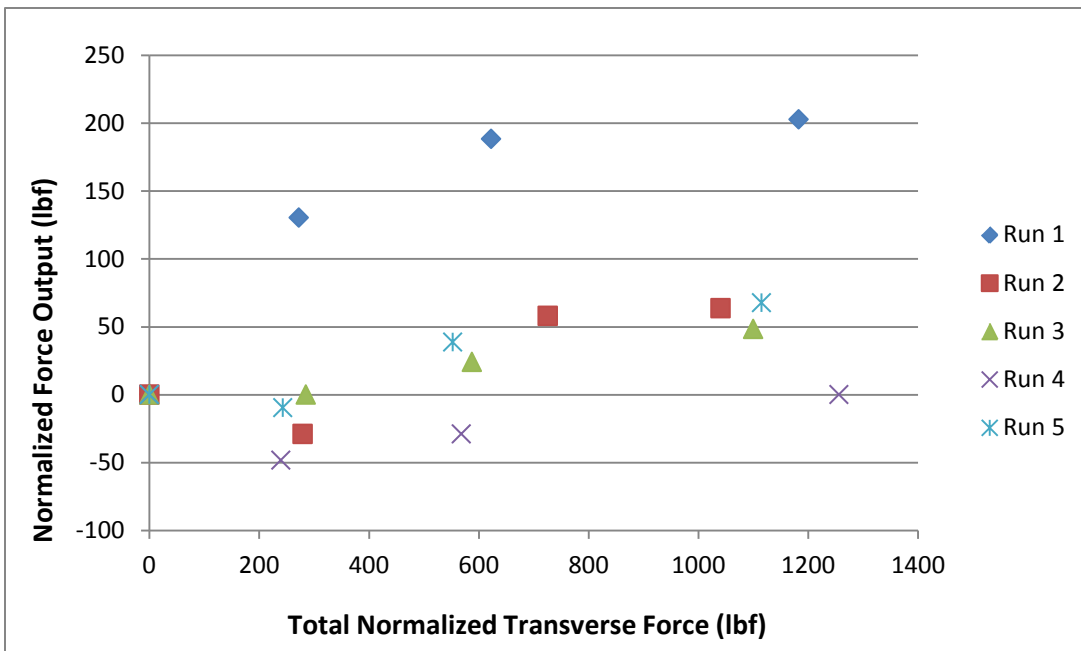
L16 – Axial Sensitivity to Transverse Loading (Rod 4)

247
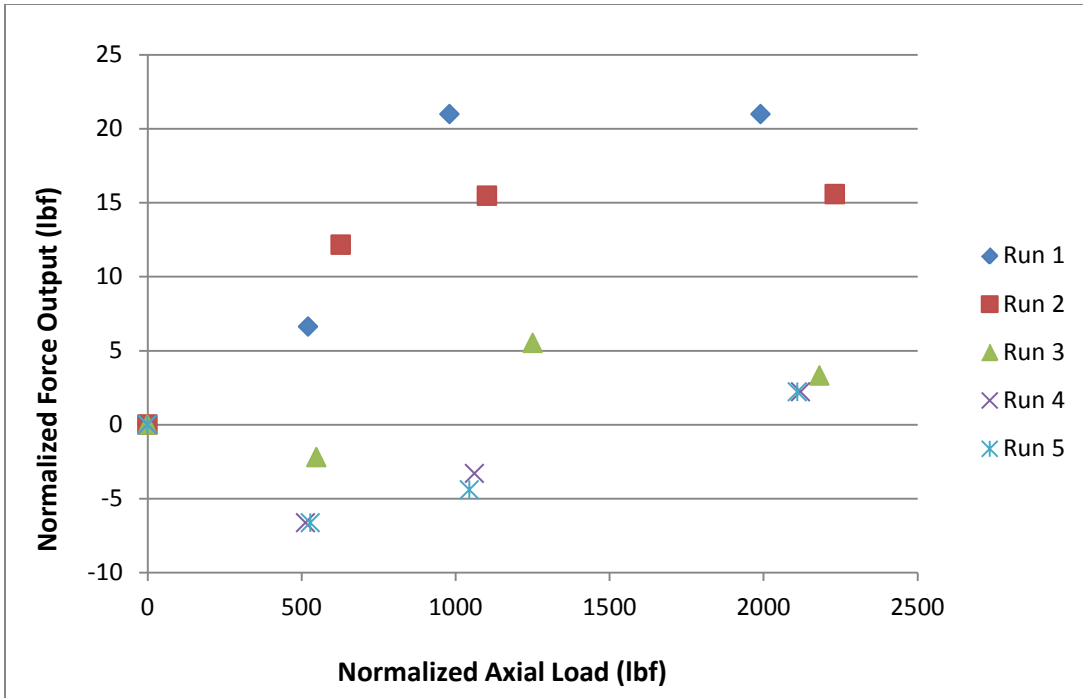
L17 – X Sensitivity to Axial Loading (Rod 4)
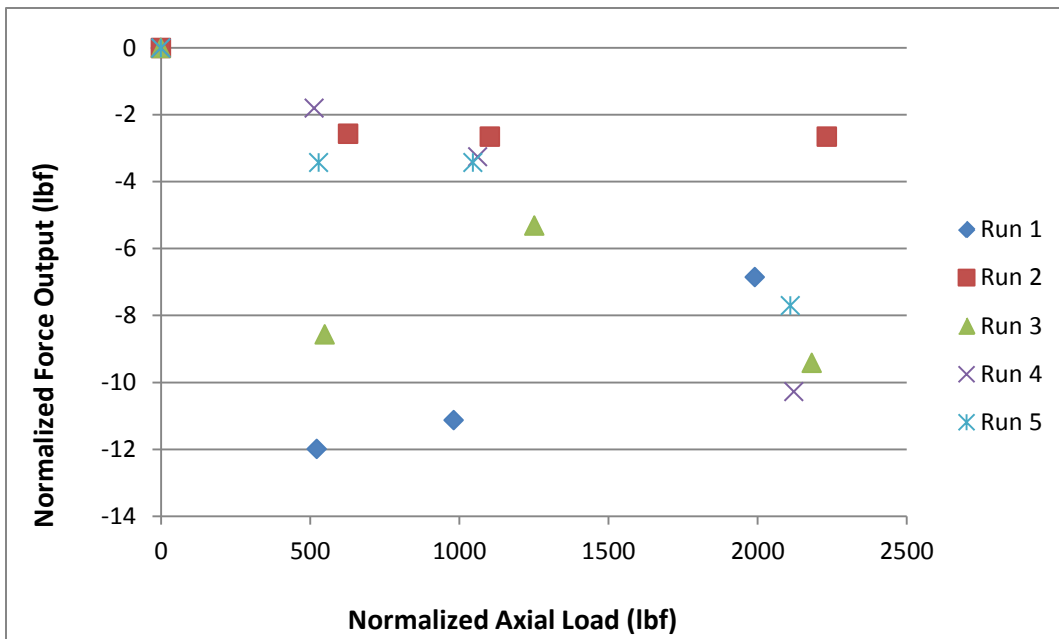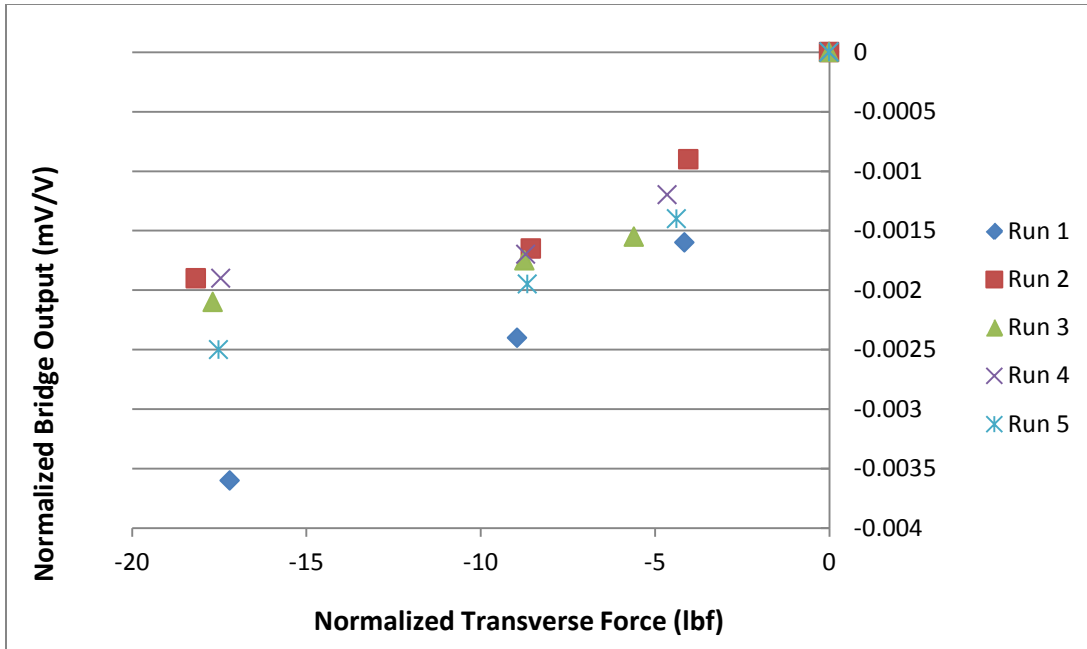

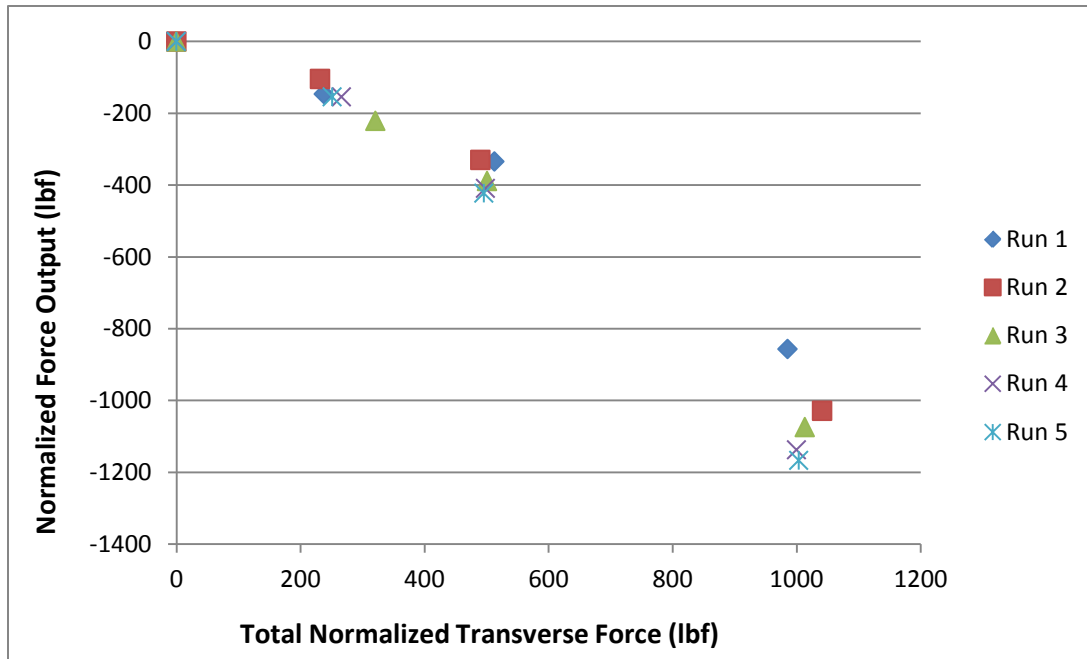**L18 – Y Sensitivity to Axial Loading (Rod 4)**

248
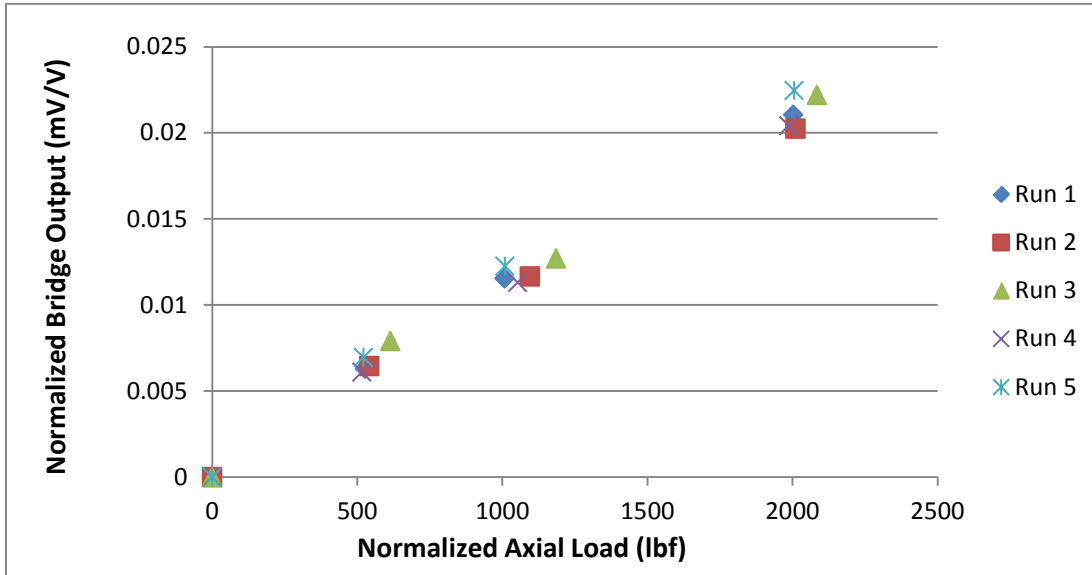
Rod 5

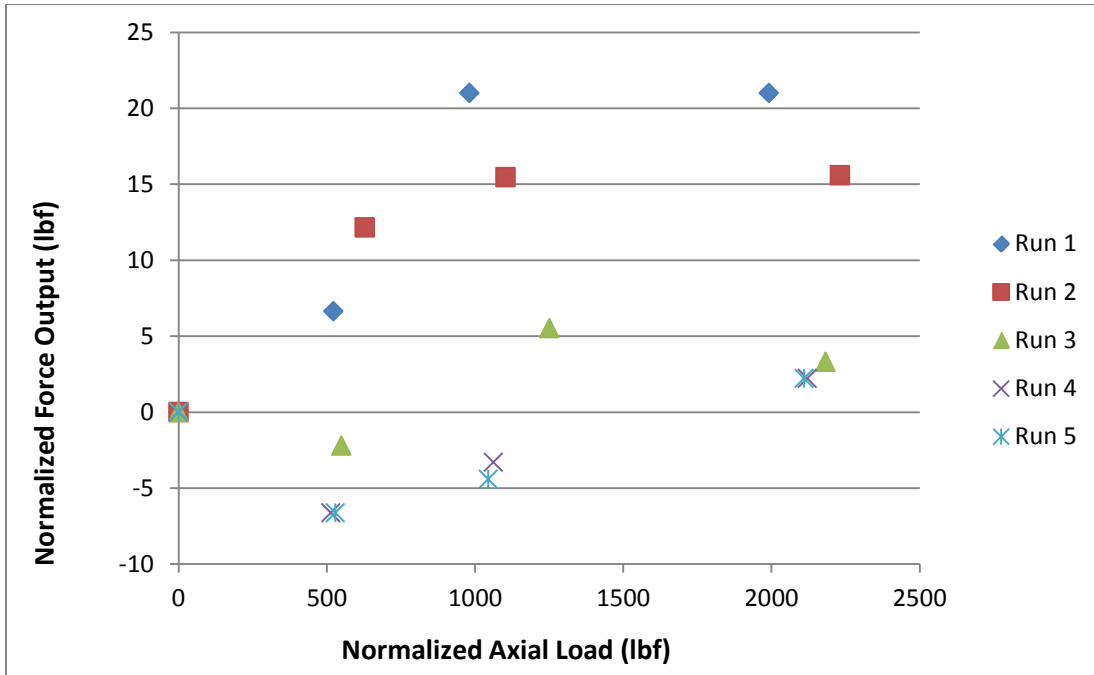**L19 – Axial Calibration (Rod 5)**
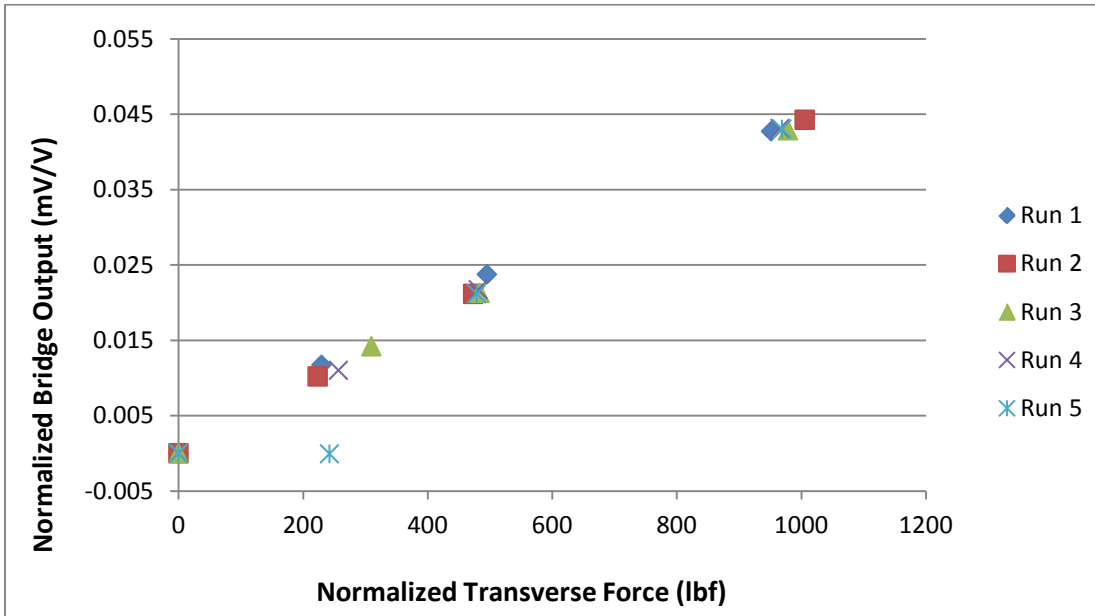
L20 – X Calibration (Rod 5)
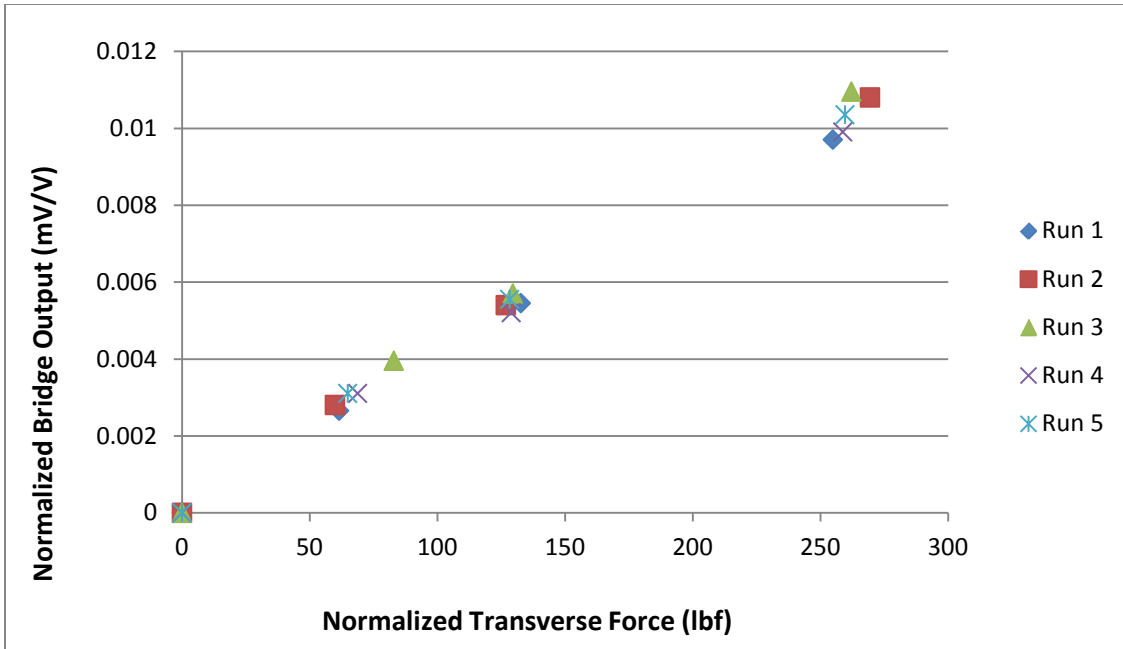
L21 – Y Calibration (Rod 5)
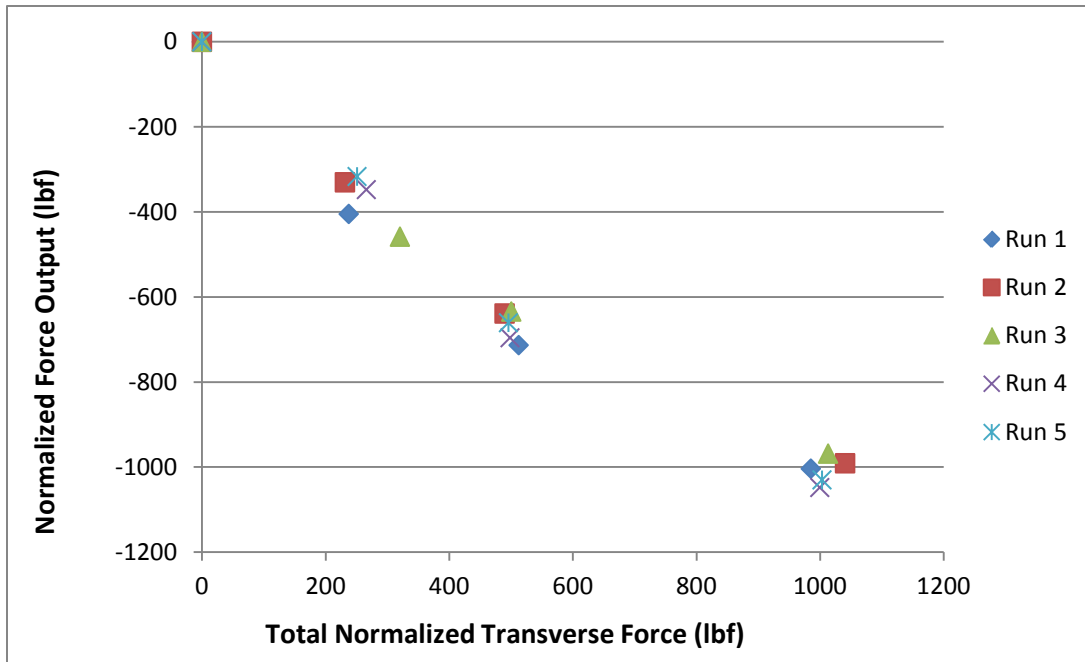
L22 – Axial Sensitivity to Transverse Loading (Rod 5)

L23 – X Sensitivity to Axial Loading (Rod 5)

L24 – Y Sensitivity to Axial Loading (Rod 5)

Rod 6

L25 – Axial Calibration (Rod 6)
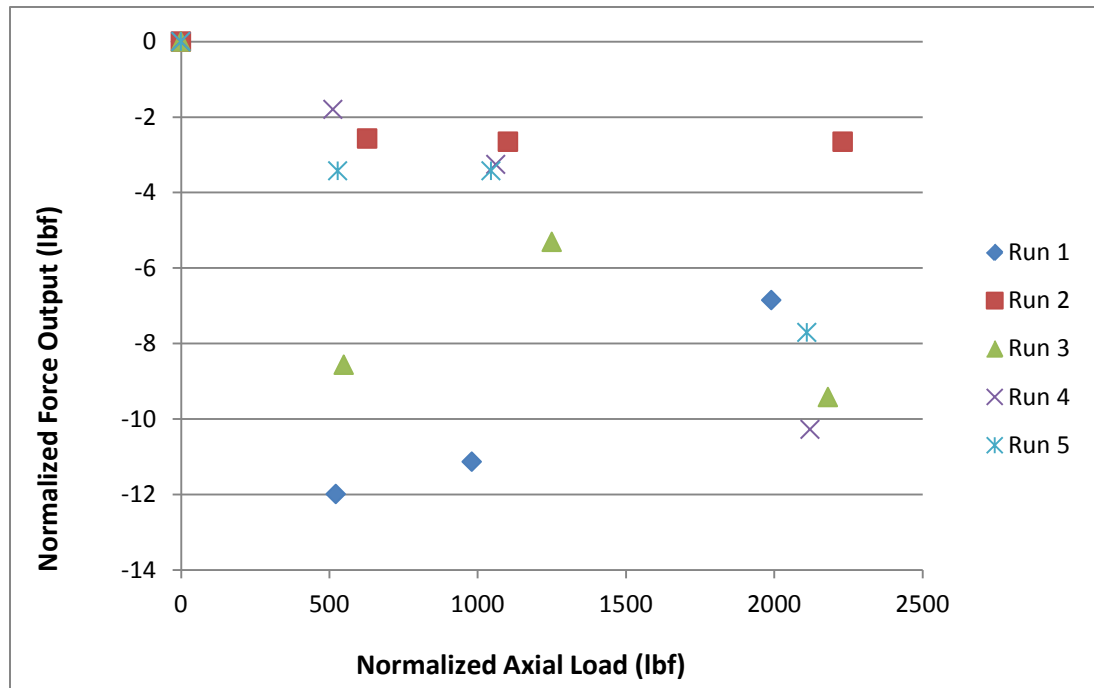

L26 – X Calibration (Rod 6)

L27 – Y Calibration (Rod 6)

L28 – Axial Sensitivity to Transverse Loading (Rod 6)

L29 – X Sensitivity to Axial Loading (Rod 6)

L30 – Y Sensitivity to Axial Loading (Rod 6)